

Ray-based Stochastic Inversion of Pre-stack Seismic Data for Improved Reservoir Characterisation

Proefschrift

ter verkrijging van de graad van doctor
aan de Technische Universiteit Delft,
op gezag van de Rector Magnificus prof. dr. ir. J.T. Fokkema,
voorzitter van het College voor Promoties,
in het openbaar te verdedigen,
op maandag 3 december 2007 om 10:00 uur

door

Dennis Wilhelmus VAN DER BURG

mijnbouwkundig ingenieur

geboren te Zoetermeer

Dit proefschrift is goedgekeurd door de promotor:

Prof. dr. ir. C.P.A. Wapenaar

Samenstelling promotiecommissie:

| | |
|--------------------------------|--|
| Rector Magnificus | voorzitter |
| Prof. dr. ir. C.P.A. Wapenaar, | Technische Universiteit Delft, promotor |
| Prof. dr. ir. J.T. Fokkema, | Technische Universiteit Delft |
| Prof. dr. ir. A. Gisolf, | Technische Universiteit Delft |
| Prof. dr. ir. R.J. Arts, | Technische Universiteit Delft |
| Prof. dr. W.A. Mulder, | Technische Universiteit Delft |
| Drs. A.R. Verdel, | Shell International Exploration and Production |
| Dr. G. Lambaré, | École des Mines de Paris / CGGVeritas |

Drs. A.R. Verdel heeft als begeleider in belangrijke mate aan de totstandkoming van het proefschrift bijgedragen.

ISBN 978-90-9022521-0

Copyright © 2007, by D.W. van der Burg, Section of Applied Geophysics and Petrophysics, Department of Geotechnology, Faculty of Civil Engineering and Geosciences, Delft University of Technology, Delft, The Netherlands.

All rights reserved. No part of this publication may be reproduced, stored in a retrieval system or transmitted in any form or by any means, electronic, mechanical, photocopying, recording or otherwise, without the prior written permission of the author.

SUPPORT

The research reported in this thesis has been financially supported by Shell International Exploration and Production.

Typesetting system: L^AT_EX 2_ε

Printed in The Netherlands by Sieca Repro Delft

Summary

Ray-based stochastic inversion of pre-stack seismic data for improved reservoir characterisation

To estimate rock and pore-fluid properties of oil and gas reservoirs in the subsurface, techniques can be used that invert seismic data. Hereby, the detailed information about the reservoir that is available at well locations, such as the thickness, wave propagation velocity, porosity, and pore-fluid type of individual layers, is extrapolated to all locations in the reservoir on the basis of seismic reflections. The initial layered reservoir model of which the properties are updated using the inversion is derived from well-log data, seismic trace data at the well location, seismic reflection picks and geological information. An advantage of the class of stochastic inversion algorithms is that also uncertainties in the property estimates can be computed.

Standard inversion techniques invert the seismic reflections, present in the form of band-limited signals called wavelets, from migrated data using a 1D convolutional forward modelling kernel; these methods thereby rely on the preceding migration procedure to take into account the propagation effects of seismic waves travelling through the subsurface. In practice however, inevitably wavelet distortion as a function of reflector dip and reflection angle is present on the migration image, and angle-range substacks, for enhancing signal-to-noise ratios, blur the reflection-angle information that is needed for resolving reservoir parameters. Any possible flaws in the migration cannot be accommodated for by the inversion.

To overcome the above-mentioned difficulties, in this thesis an alternative approach to stochastic inversion is introduced, in which the original wave-

path and reflection-angle information is taken inside the inversion. This means that the data must be inverted pre-stack before migration, which has the advantages that angle-dependent reflection information is not blurred and that migration-induced wavelet distortion does not occur. The reflection response corresponding with these data is modelled using 3D elastodynamic ray-tracing. The usage of the ray-tracer as forward modelling engine makes it possible to interweave seismic trace-inversion with Kirchhoff-type migration, in which ray-tracing is used as well. The new method is called ray-based stochastic inversion, and can be regarded as a generalisation of current amplitude-versus-offset/amplitude-versus-angle (AVO/AVA) inversion techniques. The new method is designed to outperform standard stochastic inversion techniques in cases of reservoir parameter estimation in a structurally complex subsurface with substantial lateral velocity variations and significant reflector dips.

In this thesis, also a simplification of the new method is presented for inverting the normal-incidence response from reservoirs with approximately planar layering at the subsurface target locations selected for inversion. The simplification concerns the use of 1D convolution to model the reflection response from the target; the effects of wave propagation in the overburden are still modelled using 3D ray-tracing. 1D convolution has the important practical advantage of being readily available in common inversion software. The simplified new method inverts along ray-paths that are perpendicular to the reflectors, the direction which offers optimal resolution for discerning the reservoir layering.

Results from synthetic data tests show that in strongly dipping reservoir structures, dip-dependent wavelet stretch due to migration severely deteriorates the reservoir parameter estimates obtained with standard inversion. Ray-based inversion has a much better performance in the cases shown.

Finally, in a test on field data from the Gulf of Mexico, a comparison is made between reservoir parameter estimates obtained with the simplified new method, the estimates found by conventional stochastic inversion, and the actual values at a well drilled after the inversion was done. Despite the fact that 1D convolutional ray-based stochastic inversion uses only 2% of the pre-stack data, the result indicates it has improved accuracy on the dipping part of the reservoir, where conventional stochastic inversion suffers from wavelet stretch due to migration.

Dennis van der Burg

Samenvatting

Stochastische inversie van pre-stack seismische data met behulp van de stralenbenadering van het golfveld voor een betere karakterisering van reservoirs

Om de eigenschappen te schatten van gesteenten en porievloeistoffen in aardolie- en aardgashoudende formaties in de ondergrond ('reservoirs'), kunnen technieken worden gebruikt die seismische data inverteren. Hierbij wordt de gedetailleerde kennis die beschikbaar is op de locatie van de boorputten, bijvoorbeeld de kennis over de dikte, golfpropagatiesnelheid, porositeit en porievloeistoftype van afzonderlijke gesteentelagen in het reservoir, geëxtrapoleerd naar andere lokaties in het reservoir met behulp van seismische reflecties. Het gelaagde beginmodel van het reservoir, waarvan de eigenschappen worden aangepast via inversie, wordt bepaald met behulp van boorgatmetingen, seismische data op de boorputlocatie, laaginterpretaties op seismische data en geologische informatie. Een voordeel van de klasse van stochastische inversiealgoritmen is dat ook de onnauwkeurigheden in de schattingen kunnen worden berekend.

Standaard inversietechnieken inverteren de seismische reflecties, aanwezig in de vorm van bandgelimiteerde signalen die wavelets worden genoemd, van gemigreerde data, gebruikmakend van een voorwaartse modellering gebaseerd op 1D convolutie; daarbij wordt aangenomen dat het voorafgaande migratieproces de propagatie-effecten van zich in de ondergrond voortplantende seismische golven in rekening te brengt. In de praktijk treedt echter onvermijdelijk waveletvervorming op in het migratiebeeld als functie van

hellingshoek van de reflector en reflectiehoek. Ook vertroebelt het optellen van reflectiesignalen bij het construeren van het uiteindelijke migratiebeeld de hoekafhankelijke reflectie-informatie die benodigd is voor het schatten van reservoir eigenschappen. Mogelijke tekortkomingen in het migratieproces kunnen niet meer worden tenietgedaan door de inversie.

Om bovengenoemde problemen op te lossen, wordt in dit proefschrift een alternatieve aanpak voor stochastische inversie geïntroduceerd, waarbij de oorspronkelijke informatie over golfpaden en reflectiehoeken binnen de inversie wordt gebracht. Dit betekent dat de data geïnverteerd moeten worden voordat deze worden opgeteld en gemigreerd, wat als voordeel heeft dat de hoekafhankelijke reflectie-informatie niet is vertroebeld en dat waveletvervorming als gevolg van migratie niet optreedt. De reflectierespons behorend bij deze data wordt gemodelleerd met behulp van 3D elastodynamische stralentheorie. Het gebruik van stralentheorie voor de voorwaartse modellering maakt het mogelijk om seismische inversie met Kirchhoff-type migratie te verweven; immers, Kirchhoff-type migratie maakt ook gebruik van stralentheorie. De nieuwe methode heet in het Engels ‘ray-based stochastic inversion’ en kan worden beschouwd als een generalisatie van huidige amplitude-versus-offset/amplitude-versus-reflectiehoek (AVO/AVA) inversietechnieken. De nieuwe methode is ontworpen om betere resultaten op te leveren dan de standaardtechnieken voor stochastische inversie in een ondergrond met een ingewikkelde structuur, waarin aanzienlijke laterale variaties in de golfpropagatiesnelheid en grote hellingshoeken van reflecterende laagbegrenzingsen voorkomen.

In dit proefschrift wordt ook een vereenvoudiging van de nieuwe methode geïntroduceerd om opnamen met loodrechte invalshoek te inverteren wanneer het reservoir een bij benadering evenwijdige interne gelaagdheid heeft op de lokaties waarvoor inversie uitgevoerd wordt. De vereenvoudiging bestaat uit het gebruik van 1D convolutie om de reflectierespons van het reservoir te modelleren; golfpropagatie in de bovenliggende gesteentelagen tot aan het aardoppervlak gebeurt nog steeds met behulp van 3D stralentheorie. Het gebruik van 1D convolutie heeft als praktisch voordeel dat het beschikbaar is in de meeste standaardinversiesoftware. De vereenvoudigde nieuwe methode inverteert langs straalpaden die loodrecht staan op de reflectoren; dit is de richting die optimale resolutie biedt voor het zichtbaar maken van de gelaagdheid.

Resultaten van tests op synthetische data laten zien dat in sterk hellende reservoirstructuren, hellingshoekafhankelijke waveletvervorming als gevolg van migratie de schattingen van reservoirparameters verkregen middels standaardinversie aanzienlijk verslechteren. Inversie gebaseerd op stralentheorie geeft in de getoonde voorbeelden veel betere resultaten.

In een test op seismische velddata, gemeten in de Golf van Mexico, wordt tenslotte een vergelijking gemaakt tussen reservoirparameterschattingen verkregen met de vereenvoudigde nieuwe methode, met de standaardmethode en met de werkelijke waarden verkregen uit een boorput nadat de inversie was uitgevoerd. Ondanks het feit dat de nieuwe methode maar 2% van de opgenomen data gebruikt, wijst het resultaat op een verbeterde nauwkeurigheid op het hellende gedeelte van het reservoir, het gedeelte waar standaardinversie last heeft van hellingshoekafhankelijke waveletvervorming als gevolg van migratie.

Dennis van der Burg

Contents

| | |
|--|------------|
| Summary | i |
| Samenvatting | iii |
| Table of Contents | vii |
| List of Abbreviations | xi |
| 1 Introduction | 1 |
| 1.1 Imaging subsurface structures | 2 |
| 1.2 Zooming in on the target | 3 |
| 1.2.1 Estimating reservoir parameters | 5 |
| 1.2.2 Limitations of current inversion methods | 5 |
| 1.3 New approach to reservoir parameter estimation | 7 |
| 1.3.1 Principles of ray-based inversion | 7 |
| 1.3.2 Principles of the ray-method | 8 |
| 1.4 Potential benefits from the new approach | 11 |
| 1.5 Research objective | 12 |
| 1.6 Outline of the thesis | 12 |
| 2 Stochastic inversion | 15 |

| | | |
|----------|--|-----------|
| 2.1 | Inversion theory | 16 |
| 2.1.1 | Introduction to inverse problems | 16 |
| 2.1.2 | Introduction to probability theory | 18 |
| 2.1.3 | Bayesian inversion | 22 |
| 2.1.4 | Estimating uncertainties with Monte Carlo | 24 |
| 2.2 | Stochastic trace inversion | 26 |
| 2.3 | Workflow for stochastic inversion | 29 |
| 2.4 | Inversion domain - the migrated image | 32 |
| 2.4.1 | TA Kirchhoff migration: retrieving reflection coefficients | 32 |
| 2.4.2 | Vertical and lateral resolution | 42 |
| 2.4.3 | Pulse distortion | 43 |
| 2.5 | Forward modeller - 1D convolutional modelling | 48 |
| 2.6 | Discussion | 52 |
| 3 | Ray-based stochastic inversion | 55 |
| 3.1 | From stochastic inversion to RBSI | 56 |
| 3.1.1 | RBSI principle | 57 |
| 3.1.2 | Linking inversion with Kirchhoff-type migration | 60 |
| 3.1.3 | RBSI in ‘layer-stripping’ mode | 62 |
| 3.2 | Workflow for RBSI | 64 |
| 3.3 | Inversion domain - the recording time domain | 69 |
| 3.4 | Forward modeller - 3D elastodynamic ray-tracing | 73 |
| 3.4.1 | Ray-validity conditions | 74 |
| 3.4.2 | Ray-amplitudes in a 3D configuration | 76 |
| 3.4.3 | Ray-amplitudes in a 2.5D caustic-free NI configuration | 82 |
| 3.5 | Discussion | 85 |
| 3.6 | Special case - 1D convolutional RBSI | 87 |
| 3.6.1 | Principles | 88 |
| 3.6.2 | Theory | 90 |
| 4 | Synthetic data tests | 95 |
| 4.1 | Lateral layer-density variations | 96 |
| 4.1.1 | Gaussian density model | 96 |
| 4.1.2 | Wedge-like density model | 105 |
| 4.2 | Lateral P-wave velocity and thickness variations | 107 |

| | | |
|----------|--|------------|
| 4.2.1 | Single dipping layer | 107 |
| 4.2.2 | Five plane-parallel dipping layers | 115 |
| 4.2.3 | Gaussian model with target of five layers | 120 |
| 4.3 | Rock model test | 134 |
| 4.3.1 | Model geometry | 134 |
| 4.3.2 | Rock models | 135 |
| 4.3.3 | Exact rock parameters | 138 |
| 4.3.4 | Normal-incidence dataset | 140 |
| 4.3.5 | Estimated rock parameters by 1D convolutional RBSI | 140 |
| 4.4 | Offset tests | 141 |
| 4.4.1 | Model geometry | 142 |
| 4.4.2 | Prestack unmigrated datasets | 143 |
| 4.4.3 | Ideal stacked migrated datasets | 147 |
| 4.4.4 | Inversion results: SI vs. RBSI | 147 |
| 4.5 | Discussion | 149 |
| 5 | Field data test | 151 |
| 5.1 | Seismic data description | 152 |
| 5.1.1 | Acquisition parameters | 154 |
| 5.1.2 | Processing before migration | 155 |
| 5.1.3 | True-amplitude pre-stack depth migration | 159 |
| 5.2 | Inversion strategy | 160 |
| 5.3 | Seismic data selection for inversion | 162 |
| 5.3.1 | 2.5D setting | 163 |
| 5.3.2 | Proximity of wells | 164 |
| 5.3.3 | Data quality | 165 |
| 5.4 | Model geometry | 169 |
| 5.5 | Applying SI | 170 |
| 5.5.1 | Wavelet derivation | 170 |
| 5.5.2 | Prior model | 173 |
| 5.5.3 | Inversion results | 174 |
| 5.6 | Applying 1D convolutional RBSI | 174 |
| 5.6.1 | Pre-stack seismic data selection | 174 |
| 5.6.2 | Wavelet derivation | 180 |
| 5.6.3 | Transforming the SI prior model | 181 |
| 5.6.4 | Overburden amplitude correction | 184 |

| | | |
|----------|--|------------|
| 5.6.5 | Inversion results | 190 |
| 5.7 | Comparison at Well-II | 192 |
| 5.8 | Discussion | 193 |
| 6 | Conclusions and recommendations | 199 |
| 6.1 | Conclusions | 200 |
| 6.2 | Recommendations for further research | 200 |
| | Bibliography | 203 |
| | Curriculum Vitae | 211 |
| | Acknowledgements | 213 |

List of Abbreviations

| | |
|--------|---------------------------------|
| AVO | Amplitude variation with offset |
| AVA | Amplitude variation with angle |
| CMP | Common midpoint |
| DMO | Dip moveout |
| NI | Normal-incidence |
| NMO | Normal moveout |
| PreSDM | Pre-stack depth migration |
| PreSTM | Pre-stack time migration |
| RBSI | Ray-based stochastic inversion |
| SI | Stochastic inversion |
| SF | Sand-fraction |
| S/N | Signal-to-noise ratio |
| TA | True-amplitude |

Introduction

Inversion of seismic data is commonly used in oil and gas field development for refining structural interpretation and reservoir geometry, reservoir characterisation, property prediction, and reducing uncertainties in field development. Hereby, the detailed information about the reservoir known at the wells is extrapolated to all locations in the reservoir on the basis of seismic reflections. At reservoir level, a link between the seismic data at the well location and the well needs to be established with a seismic-to-well tie.

Specifically challenging is the accurate reservoir parameter determination, including uncertainty estimation, in a structurally complex subsurface with substantial lateral velocity variations and significant reflector dips. In this thesis, a new inversion method is presented for estimation of reservoir parameters from seismic data, which is suitable for use in such subsurface settings. The method, called ray-based stochastic inversion, uses ray-based modelling and inverts pre-stack unmigrated data.

The basic principles of seismic exploration of the Earth's subsurface, yielding the seismic data to be inverted, and the basics of conventional versus novel inversion will be explained in this first chapter, thereby introducing seismic terms used throughout the remainder of this work. The chapter ends with the formulation of the research goal and an outline of the thesis.

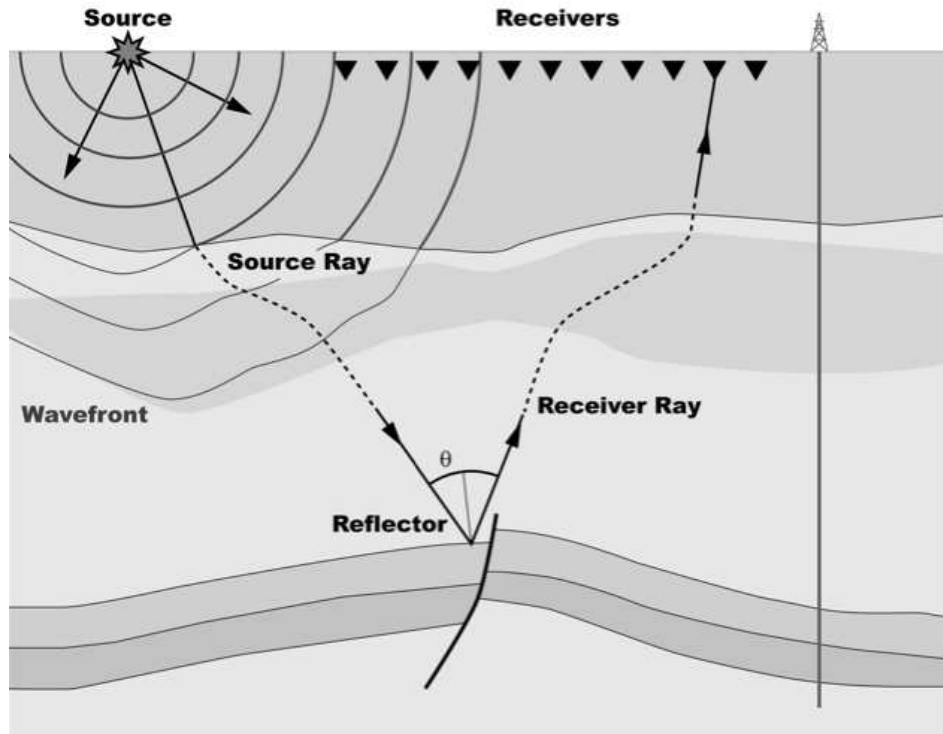


Figure 1.1: A seismic experiment at the Earth's surface; axes display horizontal distance vs. depth. A single wave path from source to receiver is shown, reflecting at a contrast between two layers in the subsurface. The normal to the contrast at the reflection point divides the angle between source and receiver ray in two equal parts θ : the angle of incidence and the reflection angle.

1.1 Imaging subsurface structures

Exploration seismology is aimed at producing a migration image, revealing the structures in the Earth's subsurface. To obtain such an image, e.g. for pinpointing the location of a gas or oil bearing reservoir positioned at a few kilometers depth, a seismic survey has to be deployed.

In Figure 1.1, the most important elements of a seismic survey are shown. From a seismic source, sound waves travel in all directions through the subsurface, forming wavefronts. Part of the wavefield reflects back at subsurface

contrasts in medium properties, to arrive at receivers placed at the surface. One of the paths from source to receiver is depicted, consisting of a part from the source to the subsurface contrast (reflector), the source *ray*, and a part from the contrast to the receiver, called receiver ray. Note that, strictly speaking, the concept of rays so conveniently used in this description, is a high-frequency approximation. At the contrast, specular *reflection* takes place with a certain reflection angle θ , measured between source or receiver ray and the normal to the reflector.

The traveltimes of the reflection responses recorded at the receiver gives information about the location of the reflection point, while the amplitude carries information on the size of the contrast. During a seismic survey, recordings are made for many different shot and receiver positions, yielding sufficient information to build an image of subsurface contrasts with a procedure called *migration*. At the seismic data processing centre, the data, consisting of all reflection responses recorded during the survey, are first pre-processed for removal of undesired events and for migration velocity model building. Once a good velocity model has been found, which is usually the most difficult task in the entire processing sequence, one of the many available migration algorithms is chosen to migrate the data [Yilmaz, 2001; Sheriff and Geldart, 1995; Gray et al., 2001].

Ideally, migration yields an accurate image of the Earth's reflectivity [Black et al., 1993], reflectivity being a function of subsurface density contrasts and wave propagation velocity contrasts. In such a migration image in depth, schematically displayed in Figure 1.2, contrasts are depicted on their correct positions by a pulse in depth (corresponding to a wavelet in the time-domain), of which the amplitude is a measure of the wave propagation velocity and density differences between both sides of the contrast.

1.2 Zooming in on the target

The input data for migration, i.e. the recorded reflection responses as a function of traveltimes, are *band-limited* due to the finite duration of the source wavelet. The used source wavelet causes the reflections to be recorded as wavelets too. The image obtained by migration is band-limited as well: the time pulses from the input data are converted to depth pulses of a certain length when migrated to depth [Tygel et al., 1994].

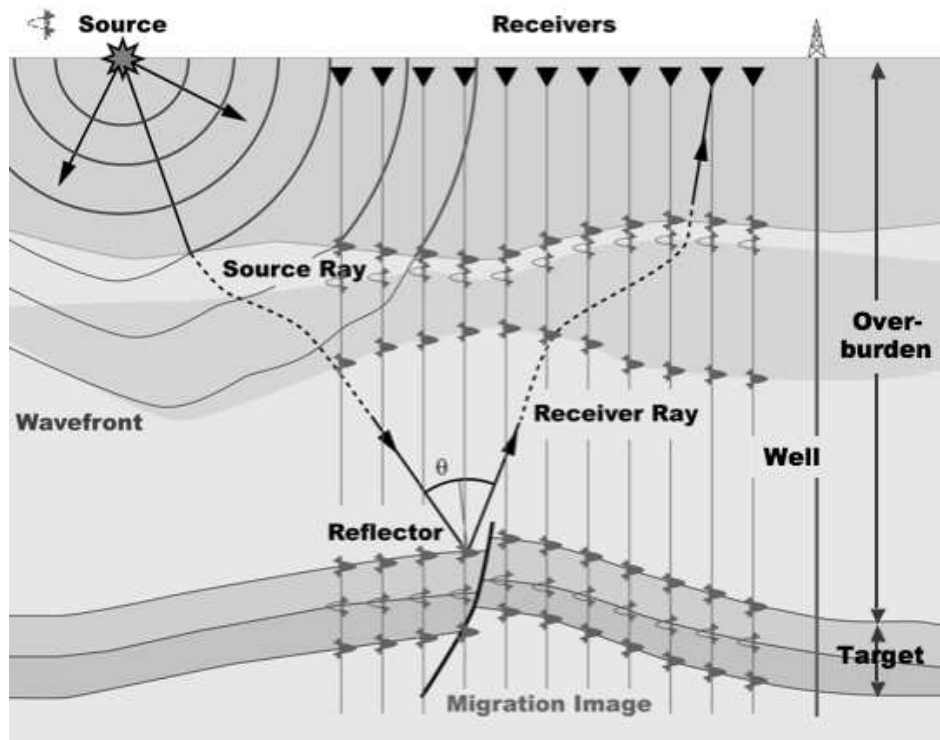


Figure 1.2: Migration image of subsurface contrasts; axes display horizontal distance vs. depth. The image is spatially band-limited due to the finite duration of the source pulse. The area of interest is labelled 'target', and is intersected by a well.

A wavelength can be assigned to the depth pulses. Dominant wavelengths at reservoir depths on the migration image in the order of hundreds of meters are quite common for exploration seismic surveys, see e.g. [Yilmaz \[2001, p. 1801\]](#); this seriously confines the minimum thickness of layers that still can be discerned on the image. As a rule of thumb, a layer that has a thickness of less than 1/8-th of a dominant wavelength is not discernable anymore [[Widess, 1973](#); [Kallweit and Wood, 1982](#)].

It is the area of interest on the migration image, the *target* (Figure 1.2), where we would like to resolve layer thicknesses below the seismic resolution limit, to reduce uncertainties in reservoir development, e.g. for determining the

position of thin reservoir sands or optimizing the placement of development wells. In the *overburden* overlying the target, the resolution offered by the migration image is generally sufficient.

■ 1.2.1 Estimating reservoir parameters

In the target area, *seismic trace inversion* integrates seismic data, information from nearby wells (Figure 1.2) and geological information, to make it possible to estimate from the migration image the thicknesses of fine layers, as well as many other reservoir layer parameters like velocity, density, porosity, pore-fluid type and pore-fluid saturation. This is normally accomplished in a trace-by-trace, iterative fashion whereby an initial subsurface model, derived from nearby well-log data and geological knowledge about the region, is updated at the trace location. Initial positioning of reflectors in the starting model is derived from seismic reflection event picks, taken from the migration image.

The wavelet for inversion is derived from a seismic-to-well tie (which is an inversion procedure by itself). In practice, the wavelet on the migration image will be similar, but not identical to the source wavelet due to a number of factors. For example, preferred absorption of high frequencies occurs during wave propagation in dissipative media will change the shape of the wavelet [Aki and Richards, 1980, ‘frequency-dependent Q-factor’].

Many trace inversion techniques exist; a recent overview is given by Veeken and Da Silva [2004]. Throughout this thesis, the *stochastic inversion* kernel will be used. In stochastic trace inversion, Bayes’ rule is applied to trace inversion, enabling an elegant incorporation of prior information available from geology and well-logs, and at the same time allowing a quantification to be made of uncertainties in reservoir parameter estimates [Duijndam, 1988a,b]. In Chapter 2, seismic trace inversion and the stochastic inversion kernel are explained in detail.

■ 1.2.2 Limitations of current inversion methods

A basic flow sheet for inversion is given at the right-hand side of Figure 1.3. The seismic trace inversion method inverts migrated data using a 1D convolutional forward modelling kernel; realistic wave path information is not used in the inversion process. Conventional trace inversion ideally relies

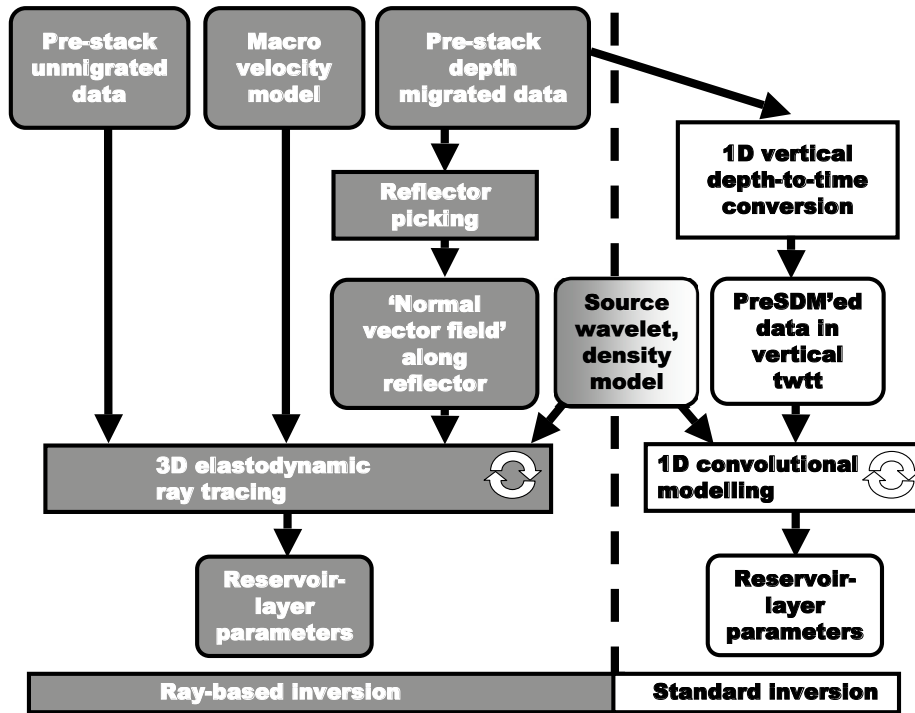


Figure 1.3: Flow chart for the new ray-based inversion (left) and the standard method (right). Both employ stochastic inversion kernels, however the new scheme uses 3D ray-based modelling, and is applied to pre-stack unmigrated data.

on so-called true-amplitude pre-stack depth migration for removing all wave propagation effects, including those related to interface transmissions, within overburden and target zone. Pre-stack depth migration is required in case of strong lateral subsurface velocity variations.

However, the 1D convolutional kernel does not take into account that the migration image displays finite lateral resolution and limited illumination of reflectors [Chen and Schuster, 1999; Toxopeus et al., 2003]. The same holds for dip-dependent pulse distortion [Tygel et al., 1994] on the migration image. Consequently, also the true-amplitude migration mentioned above, besides the fact that it is often not available, does not yield the perfect band-limited image of the Earth's reflectivity as required for 1D convolutional

forward modelling. Moreover, the migration image is the fixed result of an extensive, separate processing scheme. Some of the processing steps, such as angle-range substacks for enhancing signal-to-noise ratios, blur the reflection angle information that is crucial for resolving reservoir parameters [Levin, 1998]. Any possible flaws in the preceding migration have to be taken for granted and cannot be accommodated for by the inversion. Above-mentioned complications are suspected to degrade inversion results, especially in a structurally complex subsurface with substantial lateral velocity variations. In Chapter 2, current inversion practices will be looked upon more closely.

1.3 New approach to reservoir parameter estimation

For inversion of rock and pore-fluid properties in a laterally strongly varying, fine-layered target reservoir sequence, it is proposed to bring the original ray-path and reflection angle information, contained in the pre-stack unmigrated data, inside the inversion algorithm. Doing so, the migration-related limitations of inversion described in the previous section can thus be lifted. Below, the principles of the new inversion method, that forms the subject of this thesis, are outlined.

■ 1.3.1 Principles of ray-based inversion

3D elastodynamic ray-tracing for the forward modelling of pre-stack unmigrated data, founded on a parameterisation of the reflection process in terms of reflection angles, is the basic ingredient of the new inversion technique. Therefore, the ray-method is briefly described in the next subsection.

The subsurface model for the new method is hybrid: a coarse subsurface macro-model describes the elastic parameter distribution in the overburden, whereas the target is described by a detailed layered model in which all reservoir parameters of interest for inversion are incorporated. The coarse overburden model may consist of a single grid of elastic parameters P-wave velocity, S-wave velocity and density, or a set of grids bounded by interfaces. The detailed thin-layered target model, which can only be built with the aid of well-logs giving rock and pore-fluid information on a sub-seismic resolution, is characterised by layer parameters such as P-wave velocity and

density of mineral grains and pore-fluid, porosity, pore-fluid type, pore-fluid saturation, sand-fraction and thickness. From such parameters, the three elastic layer-properties are subsequently calculated for each target layer using lithology-dependent rock models.

Ray-based modelling by the new method requires that reflectors be picked on the migration image for the purpose of generating reflector normal vector fields. Ray-tracing is used for mapping reflection points in the target, connecting a ray-pair, to source/receiver positions at the surface, as a function of reflection angle (Figure 1.4). In the ideal case, isolated inversions are carried out for a selected reflection angle (or for a reflection angle range) and for a pre-specified set of reflectors in the target zone. The parameterisation of the reflection process in terms of reflection angle follows naturally and logically from the important role that the reflection coefficient as a function of reflection angle plays in estimating reservoir properties.

Reservoir parameters are estimated by iteratively updating the layered target model until a satisfactory fit is obtained between measured and modelled reflections. More specifically, ray-tracing is performed to the target interfaces, and synthetic traces are generated using a wavelet derived from the data. In each iteration, the synthetic traces are compared, in the time window corresponding to the target zone, with the traces having the same source/receiver positions from the pre-stack unmigrated dataset.

The proposed workflow is depicted on the left hand side of Figure 1.3. Note that the new approach concerns the integration of existing technologies: the building blocks, such as the elastodynamic ray tracer, the pre-stack depth migration and the stochastic inversion kernel, are all readily available. The method will be introduced formally in Chapter 3.

■ 1.3.2 Principles of the ray-method

3D elastodynamic ray-tracing forms the basic ingredient of the new inversion technique. It is useful to briefly describe the ray-method below; meanwhile, a few more concepts are introduced that are used throughout the thesis. An exhaustive treatment of the ray-method is found in Červený [2001]. Ray-amplitudes are discussed in detail in section 3.4.

In the ray-method, a high-frequency approximate solution of the acoustic or elastodynamic equation for wave propagation is derived using the ray se-

ries approach. The derivation of the acoustic and elastodynamic wave equation from generalised Newton's law and Hooke's law is explained in many textbooks, e.g. [Wapenaar and Berkhout \[1989, Chapter I, II\]](#). For wave-propagation in an inhomogeneous, isotropic, elastic subsurface, the (source-free) elastodynamic equation reads [[Červený, 2001, Eq. \(2.1.4\)](#)],

$$\rho \frac{\partial^2 u_i}{\partial t^2} = \frac{\partial \tau_{ij}}{\partial x_j}, \quad (1.1)$$

which relates the spatial variations of stress tensor components τ_{ij} [Pa = kg/(m s²)] to the time variations of the particle displacement vector components u_i [m], with ρ the density [kg/m³]. Einstein's summation convention is used to write this equation in a compact form. The subscripts take values 1, 2, or 3 and refer to the component in corresponding direction, in a right-handed Cartesian coordinate system with positions described by x_i . To obtain expressions for the kinematic and dynamic properties of the wave-field, in the elastodynamic equation of motion Eq. (1.1), a ray series expansion solution in inverse powers of frequency is substituted, of a form valid only in the high-frequency approximation,

$$u_i(\vec{x}, t) = \text{Re} \left[\sum_{n=0}^{\infty} U_i^{(n)}(\vec{x}) F_n(t - \tau(\vec{x})) \right], \quad (1.2)$$

with t denoting traveltime, F_n the so-called analytical signal, 'Re' indicating taking the real part to obtain a physically meaningful solution, and the dynamic and kinematic behaviour contained in amplitude coefficients $U_i^{(n)}(\vec{x})$ and eikonal $\tau(\vec{x})$, respectively; see e.g. [Červený \[2001\]](#) or [Verdel \[1983\]](#) for detailed derivations. Solutions are sought for $\tau(\vec{x})$, yielding ray-paths and traveltimes via the system of eikonal equations,

$$((\nabla\tau)^2 - \alpha^{-2}) ((\nabla\tau)^2 - \beta^{-2}) = 0, \quad (1.3)$$

in which $(\nabla\tau)^2$ is a shorthand for $\nabla\tau \cdot \nabla\tau$. A wave satisfying Eq. (1.3) is called a compressional wave (P-wave) if $(\nabla\tau(\vec{x}))^2 = \alpha^{-2}(\vec{x})$, or a shear wave (S-wave) if $(\nabla\tau(\vec{x}))^2 = \beta^{-2}(\vec{x})$; $\alpha(\vec{x})$ and $\beta(\vec{x})$ are the wave propagation velocities of the respective waves, expressed as a function of the medium parameters density $\rho(\vec{x})$ and Lamé coefficients $\lambda(\vec{x})$ and $\mu(\vec{x})$,

$$\alpha = \sqrt{\frac{\lambda + 2\mu}{\rho}}, \quad \beta = \sqrt{\frac{\mu}{\rho}}. \quad (1.4)$$

In the rest of this thesis, v_p is used as notation for α , and v_s for β . From Eq. (1.3) it follows that in an inhomogeneous isotropic elastic subsurface, the P- and S-waves can propagate independently in the high frequency approximation. In this work, we will model only the propagation of P-waves. Furthermore, solutions are sought for $U_i^{(n)}(\vec{x})$, yielding the amplitudes via the transport equations for P- and S-waves,

$$\frac{\partial U_i}{\partial s} + \frac{1}{2} U_i \left(v \nabla^2 \tau + \frac{\partial \ln(\rho v^2)}{\partial s} \right) = 0, \quad (1.5)$$

with s the arclength along the ray, and v the corresponding velocity for P- or S-waves. Usually, it is sufficient to consider only the leading term ($n = 0$) of equation (1.2): for the zero-order amplitude function $U_3^{(0)}(\vec{x})$ and analytical signal $F_0(t)$, equations are given in section 3.4.

In principle, the approximate expression for $\vec{u}(\vec{x}, t)$ obtained by ray-theory gives valid results only for high frequencies ω or, equivalently, small wavelengths λ in relation to the variations present in the medium. More formally phrased, in the application regime for ray-tracing, the following condition must be fulfilled: $\lambda \ll l_i$, where λ is the dominant wavelength of the regarded wave, and l_i are lengths describing the scale of medium property variations in the subsurface, and/or radii of curvature of layer-interfaces [Červený, 2001, section 5.9.1]. The ray-validity conditions are described in more detail in section 3.4.

Although a fine-layered target is not strictly obeying all ray-tracing validity conditions, in this work primaries-only ray-tracing is used to model the target's reflection response, in order to achieve sub-wavelength resolution at target-level through inversion of the recorded response. Hereby it is assumed that the total reflection response can be linearised as the sum of the separate reflection responses of the individual contrasts. These separate responses can be modelled by ray-tracing without problems. For this approach to be a success the contrasts between the thin layers must be small, otherwise interactions between the reflections have to be taken into account by special ray-codes [O'Doherty and Anstey, 1971].

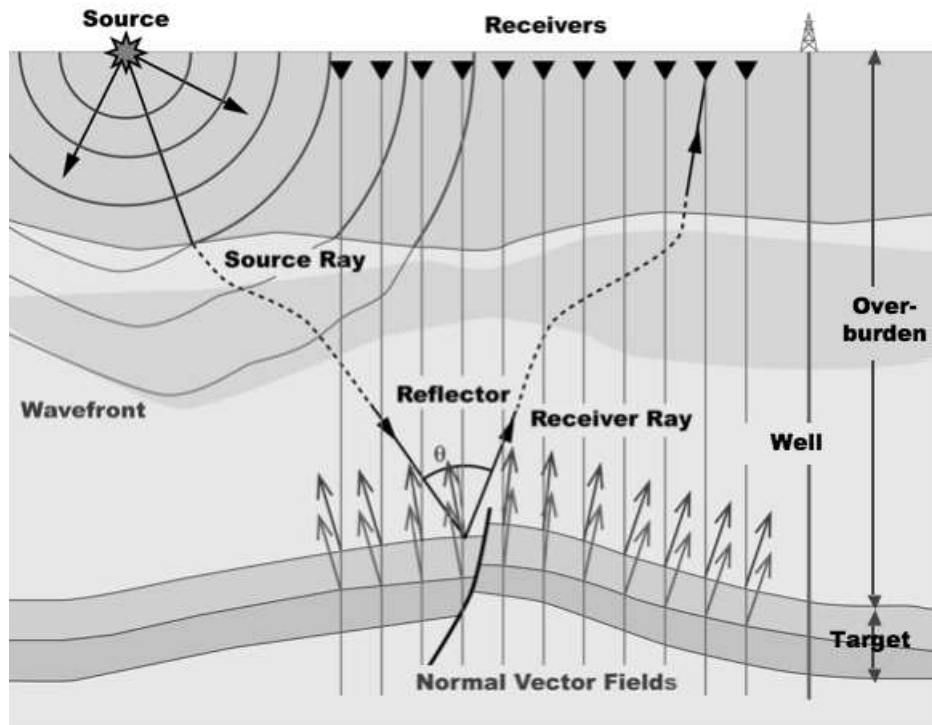


Figure 1.4: Subsurface with an inversion target. A ray-pair to the target is shown, with reflection angle θ . Normal-vector fields in the target, needed to map reflection points to source/receiver positions via ray-tracing, are indicated by arrows.

1.4 Potential benefits from the new approach

The potential benefits of the new method include the following. Firstly, it is expected that by incorporating the original ray-path and reflection angle information, contained in the pre-stack unmigrated data, into the inversion algorithm, a more accurate reflection amplitude representation in the target zone can be obtained, and hence a more accurate description of reservoir parameter distributions, in comparison with existing inversion practices. Conventionally, seismic data is inverted in which the amplitude information is (partly) lost during the stacking and migration processes (or even in earlier

pre-processing steps).

Evenly important is that with the new approach, it would become possible to re-use selected parts of wave path information already used in (ray-based types of) migration, creating a direct link between migration and trace inversion, at the same time reducing the amount of extra computing-power required to invert on unmigrated data. The wave path information contained in the migration operators, as it was used in the preceding migration, is normally not exploited after finalisation of the migration process. At least part of that information could be re-used with the new method.

1.5 Research objective

The objective of this research is to develop a novel stochastic inversion method that is suitable for use in complex velocity media. The novelty lies in the fact that two existing techniques, stochastic inversion and ray-based modelling, are combined. The inversion will be performed in the pre-stack unmigrated domain.

It is assumed that, prior to inversion, pre-stack depth migration has been applied to the seismic data. In contrast to currently available inversion techniques, wave path information as it was used in the preceding depth migration will be exploited in the new inversion approach.

1.6 Outline of the thesis

Since the new approach to inversion integrates different techniques, it is necessary to cover a broad range of subjects: the thesis is set up as follows. Chapter 2 introduces the conventional scheme for seismic trace inversion using the stochastic inversion kernel, called Stochastic Inversion (SI). The stochastic inversion kernel is presented first, by introducing Bayesian inversion theory, and its application to seismic trace inversion. Then, an SI-workflow is given for the estimation of reservoir parameters from seismic data. Finally, the focus is put on the two fundamental differences between the conventional and new inversion method: the inversion domain, and the forward modeller used. These are, for SI, the migrated image and the 1D convolutional model, respectively.

The third chapter presents the new inversion scheme, Ray-Based Stochastic Inversion (RBSI). The principles of the method and an RBSI-workflow are given for reservoir parameter estimation. As in the previous chapter, the two fundamental differences are highlighted between the conventional and new inversion method: RBSI inverts pre-stack unmigrated data, and uses 3D elastodynamic ray-tracing as forward modeller. It is this forward modeller that enables a link with Kirchhoff-type migration, which uses ray-tracing as well, for generation of traveltimes tables and migration weights. The discussion of a special case of RBSI, 1D Convolutional RBSI, concludes this chapter.

The potential of the new inversion method is investigated in the next two chapters. First, in Chapter 4, this is done by performing tests on synthetic models. RBSI is tested against SI in inversion for density on a model with Gaussian reflectors and layer-density variations, and also for a wedge model. Using the test results, an assessment is carried out of the largest sources of misestimation in SI. Subsequently, 1D Convolutional RBSI is tested against SI in inversion for P-velocity and thickness for a series of models, ranging from the simple but illustrative single dipping layer to complex multi-layer models. Finally, a few simple offset tests are done, to illustrate the advantages of the RBSI-workflow in a more general case.

Chapter 5 describes the testing of the new inversion method on field data from the Gulf of Mexico. The real dataset was carefully chosen to include an inversion target with a relatively simple horizontal part, gradually changing into a complex part with a substantial dip more suitable for (1D convolutional) RBSI. Starting with the same prior reservoir model as SI, inversion is done using the new scheme for the key reservoir parameters P-velocity, layer thickness and sand-fraction. The chapter concludes with a comparison of the results with those obtained by SI, and with the actual values along a borehole drilled through the inversion target later on.

Assembling the information gathered in all previous chapters, in Chapter 6 conclusions are drawn with respect to the novel inversion method and a set of recommendations is formulated for future research on ray-based inversion. Finally, note that for the reader's convenience, the chapters are set up to be separately readable as much as possible. This choice will however lead to some redundancy in the text and figures.

Stochastic inversion

After the first phase of seismic exploration and processing, a migration image of subsurface structures has been built, and the area of interest has been successfully localised in the subsurface (Chapter 1). In the next phase, we would like to extract from the seismic data more information about the target, such as the positioning of thin layers, as well as the spatial distribution of many other layer parameters, like porosity, fluid type and saturation. It is here, that seismic trace inversion comes in.

In this chapter, it is explained how trace inversion for reservoir parameters commonly is achieved, so that the analogies and differences with the new inversion scheme (Chapter 3), and the need for that new scheme, can be better appreciated. The method discussed is a scheme for seismic trace inversion using a stochastic inversion kernel, a Stochastic Inversion (SI) scheme.

The chapter is structured as follows. First, in order to gain more understanding of SI, inversion theory is introduced in general, and Bayesian inversion theory in particular, followed by application of the latter on seismic traces. Subsequently, by means of the SI workflow, the various aspects of seismic trace inversion are illuminated. Finally, attention is on two major aspects discerning SI from the new method: the domain of inversion and the for-

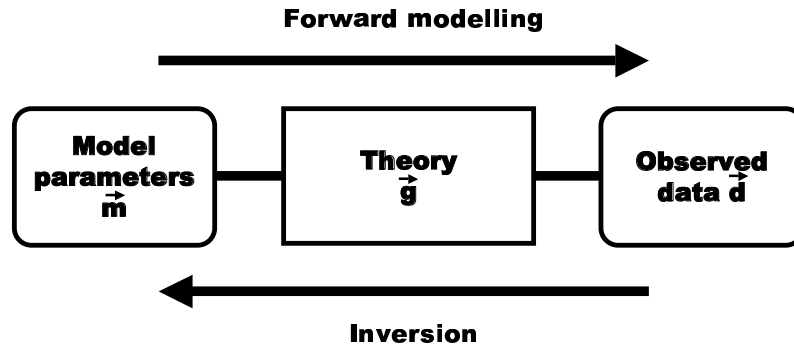


Figure 2.1: Forward modelling and inversion. Data \vec{d} are the measured outcome of an experiment. After *Duijndam and Drijkoningen [1997, Figure 1.1]*.

ward modeller; for SI these are the migrated image and 1D convolutional modelling, respectively. The chapter ends with a discussion.

2.1 Inversion theory

Stochastic trace inversion is a specific subset of trace inversion techniques, which allows a quantification to be made of uncertainties in reservoir parameter estimates. This is achieved by applying Bayes' rule to seismic trace inversion (section 2.2). As a prelude, the Bayesian approach to inversion is introduced in this section. To that end, first the general concept of parametric inversion, or parameter estimation, is explained. Then, the fundamentals of probability theory are reviewed. Subsequently, Bayes' rule is derived. Finally, the method used in this thesis for evaluating Bayesian inversion results, including uncertainties, is discussed.

■ 2.1.1 Introduction to inverse problems

Consider an experiment and its measured outcome, and a theory well explaining the phenomena encountered in the experiment. Given the theory and the set of parameters associated with the theory and the experiment, the measured data can be predicted, in principle. This is called the forward problem, see Figure 2.1. From this figure, it is also seen that, obviously, the

reverse of the situation just described is called the inverse problem: given the observations made during an experiment, and the appropriate theory, the unknown model parameters are estimated.

Let the data, consisting of M observations, be put in a column vector $\vec{d} = (d_1, d_2, \dots, d_M)^T$ (with the “ T ” denoting transposition), and N model parameters be put in $\vec{m} = (m_1, m_2, \dots, m_N)^T$. Using the parameters, the theory \vec{g} describes the outcome \vec{d} of the experiment; this can be written as the forward model $\vec{d} = \vec{g}(\vec{m})$. If a noise-term $\vec{n} = (n_1, n_2, \dots, n_M)^T$ is added to take into account theoretical or experimental errors, the result is the so-called standard reduced model [Duijndam and Drijkoningen, 1997, Eq. (4.5)],

$$\vec{d} = \vec{g}(\vec{m}) + \vec{n} . \quad (2.1)$$

In the particular case that $\vec{g}(\vec{m})$ can be written as,

$$\vec{g}(\vec{m}) = A\vec{m} , \quad (2.2)$$

with matrix A of size $M \times N$ independent of \vec{m} , the forward model is called linear in \vec{m} , and can be analysed more easily, see Duijndam and Drijkoningen [1997, Chapter 2].

Regarding the relation between inversion solutions \vec{m} and the forward model $\vec{g}(\vec{m})$, two situations can occur [Duijndam and Drijkoningen, 1997, section 1.4]. Firstly, it is possible that no \vec{m} can be found such that $\vec{d} = \vec{g}(\vec{m})$. In this case the solution is *non-existent*, e.g. because the forward model \vec{g} does not completely describe the finer details in the experiment. As long as $\vec{g}(\vec{m})$ approaches \vec{d} close enough for parameters \vec{m} in the range of interest, this is acceptable.

The second case arises when multiple solutions \vec{m} give the same optimal set of modelled measurements \vec{d} , e.g. $\vec{g}(\vec{m}_1) = \vec{g}(\vec{m}_2)$. Without more information, it is not possible to prefer one of the solutions above the other: a more fundamental *non-uniqueness* problem has arisen. By bringing in additional information using the Bayesian inversion technique (section 2.1.3), the non-uniqueness problem can be alleviated.

Due to measurement-noise and incomplete forward models, *uncertainties* appear in data and theory. With Bayesian inversion, uncertainties in data and theory can be handled adequately. It will be shown that results obtained with this inversion technique not only consist of a set of optimal parameters, but include their associated uncertainties as well.

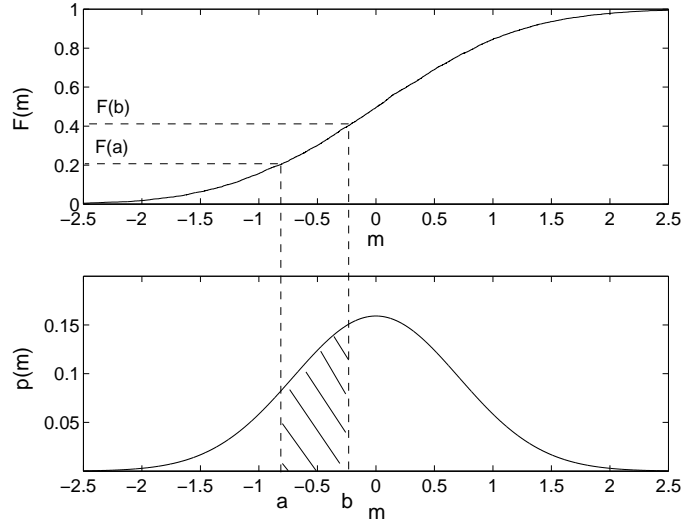


Figure 2.2: Cumulative distribution function $F(m)$ and associated probability density function $p(m)$ for a Gaussian distributed stochastic M [Eq. (2.25)], with for this plot $\sigma = 1$ and $\mu = 0$. The shaded area represents $\mathbf{P}(a \leq M \leq b)$, see Eq. (2.10). After [Duijndam and Drijkoningen \[1997, Figure 3.1\]](#).

■ 2.1.2 Introduction to probability theory

Before the Bayesian inversion method is presented, the concepts from probability theory that are necessary for the derivation of Bayes' rule are reviewed in this subsection. In one go, statistical terms used throughout this work are introduced. The shown material can be found in any decent textbook on statistics, as well as in [Duijndam \[1988a\]](#), [Duijndam and Drijkoningen \[1997\]](#) and [Tarantola \[2005\]](#).

Consider a continuous variable M in \mathbb{R} , which is the numerical result of an experiment; such a variable is called a stochastic variable or *stochast*. The probability \mathbf{P} , called degree of belief in the Bayesian approach, that the stochast M is less than or equal to a certain value m is written as,

$$\mathbf{P}(M \leq m), \quad (2.3)$$

with $0 \leq \mathbf{P} \leq 1$: for $\mathbf{P}(M \leq m) = 1$, the proposition $M \leq m$ is true; for $\mathbf{P}(M \leq m) = 0$, the proposition is false. The cumulative distribution

function (cdf) F of stochast M is defined as,

$$F(m) = \mathbf{P}(M \leq m) , \quad (2.4)$$

with,

$$\lim_{m \rightarrow \infty} F(m) = 1 , \quad (2.5)$$

$$\lim_{m \rightarrow -\infty} F(m) = 0 . \quad (2.6)$$

The probability density function (pdf) p of stochast M is defined as,

$$p(m) = \frac{dF(m)}{dm} , \quad (2.7)$$

and as a consequence,

$$F(m) = \int_{-\infty}^m p(u) du , \quad (2.8)$$

with $F(m)$ continuous, non-decreasing and differentiable. A probability density function meets the condition $p(x) \geq 0$; moreover, a strict pdf is normalised:

$$\int_{-\infty}^{\infty} p(m) dm = 1 . \quad (2.9)$$

The probability that M assumes a value within the range $[a, b]$ is,

$$\mathbf{P}(a \leq M \leq b) = \int_a^b p(m) dm = F(b) - F(a) . \quad (2.10)$$

Figure 2.2 illustrates the relationship between $F(m)$ and $p(m)$. The shaded area in the lower graph represents $\mathbf{P}(a \leq M \leq b)$.

Now consider a set of N stochasts M_1, M_2, \dots, M_N and a set of N values m_1, m_2, \dots, m_N . The stochasts and values are gathered in vectors \vec{M} and \vec{m} . The joint probability of propositions $M_1 \leq m_1, M_2 \leq m_2, \dots, M_N \leq m_N$ occurring together (i.e. in conjunction) is given by the joint cumulative distribution function F of \vec{M} :

$$F(\vec{m}) = \mathbf{P}(M_1 \leq m_1 \wedge M_2 \leq m_2 \wedge \dots \wedge M_N \leq m_N) , \quad (2.11)$$

where the shorthand $F(\vec{m})$ for $F(m_1, m_2, \dots, m_N)$ has been applied. The joint probability density function p of \vec{M} is defined as,

$$p(\vec{m}) = \frac{\partial^N F(\vec{m})}{\partial m_1 \partial m_2 \dots \partial m_N}, \quad (2.12)$$

in which $p(\vec{m})$ is the abbreviated notation for $p(m_1, m_2, \dots, m_N)$; note that the order of elements in vector \vec{m} is of no importance, since the order of differentiation does not matter. As a multidimensional analogy of Eq. (2.10), the probability of stochast \vec{M} taking values in volume A is,

$$\mathbf{P}(\vec{M} \in A) = \iiint \dots \int_A p(\vec{m}) \, dm_1 dm_2 \dots dm_N. \quad (2.13)$$

Given two sets of variables \vec{M} and \vec{D} , the *marginal* pdf gives the information on one set of variables regardless of the other set. It is obtained by integrating the joint pdf over the disregarded set of variables; e.g. the marginal pdf $p(\vec{d})$ for \vec{D} disregarding \vec{M} is given by,

$$p(\vec{d}) = \iiint \dots \int_{-\infty}^{\infty} p(\vec{d}, \vec{m}) \, dm_1 dm_2 \dots dm_N, \quad (2.14)$$

where $p(\vec{d}, \vec{m})$ stands for $p(d_1, \dots, d_M, m_1, \dots, m_N)$. The shorthand version of the previous equation is,

$$p(\vec{d}) = \int_{-\infty}^{\infty} p(\vec{d}, \vec{m}) \, d\vec{m}. \quad (2.15)$$

The *conditional* pdf gives the information on one set of variables, when values for the other set of variables have become available. Intuitively, it should be proportional to the joint pdf with the values for the other set filled in. The conditional pdf $p(\vec{m}|\vec{d})$ for \vec{M} given values for \vec{D} , is defined as:

$$p(\vec{m}|\vec{d}) = \frac{p(\vec{m}, \vec{d})}{p(\vec{d})}, \quad (2.16)$$

in which the denominator $p(\vec{d})$, with the obtained values for \vec{D} substituted, is a scaling factor making $p(\vec{m}|\vec{d})$ a strict pdf [see Eq. (2.9)]. Note that $p(\vec{m}, \vec{d}) = p(\vec{d}, \vec{m})$.

Two sets of variables \vec{M} and \vec{D} are independent when their joint pdf can be written as the product of their individual (marginal) probability density functions,

$$p(\vec{m}, \vec{d}) = p(\vec{m}) \cdot p(\vec{d}) . \quad (2.17)$$

It follows from Eq. (2.16) that in that case,

$$p(\vec{m}|\vec{d}) = p(\vec{m}), \quad p(\vec{d}|\vec{m}) = p(\vec{d}) . \quad (2.18)$$

The expectation or mean μ_i of values m_i from \vec{M} are defined as,

$$\mu_i = \mathbf{E}(m_i) = \int_{-\infty}^{\infty} m_i p(\vec{m}) d\vec{m} , \quad (2.19)$$

with $i \in \{1, 2, \dots, N\}$. These N equations can be rewritten as follows [Duijndam and Drijkoningen, Eq. (3.46)],

$$\vec{\mu} = \mathbf{E}(\vec{m}) = \int_{-\infty}^{\infty} \vec{m} p(\vec{m}) d\vec{m} . \quad (2.20)$$

This equation should be evaluated separately for each value m_i from vector \vec{M} ; the $p(m_i)$ then appearing in the equation is the marginal pdf for M_i disregarding the remainder of the variables from \vec{M} .

The covariance between two variables M_i and M_j gives an indication of the dependence between the variables, i.e. how much the two variables vary together. The covariance matrix \mathbf{C} , containing covariances between elements of the vector of variables \vec{M} , is defined as,

$$\mathbf{C} = E[(\vec{m} - \vec{\mu})(\vec{m} - \vec{\mu})^T] = \int_{-\infty}^{\infty} (\vec{m} - \vec{\mu})(\vec{m} - \vec{\mu})^T p(\vec{m}) d\vec{m} , \quad (2.21)$$

which is shorthand for,

$$c_{ij} = E[(m_i - \mu_i)(m_j - \mu_j)] = \int_{-\infty}^{\infty} (m_i - \mu_i)(m_j - \mu_j) p(\vec{m}) d\vec{m}, \quad (2.22)$$

where c_{ij} indicate the elements of matrix \mathbf{C} . On the diagonal of this matrix are found the variances $\sigma_i^2 = c_{ii} = E[(m_i - \mu_i)^2]$ of variables M_i . The square roots σ_i of the variances are called standard deviations. From the standard deviations σ_i and covariances c_{ij} , one can calculate correlation

coefficients ρ_{ij} , which indicate the *linear* dependency between M_i and M_j . The correlation coefficients are defined as,

$$\rho_{ij} = \frac{c_{ij}}{\sigma_i \sigma_j}, \quad (2.23)$$

and have properties $-1 \leq \rho_{ij} \leq 1$ and $\rho_{ii} = c_{ii}/\sigma_i^2 = 1$.

Finally, several often-used types of probability density functions exist, see e.g. Tarantola [2005, Chapter 6]. The most often used one is the *Gaussian* or normal pdf:

$$p(\vec{m}) = \frac{1}{(2\pi)^{N/2} [\det \mathbf{C}]^{1/2}} e^{-\frac{1}{2}(\vec{m}-\vec{\mu})^T \mathbf{C}^{-1}(\vec{m}-\vec{\mu})}, \quad (2.24)$$

or for $N = 1$,

$$p(m) = \frac{1}{\sigma\sqrt{2\pi}} e^{-\frac{1}{2}\left(\frac{m-\mu}{\sigma}\right)^2}. \quad (2.25)$$

Other types of pdfs may be more appropriate in certain cases, e.g. it is known that the amplitude distribution of a series of primary reflection coefficients derived from sonic well-logs is non-Gaussian [Walden, 1985]. We will assume that the Gaussian distribution describes the variation of reservoir-layer properties around their mean values in the reservoir model.

In the next subsection, the Bayesian parameter estimation method is introduced. With this method, it is possible to adequately deal with uncertainties in data and theory. Furthermore, the technique elegantly enables the combination of different sources of information, usually leading to a more accurate parameter estimation.

■ 2.1.3 Bayesian inversion

From the material discussed in the previous subsection, Bayes' rule is easily obtained as follows [Duijndam, 1988a]. Combining Eq. (2.16) and the similar relation $p(\vec{m}, \vec{d}) = p(\vec{d}, \vec{m}) = p(\vec{d}|\vec{m})p(\vec{m})$ yields Bayes' rule,

$$p(\vec{m}|\vec{d}) = \frac{p(\vec{d}|\vec{m})p(\vec{m})}{p(\vec{d})}. \quad (2.26)$$

In this equation, $p(\vec{m}|\vec{d})$ is the *a posteriori* pdf, giving all information on the model parameters \vec{m} given the observed data \vec{d} , i.e. the solution of the inverse

problem. The conditional pdf $p(\vec{d}|\vec{m})$ contains the information on data \vec{d} given the model parameters, i.e. it holds the theory, required to forward model the data \vec{d} from parameters \vec{m} . After the measurements are done, it can be seen as a function of \vec{m} only and is then called the *likelihood* function $l(\vec{x})$. The term $p(\vec{m})$ is the marginal pdf for \vec{m} of $p(\vec{m}, \vec{d})$, giving information on model parameters \vec{m} disregarding the measured data \vec{d} : this is the *a priori* information on the parameters. The last term $p(\vec{d})$ is a constant scaling factor after the data \vec{d} are measured, rendering Eq. (2.26) a strict pdf.

Especially appealing is the way Bayes' rule describes the process of learning by experience, allowing the integration of information from different sources [Duijndam, 1987]. This process can be shown as follows. Suppose data \vec{d}_1 were used to estimate the \vec{m} , using Eq. (2.26), and that new data \vec{d}_2 are measured. Applying Bayes' rule gives:

$$p(\vec{m}|\vec{d}_1, \vec{d}_2) = \frac{p((\vec{d}_1, \vec{d}_2)|\vec{m})p(\vec{m})}{p(\vec{d}_1, \vec{d}_2)}. \quad (2.27)$$

Repeatedly applying Eq. (2.16) on the equation above yields,

$$\begin{aligned} p(\vec{m}|\vec{d}_1, \vec{d}_2) &= \frac{p((\vec{d}_1, \vec{d}_2)|\vec{m})p(\vec{m})}{p(\vec{d}_2|\vec{d}_1)p(\vec{d}_1)} = \frac{p(\vec{d}_2, \vec{d}_1, \vec{m})}{p(\vec{d}_2|\vec{d}_1)p(\vec{d}_1)} \\ &= \frac{p(\vec{d}_2|(\vec{d}_1, \vec{m}))p(\vec{d}_1, \vec{m})}{p(\vec{d}_2|\vec{d}_1)p(\vec{d}_1)} = \frac{p(\vec{d}_2|(\vec{d}_1, \vec{m}))p(\vec{d}_1|\vec{m})p(\vec{m})}{p(\vec{d}_2|\vec{d}_1)p(\vec{d}_1)} \end{aligned} \quad (2.28)$$

Furthermore, two simplifications can be made. Firstly, assuming independence of \vec{d}_1 and \vec{d}_2 yields $p(\vec{d}_2|\vec{d}_1) = p(\vec{d}_2)$ according to Eq. (2.18). Secondly, assuming conditional independence of \vec{d}_1 and \vec{d}_2 given \vec{m} implies $p(\vec{d}_2|(\vec{d}_1, \vec{m})) = p(\vec{d}_2|\vec{m})$. Inserting all of this into Eq. (2.27) gives,

$$p(\vec{m}|\vec{d}_1, \vec{d}_2) = \frac{p(\vec{d}_2|\vec{m})}{p(\vec{d}_2)} \cdot \frac{p(\vec{d}_1|\vec{m})p(\vec{m})}{p(\vec{d}_1)}. \quad (2.29)$$

The last factor in the equation above, recognised as the posterior of the first parameter estimate, has become the prior knowledge for the second estimate!

■ 2.1.4 Estimating uncertainties with Monte Carlo

Using the standard reduced model $\vec{d} = \vec{g}(\vec{m}) + \vec{n}$ [as given in Eq. (2.1)] to formulate the inverse problem, the likelihood function $l(\vec{x})$ can be written as [Duijndam and Drijkoningen, Eq. (4.8)],

$$l(\vec{m}) = p(\vec{d}|\vec{m}) = p_n(\vec{d} - \vec{g}(\vec{m})) , \quad (2.30)$$

with $p_n(\vec{n})$ the pdf of the noise \vec{n} , and \vec{n} independent of $g(\vec{m})$. As an example, consider the case that the noise is Gaussian and hence can be described using Eq. (2.24) with zero mean ($\vec{\mu} = \vec{0}$) and a covariance matrix \mathbf{C}_n . The likelihood $l(\vec{m})$ is then given by,

$$l(\vec{m}) = \frac{1}{(2\pi)^{N/2}[\det \mathbf{C}_n]^{1/2}} e^{-\frac{1}{2}(\vec{d}-\vec{g}(\vec{m}))^T \mathbf{C}_n^{-1}(\vec{d}-\vec{g}(\vec{m}))} . \quad (2.31)$$

The solution of the inverse problem now follows from Bayes' rule, given in Eq. (2.26): multiplying the likelihood $l(\vec{m})$ by prior information $p(\vec{m})$ and dividing it by the constant $p(\vec{d})$ yields the a posteriori pdf $p(\vec{m}|\vec{d})$. However, for more than three parameters, it is hard to inspect the a posteriori pdf. In this work, a Monte Carlo algorithm [Duijndam and Drijkoningen, 1997; Leguijt, 2001] is applied to find the *global* extreme and the shape of the posterior pdf, providing parameter estimates and their associated uncertainties. Local optimisation techniques, such as conjugate gradient, often give difficulties with inversion problems using non-linear forward models, because they have no means to escape from local extrema that might be present in the corresponding posterior pdf.

With an increasing amount of parameters, the model space to be sampled grows quickly out of bounds. The crude Monte Carlo method randomly takes samples to estimate the posterior pdf, i.e. the uniform distribution is used to draw samples from parameter space. However, by applying *importance sampling*, the space to be searched is reduced, e.g. by taking samples from the Gaussian instead of uniform distribution, based on prior information, or by putting constraints on the parameters (e.g. if one of the parameters were density, it cannot be negative). Furthermore, a guided ‘‘Markov Chain’’ Monte Carlo method (as used in this thesis) ‘learns’ during the search, making it possible to estimate many more parameters than with crude Monte Carlo, in a statistically sensible way [Sambridge and Mosegaard, 2002; Duijndam and Drijkoningen, 1997].

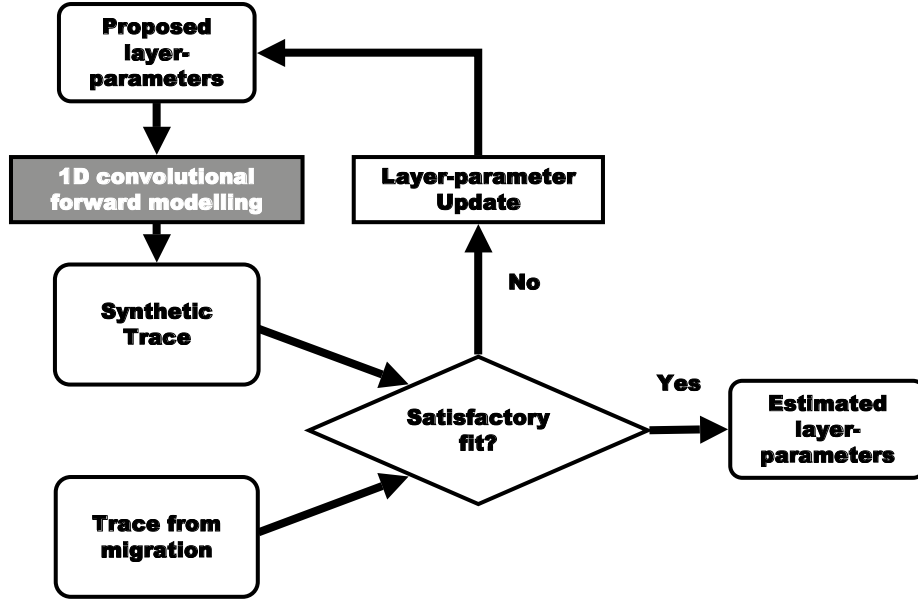


Figure 2.3: Iterative trace inversion loop (Figure courtesy of J. Leguijt). A Markov Chain Monte Carlo algorithm is used to propose parameter updates in order to properly sample the parameter space.

The guided Monte Carlo search finishes with a collection of S model parameter sets \vec{m}_i ($i \in \{1, 2, \dots, S\}$) that properly samples the posterior pdf (each parameter set defines a model; the amount of sets S is user-definable). The estimated mean and covariance of model parameters \vec{m} can be obtained simply by averaging the sets found by Monte Carlo [Duijndam and Drijkoningen, Eqs. (8.23) and (8.24)]:

$$\langle \vec{m} \rangle = \frac{1}{S} \sum_{i=1}^S \vec{m}_i, \quad (2.32)$$

$$\langle \mathbf{C} \rangle = \frac{1}{S} \sum_{i=1}^S (\vec{m}_i - \langle \vec{m} \rangle)(\vec{m}_i - \langle \vec{m} \rangle)^T. \quad (2.33)$$

2.2 Stochastic trace inversion

In the following, it is shown how the 1D convolutional forward model commonly used in trace inversion techniques, can be fit into the inversion- and Bayesian-theory introduced in section 2.1; doing so, trace inversion becomes stochastic trace inversion. For the workflow around stochastic trace inversion, see section 2.3. For a more detailed treatment of the complete forward modelling step, see section 2.5.

In simple terms, it can be stated that in stochastic trace inversion, estimates of rock and pore-fluid parameters of a layered reservoir are obtained in an iterative fashion, by minimising the mismatch between a forward modelled (synthetic) part and recorded part of a seismic trace, taken from the migration image (section 2.4) at the level of the inversion target. The estimates for the reservoir parameters are obtained including their associated uncertainties. The trace inversion process, schematically depicted in Figure 2.3, is repeated for every trace in the inversion window on the migration image, in this way laterally progressing through the target.

Using the terms of section 2.1.1 on page 16, the ‘experiment’ for stochastic trace inversion is the matching of the ‘measured data’, the seismic traces from the migration image, with the forward modelled synthetic traces, obtained by inserting the layer ‘model parameters’ of the reservoir model describing the layered reservoir into the ‘theory’. The ‘theory’ describing the traces in stochastic trace inversion is the 1D convolutional model. It is defined as, see e.g. Oldenburg et al. [1983] or van Riel and Berkhout [1985],

$$s(t) = w(t) * r(t) + n(t) , \quad (2.34)$$

in which t denotes recording time, the asterisk denotes temporal convolution, $s(t)$ is the recorded seismic signal (i.e. the trace), and $w(t)$ is the seismic wavelet. The frequency content of the additive noise $n(t)$ is assumed known. The wavelet $w(t)$ is assumed known from a so-called seismic-to-well tie (section 2.5). Finally, $r(t)$ is the subsurface spiky reflectivity: the impulse response of a 1D layered earth, considering the earth as a linear system, with the expression [van Riel and Berkhout, 1985, Eq. (2)],

$$r(t) = \sum_{j=1}^N R_j \delta(t - \tau_j) , \quad (2.35)$$

with N the amount of reflectors, R_j the reflection coefficients, δ Dirac's delta function, and τ_j the lag time of j -th reflector.

Inserting Eq. (2.35) into Eq. (2.34) and discretising t , gives the following description of the trace as a sum of N reflected wavelets, with time delays τ_j and reflection coefficients R_j [van Riel and Berkhout, 1985, Eq. (4)],

$$s(t_i) = \sum_{j=1}^N R_j w(t_i - \tau_j) + n(t_i), \quad (2.36)$$

where the trace is uniformly sampled M times, on t_i ($i \in \{1, 2, \dots, M\}$).

The problem is now in the form of the standard reduced model of Eq. (2.1): $\vec{d} = \vec{g}(\vec{m}) + \vec{n}$ with,

$$\vec{d} = (s(t_1), s(t_2), \dots, s(t_M))^T, \quad (2.37)$$

$$\vec{n} = (n(t_1), n(t_2), \dots, n(t_M))^T, \quad (2.38)$$

the model parameters split up in two vectors,

$$\vec{m}_R = (R_1, R_2, \dots, R_N)^T, \quad (2.39)$$

$$\vec{m}_\tau = (\tau_1, \tau_2, \dots, \tau_N)^T, \quad (2.40)$$

and $g_i(\vec{m}_R, \vec{m}_\tau) = \sum_{j=1}^N R_j w(t_i - \tau_j)$. (In fact, R_j is reflection angle dependent and, in turn, a function of reservoir parameters like porosity and fluid-content, see section 2.5, but for simplicity that is not considered here). Subsequently, after measurement of data \vec{d} , the likelihood function is established according to Eq. (2.30), and inserted in Eq. (2.26) (Bayes' rule), together with the prior distributions $p(\vec{m})$ of the model parameters. The result is an expression in terms of a misfit function $\vec{d} - \vec{g}(\vec{m})$ [due to the inclusion of the likelihood function, see Eq. (2.30)], with which the desired posterior pdf $p(\vec{m}|\vec{d})$ can be evaluated for one set of model parameters \vec{m} at a time.

As stated in the previous section, in order to find the shape and global extreme of the posterior pdf, it is sampled in a statistically sensible way using the Markov Chain Monte Carlo algorithm. Iteratively updating a collection of initial model parameters sets \vec{m}_i^0 , the outcome is a collection of model parameter sets \vec{m}_i properly sampling the posterior pdf (Figure 2.4), with which the posterior mean and covariance of the model parameters, i.e. 'parameter

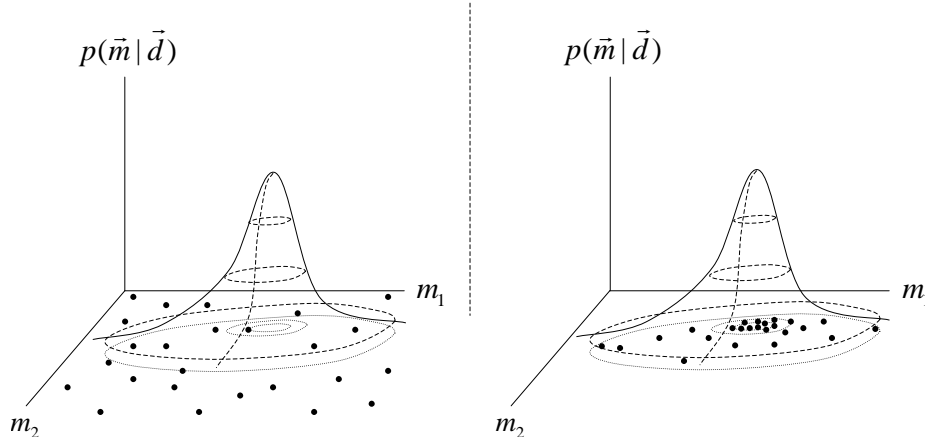


Figure 2.4: Markov Chain Monte Carlo sampling of the posterior pdf $p(\vec{m}|\vec{d})$ for a model consisting of two parameters $\vec{m} = (m_1, m_2)$. On the left-hand side an initial collection of 25 models \vec{m}_i^0 ($i \in \{1, 2, \dots, 25\}$), on the right-hand side the situation is sketched after a certain number of updates.

estimates including uncertainties’, can be calculated using Eqs. (2.32) and (2.33).

Notice that during the sampling of the posterior pdf, the forward problem $\vec{g}(\vec{m})$ is solved many times, because for each proposed update of model parameter set \vec{m} originating from \vec{m}_i^0 , the Markov Chain Monte Carlo algorithm needs to re-evaluate $p(\vec{m}|\vec{d})$ [with the expression containing the misfit function $\vec{d} - \vec{g}(\vec{m})$]. For example, in the Metropolis scheme, a new model \vec{m}' is accepted only with the probability [Sambridge and Mosegaard, 2002, Eq. (6)],

$$\mathbf{P} = \min \left(1, \frac{p(\vec{m}')}{p(\vec{m})} \right), \quad (2.41)$$

with \vec{m} the vector containing the current set of model parameters. So, it is during this sampling stage in the stochastic inversion procedure that two processes occur that were mentioned in the beginning of this section and displayed in Figure 2.3: the ‘minimising the mismatch between measured trace \vec{d} with synthetic trace $\vec{g}(\vec{m})$ ’ and ‘updating reservoir parameters in an iterative fashion’ take place in the evaluation of the misfit function $\vec{d} - \vec{g}(\vec{m})$ for

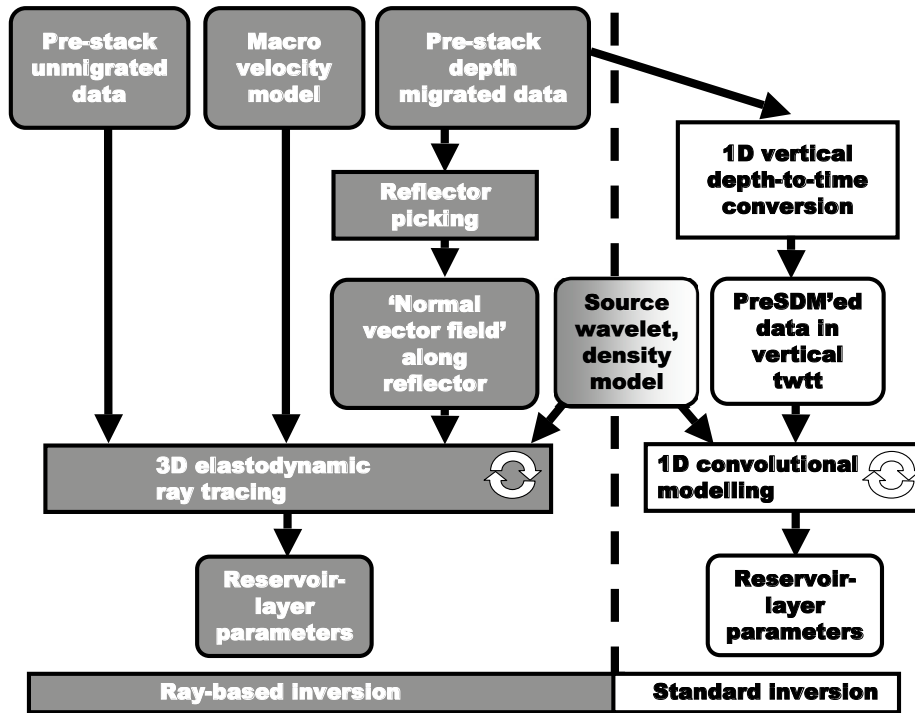


Figure 2.5: Flow chart for the new ray-based inversion (left) and the standard method (right). Both employ stochastic inversion kernels (the loops refer to the Markov Chain Monte Carlo sampling), however the new scheme uses 3D ray-based modelling, and is applied to the pre-stack unmigrated data.

each model update. In the next section, it is shown how the 1D convolutional model fits in the complete workflow for stochastic inversion.

2.3 Workflow for stochastic inversion

The workflow for stochastic trace inversion is depicted on the right-hand side of Figure 1.3, which is repeated in Figure 2.5 for convenience. In this section, attention will be focussed on the procedures required to successfully execute the workflow. Note that the inversion domain and forward modeller are the migrated image and the 1D convolutional model, respectively: sec-

tions 2.4 and 2.5 are devoted to them. Notice also from Figure 2.5, that the new inversion method shown on the left-hand side and discussed in Chapter 3, has a different inversion domain and forward modeller.

The first item of the standard inversion workflow, depicted in the upper-right part of Figure 2.5, is the input dataset: the migrated data. See section 2.4 for the migration procedure and some properties of the migrated domain. Following Veeken and Da Silva [2004], the inversion procedure starts with a quality control and pre-conditioning of the input data, corresponding to the selected target area from the migration image. The selection from the migration image of an inversion window at the reservoir level (see the upper-left part of Figure 2.12 for an impression), makes inversion a *target oriented* procedure.

Of course, the ideal input for trace inversion are traces from migrated data containing primary reflections only, of which the amplitudes are directly proportional to subsurface reflection coefficients: these are the assumptions underlying Eqs. (2.34) and (2.35). Hence, conditioning the input data e.g. involves multiple suppression (since multiple arrivals would be interpreted as primaries by 1D convolutional inversion) and other noise removal. Also, care should be taken that the pre-conditioning processes do not destroy the desired amplitude behaviour, described above, that is ideally present on true-amplitude migrated data (see the next section). Notice that above-mentioned proportionality means that a (constant) factor between amplitudes from the target on the migrated data and reflection coefficients may be present; this factor is determined using a seismic-to-well match (section 2.5), which also yields the wavelet for inversion.

The next step in the trace inversion workflow concerns 1D vertical depth-to-time conversion of the depth migrated data, to obtain the migrated image in vertical two-way traveltime; again see Figure 2.5 (right-hand side). This step is required because inversion is performed in the time-domain. Consider an acoustic subsurface, in which locations $\vec{x} = (x_1, x_2, x_3)^T$ are described using a right-handed Cartesian coordinate system, and in which the (x_1, x_2) -plane is coinciding with the surface and, following the seismological convention, x_3 is chosen positive in the direction of increasing depth in the subsurface. The trace-by-trace operation of converting depth to vertical two-way time is

described by,

$$t_v(x_1, x_2, x_3) = \int_0^{x_3} \frac{2}{v_p(x_1, x_2, \gamma)} d\gamma, \quad (2.42)$$

with $t_v(x_1, x_2, x_3)$ the vertical two-way travelttime corresponding to some depth location \vec{x} , and $v_p(x_1, x_2, x_3)$ the laterally varying P-velocity. Naturally, the factor two in the numerator of Eq. (2.42) takes into account the fact that a two-way travelttime is required while a one-way propagation velocity is given. Furthermore, note that using Eq. (2.42) results in a laterally varying stretch applied to the depth axis. Note also that depth-to-time conversion occurs along the vertical direction and not along the ray-path, which is perfectly valid since the preceding migration has removed all propagation effects: in the conversion, actual wave paths do not have to be obeyed anymore. Notice finally that Eq. (2.42) may also be used in an isotropic *elastic* subsurface, for depth-to-time conversion of depth migrated unconverted primary P-wave reflections.

The migration image in t_v is a structural, band-limited image of (reflection-angle-averaged) subsurface reflection coefficients in which depth is represented by vertical two-way travelttime, that is in principle suitable for inversion with 1D convolutional modelling. In contrast, note that unmigrated data, i.e. data before migration, represented in two-way travelttime (recording time) t , do not fulfil the assumptions underlying the 1D convolutional model, since wave propagation effects, like geometrical spreading, are still contained in them. In the following, traces from the depth migrated data at a certain lateral position (x_1, x_2) are denoted by $v(x_3)$, or after depth-to-time conversion $v(t_v)$, whereas the migrated traces *modelled* using Eq. (2.36) in vertical two-way travelttime, i.e. synthetic traces, are denoted with $s(t_v)$.

The next step in the inversion procedure is applying the actual trace inversion, which makes use of the 1D convolutional modelling kernel, on traces $v(t_v)$ from the selected target area on the migrated image in vertical two-way travelttime (see the right-hand side of Figure 2.5). In the inversion process, modelled traces $s(t_v)$ are produced and compared with $v(t_v)$. The complete inversion step is explained in detail in section 2.5, and results in posterior pdfs for each reservoir-layer parameter, i.e. estimates for the parameters including their uncertainties.

The workflow ends with a visualisation and interpretation of results; usually this is done by generating reservoir property maps including uncertainties,

and by building an updated (posterior) reservoir model that is now consistent with seismic, geologic and petrophysical data. The next section discusses in more detail the inversion domain of stochastic inversion, the migrated image.

2.4 Inversion domain - the migrated image

Stochastic inversion ideally requires true-amplitude pre-stack depth migrated data to invert on, since this type of data resembles closest the data generated in the forward modelling step of the inversion, in which a 1D convolutional model is assumed. Therefore, in this section, an algorithm that generates these data is introduced first: 3D Kirchhoff true-amplitude (TA) pre-stack depth migration (PreSDM).

From the many types of migration techniques that exist [Gray et al., 2001], Kirchhoff migration is chosen in this work, because it uses ray-tracing to calculate the traveltimes and weights necessary for the migration: this offers the link to integration with the new inversion procedure that uses ray-tracing as well. Ray-tracing, the forward modeller of the novel inversion method, is discussed in more detail in section 3.4. The choice for Kirchhoff migration automatically means that the ray-tracing validity conditions (see p. 74) are inherited.

In this section, first the Kirchhoff migration algorithm is introduced. Then, two properties of the output image it generates are looked upon more closely: the resolution on the migration image, and the presence of migration wavelet stretch. Wavelet stretch and lateral resolution are not taken into account in stochastic inversion when forward modelling a trace from the migration image using 1D convolution.

■ 2.4.1 TA Kirchhoff migration: retrieving reflection coefficients

In the following, first the seismic experiment is described which yields the data to be migrated. Then, the migration equation is given, and all the symbols in the equation are explained. Finally, a simplified migration equation is given for a special combination of subsurface and acquisition geometry.

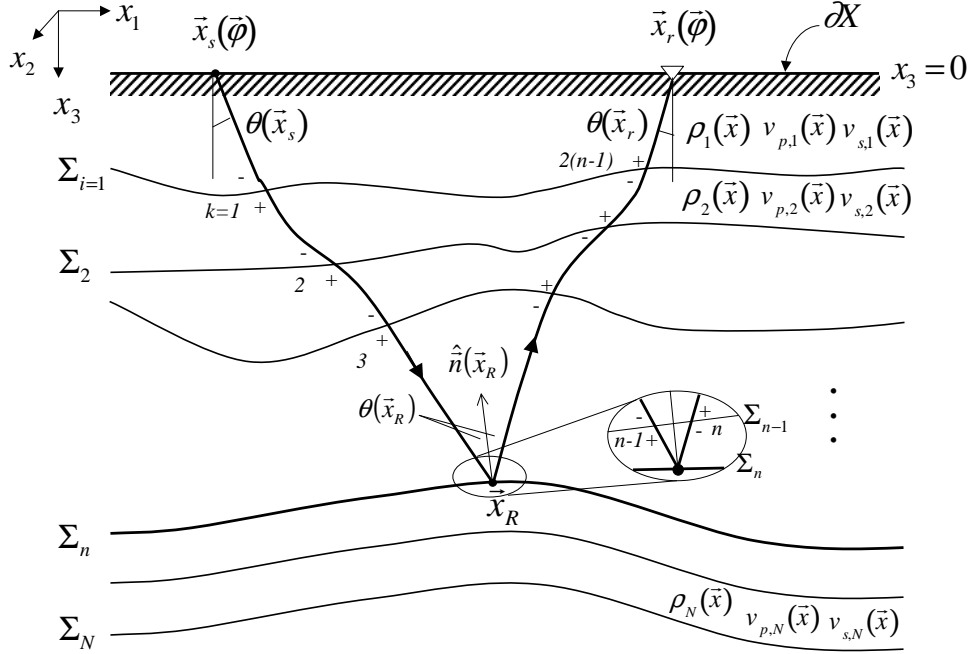


Figure 2.6: Layered isotropic elastic subsurface. A ray-path is shown from source \vec{x}_s to receiver \vec{x}_r , with reflection occurring at \vec{x}_R on interface Σ_n . See text for details.

Description of seismic experiment

Consider the isotropic elastic subsurface space $X \subset \mathbb{R}^3$ with a free surface ∂X at $x_3 = 0$, and N layers with smoothly varying elastic layer properties P-velocity, S-velocity and density $[v_{p,i}(\vec{x}), v_{s,i}(\vec{x})$ and $\rho_i(\vec{x})$, with $i \in \{1, 2, \dots, N\}$], bounded by N smoothly curved interfaces Σ_i (Figure 2.6). Interface Σ_n denotes the top of the target zone for inversion, Σ_N denotes the base. The subsurface is assumed to satisfy the ray-theoretical validity conditions, since the migration algorithm presented below relies on the ray-method to produce proper results.

At the free surface, a series of seismic experiments is performed, in which, after detonating an isotropic point source (e.g. simulating a buried dynamite charge, but not surface sources like vibroseis), the vertical component

\dot{u}_3 of particle velocity vector \vec{u} is measured in the recording time window $[0, T]$ (with T the maximum time recorded since detonation of the source) at single-component receivers. The position of a source is indicated by \vec{x}_s , that of a receiver by \vec{x}_r . It is assumed that the set of recordings contains the primary P-wave reflections that are later modelled for migration by ray-tracing.

Figure 2.6 shows a ray-path for such a primary P-wave reflection from source to receiver for a fixed source/receiver pair (\vec{x}_s, \vec{x}_r) ; $\theta(\vec{x}_s)$ and $\theta(\vec{x}_r)$ are the take-off and emergence angles. Reflection takes place at reflection point \vec{x}_R on interface Σ_n , with specular reflection angle $\theta(\vec{x}_R)$, measured with respect to the interface normal \hat{n} at $\vec{x}_R \in \Sigma_n$. Index k counts the interfaces traversed, and the signs $-$, $+$ indicate incidence and transmission sides; for clarity, an enlargement shows the counting convention at the last interface before the reflection point, Σ_{n-1} , which is not shown on the main figure.

Knowledge on the reflection amplitude behaviour as a function reflection angle or offset is crucial for reservoir parameter estimation. In the next paragraph, the true-amplitude Kirchhoff migration equation is given in a form suitable for the migration of data sorted to common offset; this makes it possible to analyse the reflection Amplitude Variation with Offset (AVO) of migrated common-offset gathers, as is commonly done with AVO inversion techniques to estimate reservoir properties, see e.g. Castagna [1993]. To obtain a simple notation of the migration equation for these common-offset sorted data, it is useful to follow the approach of Schleicher et al. [1993] in describing the source and receiver positions: the two positions of a source-receiver pair (\vec{x}_s, \vec{x}_r) are described by a single common coordinate vector $\vec{\varphi}$ (e.g. the midpoint position between \vec{x}_s and \vec{x}_r) and certain constant acquisition configuration matrices; this concept is explained in more detail shortly. In the foregoing, $\vec{\varphi} = (\varphi_1, \varphi_2)^T$, $\vec{x}_s = (x_{s,1}, x_{s,2})^T$ and $\vec{x}_r = (x_{r,1}, x_{r,2})^T$.

Migration equation

Schleicher et al. [1993] describes 3D Kirchhoff TA PreSDM of the measured dataset \dot{u}_3 as follows:

$$\langle R(\vec{x}, \theta(\vec{x})) \rangle \simeq -\frac{1}{2\pi} \iint_{\vec{\varphi} \in A} \text{Re} \left[W(\vec{\varphi}, \vec{x}) \frac{\partial}{\partial t} \dot{u}_3^{(A)}(\vec{\varphi}; t) \Big|_{t=t_d(\vec{\varphi}, \vec{x})} \right] d\varphi_1 d\varphi_2. \quad (2.43)$$

This pre-stack migration integral is often called ‘diffraction stack’ to emphasise the fact it describes a stacking procedure along diffraction traveltimes t_d . The symbols occurring in this equation will each be clarified below.

For the evaluation of this integral and the determination of the weight function W , ray-based modelling of primary P-waves in an elastic subsurface model is performed. Therefore, the migration outcome is the band-limited *primary P-wave* reflection coefficient, and all signals in the recorded data other than primary P-wave reflections are considered to be noise.

Notice that, due to the usage of $\vec{\varphi}$, Eq. (2.43) applies to a certain measurement configuration only. For data that is sorted to common offset, the migration equation is evaluated separately for every offset present in the dataset, after which the results may be stacked and averaged to obtain the final migrated image.

Migration output $\langle R(\vec{x}, \theta(\vec{x})) \rangle$ is the Zoeppritz-type displacement-normalised plane wave specular reflection coefficient (see [Aki and Richards \[1980, sec. 5.2\]](#), [Young and Braile \[1976\]](#), or [Červený \[2001, sec. 5.3\]](#)) for primary P-waves incident from above, at subsurface point \vec{x} . The brackets “ $\langle \rangle$ ” denote spatial band-limitedness on the migration image, caused by the temporal band-limitedness on the input data (due to the finite duration of the source wavelet), and finite migration interval $A \subset \partial X$, the *aperture* area in which all source and receiver positions are contained; see also Eqs. (2.56) and (2.57).

Notice that a single migrated common-offset gather contains the reflection coefficients for different reflection angles $\theta(\vec{x})$. This is even true for the reflection coefficients from a single horizontal reflector, since the velocity distribution $v_p(\vec{x})$ in the subsurface between source, receiver and reflection point may vary for different (\vec{x}_s, \vec{x}_r) -pairs from the common-offset gather; the eikonal equations given in Eq. (1.3) show that the exact P-wave ray-trajectory, hence also θ , is dependent on $v_p(\vec{x})$. Generally speaking, the observed reflection angle in a common-offset gather decreases with increasing reflector depth.

The proportionality sign (\simeq) indicates firstly that the effect of the density distribution in the subsurface on the reflection amplitudes is neglected (so that the effect of density is still incorporated into the outcome, see also p. 41). Also, it denotes that a certain constant scaling term needed to get a dimen-

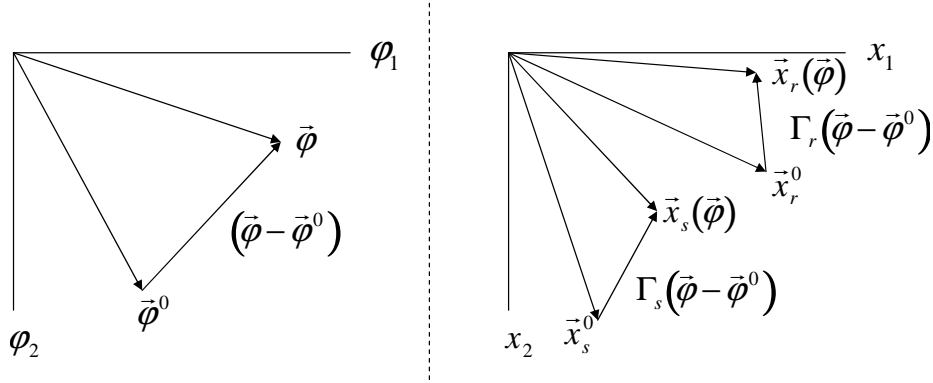


Figure 2.7: Sketch of relation between the coordinate vector $\vec{\varphi}$ and the source/receiver positions \vec{x}_s and \vec{x}_r , as described by Eqs. (2.44) and (2.45). $\vec{\varphi}^0$, \vec{x}_s^0 and \vec{x}_r^0 indicate some reference starting positions. $\vec{\varphi}$ can e.g. be interpreted as the midpoint position of a source/receiver pair (\vec{x}_s, \vec{x}_r) . Matrices Γ_s and Γ_r depend on the acquisition geometry. After [Schleicher et al. \[1993, Figure A-1\]](#).

sionless outcome has been omitted; this is a consequence of the way Schleicher introduces the pre-stack Kirchhoff migration integral, without referencing to any particular form of the wave equation.

2D coordinate vector The simple form of the migration formula is due to the introduction of coordinate vector $\vec{\varphi}$, without it the 3D Kirchhoff PreSDM formula would have involved integration over four variables, $x_{s,1}$, $x_{s,2}$, $x_{r,1}$, and $x_{r,2}$, instead of just two. The vector $\vec{\varphi}$ relates to the two position vectors \vec{x}_s and \vec{x}_r as follows (Figure 2.7), [[Schleicher et al., 1993, App. A](#)],

$$\vec{x}_s(\vec{\varphi}) = \vec{x}_s^0 + \Gamma_s(\vec{\varphi} - \vec{\varphi}^0), \quad (2.44)$$

$$\vec{x}_r(\vec{\varphi}) = \vec{x}_r^0 + \Gamma_r(\vec{\varphi} - \vec{\varphi}^0), \quad (2.45)$$

in which $(\vec{x}_s^0, \vec{x}_r^0)$ is a reference source-receiver pair defined by $\vec{\varphi}^0$, and in which Γ_s, Γ_r are constant 2×2 transformation matrices determined by the

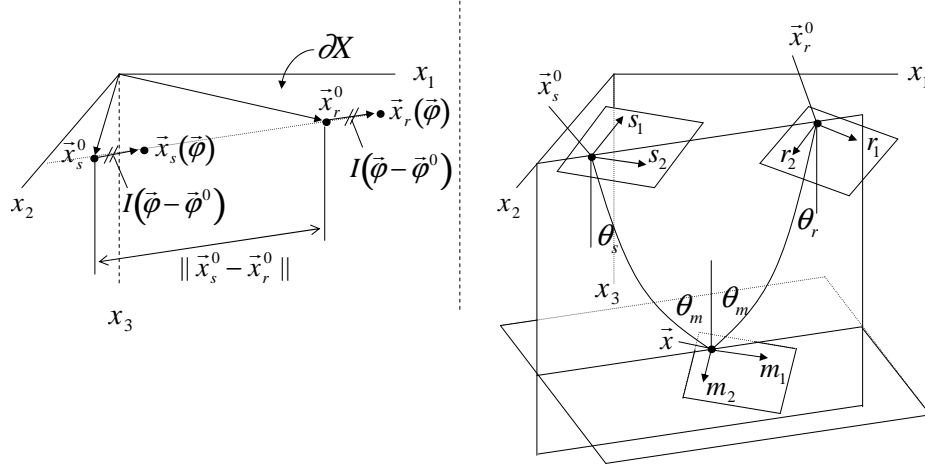


Figure 2.8: Left: Common-offset acquisition, with sources and receivers placed along a line at the surface; $\vec{\varphi}$ is the single coordinate vector. (Modified from [Schleicher et al. \[1993, Figure 5a\]](#)). Right: Three random 2D orthogonal coordinate systems at source \vec{x}_s , receiver \vec{x}_r and subsurface point \vec{x} . See the text on ‘Hessian matrices’ for details. For clearer presentation it was assumed that the ray-pair falls into the plane through \vec{x}_s , \vec{x}_r and \vec{x} . Note that θ_s , θ_r and θ_m are shorthand for angles $\theta(\vec{x}_s)$, $\theta(\vec{x}_r)$ and $\theta(\vec{x})$. (Modified from [Schleicher et al. \[1993, Figure 4b\]](#)).

data acquisition geometry,

$$\Gamma_s = \begin{bmatrix} \frac{\partial x_{s,1}}{\partial \varphi_1} & \frac{\partial x_{s,1}}{\partial \varphi_2} \\ \frac{\partial x_{s,2}}{\partial \varphi_1} & \frac{\partial x_{s,2}}{\partial \varphi_2} \end{bmatrix}, \quad \Gamma_r = \begin{bmatrix} \frac{\partial x_{r,1}}{\partial \varphi_1} & \frac{\partial x_{r,1}}{\partial \varphi_2} \\ \frac{\partial x_{r,2}}{\partial \varphi_1} & \frac{\partial x_{r,2}}{\partial \varphi_2} \end{bmatrix}. \quad (2.46)$$

To describe a position of a particular source/receiver pair from the set of all N source/receiver pairs in a survey, $\{\vec{x}_s^i, \vec{x}_r^i\}_{i=0}^{N-1}$, the corresponding vector from the set $\{\vec{\varphi}^i\}_{i=0}^{N-1}$ is inserted in Eqs. (2.44) and (2.45).

For the common-offset acquisition considered here (see the left-hand side of Figure 2.8), the matrices have the property $\Gamma_s = \Gamma_r = I$, in which I is the 2×2 identity matrix; on substitution of I in Eqs. (2.44) and (2.45) it then follows that $\vec{x}_s = \vec{x}_r + (\vec{x}_s^0 - \vec{x}_r^0)$, in which $\|\vec{x}_s^0 - \vec{x}_r^0\|$ is the offset. Hence, for zero-offset acquisition, in addition $\vec{x}_s^0 = \vec{x}_r^0$ should apply.

Recorded data The dataset to be migrated with Eq. (2.43) is the measured vertical component of the particle velocity $\dot{u}_3 = \partial u_3 / \partial t$ (in Schleicher et al. [1993], the particle displacement magnitude $\|\vec{u}\| = \sqrt{u_1^2 + u_2^2 + u_3^2}$ is used instead).

The time derivative $\partial / \partial t$ operating on \dot{u}_3 in the migration equation makes that the phase of the wavelet present on that data is preserved on the migration output, i.e. it compensates for the phase-shift effect due to the double integration [Newman, 1975].

The superscript (A) above \dot{u}_3 in the migration equation indicates that *analytical* data are being migrated. The analytical data $\dot{u}_3^{(A)}(\vec{\varphi}; t)$ are calculated from the recorded data $\dot{u}_3(\vec{\varphi}; t)$ as follows [Červený, 2001, Eq. (A.3.2)] (omitting the spatial argument $\vec{\varphi}$ for notational convenience),

$$\dot{u}_3^{(A)}(t) = \dot{u}_3(t) + j\mathcal{H}(\dot{u}_3(t)), \quad (2.47)$$

with \mathcal{H} denoting the temporal Hilbert-transform, and j the imaginary unit with property $j^2 = -1$. The temporal Hilbert transform of $\dot{u}_3(t)$ is defined as [Bracewell, 1986],

$$\mathcal{H}(\dot{u}_3(t)) = \frac{1}{\pi} \int_{-\infty}^{\infty} \frac{\dot{u}_3(\tau)}{\tau - t} d\tau = \int_{-\infty}^{\infty} \dot{u}_3(\tau) g(t - \tau) d\tau, \quad (2.48)$$

taking the Cauchy principle value in the integral to avoid the singularity at $\tau = t$; the alternative integral notation makes clear the Hilbert transform is a convolution of $\dot{u}_3(t)$ with $g(t) = -\frac{1}{\pi t}$.

The sign convention in Eq. (2.47) corresponds to the following definition of the Fourier-transform [Červený, 2001, App. A], with $\omega = 2\pi f$ the angular frequency:

$$\mathcal{F}(\dot{u}_3(t)) = \int_{-\infty}^{\infty} \dot{u}_3(t) e^{j\omega t} dt. \quad (2.49)$$

Traveltime function $t_a(\vec{\varphi}, \vec{x})$ provides the (two-way) diffraction travel-times from source-receiver pairs (with their locations uniquely identified by variable $\vec{\varphi}$) to a fixed subsurface point \vec{x} . The traveltimes may be computed by ray-tracing through the migration P-wave velocity model, that should resemble the true P-wave velocity distribution in the subsurface sufficiently well for the migration to be successful.

The two-way diffraction traveltime t_d is the sum of the one-way traveltimes from $\vec{x}_s(\vec{\varphi})$ to \vec{x} and from \vec{x} to $\vec{x}_r(\vec{\varphi})$. The summation of input data $\dot{u}_3^{(A)}(\vec{\varphi}; t)$ in Eq. (2.43) occurs along these diffraction traveltime surfaces $t = t_d(\vec{\varphi}, \vec{x})$ in the $(\varphi_1, \varphi_2; t)$ -space (see also [Yilmaz \[2001, p. 484\]](#) for an instructive geometrical explanation of Kirchhoff migration).

True-amplitude weight function $W(\vec{\varphi}, \vec{x})$ takes into account the chosen acquisition parameterisation, the passing of rays through caustic points, and removes the geometrical spreading. It is given by [[Schleicher et al., 1993](#), Eq. (19), modified for free surface and vertical displacement],

$$W(\vec{\varphi}, \vec{x}) = \sqrt{\frac{\rho(\vec{x}_r)v_p(\vec{x}_r)}{\rho(\vec{x}_s)v_p(\vec{x}_s)}} \cdot \frac{\sqrt{\cos \theta(\vec{x}_s) \cos \theta(\vec{x}_r)}}{\cos \theta(\vec{x}_r)C_0(\vec{x}_r)} \cdot e^{-j\frac{\pi}{2}\kappa(\vec{x}_s, \vec{x}_r)} \cdot \frac{\left| \det \left(\Gamma_s^T N(\vec{x}_s, \vec{x}) + \Gamma_r^T N(\vec{x}_r, \vec{x}) \right) \right|}{\sqrt{\left| \det \left(N(\vec{x}_s, \vec{x}) \right) \right|} \sqrt{\left| \det \left(N(\vec{x}_r, \vec{x}) \right) \right|}}, \quad (2.50)$$

where the original equation from [Schleicher et al. \[1993\]](#) was multiplied with the P-wave velocity at the source, $v_p(\vec{x}_s)$, to be compatible with the definition of relative geometrical spreading from [Červený \[2001\]](#) used later on, see also p. 81 and [Vanelle et al. \[2006\]](#). Furthermore, following Vanelle et al., a factor was added to compensate for the effect of different density ρ and P-wave velocity at source and receiver [this is the inverse of the factor before the product in Eq. (2.52)].

The original equation from Schleicher is modified to take into account the free surface and measurement of the *vertical* component of the particle velocity as follows. Factor $C_0(\vec{x}_r)$ in the denominator of Eq. (2.50) is the free surface conversion coefficient [see Eq. (3.12)], and $\cos \theta(\vec{x}_r)$ in the denominator takes into account the fact that the vertical component of the particle velocity, \dot{u}_3 , is measured instead of the total magnitude $\|\dot{\vec{u}}\| = \sqrt{\dot{u}_1^2 + \dot{u}_2^2 + \dot{u}_3^2}$.

The exponential in Eq. (2.50), in which quantity $\kappa(\vec{x}_s, \vec{x}_r)$ is the so called KMAH index (named after Keller, Maslov, Arnold and Hörmander), takes into account the phase shift due to (line or point) **caustics**. κ is the sum of caustic indices of all caustics encountered on the ray-path from \vec{x}_s via \vec{x} to \vec{x}_r . This factor may be calculated by dynamic ray-tracing. More information on

caustics is found in e.g. [Bakker, 1998] or [Červený, 2001, section 3.10.5]. Note that the minus-sign in the exponential of Eq. (2.50) corresponds to the plus-sign in Eq. (2.47) (and to the sign convention chosen in the definition of the Fourier-transform). Also notice that near caustic points the amplitudes calculated by dynamic ray-tracing are not reliable anymore (extensions of the ray method exist that can solve this problem).

The last factor in Eq. (2.50), together with the factor $\sqrt{\cos \theta(\vec{x}_s) \cos \theta(\vec{x}_r)}$, removes the geometrical spreading and takes into account the **coordinate transformation** with respect to $\vec{\varphi}$. Transform operators Γ_s^T and Γ_r^T are defined in Eq. (2.46), and angles $\theta(\vec{x}_s)$ and $\theta(\vec{x}_r)$ are the take-off- and emergence-angles, measured with respect to the vertical, of the ray from source \vec{x}_s via subsurface point \vec{x} to receiver \vec{x}_r (see Figure 2.6; note that \vec{x} in that figure is positioned on an interface and hence is labelled \vec{x}_R).

Geometrical spreading in Schleicher's formulation of the weight function shown in Eq. (2.50), is described in terms of second-order traveltime derivatives of paraxial rays: the 2×2 matrices $N(\vec{x}_s, \vec{x})$ and $N(\vec{x}_r, \vec{x})$ appearing in the last factor of Eq. (2.50), are second-order mixed-derivative Hessian matrices of traveltimes, set up as follows.

Consider three arbitrary 2D Cartesian coordinate systems. Two of them are situated in the acquisition plane $x_3 = 0$: the first $\vec{s} = (s_1, s_2)$ is centered at \vec{x}_s , the second $\vec{r} = (r_1, r_2)$ is centered at \vec{x}_r . The third $\vec{m} = (m_1, m_2)$ is centered at a subsurface point \vec{x} and is situated in the plane of which the normal bisects the angle between the ray-pair from \vec{x} to \vec{x}_s and from \vec{x} to \vec{x}_r , into two equal angles $\theta(\vec{x})$ (Figure 2.8, right-hand side). These coordinate systems are used to describe the location of points $\{\vec{x}'_s, \vec{x}'_r, \vec{x}'\}$ of a paraxial ray in the vicinity of the points $\{\vec{x}_s, \vec{x}_r, \vec{x}\}$ of the central ray.

The function $\tau(\vec{x}'_s, \vec{x}')$ describes the traveltime along the ray from \vec{x}'_s to \vec{x}' . Using all the above, and introducing the shorthand notations $N_s = N(\vec{x}_s, \vec{x})$, $N_r = N(\vec{x}_r, \vec{x})$, the Hessian matrices can be written as,

$$N_s = \begin{bmatrix} \frac{\partial^2 \tau(\vec{x}'_s, \vec{x}')}{\partial s_1 \partial m_1} & \frac{\partial^2 \tau(\vec{x}'_s, \vec{x}')}{\partial s_1 \partial m_2} \\ \frac{\partial^2 \tau(\vec{x}'_s, \vec{x}')}{\partial s_2 \partial m_1} & \frac{\partial^2 \tau(\vec{x}'_s, \vec{x}')}{\partial s_2 \partial m_2} \end{bmatrix}, \quad N_r = \begin{bmatrix} \frac{\partial^2 \tau(\vec{x}'_r, \vec{x}')}{\partial r_1 \partial m_1} & \frac{\partial^2 \tau(\vec{x}'_r, \vec{x}')}{\partial r_1 \partial m_2} \\ \frac{\partial^2 \tau(\vec{x}'_r, \vec{x}')}{\partial r_2 \partial m_1} & \frac{\partial^2 \tau(\vec{x}'_r, \vec{x}')}{\partial r_2 \partial m_2} \end{bmatrix}. \quad (2.51)$$

These second order mixed-derivative matrices are evaluated at the origins of the introduced 2D coordinate systems, so at $\vec{s} = \vec{m} = \vec{0}$ for N_s or at $\vec{r} = \vec{m} = \vec{0}$ for N_r . The evaluation can be readily done with dynamic ray-

tracing, see [Červený, 2001, section 4.6].

Remark on the term “true-amplitude” In most literature, the phrase “true-amplitude” (TA), as used in Eqs. (2.43) and (2.50), indicates compensation of the recorded reflection amplitudes for geometrical spreading loss only, so that the resulting TA reflections in Eq. (2.43) still include the losses in amplitude due to transmissions across all interfaces along the ray [Schleicher et al., 1993],

$$T(\vec{\varphi}, \vec{x}) = \sqrt{\frac{\rho(\vec{x}_s)v_p(\vec{x}_s)}{\rho(\vec{x}_r)v_p(\vec{x}_r)}} \prod_{k=1}^{2(n-1)} T_k \sqrt{\frac{(\rho v_p \cos \theta)_{k+}}{(\rho v_p \cos \theta)_{k-}}}, \quad (2.52)$$

with k counting the interfaces traversed in the path from source \vec{x}_s via subsurface point \vec{x} to receiver \vec{x}_r , and with T_k being the Zoeppritz-type displacement-normalised plane wave transmission coefficient for unconverted P-waves, at encountered interface k in the direction of propagation (Figure 2.6, with $\vec{x} = \vec{x}_R$). The signs $-$ and $+$ indicate the incidence- and transmission-side of the encountered interface, at which ρ , v_p and θ are evaluated; θ is the angle between the ray and interface normal. Transmission losses are discussed in more detail in section 3.4.

Arguments in favour of the approach to compensate for geometrical spreading only are, that the transmission term given by Eq. (2.52) is close to unity and is only slowly laterally varying for a fair amount of realistic subsurface models, and that an accurate density-model needed for the removal of the transmission term, is hardly ever available. However, the stochastic inversion assumes this term having been determined and subsequently removed.

Migration equation for zero-offset caustic-free data

In the synthetic data examples of Chapter 4, the subsurface and acquisition geometry are chosen such, that no caustic points occur along ray-paths; in that case, $\kappa = 0$ so that the exponential in the weight function of Eq. (2.50) disappears. Furthermore, apart from the offset test, the examples from Chapter 4 use a zero-offset acquisition: $\vec{x}_s = \vec{x}_r$, so that either \vec{x}_s or \vec{x}_r describe source and receiver positions fully and may be substituted for $\vec{\varphi}$. In that case, also $\Gamma_s = \Gamma_r = I$ and $N_s = N_r$. It follows that the last term in Eq. (2.50)

becomes,

$$\frac{|\det(\Gamma_s^T N_s + \Gamma_r^T N_r)|}{\sqrt{|\det(N_s)|}\sqrt{|\det(N_r)|}} = \frac{|\det(2N_s)|}{\sqrt{|\det(N_s)|}\sqrt{|\det(N_s)|}} = 4. \quad (2.53)$$

Moreover, $\cos \theta(\vec{x}_s) = \cos \theta(\vec{x}_r)$: the cosine-terms in Eq. (2.50) cancel. Applying before-mentioned simplifications to Eqs. (2.50) and (2.43) yields for the 3D Kirchhoff TA PreSDM of a measured zero-offset caustic-free particle velocity dataset,

$$\langle R(\vec{x}) \rangle \simeq -\frac{2}{\pi} \iint_{\vec{x}_r \in A} \frac{1}{T(\vec{x}_r)C_0(\vec{x}_r)} \frac{\partial}{\partial t} \dot{u}_3(\vec{x}_r; t)|_{t=t_d} dx_{r,1} dx_{r,2}, \quad (2.54)$$

in which a term was added, Eq. (2.52) adjusted for normal-incidence rays, to take into account transmission losses,

$$T(\vec{x}_r = \vec{x}_s) = \prod_{k=1}^{2(n-1)} T_k. \quad (2.55)$$

With accurate macro-velocity and density models, the equation above yields the true band-limited reflection coefficient, as desired by stochastic inversion. The final migration image is built by evaluating Eq. (2.54) at regular intervals Δx_1 , Δx_2 and Δx_3 within predetermined bounds (i.e. on the sub-surface positions specified by a migration output grid), and assembling the result in traces $v(x_3)$ for the various output positions (x_1, x_2) .

■ 2.4.2 Vertical and lateral resolution

The depth-migrated image is vertically and laterally band-limited, mainly due to the finite duration of the source-wavelet, and the limited illumination aperture. Starting with the vertical resolution, let the dominant wavelength on the depth-migrated image be λ_d ; the dominant wavelength is defined as the distance between successive principal troughs (or peaks) of the wavelet, see e.g. Kallweit and Wood [1982] or Sheriff [2002]. For a thin layer to be resolved on the migration image, according to Widess' resolution criterion [Widess, 1973; Kallweit and Wood, 1982] it needs to extend a vertical thickness h of,

$$h > \frac{1}{8} \lambda_d. \quad (2.56)$$

From [Chen and Schuster \[1999, Eq. \(20\)\]](#), in which Rayleigh's resolution criterion [[Kallweit and Wood, 1982](#)] is used, the *lateral* resolution Δr_1 on the Kirchhoff-type 3D pre-stack depth migrated image in the x_1 -direction is given by,

$$\Delta r_1 = \frac{\lambda_d x_3}{L_{\max}}. \quad (2.57)$$

An analogous expression exists for the x_2 -direction [[Chen and Schuster, 1999](#)]. In Eq. (2.57), λ_d is the dominant wavelength on the seismic image, and x_3 is the observation-depth on the image. The maximum migration aperture half-length in the x_1 -direction, L_{\max} , is a function of the acquisition geometry: it is given by $L_{\max} = \max \{L_r, L_s\}$, with $2L_r$ the separation between the receivers having maximum and minimum x_1 -coordinate, and $2L_s$ the similar relation for the sources.

So, Eq. (2.57) specifies that the lateral resolution is linearly proportional to the observation depth and dominant wavelength, and inversely proportional to migration aperture half-length L_{\max} . The role of migration aperture in Kirchhoff migration is discussed in more detail in [Hertweck et al. \[2003\]](#). Note finally that Rayleigh's resolution criterion leads to a minimum separation between events which is about 4 times larger than that obtained with Widess' resolution criterion.

Edge diffractions [[Torey, 1970](#); [Berryhill, 1977](#)] that may be present on the unmigrated data due to discontinuities in the subsurface reflectors are effectively removed by the migration algorithm. Of course, many other factors are also involved in determining the final threshold of resolution on the migration image, such as signal-to-noise ratio on the input data for migration, and migration noise.

■ 2.4.3 Pulse distortion

Regardless of the employed migration algorithm, pulse distortion occurs on the migrated image [[Levin, 1998](#); [Tygel et al., 1994](#); [Brown, 1994](#); [Black et al., 1993](#)]. This distortion involves a migration-induced lengthening, or stretch, of the wavelet with respect to the wavelet present on the pre-stack unmigrated data (which is here assumed to have a fixed shape). The amount of lengthening is a function of reflection angle, reflector dip and velocity. In the following, a ratio between wavelet duration in two-way traveltime (i.e. before migration) and wavelet length after depth migration is defined.

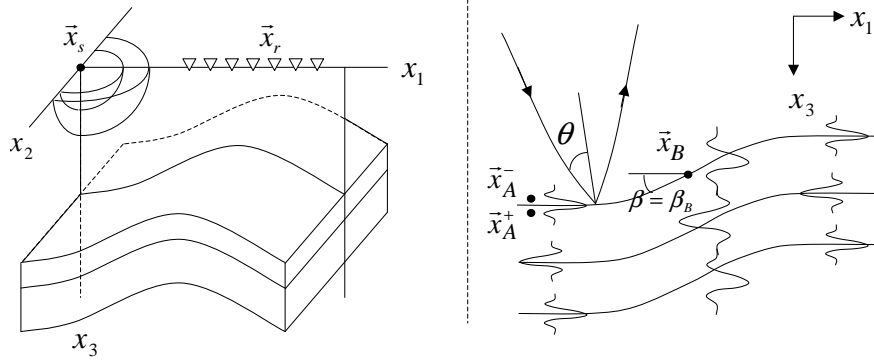


Figure 2.9: Left: 2.5D setting. The acquisition survey is confined to a line in the x_1 -direction, above a 3D subsurface that is invariant in the x_2 -direction. Two spherical wavefronts are shown, spreading in all 3 dimensions from a point source at \vec{x}_s . Right: Three interfaces with varying dip β in a 2.5D setting, with three corresponding traces from the depth migrated image exhibiting wavelet stretch.

Subsequently, two specific cases of pulse distortion are shown, together with a brief indication of their relevance to trace inversion.

Consider a seismic survey with, to facilitate the following analysis, a 2.5D setting [Bleistein et al., 2001, p.123]: in such a setting, subsurface parameters vary only in one lateral direction (say along x_1) and the depth direction (x_3), while the measurements at the surface are taken only along the single lateral direction. However, wave propagation is still fully 3D and not confined to the 2D (x_1, x_3) -plane. This 2.5D case is depicted on the left-hand side of Figure 2.9. For migrated primary unconverted P-wave reflection data acquired in a 2.5D setting with an isotropic elastic subsurface, the governing expression that measures wavelet stretch in the vertical direction is [Tygel et al., 1994],

$$m_0(v_p(\vec{x}), \theta, \beta) = \frac{2}{v_p} \cos \theta \cos \beta, \quad (2.58)$$

with $m_0 = \Delta\tau/\Delta x_3$ the ratio between a small time interval $\Delta\tau$ in the two-way recording time domain and the corresponding depth interval Δx_3 in the depth migrated domain. In Eq. (2.58), θ is the angle of incidence of the ray-pair to the reflection point, and β the reflector dip measured from the

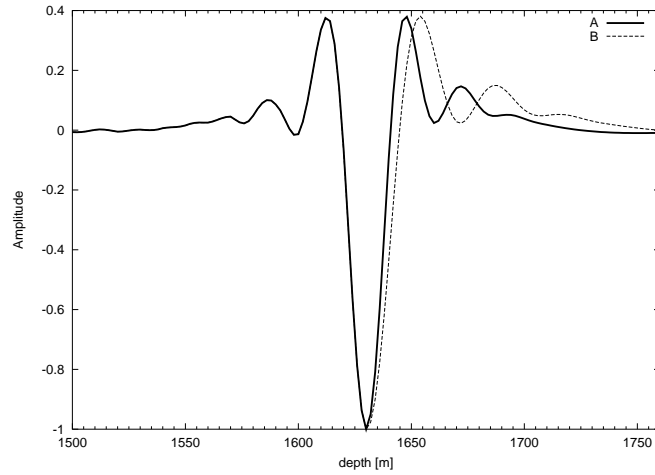


Figure 2.10: Wavelet asymmetry of wavelet “B” after depth migration of a contrast with $v_p(x_{A,3}^-) = 2200$ m/s and $v_p(x_{A,3}^+) = 3000$ m/s. See the text for details on the symmetrical reference wavelet “A”. Amplitudes are normalised to unity.

horizontal at the same location (see Figure 2.9, right-hand side). The P-wave velocity is indicated by $v_p(\vec{x})$. For blocky velocity models, the stretch-evaluation point \vec{x} on the depth migrated image must be chosen just above or below the velocity discontinuity. Notice further that Eq. (2.58) is also perfectly valid in a 3D setting; in that case, θ and β are measured in the so-called plane of reflection [Tygel et al., 1994]. Finally notice that in the following equations, the invariant x_2 -direction due to the 2.5D setting will be omitted.

Wavelet asymmetry

As a first example, consider a reflector dipping with angle $\beta = \beta_A$ at subsurface point \vec{x}_A on a zero-offset ($\theta = 0$)[†] depth migrated image (Figure 2.9, right-hand side). Using Eq. (2.58), the migration-induced stretch in the depth

[†]Strictly speaking, only in a subsurface with not too large dips, zero-offset data and normal-incidence data ($\theta = 0$) are equivalent, otherwise reflections with $\theta \neq 0$ may still occur for a zero-offset acquisition geometry.

domain at point $\vec{x}_A^+ = (x_{A,1}, x_{A,3}^+)^T$ just below the interface, relative to the stretch at position $\vec{x}_A^- = (x_{A,1}, x_{A,3}^-)^T$ just above it, is written as,

$$\frac{\Delta x_3(\vec{x}_A^+)}{\Delta x_3(\vec{x}_A^-)} = \frac{[\Delta x_3/\Delta\tau](\vec{x}_A^+)}{[\Delta x_3/\Delta\tau](\vec{x}_A^-)} = \frac{m_0(v_p(\vec{x}_A^-), \theta = 0, \beta_A)}{m_0(v_p(\vec{x}_A^+), \theta = 0, \beta_A)} = \frac{v_p(\vec{x}_A^+)}{v_p(\vec{x}_A^-)}. \quad (2.59)$$

where it was used that $\Delta\tau$ is constant on the recorded data. Hence, for $v_p(x_{A,3}^-) \neq v_p(x_{A,3}^+)$ at $x_1 = x_{A,1}$, a zero-phase wavelet of duration T_d centered around a reflector, will be *asymmetric* after depth migration (using a migration velocity model with mentioned v_p -jump at the reflector), because the equal time intervals $T_d/2$ around the reflector will convert to different depth intervals $\lambda_d(\vec{x}_A^\pm)/2$. In the case that $v_p(x_{A,3}^+) > v_p(x_{A,3}^-)$, the deeper part of the wavelet in the depth domain will be longer, as will be confirmed with a numerical test below. Observe finally that the wavelet asymmetry described in this paragraph, is introduced by the v_p -jump in the migration velocity model (which in practice will not always coincide with the true interface position).

Figure 2.10 shows an enlargement of trace $s(x_1 = x_{A,1}, x_3)$ taken from a zero-offset depth migrated section, around a single interface with $v_p(x_{A,3}^-) = 2200$ m/s and $v_p(x_{A,3}^+) = 3000$ m/s (which is dipping with angle $\beta = 45^\circ$). The used migration velocity model was exact and included the velocity jump at the interface. The wavelet ‘‘B’’ appearing on this trace from the depth migrated image is clearly asymmetrical, while the wavelet at this interface before migration, taken from a trace of the normal-incidence dataset, was symmetrical (Figure 2.11, wavelet ‘‘A’’). The symmetrical reference wavelet ‘‘A’’ on Figure 2.10 was obtained by migrating the same normal incidence dataset while providing a velocity model with a homogeneous $v_p = 2200$ m/s below the interface, so that $v_p(x_{A,3}^-) = v_p(x_{A,3}^+) = 2200$ m/s. From Eq. (2.59), the amount of stretch in the depth domain on the deeper side of the interface with respect to the shallow side (i.e. the amount of asymmetry of the wavelet), as visible on wavelet ‘‘B’’ from Figure 2.10, is $v_p(\vec{x}_A^+)/v_p(\vec{x}_A^-) = [2200 \text{ m/s}]/[3000 \text{ m/s}] \approx 1.36$.

One aspect of 1D vertical depth-to-time conversion that is beneficial to trace inversion is that it eliminates the above-mentioned wavelet asymmetry (although a stretch remains in comparison with the wavelet on the recorded data before migration in the two-way traveltime domain, see the next subsection). After 1D vertical depth-to-time conversion of trace $s(x_{A,1}, x_3)$ to

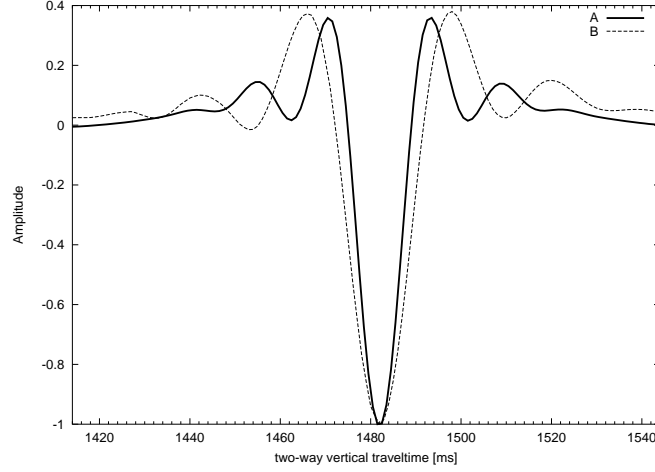


Figure 2.11: Wavelet “B” shows the depth migrated wavelet “B” of Figure 2.10 after 1D vertical depth-to-time conversion. The wavelet is symmetrical again, but stretched compared to wavelet “A”, which was taken from the normal-incidence dataset. Amplitudes are normalised to unity.

$s(x_{A,1}, t_v)$, the asymmetrical wavelet in depth obtained after depth migration (Figure 2.10, wavelet “B”) is symmetrical again in vertical two-way traveltime t_v (Figure 2.11, wavelet “B”). This can be seen by calculating t_v , using Eq. (2.42), for the shallow part and stretched deeper part of the wavelet, that is centralised around depth $x_{A,3}$ (with x_3 abbreviated to z):

$$t_v^{\text{upper}} = \int_{z_A - \frac{\lambda_d}{2}}^{z_A} \frac{2}{v_p(z)} dz = \frac{2}{v_p(z_A^-)} \int_{z_A - \frac{\lambda_d}{2}}^{z_A} dz = \frac{\lambda_d}{v_p(z_A^-)} \quad (2.60)$$

$$t_v^{\text{lower}} = \int_{z_A}^{z_A + \alpha} \frac{2}{v_p(z)} dz = \frac{2}{v_p(z_A^+)} \int_{z_A}^{z_A + \alpha} dz = \frac{\lambda_d}{v_p(z_A^+)} \quad (2.61)$$

in which the two short-hand notations $\lambda_d = \lambda_d(\vec{x}_A^-)$ and $\alpha = \lambda_d(\vec{x}_A^+)/2 = \lambda_d(\vec{x}_A^-)/2 \cdot v_p(\vec{x}_A^+)/v_p(\vec{x}_A^-)$ were used. Hence, after 1D vertical depth-to-time conversion, the asymmetry has disappeared: $t_v^{\text{upper}}/t_v^{\text{lower}} = 1$.

Wavelet stretch

As a second example, consider the stretch induced by a reflector dip $\beta = \beta_B$ at position \vec{x}_B , relative to the stretch at point \vec{x}_A with zero dip, on the zero-offset migrated image,

$$n'_0(\beta_B) = \frac{m_0(v_p(\vec{x}_A), \theta = 0, \beta = 0)}{m_0(v_p(\vec{x}_B), \theta = 0, \beta = \beta_B)} = \frac{v_p(\vec{x}_B)}{v_p(\vec{x}_A)} \frac{1}{\cos \beta_B}. \quad (2.62)$$

As shown in the previous subsection, stretching due to velocity on the zero-offset depth-migrated image is eliminated by 1D vertical depth-to-time conversion: a scaling of the migration image along the vertical with local velocity occurs [Eq. (2.42)], effectively removing the velocity dependency in the stretch-equation above. This yields the expression for the dip-dependent migration-induced wavelet stretch $n_0(\beta)$ on the depth-to-vertical-time converted migrated image:

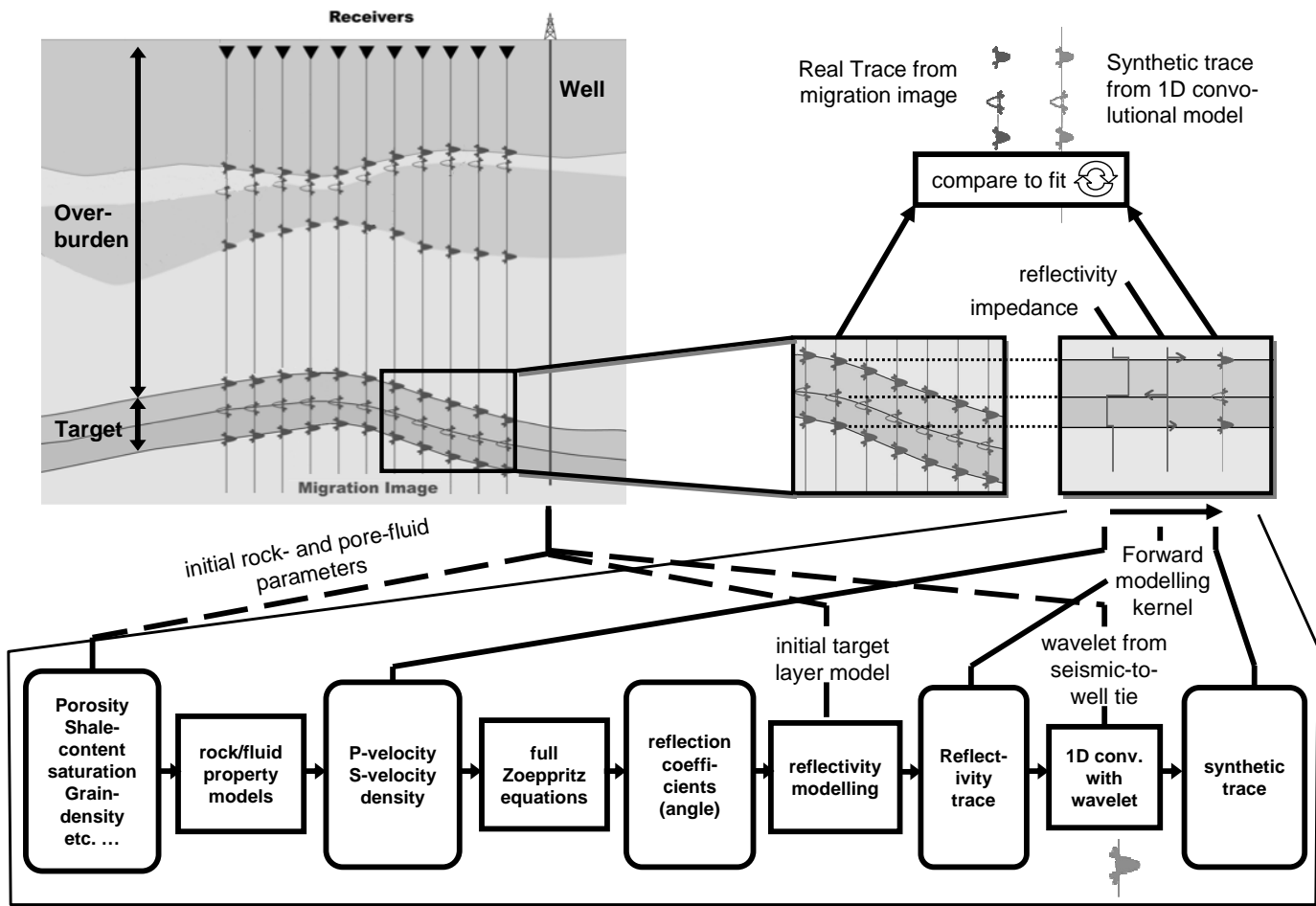
$$n_0(\beta) = \frac{1}{\cos \beta}. \quad (2.63)$$

In practice this means that the wavelet representing the position of a reflector on the migration image in vertical two-way time is increasingly stretched with increasing reflector dip β . Regard again wavelet “B” in Figure 2.11, taken at an interface dipping with angle $\beta = 45^\circ$ from the depth migrated, 1D vertical depth-to-time converted data in vertical two-way traveltime. It shows the stretch $n_0(\beta = 45^\circ)$, as compared to a wavelet from the same interface at zero dip. The reference wavelet “A” without stretch in Figure 2.11, actually was not taken from depth-to-time converted data at zero dip, but (as mentioned in the previous example) from the normal-incidence data at the interface dipping with 45° : this wavelet is equal to the wavelet from the depth-to-time converted migrated image at zero dip, apart from an amplitude scaling factor due to the removal by TA migration of amplitude losses related to wave propagation effects (such as geometrical spreading and interface transmissions).

2.5 Forward modeller - 1D convolutional modelling

In order to model traces within the target zone on the 1D vertical depth-to-time converted, depth migration image, conventional stochastic inversion

Figure 2.12: Trace inversion overview, with detailed forward modelling step (p. 51).



makes use of a 1D convolutional forward modelling kernel, as was pointed out briefly in section 2.2. The mathematical formulation of 1D convolutional modelling was introduced already in section 2.2 to explain the relation between stochastic trace inversion and Bayesian theory. In this section, this forward modelling step in stochastic inversion, and its place in the total inversion scheme, is explained in more detail.

An example target zone for inversion is schematically depicted by a box around an area of interest on the migration image, in the upper left of Figure 2.12; only the traces from the depth-to-time converted migration image within the target zone are modelled, in the vertical two-way traveltime-interval bounded by the traveltimes that correspond to top and bottom of the target zone. A different local 1D model is used for every trace that is forward modelled, progressing sequentially through the 3D target.

Before the forward modelling of the portion of the trace $v(t_v)$ from the depth-to-time converted migration image that falls within the target can take place, the initial reflectivity trace $r(t_v)$ for the current position in the target, and the wavelet for inversion $w(t_v)$ need to be determined. Both are constituents of the 1D convolutional model of Eq. (2.34) that is used to generate the forward modelled trace $s(t_v)$,

$$s(t_v) = w(t_v) * r(t_v) + n(t_v) , \quad (2.64)$$

in which the traveltime is specified more precisely as the vertical two-way traveltime t_v , since the forward modelling takes place in the depth-to-time converted migrated domain.

Wavelet $w(t_v)$ is usually taken the same for all traces in the inversion target of the migration image. It is derived from a seismic-to-well match at the well position near the inversion target (Figure 2.12, upper left), see e.g. White and Simm [2003]; Veeken and Da Silva [2004]; Duijndam and Drijkoningen [1997]. This process can be summarised as follows: from the acoustic impedance well-log, a reflectivity trace is computed that is considered correct for the target zone. This reflectivity trace is convolved with a first-estimate seismic wavelet to produce a synthetic trace for the inversion window at the well position. In the target zone, this synthetic trace is then compared to the actual trace from the migration image. Iteratively updating the seismic wavelet, until the match between synthetic and actual trace is optimal, yields the desired wavelet for inversion.

The initial spiky reflectivity trace is built from a local 1D subsurface model at target level (see the next paragraph for a more detailed description of this building process) that varies from trace to trace in the inversion target. The local 1D prior model at the trace position, that includes prior reservoir parameter uncertainties, is derived from a detailed 3D reservoir model made from local petrophysical data at nearby wells, regional geological knowledge and structural information from the migrated image.

The complete forward modelling step performed in a single iteration loop (see Figure 2.3) of stochastic inversion is graphically depicted from left to right in the lower half of Figure 2.12. Initial estimates of rock and pore-fluid properties, obtained from the detailed reservoir model at the current trace position, are inserted into a 1D rock/fluid property model appropriate for each identified layer in the inversion target. Using these rock models, the elastic layer-properties P-velocity, S-velocity and density (v_p , v_s and ρ) are calculated from the basic constituents of that rock. As an example, the so-called critical concentration model calculates the v_p, v_s and ρ of sands, carbonates or dolomites from the properties v_p, v_s and ρ of the grains, and the actual and critical porosity of the matrix surrounding the grains [Chen, 1992]. The foundations of rock modelling are explained in, for instance, Mavko [1998].

Subsequently, with the full Zoeppritz-equations, given in e.g. Young and Braile [1976]; Sheriff [2002], or approximations (see e.g. Shuey [1985]; Bortfeld [1961]; Aki and Richards [1980, p.153]), the reflection coefficients $R(\theta)$ at each layer-interface as a function of angle of incidence θ are calculated (usually $\theta = 0$ is chosen), locally assuming a 1D layered earth. With initial thicknesses taken from the well, the spiky reflectivity trace $r(t_v)$ is built using Eq. (2.35),

$$r(t_v) = \sum_{j=n}^N R_j(\theta) \delta(t_v - \tau_j), \quad (2.65)$$

in which the following refinements were made: t_v is substituted for t , the summation occurs over the interfaces n through N in the target for inversion (with the interface numbering corresponding to that of Figure 2.6), and the dependency of R on reflection angle θ is explicitly shown. As before, R_j and τ_j are the reflection coefficients and the lag times in vertical two-way traveltimes of j -th reflector, and δ is Dirac's delta function.

Note that $R_j(\theta)$ in Eq. (2.65) must correspond to the type of reflection coefficient present on the depth-to-time converted migrated data that are inverted; e.g. when using Eq. (2.54) for migration, R_j is the normal-incidence ($\theta = 0$) displacement-normalised plane wave specular reflection coefficient for primary unconverted P-waves. The spiky reflectivity trace resulting from Eq. (2.65) is convolved, according to Eq. (2.34), with wavelet $w(t_v)$ from the seismic-to-well tie, to generate the desired forward modelled trace on the migration image, at the current position in the inversion target.

As mentioned before, the forward modelling step is repeated while iteratively updating the reservoir parameters, until the mismatch is minimised between the forward modelled and recorded part of the seismic trace (upper right of Figure 2.12, and Figure 2.3), taken from the migration image at the level of the inversion target — at that stage, the estimates for reservoir rock and pore-fluid properties, including their associated posterior uncertainties, are yielded at the current position in the inversion target. The entire trace inversion process is repeated for each trace in the inversion target on the depth-to-time converted migration image, to finally yield the updated (posterior) reservoir model including uncertainties.

2.6 Discussion

For laterally variable subsurface media, conventional seismic trace inversion ideally relies on TA PreSDM for removing all wave propagation effects, including those related to interface-transmissions, within overburden and target zone. Only then, an image is produced that approximates a 3D reflectivity sequence in (x_1, x_2, t_v) convolved with wavelet $w(t_v)$ along the vertical direction. In such a 3D band-limited reflectivity sequence, at a fixed surface position (x_1, x_2) , we then have a 1D reflectivity sequence convolved with the wavelet, so that Eq. (2.34) adequately describes these data.

In practice however, TA PreSDM does not yield the perfect band-limited image of the Earth's reflectivity: in section 2.4 it was shown that the image has a lateral resolution dependent on the migration aperture, depth of observation and the dominant wavelength. Also, a finite migration aperture (as encountered in practice) limits the maximum dip of structures that can be seen on the migration image: the steeply dipping parts are not imaged, see e.g. Hertweck et al. [2003], and Toxopeus et al. [2003, Fig. 7]. These effects

are not included in the 1D convolutional modelling. Notice that one can try to improve the migration image before inversion by using other types of migration, such as two-way wave-equation migration or iterative migration; also with these types obtaining a TA result is not a trivial exercise.

Apart from these effects, it often occurs that reflection angle information needed for resolving reservoir parameters is blurred by processing steps, such as angle-range substacks for enhancing signal-to-noise ratios [Levin, 1998]. Furthermore, it was presented in section 2.4 that on the migration image, wavelet distortion inevitably occurs. However, most trace inversion algorithms make use of a *stationary* wavelet, or one of which the phase can be adjusted at most. Note that some inversion methods derive an offset-dependent wavelet that is different for each migration substack input to inversion [Guilloux et al., 2004]. Also attempts are being made to deliver a stretch-free Kirchhoff-migration, at least removing the stretch due to reflection angle θ [Perez and Marfurt, 2007].

As mentioned before, the inversion procedure totally relies on the separate pre-processing step of migration to remove effects of wave propagation. This also means that migration artifacts, imperfect removal of reverberations, or inaccuracies due to a wrong velocity model in the inversion target have to be taken for granted and cannot be accommodated for by the inversion.

The inversion process has to deal in some manner with all above-mentioned complications, which are suspected to degrade inversion results, especially in a structurally complex subsurface with substantial lateral velocity variations and significant reflector dips. Of course, inversion is an iterative procedure (Figure 2.3) thus the forward modelling has to be fast, justifying the choice for 1D convolution. However, with processing power of computers yearly still increasing according to Moore's law [Moore, 1965], this advantage in speed becomes less important; more advanced forward modelling kernels become feasible.

One possible way to improve the inversion kernel could be forward modelling migrated traces with a so-called *resolution function*, replacing the 1D convolutional model, to incorporate the effects introduced by migration into the inversion kernel. More on the resolution function can be found in Toxopeus et al. [2003, 2004]. In the next chapter however, a different approach is chosen that avoids the complications mentioned above: employing the original wave-path and reflection angle information inside the inversion kernel.

Box 2.1: Stacking in Astronomy

Contrary to the concept of seismic interferometry [Draganov et al., 2007] that is currently receiving much attention in geophysics and was first successfully applied by astronomers in solar seismology, a few years ago stacking was (re)discovered[†] by amateur astronomers as a useful procedure to enhance signal-to-noise ratio; something that was already known for a long time in geophysics [Mayne, 1962].

When observing heavenly bodies, the Earth's atmosphere acts as a source of noise since it is in continuous motion - it acts like an ever-changing lens which constantly displaces the observed position of stars; an effect we see as the 'twinkling' of stars in the sky. This twinkling of stars may be very romantic, it is not much loved by astronomers; in their jargon they refer to it as 'bad seeing'.

The idea is to neutralise the noise of the atmosphere by shifting and stacking a large amount of images taken in a short time-span. Take for example the pictures of the beautiful planet Saturn: on the left-hand side of Figure 2.13, a few images of a set of 90 are displayed taken at a rate of 30 Hz. Subsequently, the images are stacked, and on the right-hand side we see the result!

The pictures were taken in Rijswijk by the author using a Vixen 90 mm refraction telescope and a Nikon CP4300 digital camera.

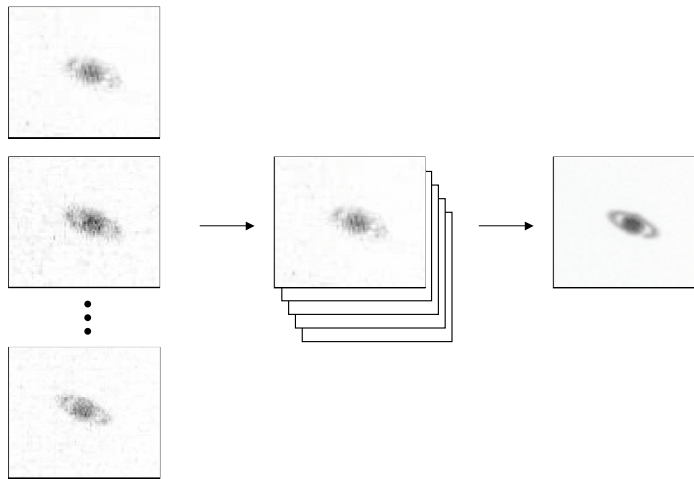


Figure 2.13: Stacking images of Saturn.

[†] The foundation of the technique was laid by Fried [1966].

Ray-based stochastic inversion

Stochastic trace inversion does not always yield accurate reservoir parameter estimates, due to the nature of the inversion domain, the migrated image which is the predetermined result of an extensive processing sequence, and due to the fact that the 1D convolutional modeller does not give the correct migration response (Chapter 2).

In this chapter, therefore, a novel seismic inversion method for improved reservoir parameter estimation, ray-based stochastic inversion (RBSI), is introduced. The scheme is based on high-frequency asymptotic ray theory, which has the added potential benefit of providing a transparent link between Kirchhoff pre-stack depth migration and stochastic inversion for reservoir properties (Figure 3.1). The method has in common with stochastic inversion, that it is a Bayesian type of inversion.

This chapter is structured in a similar manner as the previous chapter, thus using the sequence: workflow - inversion domain - forward modeller; for RBSI, the inversion domain and forward modelling kernel are the pre-stack unmigrated image and 3D elastodynamic ray-tracing, respectively. However,

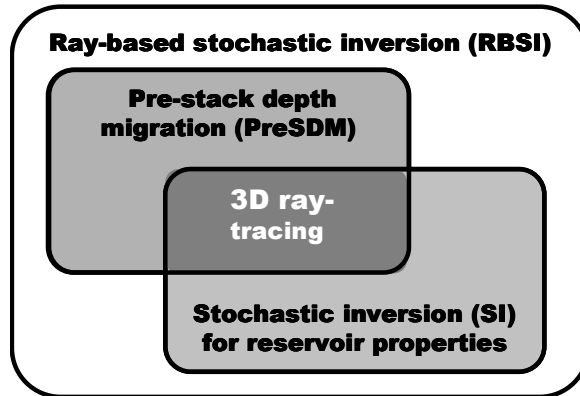


Figure 3.1: Ray-based stochastic inversion. 3D elastodynamic ray-tracing as the integrating tool between Kirchhoff pre-stack depth migration and stochastic inversion for reservoir parameters.

the chapter starts with a description of RBSI principles, and the presentation of two ways in which parameter updating in the target can be done. In the section on forward modelling, the method of ray-tracing is formally introduced. At the end of the chapter, the advantages and drawbacks of the RBSI approach as compared to existing trace inversion techniques are explored—numerical experiments on synthetic- and field data (Chapters 4 and 5) will test the potential of RBSI in practice. Finally, a special case of RBSI is presented, in which the 1D convolutional forward modelling kernel as found in much inversion software is applied, hereby reducing the range of application but offering substantial practical advantages.

3.1 From stochastic inversion to RBSI

For inversion of rock- and pore-fluid properties in a laterally strongly varying, fine-layered target reservoir sequence, it is proposed in this thesis to employ the original ray-path and reflection-angle information, contained in the pre-stack unmigrated data (recording time domain), inside the inversion algorithm. This change with respect to conventional stochastic inversion (SI, Chapter 2) is anticipated to yield a more accurate reflection amplitude repre-

Table 3.1: *Conventional stochastic inversion vs. Ray-based stochastic inversion.*

| | Conventional SI | Ray-based SI |
|------------------|-----------------|-----------------------------|
| Inversion domain | migrated domain | recording time domain |
| Forward modeller | 1D convolution | 3D elastodynamic ray-tracer |

sensation in the target zone and hence a more accurate description of reservoir parameter distributions. The new scheme is called ray-based stochastic inversion (RBSI), to emphasise that Bayesian inversion now takes place in the recording time domain, using 3D elastodynamic ray-tracing as forward modeller. Table 3.1 summarises key discriminators as compared with SI.

■ 3.1.1 RBSI principle

For RBSI, the isotropic elastic subsurface space $X \subset \mathbb{R}^3$ with surface boundary ∂X at $x_3 = 0$ is parameterised as an overburden macro-model overlying a layered target reservoir sequence (Figure 3.2) and is assumed to satisfy the standard ray-theoretical validity conditions, given in section 3.4.

In RBSI, 3D elastodynamic ray-tracing is used as forward modeller, instead of the 1D convolutional model of SI. Concentrating on unconverted, primary P-wave reflections, the key vehicle for RBSI is formed by a single pair of P-wave rays leaving the specular reflection point \vec{x}_R , on the n -th reflection surface Σ_n (within the reservoir sequence), at angles $\theta_n^+ = \theta_n^-$ to the normal-vector $\hat{n}(\vec{x}_R)$ on Σ_n , see Figure 3.2.

As was the case in SI, layer parameters in the inversion target are iteratively updated using a guided Monte Carlo algorithm (section 2.1.4), but this time the mismatch is minimised between the reflection response, forward modelled by 3D elastodynamic ray-tracing, and the real recordings from the pre-stack unmigrated data, see Figure 3.3. For more details on the ray-tracing used and the restrictions it puts on the target model, see section 3.4.

In this work, the receivers measure the vertical component of the particle velocity \dot{u}_3 as a function of recording time t ; a recording at receiver \vec{x}_r due to a source at \vec{x}_s is called a trace $\dot{u}_3(\vec{x}_s, \vec{x}_r; t)$ (note that in Chapter 2 the notation $\dot{u}_3(\vec{\varphi}; t)$ was used, with $\vec{\varphi}$ uniquely defining the source-receiver pair $\{\vec{x}_s, \vec{x}_r\}$). A trace contains the reflection responses from several interfaces;

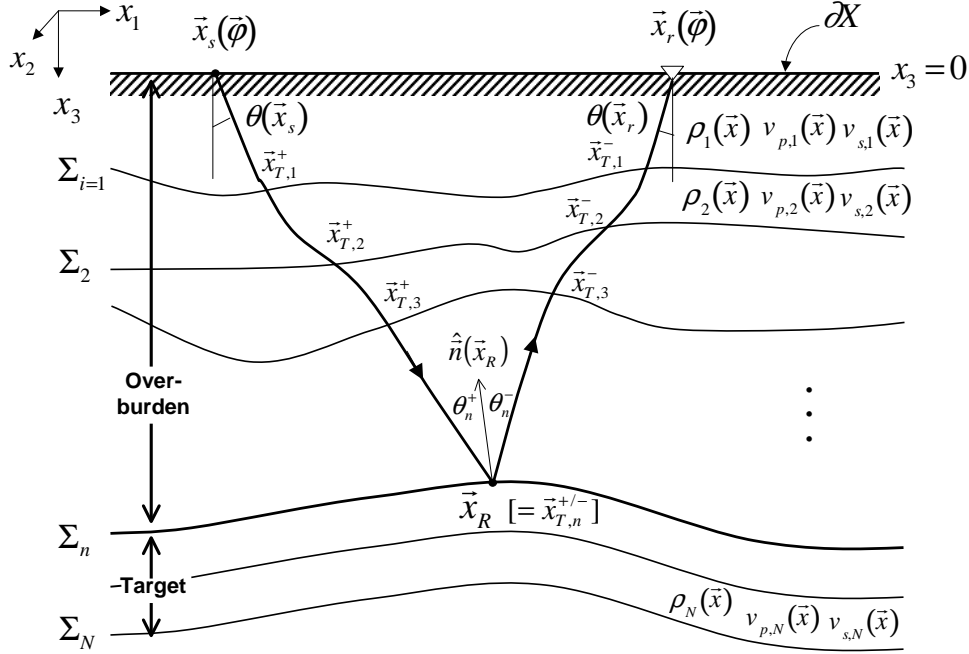


Figure 3.2: Subsurface parameterisation for RBSI, with overburden and target. Notice the different convention for labelling traversed interfaces along the ray-path, and for labelling the reflection angle, as compared to Figure 2.6. The numbering corresponds to the structural interfaces instead of the encountered interfaces.

the portion containing the response from the target interfaces is denoted by $\dot{u}_3(\vec{x}_s, \vec{x}_r, \vec{x}_{R,i}; t)$ with $i \in \{n, \dots, N\}$ (assuming a single response from each reflector). By forward modelling of traces $\dot{u}_3(\vec{x}_s, \vec{x}_r, \vec{x}_{R,i}; t)$ with ray-tracing, source and receiver positions $\{\vec{x}_s, \vec{x}_r\}$ are mapped via ray-paths to subsurface reflection points $\vec{x}_{R,i}$ in the target interval. In the target, the parameter updating takes place, until a satisfactory fit is obtained between real traces $\dot{u}_3(\vec{x}_s, \vec{x}_r, \vec{x}_{R,i}; t)$ and the forward modelled traces $s(\vec{x}_s, \vec{x}_r, \vec{x}_{R,i}; t)$. The mapping of \vec{x}_R is uniquely defined by initial directions (θ_n^+, ϕ) (with θ_n^+ measured from $\hat{n}(\vec{x}_R)$ in the plane of propagation at angle ϕ with the azimuth), and by migration velocity model $v_p(\vec{x})$. The migration velocity model generally is smooth without interfaces; initial target layers need to be

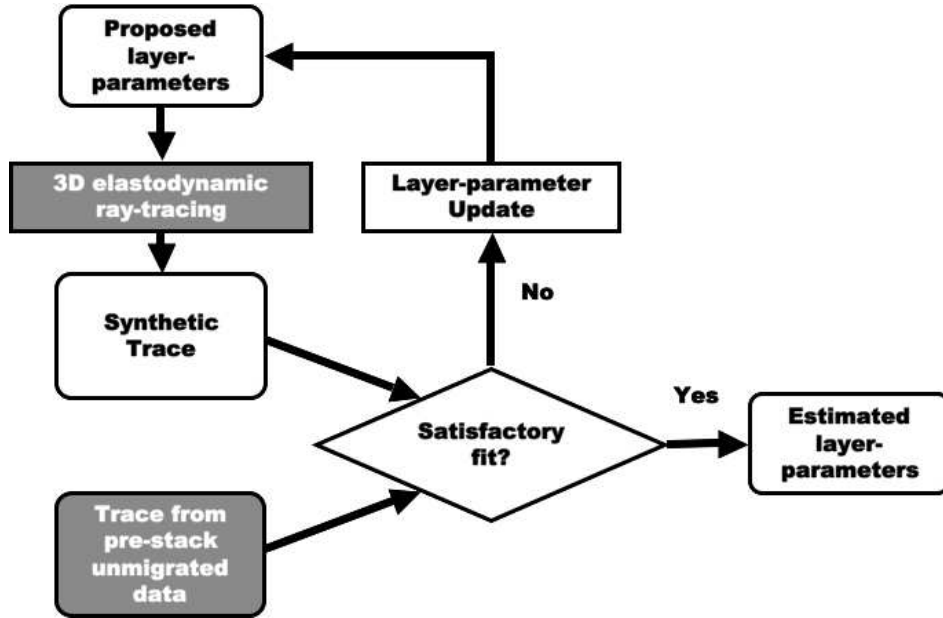


Figure 3.3: Iterative inversion loop for RBSI. A Markov Chain Monte Carlo algorithm is used to propose parameter updates. In grey boxes, the changes are indicated, as compared to SI (Figure 2.3).

inserted before any specular reflection point ray-tracing can commence. To that end, a clearly distinguishable target interface Σ_n is picked from the depth migrated image, and inserted in the velocity-depth model. Subsequently, initial target layers and interfaces are built around it to generate the prior model for RBSI (using petrophysical and geological information, similar to initial model building in SI). With the initial target interfaces Σ_i in place ($i \in \{n, \dots, N\}$), reflector normal vector fields $\hat{n}(\Sigma_i)$ can be generated for the ray-tracing, see Figures 3.2 and 1.4.

For RBSI, the process of generating synthetic traces from rock- and pore-fluid properties is not much different from that applied in SI (depicted in the flow chart on Figure 2.12); both use rock models to calculate the elastic layer-properties and the Zoeppritz equations to compute reflection coefficients $R(\theta_n^+)$. As depicted in Figure 3.3, the main difference lies in the fact

that the synthetic traces for RBSI are not generated via 1D convolution of a reflectivity trace, but via 3D elastodynamic ray-tracing in a target model. Trace recordings from the pre-stack unmigrated dataset, corresponding to ray-pairs having the same angle of incidence θ_n^+ , are conveniently located together in angle-gathers. The normal-incidence gather is one well-known example ($\theta_n^+ = 0$); it is extensively used in the numerical tests of Chapters 4 and 5. Inverting on different angle-gathers should in principle lead to the same estimated parameters, giving a data redundancy that can be used to reduce uncertainty. In amplitude-versus-offset/amplitude-versus-angle (AVO/AVA) inversion techniques, the angle-information is made use of as well, albeit in the form of migrated substacks.

Note that also a trace from a NI-section carries information on layer-properties related to v_s , albeit not at reflection points \vec{x}_R , where the expression for $R(\theta_n^+ = 0)$ is independent of v_s (Eq. 3.17), but at overlying transmission points \vec{x}_T in the target where transmission with incident angles $\theta \neq 0$ usually occur, introducing v_s into the expressions for transmission coefficients T (e.g. compare Eq. (5.3.3) with Eq. (5.3.18) in Červený [2001]). Even at \vec{x}_R an ‘estimate’ for properties related to v_s is made, using the prior information on v_s .

■ 3.1.2 Linking inversion with Kirchhoff-type migration

The subsurface model for RBSI is hybrid, with a coarse elastic subsurface macro-model in terms of v_p , v_s , and ρ for the overburden, and a detailed layered model in the target, specified in terms of reservoir rock- and pore-fluid parameters (Figure 3.4). The overburden is assumed known from migration, hence the macro-model for the overburden is fixed—updating only occurs in the layered target model.

Notice that in practice, it is difficult to determine v_s and especially ρ for the overburden. Commonly, it is assumed that lateral variations in ρ are slow so that the impact on reflection amplitudes is minimal. In the absence of more detailed information, S-wave velocities in the overburden are often simply calculated as a fixed fraction of v_p , and densities taken constant.

Also note that for Kirchhoff-type migration, three important grids with different cell-spacing can be defined: the above-mentioned relatively coarse grid often called ‘migration velocity grid’, on which the elastic parameters

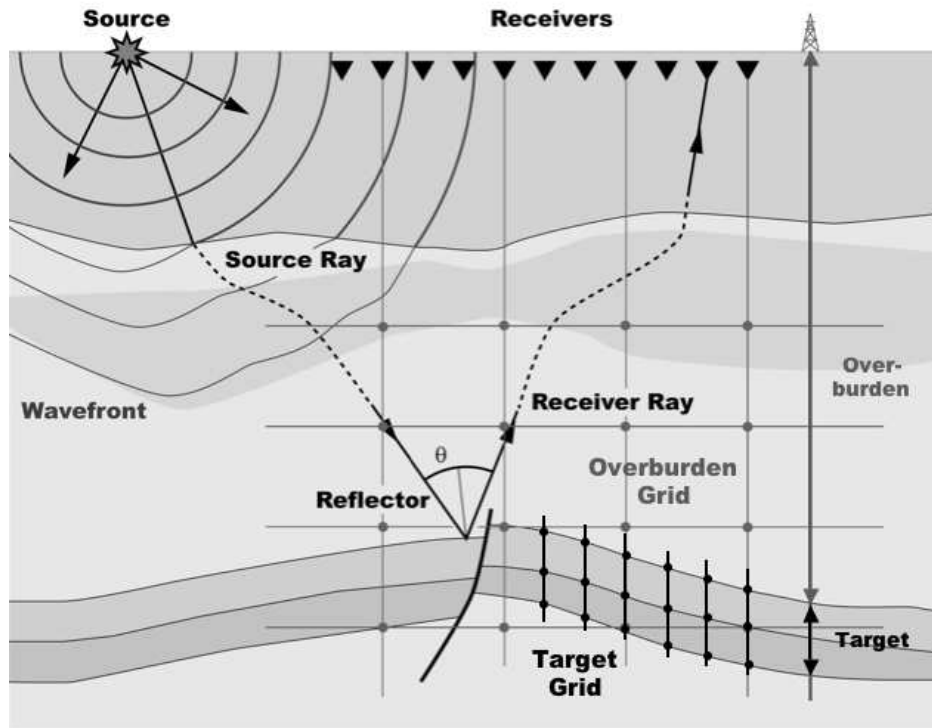


Figure 3.4: Hybrid subsurface model for RBSI, consisting of a coarse grid of elastic parameters (grey) for the overburden, and a detailed layered model of reservoir parameters (black) in the target.

are defined, a finer ‘ray-trace diffraction grid’ specifying the positions of points from which rays are traced to the surface, to calculate traveltimes, amplitudes and other ray-properties needed in the diffraction stack, and the finest ‘migration output grid’ defined by the spacing between the traces on the migration image and the spatial sampling of depth on those traces.

The connection between ray-based inversion and Kirchhoff-type migration is made as follows. With the overburden assumed known, for ray-tracing through the overburden, in principle the rays calculated on the diffraction grid for preserved-amplitude Kirchhoff-type migration can be re-used (interpolating between them if necessary), to save computing time. New ray-tracing by the forward modelling kernel of RBSI is then only performed in

the target, with ray transmission locations and angles at the top target interface linking overburden- and target ray-paths. However, this procedure has not been explored more closely in this work. It appeared unnecessary to apply the procedure in the numerical tests of Chapters 4 and 5: the 2.5D configurations used there, did not nearly demand as much CPU-time as true 3D configurations would do.

■ 3.1.3 RBSI in ‘layer-stripping’ mode

In SI, the traces from the migrated image, that are forward modelled using the 1D convolutional model, are laid out vertically over the target (usually, see e.g. Levin [1998] or Vermeer [1990, Figure 2.2] for some horizontal-trace displays) the direction corresponding to depth. This makes it possible to invert trace-by-trace, starting the estimation of layer parameters at a certain horizontal position and then progressing laterally through the target.

However, in general, RBSI cannot be performed trace-by-trace. To understand this, consider the following. Traces from the pre-stack unmigrated data reside in the recording time domain; mapping of the recorded reflections to corresponding reflection points in the spatial domain is done with ray-tracing, using the migration image and velocity model. It then appears, that a single trace from the pre-stack unmigrated data is associated with reflection- and transmission points that are distributed over a volume, rather than along a line (Figure 3.5a). The reflection responses on the trace cannot be handled separately due to wavelet-interference. The information from a single trace should then be used for estimation at once of layer properties at the respective reflection- and transmission positions. However, *different* traces generally have *overlapping* volumes of reflection- and transmission points (Figure 3.5a), hence also overlapping volumes of parameter estimation, preventing a separate trace-handling for RBSI. In the overlapping area, all information must be used for parameter estimation, not only that corresponding to one trace.

The only way to correctly deal with this situation is to update the 3D target subsurface model *as a whole*, using the guided Monte Carlo technique. Both layer-parameters and their spatial distribution would be updated, as well as the interface positions. After each update, all relevant pre-stack unmigrated traces (e.g. the NI-section) are forward modelled again and compared to the

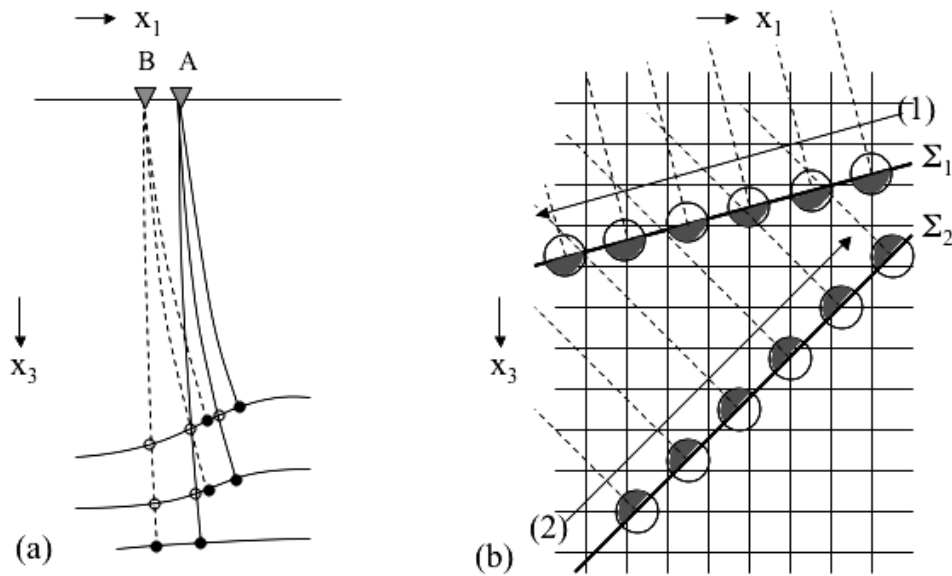


Figure 3.5: (a) NI ray-paths from geophones A (solid) and B (dashed) to three subsurface reflectors. Open circles denote transmission points. (b) RBSI in ‘trace-by-trace’ mode, for two target-interfaces Σ_1 and Σ_2 . Circles denote reflection points; dashed lines indicate normal directions on the interfaces. See text for details.

measured data. This approach involves a considerable change in the way how model-building and updating is done, compared to the usual 1D models of SI built separately for each trace in the migrated domain.

However, if separation between the layers in the inversion target is large enough to prevent interference of target interface reflection responses on the recorded pre-stack unmigrated traces, RBSI can be performed in a more traditional, trace-by-trace, layer-by-layer mode. Each of the reflection points corresponding to a trace recording (Figure 3.5a) can then be handled separately with the following procedure. Notice that the prevention of wavelet interference in the target on the normal-incidence section requires the target layer-thicknesses to be larger than the dominant wavelength λ_d .

Assuming the overburden known, layer parameters on the lower side of the top target interface Σ_n are iteratively updated, passing laterally over the inter-

face trace-by-trace, using the guided Monte Carlo algorithm to minimise the mismatch between the modelled $s(\vec{x}_s, \vec{x}_r, \vec{x}_{R,n}; t)$ and real $\dot{u}_3(\vec{x}_s, \vec{x}_r, \vec{x}_{R,n}; t)$ portions of traces containing the reflection response of the considered interface. Once the properties are estimated at a lower side of an interface, they are extrapolated vertically downwards through the layer, to the upper side of the underlying interface, so that they can be used as knowns for the inversion over the next interface. Hereby, it is assumed that the property variations inside the layer are known; e.g. geological information may indicate that the layer properties vary laterally, but not vertically inside the layer (inside the layer, the properties then are a function of (x_1, x_2) only).

The procedure is repeated for all layers inside the target, progressing downward through the inversion interval, until the properties of each layer are estimated. This process is schematically depicted in Figure 3.5b, for two interfaces Σ_1 and Σ_2 that both fall in the target area: RBSI is first performed over interface Σ_1 , laterally progressing over the interface as indicated by arrow (1), for the unknown layer properties at the lower side of Σ_1 (indicated by shaded circles). Subsequently, the inversion results are downwards extrapolated to Σ_2 (assuming that the vertical property variations inside the layer are known), where they are used as knowns for the second sweep of RBSI, along Σ_2 as indicated by arrow (2), for properties below Σ_2 .

An example of the application of this type of RBSI on synthetic data, to determine a laterally varying density distribution that cannot be retrieved with usual inversion, is given in Chapter 4. In section 3.6, a simplified variant of RBSI is presented, that can be applied trace-by-trace without the need of large separation between the target interfaces. In the next section, the differences are discussed between the workflow for RBSI and SI.

3.2 Workflow for RBSI

The process of ray-based stochastic inversion is schematically depicted on the left-hand side of Figure 1.3, which is repeated in Figure 3.6 for convenience. In this section, the practical aspects for a successful execution of this scheme are discussed. These aspects are especially relevant for the field data test of Chapter 5. The main differences with the stochastic inversion method (Chapter 2), are the inversion domain and forward modeller, respectively the pre-stack unmigrated image and 3D elastodynamic ray-tracing; these are

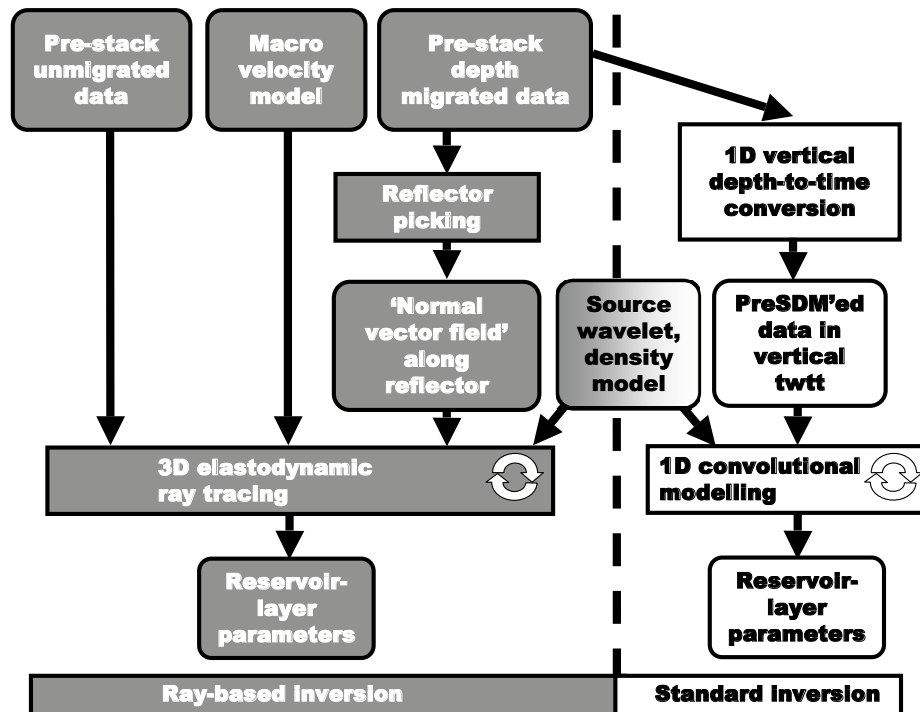


Figure 3.6: Flow chart for the new ray-based inversion (left) and the standard method (right). Both employ stochastic inversion kernels (the loops refer to the Markov Chain Monte Carlo sampling), however the new scheme uses 3D ray-based modelling, and is applied to the pre-stack unmigrated data.

described in more detail in sections 3.3 and 3.4.

Quality check on seismic datasets

In the upper part of Figure 3.6, it can be seen that RBSI makes use of two seismic datasets, the pre-stack unmigrated data and the pre-stack depth migrated data. Following the workflow for SI described in section 2.3, the RBSI procedure starts with a quality control and pre-conditioning of these input data. The migration image should be of good enough quality to allow the picking of reflector normal vector fields in the target area.

For RBSI however, not only the migration image, but also the pre-stack un-

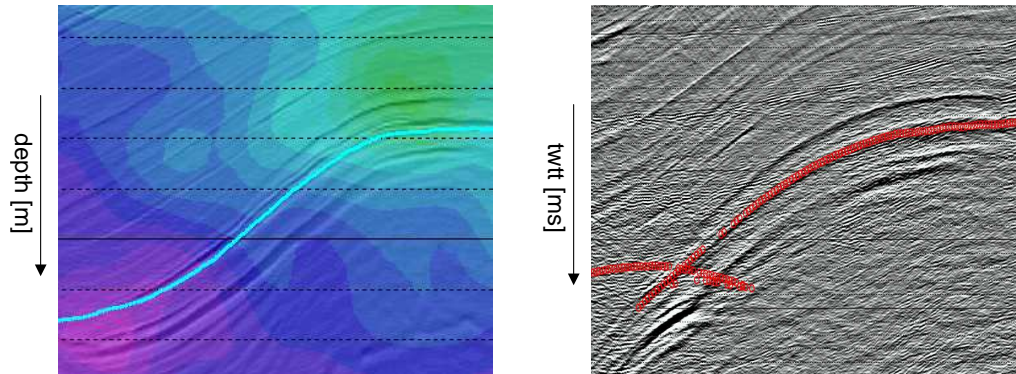


Figure 3.7: On the left, a target zone on a migrated dataset, plotted on top of the migration velocity model. The picked reference reflector is depicted in cyan. On the right, the corresponding (near) normal-incidence section. In red, traveltimes calculated by ray-tracing to the reference reflector.

migrated data corresponding to the inversion target is checked for quality: this is the dataset on which the actual inversion takes place. To determine which traces from the pre-stack data contain reflections from the inversion target (so to determine which portion of the data should be checked), ray-tracing is performed to a target interface; this yields the relevant source/receiver combinations to be fetched from the pre-stack unmigrated data. This operation requires picking of the target interface from the migration image, and knowledge of the correct overburden migration velocity model, as indicated on Figure 3.6. Often, the required information is already available from ray-tracing done for Kirchhoff-type migration.

On the selected portion of pre-stack unmigrated data, the signal-to-noise ratio must be sufficient to allow visual inspection of the target area—the inversion algorithm cannot make reliable estimates if even this is not possible. To indicate the target area on the pre-stack data, the traveltimes to the chosen target interface calculated by ray-tracing can be plotted in the data; doing so, also the quality of the migration velocity model can be checked by verifying whether the traveltimes coincide with the interpretation of the target interface (Figure 3.7). If signal-to-noise (S/N) ratio is unsatisfactory, the

S/N can be increased by stacking, although this operation will ‘blur’ the reflection coefficient information contained in the signal, due to summing and averaging of reflection responses corresponding to different reflection angles.

Amplitude-preserving pre-conditioning

Again, care should be taken that the pre-conditioning processes do not destroy the real amplitude behaviour, this time on the pre-stack unmigrated data: only amplitude-preserving processing should be applied if one plans to perform RBSI. The ideal input data for RBSI do contain wave propagation effects such as spherical spreading and transmission losses.

Most conveniently, RBSI is able to use the pre-stack unmigrated data that was pre-processed for depth migration. Such pre-processing typically includes filtering to change the wavelet to zero-phase, multiple removal, deabsorption (inverse Q filtering), static corrections and data regularisation [Yilmaz, 2001]. The signal processing should be applied while preserving amplitudes as much as possible, a common practice nowadays for proper TA PreSDM.

It is not needed to apply 1D vertical depth-to-time conversion to the migrated data when picking target reflectors for RBSI. To the contrary, this reflector picking is best done in the depth-domain, not in the vertical two-way traveltimes domain; only then the reference interface can be directly imported in the velocity-depth model, for ray-tracing to the target.

Wavelet extraction

In forward modelling of the reflection response from the target, a seismic wavelet is needed to generate synthetic traces. Theoretically, the wavelet as is derived for SI by a seismic-to-well tie on the migrated data (section 2.3), can also be used for RBSI (as depicted in Figure 3.6), provided that it is derived from the migrated data in the vertical two-way traveltimes domain, on a horizontal part of the structure. To see this, notice that the migrated image of a 1D structure after depth-to-time conversion is exactly equivalent to the normal-incidence section from the recorded dataset, and that no migration wavelet stretch occurs for zero dip, see Eq. (2.63). This approach has been used for most tests in the next chapters.

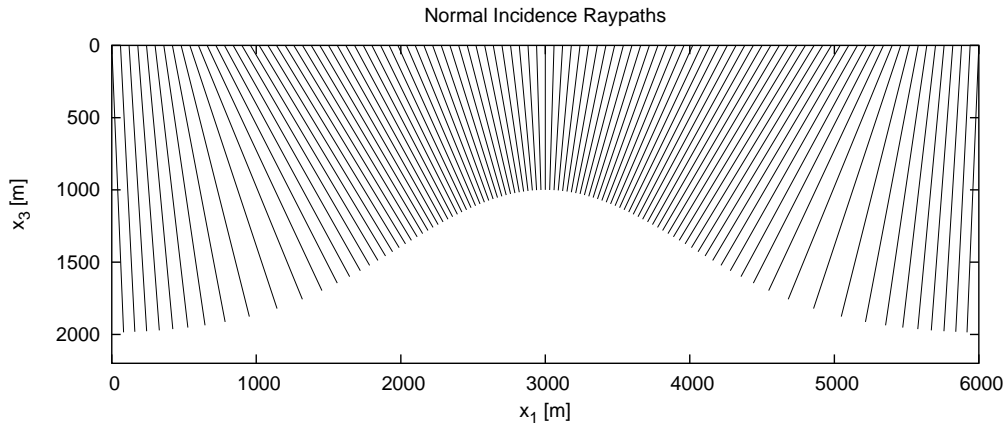


Figure 3.8: Normal-incidence rays to a curved reflector, displaying varying reflection point spacing along the interface due to reflector curvature. The overburden velocity model is homogeneous, and the shot-point spacing at the planar acquisition surface is regular.

In practice, however, various tapering filters affecting the wavelet may be applied during Kirchhoff migration, to improve the migration image. In that case, the wavelet before and after migration would be different, so that the wavelet for SI can no longer be used. Also the source wavelet mostly is either not available or is not representative for the wavelet on the recorded data, because of dispersion effects occurring during wave propagation in the subsurface, or because of the pre-processing of the data. One approach to obtain the wavelet before migration would be to perform a non-standard seismic-to-well tie, which includes wave propagation effects, on a trace from e.g. the normal-incidence section. For a vertical well, this well tie would need to be performed at a horizontal part of the structure, so that ray-path and well-trajectory coincide in the target area.

Inversion, and visualisation of results

After derivation of the proper wavelet, the inversion algorithm is run on the pre-stack unmigrated data; this data is forward modelled by 3D elastodynamic ray tracing, using the macro velocity and density model for the overburden, and a reservoir model tied to the reference reflector for the target. Fi-

nally, the obtained reservoir-layer parameters are visualised and interpreted. The visualisation of the RBSI-results obtained along the ray-paths generally involves interpolation to a regular grid in depth, due to the fact that, usually, a regular distribution of shot/receiver positions at the surface does not lead to a regular reflection point distribution on a reflector in the subsurface, due to reflector curvature (Figure 3.8) and/or inhomogeneous overburden.

In the next section, the first major difference between SI and RBSI methods is discussed: the inversion domain, which is the recording time domain in the case of RBSI. The data to be inverted are pre-stack unmigrated data.

3.3 Inversion domain - the recording time domain

Ray-based stochastic inversion operates on pre-stack unmigrated data; inside the inversion loop (Figure 3.3), this data is matched with data that is forward modelled with 3D elastodynamic ray-tracing. In this section, advantages and disadvantages are discussed of performing the inversion in the recording time domain.

The outstanding advantage of inverting pre-stack unmigrated data is that all original reflection angle information is directly available for the inversion algorithm, without having been affected by processes such as stacking; the availability of the original reflection angle information is crucial for obtaining good inversion results.

The signal-to-noise ratio (S/N) on the pre-stack unmigrated data, e.g. on common-offset gathers, is low compared to stacked migrated data. Ideally, stacking improves S/N with a factor \sqrt{n} (or in decibels: a gain of $20 \log \sqrt{n}$), where n is the subsurface multiplicity or fold. Hence, if the S/N is unsatisfactory, a way to improve it is to build offset-range or angle-range substacks of a certain fold, so to apply stacking as usually done in migration workflows. However, in the synthetic data test of section 4.4, it will be demonstrated that this operation ‘blurs’ the angle-dependent reflection coefficient information contained in the signal, due to the summing and averaging over different reflection angles; preserving this information is the main incentive for working in the pre-stack unmigrated domain!

An inconvenience of inverting traces from pre-stack unmigrated data is that recordings corresponding to source-receiver pairs regularly distributed at the surface, generally yield inversion results obtained at irregularly distributed

reflection points on interfaces in the target. This requires additional resampling and/or interpolation of RBSI-results if a comparison is made with the SI-results, obtained on a regular migration output grid. Note that by ray-tracing through the (known) overburden velocity model, to the interfaces in the target picked from the migration image, the trace positions from the pre-stack unmigrated data are linked to reflection points in the target. Hence, reflector illumination depends on acquisition geometry, which is the distribution of sources and receivers at the surface, on the overburden velocity model and on the reflector-shape. As an example, Figure 3.8 displays the illumination of a curved reflector, with homogeneous velocity model and normal-incidence acquisition. In this case, the irregular reflection point distribution is caused by reflector curvature alone.

Resolution

An advantage of the unmigrated domain concerning resolution in the direction perpendicular to the reflectors is (obviously) the absence of migration stretch. For example, on the normal-incidence section, the display direction for each trace from that section is along the ray-path in the direction of propagation, and thus always perpendicular to the reflector of interest (Figure 3.8): the direction of best axial resolution for that reflector [Levin, 1998]. On the zero-offset migration image, the same applies for horizontal reflectors, since the (usually) vertical trace-display is perpendicular to them. However, dipping reflectors are encountered with an angle, causing wavelet stretch as a function of dip β , see Eq. (2.63).

Lateral resolution on the pre-stack unmigrated data is limited by the fact that one trace contains not only energy from the reflection point, but also from a region around it called the (first) Fresnel zone. This zone extends away from the reflection point up to a distance called the Fresnel radius [Sheriff, 1980],

$$r_F = \sqrt{\frac{\lambda_d x_3}{2} + \frac{\lambda_d^2}{16}} \approx \sqrt{\frac{\lambda_d x_3}{2}}, \quad (3.1)$$

with λ_d the dominant wavelength and x_3 the depth of observation. Migration collapses these zones, so that an improved lateral resolution after migration is reached given by Eq. (2.57). Therefore, in the RBSI-scheme, extensive usage is made of the migrated data: target reflectors are picked from the

migration image, and the ray-tracing to connect trace positions from the pre-stack unmigrated data with reflection points in the target is done in the migration velocity model. Nevertheless, traces to be inverted by RBSI do come from the pre-stack unmigrated data, hence they contain additional reflection information from a zone surrounding the reflection point. However the maximum sensitivity is at the reflection point, and hindrance only occurs if lateral variations are present within the Fresnel-zone. Note that the evaluation at a point instead of a zone is consistent with the high-frequency approximation in ray-theory.

Finally, on pre-stack unmigrated data, events may be recorded that are not modelled by 3D elastodynamic ray-tracing, and thus must be regarded as noise in the context of RBSI. For example, edge diffractions may be present in the data. A closer look at edge diffractions is taken in the subsection below.

Edge diffractions

Edge diffractions [Trorey, 1970; Berryhill, 1977] may be present on the unmigrated data due to discontinuities in the elastic properties of the subsurface violating the ray-tracing validity conditions. The ‘sudden’ change in elastic properties should occur within a dominant wavelength; this can happen e.g. at interface discontinuities along a fault plane. The edge diffractions disturb the inversion process, since they interfere with the primary reflections on the data.

For a horizontal reflector, the reflection signal is disturbed up to a significant distance from the edge, as depicted on the left of Figure 3.9. The figure shows a normal-incidence recording of an edge diffraction at 0 m horizontal distance, caused by the termination of a horizontal contrast in density ρ at 1500 m depth, with $R(\theta = 0) = 0.06$, in a subsurface with homogeneous parameters $v_p = 3000$ m/s and $\rho = 1500$ kg/m³ above the contrast. The edge diffraction is modelled in the time domain using Eq. (A-311) from Trorey [1970]. A polarity reversal occurs at 0 m horizontal distance. In the trace display at the upper-left of Figure 3.9, the polarity reversal is not well visible, because the edge diffraction interferes with the reflection response of interest (having constant amplitude) from the horizontal density contrast. However, from the graph on the lower-left panel of the same figure, in which

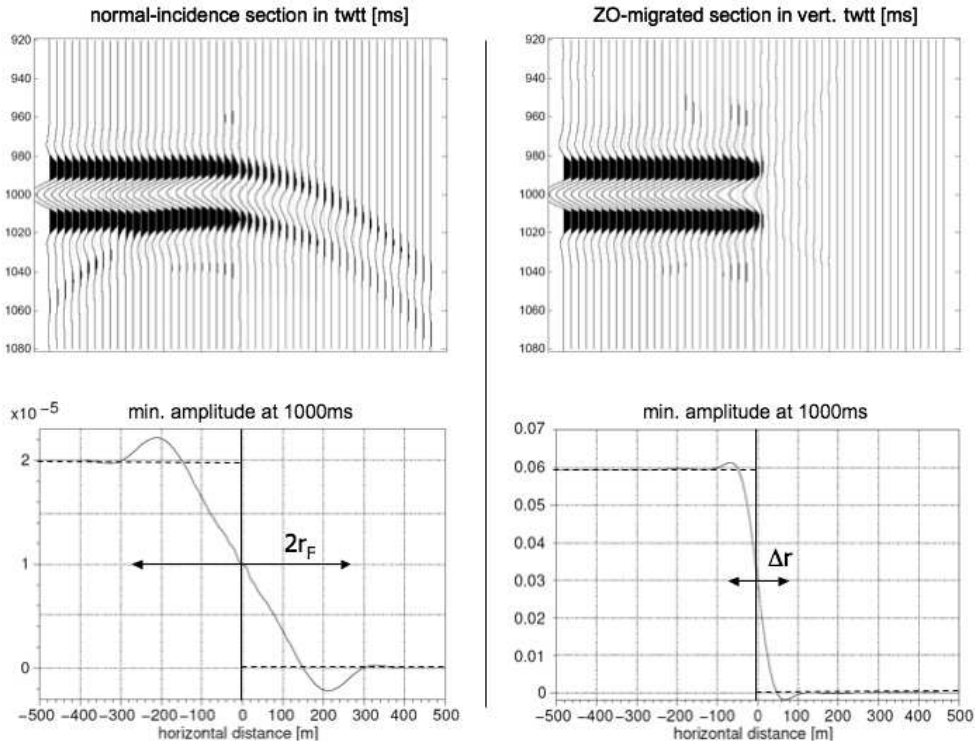


Figure 3.9: Edge diffraction on normal-incidence section (left); comparison with true-amplitude zero-offset migrated result (right). The edge is positioned at 0 m horizontal distance, at the right end of a horizontal reflector with contrast $R(\theta = 0) = 0.06$. Fresnel width is $2r_F \approx 510$ m and $\Delta r \approx 130$ m. See text for details.

the amplitude is displayed as measured on the NI-section at 1000 ms two-way traveltime, the presence of the polarity reversal can be deduced.

To quantify the distance up to which significant interference occurs between reflection and edge diffraction, as observed on the left-hand side of Figure 3.9, the concept of Fresnel radius again can be used, with the evaluation point on the reflector positioned on the edge. However, notice that for edge diffractions, contrary to the conditions for which the Fresnel zone is derived, the wavelet shape changes with increasing distance from the edge, that destructive instead of constructive interference occurs close to the edge, and that the amplitude decreases rapidly away from the edge.

Nevertheless, it is assumed that the major part of interference due to the edge

diffraction occurs within the first Fresnel zone, of which the radius is given by Eq. (3.1). Inserting $x_3 = 1000$ m and $\lambda_d = v_p/f_d = 3000$ m/s/35 Hz = 85 m into Eq. (3.1) gives $2r_F \approx 510$ m. Note that, although good enough for the example above, the concept of Fresnel radius is valid only for *monochromatic* waves in homogeneous media; for band-limited signals, containing more than one frequency, the zone of influence should be used [Brühl et al., 1996].

For comparison, the right-hand side of Figure 3.9 shows the true-amplitude zero-offset Kirchhoff-migrated result, using an aperture size of $2L_{max}^x = 1000$ m. The edge diffraction has been destructively stacked away by the migration process because of its polarity reversal at the apex, hence it does not appear anymore on the migration image. From Eq. (2.57) it follows that the lateral resolution is $\Delta r \approx 130$ m, which is a considerable improvement as compared to $2r_F$.

One possibility to deal with the disturbing edge diffractions in the unmigrated data, is to first interpret edges on the migration image, and then forward model the resulting edge diffractions in the unmigrated domain (expressions for the forward modelling in the time domain are found in Trorey [1970]). With ‘edge diffraction migration’ techniques, as proposed in e.g. Landa et al. [1987]; Kanasewich and Phadke [1988]; Khaidukov et al. [2004], the process of finding edges on the migration image is facilitated. Already kinematic modelling of the edge diffractions in the pre-stack unmigrated data is useful, since in that way potentially troublesome areas for RBSI can be identified. With dynamic modelling, that would require TA PreSDM, it would even be possible to subtract edge diffraction contributions from the unmigrated data, leaving a clean image for RBSI.

In the following section, the focus is on the second major difference between SI and RBSI methods: the forward modeller, which is 3D elastodynamic ray-tracing in the case of RBSI. The ray-tracing is used to forward model pre-stack unmigrated data.

3.4 Forward modeller - 3D elastodynamic ray-tracing

In order to model traces in the recording time domain, RBSI makes use of an elastodynamic ray-tracing kernel. Ray-theory is a high-frequency asymptotic method based on an approximate solution of the equation for wave-pro-

pagation through an acoustic or elastic subsurface. In Chapter 1, the form of the solution for the elastodynamic equation was shown. In ray-tracing, only the leading term of the formal asymptotic ray series expansion of the elastodynamic equation is used. Ray-tracing has two different operational modes: in kinematic ray-tracing, only ray-paths and traveltimes are calculated using the eikonal equations, whereas in (elasto)dynamic ray-tracing also particle displacement amplitudes are calculated using the transport equations, see section 1.3.2. For an exhaustive treatment of the method, the reader is referred to Červený [2001]. The aspects of the method relevant to RBSI are discussed below.

Dynamic ray-tracing makes it possible to calculate ray theoretical seismograms for elastic subsurface models. The reflection traveltimes and amplitudes calculated by the ray-tracer are converted to synthetic traces by convolution with the seismic wavelet $w(t)$, using Eqs. (2.34) and (2.35), but now with τ_j the traveltimes calculated by ray-tracing and R_j the calculated ray-amplitudes. In RBSI, the calculated synthetic traces are used to invert recorded seismic data. The elastic model parameters $v_p(\vec{x})$, $v_s(\vec{x})$ and $\rho(\vec{x})$ are coupled to rock- and pore-fluid properties via rock/fluid models.

■ 3.4.1 Ray-validity conditions

General validity-conditions of the ray method are given in Červený [2001, section 5.9.1] and Červený et al. [1977, Chapter 8]. The first condition, already discussed in Chapter 1 but repeated here for convenience, states that the dominant wavelength λ has to be smaller than the scale of medium property variations in the subsurface and of interface curvatures. Hence, a valid subsurface for RBSI consists of layers bounded by ‘smoothly curved’ interfaces and having ‘smoothly varying’ layer properties, with the quoted words indicating the relation with wavelength of the observed wave. More specifically, for ray-tracing across interfaces, ray-theory requires at least C_2 -smoothness of Σ_n [Červený, 2001, section 4.4.1] (i.e. Σ_n being twice continuous differentiable), determined from reflection event picks on the migrated image for the sake of generating reflector normal vector fields (see Figure 3.10 for an interface which is not C_2 -smooth).

The second ray-validity condition states that the ray approximation becomes poor near areas with irregular behaviour of the wavefield, e.g. near caustic

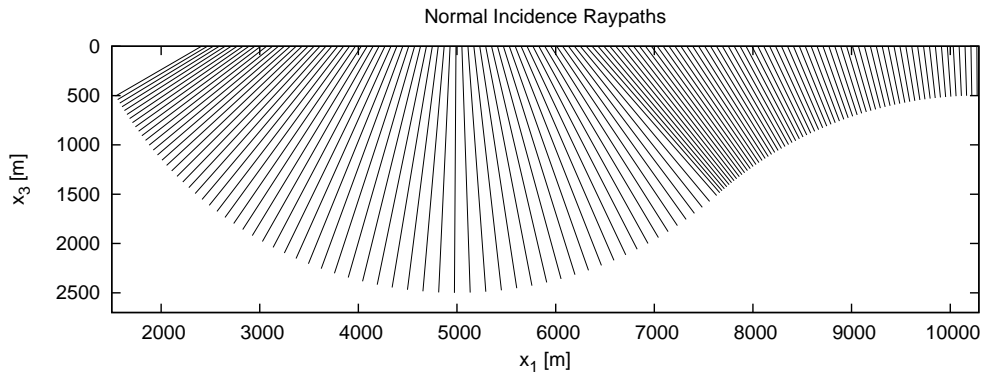


Figure 3.10: Normal-incidence rays to a curved reflector that is not C_2 -smooth. The point of non-smoothness on the interface is revealed by a sudden jump in the reflection point distribution (compare with the smooth interface of Figure 3.8), even though the overburden velocity model is homogeneous, and the shot-point spacing at the planar acquisition surface is regular.

points or transition zones between shadow and illuminated regions in the subsurface, so that RBSI should also not be applied close to these. More sophisticated ray-tracing methods exist to overcome this shortcoming, see e.g. Popov [1982], and could be employed in the RBSI-scheme instead of standard ray-tracing.

For angles of incidence θ larger than the critical angle θ_c , transmission generates evanescent waves which cannot be modelled with the standard ray-method [Červený, 2001, section 3.2.3]. The critical angle is the angle of incidence for which the transmitted ray is tangent to the interface (i.e. the transmission angle θ_t equals 90°). Postcritical incidence does not occur if the velocity drops at the transmission-side: upon inserting $\theta_t = 90^\circ$ in Snell's law (or Snel's law? See Box 3.1), $\sin \theta / \sin \theta_t = v_i / v_t$ (with P- or S-wave propagation velocity at incidence and transmission side indicated by v_i and v_t), it follows that $\sin \theta_c = v_i / v_t$, from which it can be seen that no solutions for θ_c exist if $v_i > v_t$.

To forward model the reflection response of the inversion target, which is made up of layers that are thinner than the dominant wavelength, RBSI will use primaries-only ray-tracing. Hereby it is assumed that any fine-layering effects that may appear, like the apparent amplitude-variation-with-angle ef-

fects of internal multiple reflections and wave conversions/interactions in thin-layered structures [Wapenaar et al., 1999; Simmons and Backus, 1994; O’Doherty and Anstey, 1971] are neglected or assumed to have been compensated for, so that the total primary reflection response from the target can be linearised as the sum of separate reflection responses of the individual contrasts. Alternatively, wave-mode conversions and multiples could be included in the ray-tracing used by RBSI.

■ 3.4.2 Ray-amplitudes in a 3D configuration

In this and the next subsection, ray-tracing formulations for unconverted primary P-wave reflection responses are given for two subsurface configurations. First the formulation for a general 3D configuration is given, which is then used to derive a simpler formulation for a caustic-free 2.5D configuration with normal-incidence acquisition. Most examples in the next chapters will make use of the latter configuration.

For the 3D configuration, consider a 3D isotropic, laterally varying, layered elastic subsurface, with target interface Σ_n underlying the n -th layer (Figure 3.2). The receiver and omnidirectional point source are positioned at locations \vec{x}_r and \vec{x}_s on the surface ∂X . No overturned reflectors are present, and only subcritical angles of incidence are considered.

Displacement vector

The vertical component u_3 of the particle displacement vector, due to an unconverted primary P-wave reflecting at \vec{x}_R on Σ_n , using ray-theory can be expressed as [Červený, 2001, Eqs. (5.2.1) and (6.1.1)],

$$u_3(\vec{x}_s, \vec{x}_r, \vec{x}_R; t) = \text{Re}\{U_3^{(0)}(\vec{x}_s, \vec{x}_r, \vec{x}_R)F_0(t - \tau(\vec{x}_s, \vec{x}_r, \vec{x}_R))\}, \quad (3.2)$$

where the expression on the right-hand side represents the leading term (denoted by zeros) of the formal asymptotic ray series expansion solution of the general elastodynamic wave equation Eq. (1.1), see section 1.3. It is convenient to perform the calculation for u_3 using the *analytical* source wavelet F_0 and the *complex-valued* displacement amplitude function $U_3^{(0)}$; afterwards, the real-valued solution is obtained by taking the real part, $\text{Re}\{\}$, of the result [Červený, 2001, section A.3].

The analytical source wavelet $F_0(t)$, with t being the two-way traveltime (recording time), is defined as $F_0(t) = \mathcal{F}_0(t) + i\mathcal{G}_0(t)$, with \mathcal{G}_0 the Hilbert transform [see Eq. (2.48)] of the bandlimited source wavelet \mathcal{F}_0 (having unit amplitude) for the zero-order approximation of the ray series solution. The wavelet is placed at τ , the two-way traveltime to reflection point \vec{x}_R .

Amplitude function

The vertical component $U_3^{(0)}$ of the vectorial complex-valued displacement amplitude function $\vec{U}^{(0)}$ is given by,

$$U_3^{(0)}(\vec{x}_s, \vec{x}_r, \vec{x}_R) = \frac{e^{-i\frac{\pi}{2}\kappa(\vec{x}_s, \vec{x}_r)}}{\mathcal{L}(\vec{x}_s, \vec{x}_r)} C_0(\vec{x}_r) R(\vec{x}_R, \theta_n^+) T(\vec{x}_s, \vec{x}_r) A_0(\vec{x}_s), \quad (3.3)$$

where Eq. (5.2.88) of Červený [2001] was used as a starting point. In the following, the components of this equation are described in more detail; new concepts are introduced where necessary.

Isotropic point source The rightmost symbol of Eq. (3.3) represents the amplitude of the isotropic point source placed at \vec{x}_s . The isotropic point source is represented by $S(\vec{x}, t) = F_0(t) A_0(\vec{x}_s) \delta(\vec{x} - \vec{x}_s)$, in which δ is Dirac's delta-pulse. The amplitude radiated in each direction is assumed equal, so it can be plainly indicated with $A_0(\vec{x}_s)$ without additional arguments specifying direction, following Eq. (5.2.31) of Červený [2001]. Expressions exist to describe the effect of the free surface at the source, but for simplicity it is assumed here that this effect is already taken into account.

Transmission coefficients Scalar $T(\vec{x}_s, \vec{x}_r)$ accounts for the amplitude losses due to transmissions across all interfaces along the ray. The expression for T was given before in Eq. (2.52) but is repeated below for convenience,

$$T = \sqrt{\frac{\rho(\vec{x}_s) v_p(\vec{x}_s)}{\rho(\vec{x}_r) v_p(\vec{x}_r)}}^{2(n-1)} \prod_{k=1}^{n-1} T_k \sqrt{\frac{(\rho v_p \cos \theta)_{k+}}{(\rho v_p \cos \theta)_{k-}}}, \quad (3.4)$$

with k counting the interfaces along the ray (Figure 3.2), and $-$ denoting evaluation at the point of incidence at the side of the incoming ray, $+$ at the

point of transmission of the outgoing ray of the encountered interface. T_k is the Zoeppritz particle displacement-normalised plane wave transmission coefficient for unconverted P-waves, corresponding to traversal of interface k in the direction of propagation. Angle θ is the angle between ray and interface normal \hat{n} at the $-$ or $+$ side.

Note that Červený [2001] uses the notation $\cos \theta = \sqrt{1 - v_p^2 p^2}$, with $p = \sin \theta / v_p$ the horizontal slowness (or ray-parameter) and imaginary square roots taken positive; this choice is consistent with the definition of the Fourier transform in Eq. (2.49) and assures that evanescent waves decrease in amplitude with away from the interface.

Furthermore, Červený [2001] considers the term of Eq. (3.4) before the product to be part of the relation for continuation of amplitudes along a ray between points \vec{x}_s and \vec{x}_r in medium without interfaces, and hence excludes it from his product of transmission/reflection coefficients \mathcal{R}^C in Eq. (5.2.88). The last term of Eq. (3.4) is in agreement with the concept of energy-flux-normalised transmission/reflection coefficients, presented by Červený [2001] in Eq. (5.3.10). In analogy to that equation, the flux-normalised transmission coefficient \mathcal{T}_k may be written as,

$$\mathcal{T}_k = T_k \sqrt{\frac{(\rho v_p \cos \theta)_{k+}}{(\rho v_p \cos \theta)_{k-}}}, \quad (3.5)$$

which is easily recognised in Eq. (3.4). The flux-normalised transmission coefficient has the convenient property of being reciprocal, which means that the coefficient is the same for a ray traversing an interface and the ray traversing the interface along the same path but in opposite direction.

To avoid possible confusion, it is noteworthy to state here that the expression for the elastic flux-normalised P-wave transmission coefficient given by Eq. (3.5), is slightly different from the form usually found in the literature to describe flux-normalisation in the acoustic case. In that case, a P-wave potential-field description is used for deriving the transmission coefficient, whereas in this work the P-wave transmission coefficient was described in terms of particle displacement. The relation between both types of transmission coefficients is [de Haas, 1992, Eq. (A15)],

$$T_{k,\text{disp}} = T_{k,\text{pot}} \frac{(\rho v_p)_{k-}}{(\rho v_p)_{k+}}. \quad (3.6)$$

Inserting this equation into Eq. (3.5),

$$\mathcal{T}_k = T_{k,\text{disp}} \sqrt{\frac{(\rho v_p \cos \theta)_{k+}}{(\rho v_p \cos \theta)_{k-}}}, \quad (3.7)$$

gives,

$$\mathcal{T}_k = T_{k,\text{pot}} \sqrt{\frac{(\rho v_p)_{k-}^2}{(\rho v_p)_{k+}^2}} \sqrt{\frac{(\rho v_p \cos \theta)_{k+}}{(\rho v_p \cos \theta)_{k-}}} = T_{k,\text{pot}} \sqrt{\frac{(\rho v_p)_{k-} (\cos \theta)_{k+}}{(\rho v_p)_{k+} (\cos \theta)_{k-}}}. \quad (3.8)$$

which is the form that is found for the acoustic flux-normalised P-wave transmission coefficients derived using a P-wave potential-field description in e.g. Červený [2001, Eq. (5.1.16) and p. 457] or Wapenaar [1998].

Later on, it will also appear handy to have Eq. (3.4) with the running index i corresponding to the structural interfaces defined in Figure 3.2, rather than to interfaces encountered along the ray,

$$T = \sqrt{\frac{\rho(\vec{x}_s) v_p(\vec{x}_s)}{\rho(\vec{x}_r) v_p(\vec{x}_r)}} \prod_{i=1}^{n-1} \left[T_i^+(\vec{x}_{T,i}^+, \theta_i^+) T_i^-(\vec{x}_{T,i}^-, \theta_i^-) \times \sqrt{\frac{[\rho_{i+1} v_{p,i+1} \cos \theta_{t,i}^+](\vec{x}_{T,i}^+)}{[\rho_i v_{p,i} \cos \theta_i^+](\vec{x}_{T,i}^+)}} \sqrt{\frac{[\rho_i v_{p,i} \cos \theta_{t,i}^-](\vec{x}_{T,i}^-)}{[\rho_{i+1} v_{p,i+1} \cos \theta_i^-](\vec{x}_{T,i}^-)}} \right], \quad (3.9)$$

with T_i^+ the Zoeppritz transmission coefficient at layer i for incidence from above, T_i^- from below, transmission points $\vec{x}_{T,i}$ as defined on Figure 3.2, and angles θ as defined on Figure 3.11. Notice that for a constant propagation velocity in the entire subsurface, Eq. (3.9) can be rewritten as,

$$T = \prod_{i=1}^{n-1} \left[T_i^+(\vec{x}_{T,i}^+, \theta_i^+) T_i^-(\vec{x}_{T,i}^-, \theta_i^-) \right] \times \sqrt{\frac{\rho(\vec{x}_s)}{\rho(\vec{x}_r)}} \prod_{i=1}^{n-1} \left[\sqrt{\frac{\rho_{i+1}(\vec{x}_{T,i}^+)}{\rho_i(\vec{x}_{T,i}^+)}} \sqrt{\frac{\rho_i(\vec{x}_{T,i}^-)}{\rho_{i+1}(\vec{x}_{T,i}^-)}} \right], \quad (3.10)$$

in which the product in the upper line equals term T from van der Burg et al. [2004, Eq. (2)], and in which the complete lower line is equivalent to term

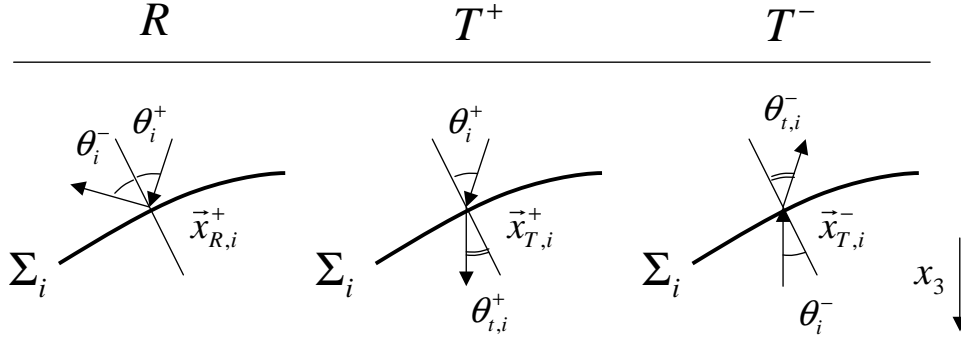


Figure 3.11: Notations used for properties related to reflection from above R , and transmission from above T^+ and below T^- , with i referring to layer-interfaces. Angles θ_i are measured with respect to the normal to interface Σ_i , at the reflection or transmission points $\vec{x}_{R,i}$, $\vec{x}_{T,i}$.

D from van der Burg et al. [2004, Eq. (3)],

$$\sqrt{\frac{\rho(\vec{x}_s)}{\rho(\vec{x}_r)}} \prod_{i=1}^{n-1} \left[\sqrt{\frac{\rho_{i+1}(\vec{x}_{T,i}^+)}{\rho_i(\vec{x}_{T,i}^+)}} \sqrt{\frac{\rho_i(\vec{x}_{T,i}^-)}{\rho_{i+1}(\vec{x}_{T,i}^-)}} \right] = \prod_{i=1}^n \left[\sqrt{\frac{\rho_i(\vec{x}_{T,i-1}^+)}{\rho_i(\vec{x}_{T,i}^+)}} \sqrt{\frac{\rho_i(\vec{x}_{T,i}^-)}{\rho_i(\vec{x}_{T,i-1}^-)}} \right] \quad (3.11)$$

where it was used on the right-hand side that $\vec{x}_{T,0}^+ = \vec{x}_s$, $\vec{x}_{T,0}^- = \vec{x}_r$ and $\vec{x}_{T,n}^+ = \vec{x}_{T,n}^- = \vec{x}_R$ (Figure 3.2), which enables incorporation of $\sqrt{\rho(\vec{x}_s)/\rho(\vec{x}_r)}$ into the product for this constant v_p case.

Reflection coefficient Scalar $R(\vec{x}_R, \theta_n^+)$ in Eq. (3.3) is the Zoeppritz particle displacement- normalised plane wave specular reflection coefficient for unconverted P-waves, at subsurface point \vec{x}_R on contrast Σ_n , for angle of incidence θ_n^+ as defined on Figure 3.2; in this work the models are such that only reflections from above occur, so there is no need to complicate the notation to R^+/R^- as was necessary for the transmissions.

Note that R is equal to its energy flux-normalised counterpart \mathcal{R} [Červený, 2001, Eq. (5.3.13)]: the equation for the flux-normalised reflection coefficient is equal in form to Eq. (3.5), however for specular reflection, k_+ and k_- are on the same side of the interface, and the angle of incidence equals the reflection angle, so that the last term cancels.

Interface conversion coefficient At the free surface, incident P-waves from below are reflected to P- and S-waves only; no transmission takes place. The interface conversion coefficient C_0 takes this effect into account for receivers placed at the Earth's free surface. C_0 evaluated at \vec{x}_r is,

$$C_0(\vec{x}_r) = \frac{2(1 - 2v_s^2 p^2) \sqrt{1 - v_p^2 p^2}}{(1 - 2v_s^2 p^2)^2 + 4p^2 v_s^3 v_p^{-1} \sqrt{1 - v_p^2 p^2} \sqrt{1 - v_s^2 p^2}}, \quad (3.12)$$

where Eqs. (5.3.33), (5.3.5) and (5.3.9) of Červený [2001] were used. In the equation, v_p, v_s are all taken at the receiver position, $p = \sin \theta_0 / v_p$ is the horizontal slowness for the incident P-wave with θ_0 the angle of incidence at the receiver, i.e. the angle with the vertical for a flat surface $x_3 = 0$ (Figure 3.2). Note that $C_0(\vec{x}_r)$ agrees with the value given by Aki and Richards [1980, p.190],

$$C_0(\vec{x}_r) = \frac{\frac{-2v_p \cos \theta_0}{v_s^2} \frac{\cos \theta_0}{v_p} \left(\frac{1}{v_s^2} - 2p^2 \right)}{\left(\frac{1}{v_s^2} - 2p^2 \right)^2 + 4p^2 \cdot \frac{\cos \theta_0}{v_p} \frac{\cos \theta_0^S}{v_s}}, \quad (3.13)$$

where θ_0^S is the angle of reflection at the receiver of the P-to-S converted wave; this can be seen by substituting $\cos \theta_0 = \sqrt{1 - v_p^2 p^2}$ and $\cos \theta_0^S = \sqrt{1 - v_s^2 p^2}$ (using $p = \sin \theta_0 / v_p = \sin \theta_0^S / v_s$ and trigonometrical relation $\sin^2 x + \cos^2 x = 1$), and multiplying numerator and denominator by v_s^4 .

KMAH index (caustics) Phase shifts due to passage through caustic points are handled by KMAH index κ , which in isotropic media equals the sum of caustic indices encountered on the total path from \vec{x}_s to \vec{x}_r , see Eqs. (3.10.50) and (5.2.46) of Červený [2001]. As on p. 39, the minus sign in the exponential of Eq. (3.3) corresponds to the sign-convention chosen in the definition of the Fourier-transform [Eq. (2.49)]. Notice again that amplitudes near caustic points calculated using standard ray-tracing are unreliable, but that extensions of the ray-method exist to overcome this problem.

Relative geometrical spreading Finally, relative geometrical spreading along the ray-path due to a point source at \vec{x}_s , including the effects of reflector curvature, is indicated by $\mathcal{L}(\vec{x}_s, \vec{x}_r)$. The spreading factor takes

into account the change in size of an elementary cross-sectional area of the ray-tube during ray-propagation from source to receiver. Many detailed expressions for \mathcal{L} in different types of media are found in Červený [2001, section 4.10], Červený et al. [1977]; Červený and Ravindra [1971]. Note that the geometrical spreading definition of Červený [2001] is adapted; geometrical spreading L from Červený and Ravindra [1971] and Červený et al. [1977] should be multiplied by a factor $v_p(\vec{x}_s)$ to comply.

The next section shows how the 3D expressions discussed in this section simplify for a caustic-free 2.5D geometry with normal-incidence acquisition.

■ 3.4.3 Ray-amplitudes in a 2.5D caustic-free NI configuration

In the synthetic data examples of Chapter 4, the subsurface and measurement configuration are chosen such that rays do not pass through caustic points. Also, most examples use a normal-incidence acquisition (NI; $\vec{x}_s = \vec{x}_r$) in a 2.5D setting (the concept of 2.5D settings is explained on p. 44). In this subsection, the ray-tracing equations valid in such a setting are derived from the general equations of the previous subsection. Again, no overturned reflectors are present, and only subcritical angles of incidence are considered.

Displacement vector

With the absence of caustics, the exponential in Eq. (3.3) equals unity because $\kappa = 0$: the vertical component $U_3^{(0)}$ of the vectorial particle displacement amplitude function becomes real-valued for subcritical reflection angles. If also using the real-valued wavelet $\mathcal{F}_0(t)$, Eq. (3.2) can be rewritten as,

$$u_3(\vec{x}_s = \vec{x}_r, \vec{x}_R; t) = U_3^{(0)}(\vec{x}_s = \vec{x}_r, \vec{x}_R) \mathcal{F}_0(t - \tau(\vec{x}_s = \vec{x}_r, \vec{x}_R)). \quad (3.14)$$

This is the vertical component of the particle displacement vector for an unconverted, primary P-wave normal-incidence reflection response of the n -th contrast Σ_n in the 2.5D case.

Amplitude function

The elements of the displacement amplitude function Eq. (3.3) other than the KMAH index discussed above, change as follows. For normal-incidence ac-

quisition and considering one single reflection point \vec{x}_R , source and receiver locations at the surface are the same ($\vec{x}_s = \vec{x}_r$), transmission locations for the up- and down-going ray-branches become equal, and the $\cos \theta$ terms in Eq. (3.4) cancel. It follows that Eq. (3.4) simplifies to,

$$T = \prod_{k=1}^{2(n-1)} T_k, \quad (3.15)$$

with k counting the interfaces along the ray, and reflection taking place on the n -th structural interface (Figure 2.6). This equation has already been used in the previous chapter, see Eq. (2.55). Alternatively, Eq. (3.9) simplifies to,

$$T = \prod_{i=1}^{n-1} T_i^+(\vec{x}_{T,i}^+ = \vec{x}_{T,i}^-, \theta_i^+) T_i^-(\vec{x}_{T,i}^+ = \vec{x}_{T,i}^-, \theta_i^-). \quad (3.16)$$

with i counting the structural interfaces above the reflecting structural interface (Figure 3.2), and the notation for transmission points \vec{x}_T and angles θ defined on Figure 3.11.

For normal-incidence, $\theta_n^+ = 0$, so that the Zoeppritz reflection coefficient simplifies to the well known form [Červený, 2001, Eq. (5.3.17)],

$$R(\vec{x}_R, \theta_n^+ = 0) = \frac{\rho_{n+1}(\vec{x}_R) v_{p,n+1}(\vec{x}_R) - \rho_n(\vec{x}_R) v_{p,n}(\vec{x}_R)}{\rho_{n+1}(\vec{x}_R) v_{p,n+1}(\vec{x}_R) + \rho_n(\vec{x}_R) v_{p,n}(\vec{x}_R)}. \quad (3.17)$$

The relative geometrical spreading $\mathcal{L}(\vec{x}_r, \vec{x}_s)$ along the ray-path, from source to receiver, decouples into two independent factors for a 2.5D setting (also for $\theta_n^+ \neq 0$) [Červený, 2001, Eq. (4.13.52)],

$$\mathcal{L}(\vec{x}_r, \vec{x}_s) = \mathcal{L}^{\parallel}(\vec{x}_r, \vec{x}_s) \mathcal{L}^{\perp}(\vec{x}_r, \vec{x}_s), \quad (3.18)$$

in which \mathcal{L}^{\parallel} refers to the in-plane relative geometrical spreading, and \mathcal{L}^{\perp} to transverse relative geometrical spreading. The transverse spreading is given by [Červený, 2001, Eq. (4.13.54)],

$$\mathcal{L}^{\perp}(\vec{x}_r, \vec{x}_s) = \left| \int_{\vec{x}_s}^{\vec{x}_r} v_p(s) ds \right|^{1/2}, \quad (3.19)$$

with the integral expressing integration of velocity along the complete ray-path from source to receiver, with s denoting the arclength.

Note that in the 2.5D case with a homogeneous medium overlying a (possibly dipping) plane reflector, Eq. (3.18) would yield,

$$\mathcal{L}^\perp(\vec{x}_r = \vec{x}_s) = \sqrt{v_p l}, \quad (3.20)$$

with l the total length of the straight NI-ray-path from source to receiver, via reflection point \vec{x}_R . Appreciating the symmetry properties of a homogeneous subsurface leads to $\mathcal{L}^\parallel = \mathcal{L}^\perp$. With a curved reflector, however, \mathcal{L}^\parallel is found to be, using Červený et al. [1977, Eq. (3.77)],

$$\mathcal{L}^\parallel(\vec{x}_r = \vec{x}_s) = \mathcal{L}^\perp \sqrt{\frac{r_c^+(\vec{x}_R) + \frac{1}{2}l}{r_c^+(\vec{x}_R)}} = \mathcal{L}^\perp \sqrt{1 + \frac{l}{2r_c^+(\vec{x}_R)}}, \quad (3.21)$$

revealing the influence of the curved reflector, with r_c^+ the reflector radius of curvature at \vec{x}_R , taking positive values if the centre of the corresponding circle of curvature resides on the upper side of the reflector (assuming ray-incidence from above and the absence of overturned reflectors).

In the 2.5D case with a subsurface consisting of a set of n flat, homogeneous layers, hence an extension of the setting for Eq. (3.20), the following equations apply,

$$\mathcal{L}^\perp = \mathcal{L}^\parallel, \quad (3.22)$$

$$\mathcal{L}^\parallel(\vec{x}_r = \vec{x}_s) = \sqrt{\sum_{i=1}^n v_{p,i} l_i}, \quad (3.23)$$

with l_i the two-way NI pathlength in layer i (overlying interface i). This follows from Červený et al. [1977, Eq. (3.77)] or Červený and Ravindra [1971, Eq. (2.143)], or can be found by using Eq. (3.19).

Applying all the simplifications discussed above to Eq. (3.3) yields the expression for the vertical component of the vectorial particle displacement amplitude function for an unconverted, primary P-wave normal-incidence reflection response of the n -th contrast in the 2.5D case,

$$U_3^{(0)}(\vec{x}_s = \vec{x}_r, \vec{x}_R) = \frac{C_0(\vec{x}_r)R(\vec{x}_R, \theta_n^+ = 0)T(\vec{x}_s = \vec{x}_r)A_0(\vec{x}_s)}{\mathcal{L}^\parallel(\vec{x}_s = \vec{x}_r)\mathcal{L}^\perp(\vec{x}_s = \vec{x}_r)}. \quad (3.24)$$

This finishes the treatment of ray-theory. In the next section, the strengths of RBSI in relation to SI are explored.

3.5 Discussion

Ray-based stochastic inversion differs from conventional stochastic inversion on two major points that are closely connected. Firstly, it performs inversion directly on the pre-stack unmigrated data, in the recording time domain. Secondly, to forward model the reflection response, 3D elastodynamic ray-tracing is used. Below, a comparison is made with the approach taken by stochastic inversion, phrasing the potential benefits and drawbacks of the new method along the way.

As was discussed in Chapter 2, stochastic inversion does not always provide an accurate estimate of reservoir parameters. First of all, this is due to the limitations of the 1D convolutional modeller in forward modelling the correct migration response. Secondly, it is due to the nature of the inversion domain (the migration image), which is the predetermined, fixed result of an extensive processing sequence, possibly with errors in the target area, which cannot be corrected anymore during the inversion.

Performing the inversion on pre-stack unmigrated data has the distinct advantage of having access to the original, unmodified, angle-dependent reflection coefficient information. This information is crucial for good inversion, as the rock- and pore-fluid parameters are estimated from it. The well-known and widely available AVO/AVA inversion techniques already make use of the angle-dependent reflection information, albeit after migration and substacking. By (sub)stacking, the angle-information is sacrificed for a better signal-to-noise ratio on the migrated image. However, the data-redundancy assumption to legitimate stacking for better S/N , applies only to the common position of the reflection point, but not to the angle-dependent reflection amplitude. Of course, also S/N on pre-stack unmigrated data may be expected to be low without any form of stacking applied.

Working with common-angle gathers or angle-range gathers seems most natural for the ‘angle-oriented’ method of RBSI. In practice, it is much easier to simply sort the pre-stack unmigrated data to common-offset gathers. Commonly, the angle-gathers are subsequently computed from the common-offset gathers using a 1D subsurface model. This approach leads to considerable inaccuracies for subsurfaces with strong lateral variations.

Obviously, migration-induced wavelet stretch as a function of reflector dip and reflection angle is absent in the pre-stack unmigrated domain, as well

as moveout stretch due to normal moveout or dip moveout processing steps (NMO/DMO). Also, the usage of ray-tracing has the added potential benefit of providing a transparent link between Kirchhoff pre-stack depth migration and stochastic inversion for reservoir properties.

On the pre-stack unmigrated data, several events are not or cannot be forward modelled by the ray-tracer, and as such must be considered as noise. For example, it was shown that edge diffractions render difficult the application of RBSI up to considerable distance away from the edge. During migration, edge diffractions are destructively stacked up, which much improves lateral resolution on the migration image near lateral discontinuities due to geological truncations.

Employment of 3D elastodynamic ray-tracing as forward modeller is much more computationally expensive than simple 1D convolution. Nevertheless, as mentioned at the end of the discussion in the previous chapter, it is opportune to improve upon the 1D convolutional forward modeller with the present- and future generation of computers. Processing time can potentially be saved by re-using ray-path information calculated for preserved-amplitude Kirchhoff-type migration. Hereby the traveltimes tables available on the coarse migration grid need to be interpolated to the fine target grid for inversion, with the cost of interpolation likely to be much smaller than the cost of a new ray-tracing job to (reflection points in) the fine target grid.

The last point discussed in this section concerns the way in which parameter-updating is done. Updating the target model-parameters in RBSI is more complicated than the trace-by-trace updating used in SI, due to overlapping volumes of reflection- and transmission points for adjacent traces from the pre-stack unmigrated dataset (Figure 3.5). However, special cases of RBSI exist, such as described in section 3.1.3 and in the next section, in which model updating can be done in a trace-by-trace manner similar to SI. In these special cases, parameter estimation still occurs along the ray-path and generally not in the vertical direction as in SI. Inverting along normal-incidence ray-paths offers the optimal resolution for discerning the layering within the target. The inversion along ray-paths as done in RBSI also implies that, for representation of inversion results on a regular grid, interpolations are generally required.

In the following two chapters, the results of numerical experiments and real-data tests are presented to determine the potential of RBSI versus SI. Before

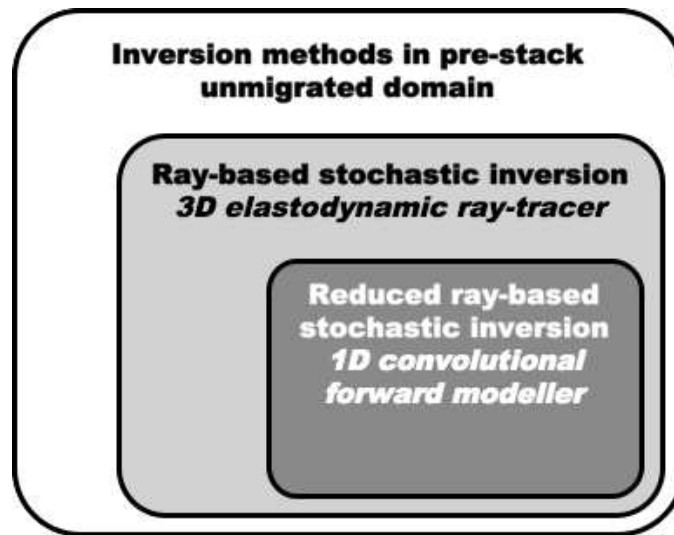


Figure 3.12: *Reduced RBSI as a special case of ray-based stochastic inversion. The forward modelling kernels are printed in italic.*

advancing to the numerical tests however, in the next section one special case of RBSI is considered that offers substantial practical benefits.

3.6 Special case - 1D convolutional RBSI

In this section, a ‘reduced’ RBSI scheme is presented in which, only in the target zone, the 3D elastodynamic ray-tracer is replaced by a 1D forward modelling kernel as found in common inversion software—offering great practical advantages. The scheme is a special case of RBSI (Figure 3.12). As long as the inversion target underlying the 3D overburden satisfies the 1D assumption reasonably well, this reduced, or 1D convolutional, scheme is a good approximation of the RBSI-scheme.

In the following, first, the principles of 1D convolutional RBSI are given. Then, a set of equations is derived describing the method and its applicability to a given reservoir configuration.

■ 3.6.1 Principles

1D convolutional RBSI uses 1D convolution to model traces from a pre-processed normal-incidence (NI) dataset in the target window; hence the inversion is carried out along NI ray-paths. As will be described on p. 92, the NI-dataset is pre-processed such that amplitude effects of wave propagation through the overburden are removed. Note that the pre-processing can only be done correctly if sufficient knowledge on the overburden is available. Just like the conventional trace inversion methods, the new method will assume this information is present. As was done for RBSI, only unconverted single P-wave reflections are considered in the following.

Using 1D convolution to model NI-data

In general, for a sequence of smooth target interfaces of arbitrary shape (Figure 3.13a), the seismic normal-incidence response recorded by a single receiver at the surface will contain information about specular reflection points $\vec{x}_{R,i}$ associated with non-overlapping ray-paths. Since the true 3D forward modelling must be employed also in the target, to correctly invert for reservoir parameters in the target of a 3D subsurface model, the replacement of 3D forward modelling by 1D forward modelling using a local 1D approximation *inside the target* will generally be inadequate.

Moreover, by using 1D convolution as the forward modeller for NI-data, also the amplitudes of the reflection responses in the target zone will be handled inadequately. This is due to the fact that traces from the NI-dataset, apart from the reflection amplitude R , also contain transmission and spreading effects because of wave propagation within the target interval, see Eq. (3.3). However, the 1D convolutional model only accounts for R , see Eqs. (2.34) and (2.35). Nevertheless, if the target satisfies certain conditions, employment in the target zone of a 1D forward modelling kernel—offering great practical advantages — while still using 3D modelling for the overburden, can be a good approximation of the, generally 3D, RBSI-scheme.

Requirements to the target zone

The conditions for applying ‘reduced’ RBSI are given in Table 3.2. The first condition listed, relates to how well the target geometry satisfies the 1D

Table 3.2: Application regime for 1D convolutional RBSI.

| |
|--|
| For 1D convolutional RBSI, the target inversion interval: |
| - consists of a set of plane-parallel layers, |
| - contains a moderate amount of layers, (typically < 10) |
| - consists of not too large impedance contrasts, (typ. $1.2 \cdot 10^6 \text{ kg/m}^2\text{s}$) |
| - has total thickness of at most a few dominant wavelengths. |

assumption. It is assumed, that the target behaves locally as a sequence of plane-parallel thin layers (Figure 3.13b). The target is allowed to incline vertically; in fact the new inversion method is expected to improve the results of SI especially on the dipping parts, on the horizontal parts SI has the advantage of a more favourable signal-to-noise ratio of the migrated sub-stack as compared to the single-fold NI-data, while it is not yet hampered by migration-induced dip-dependent wavelet stretch. As was the case for RBSI, the target is identified by a clearly distinguishable reflector, the reference reflector; for convenience, Σ_n is taken, but it does not necessarily have to be the top interface of the target interval.

The remaining conditions for applying ‘reduced’ RBSI listed in Table 3.2 relate to the impact of neglecting transmission- and spreading-losses in the target, by using the 1D convolutional model. Note that the requirements are formulated in rather general terms: they depend on the encountered target geometry and the total error one is willing to allow. Expressions that relate the error in modelled amplitude to target thickness, number of layers and size of impedance contrasts are given in the next section. Before applying 1D convolutional RBSI, the modelling error should be calculated and if considered too large, the amount of layers to be inverted in the same 1D convolutional RBSI-job should be lowered by narrowing the inversion window or splitting it in parts. An example calculation is found in Chapter 4, section 4.2.2.

The specific values found in the table are meant *only* to give the reader an idea on the order of magnitude. The mentioned average acoustic impedance in combination with the number of layers gives an amplitude error due to neglect of transmission of about 10%; assuming an average layer-thickness of 10 m and a target depth of 2 km, also the error due to neglect of spher-

ical spreading amounts to 10%. The example impedance contrast is based on values from the sandstone-shale sequence found in a Gulf of Mexico field discussed in Chapter 5. It is important that no high-contrast layers are present, like e.g. salt-layers in the presence of which impedance contrasts can easily go up to $4 \cdot 10^6 \text{ kg/m}^2\text{s}$: strong contrasts like these lead to a large amplitude error due to neglecting transmission losses even for a small number of layers, and more importantly, generate strong multiples while only the primary response is modelled with 1D convolution.

Pre-processing: removing overburden amplitude effects

In the reduced RBSI-scheme, amplitude effects due to 3D wave propagation in the complex overburden are first removed from the NI-data in a pre-processing step, before applying inversion. All amplitude effects in the target zone, apart from the primary reflections, are neglected (or assumed to be corrected for). This includes amplitude effects due to interface transmissions and spreading, and due to wave conversions and internal multiples. In this way, 1D convolution can be used to do forward modelling in the target zone.

■ 3.6.2 Theory

In this section, the 2.5D configuration of section 3.4 will be adapted, since it leads to more illustrative equations than the 3D case—in which the method is also perfectly feasible. Consider the 2.5D caustic-free isotropic-elastic subsurface model of Figure 3.13b, consisting of an inhomogeneous overburden overlying a set of $N - n$ homogeneous plane-parallel layers. The dip angle of the package of layers in the target zone is β , and vertical thicknesses are $h_i < \lambda_d$, with λ_d the dominant wavelength. The real layer-thicknesses h'_i are related to the vertical thicknesses h_i via the dip angle β , as shown in the following equation,

$$h'_i = h_i \cos \beta . \quad (3.25)$$

The two-way path lengths through the overburden and target are l_B and l_T (with $l_B \gg l_T$). Two-way path lengths through an individual layer are l_i . Overburden P-velocity- and density- macro models $v_{p,B}(\vec{x})$, $\rho_B(\vec{x})$ are assumed known; the unknown layer P-velocities and densities in the target are denoted as $v_{p;i}$, ρ_i .

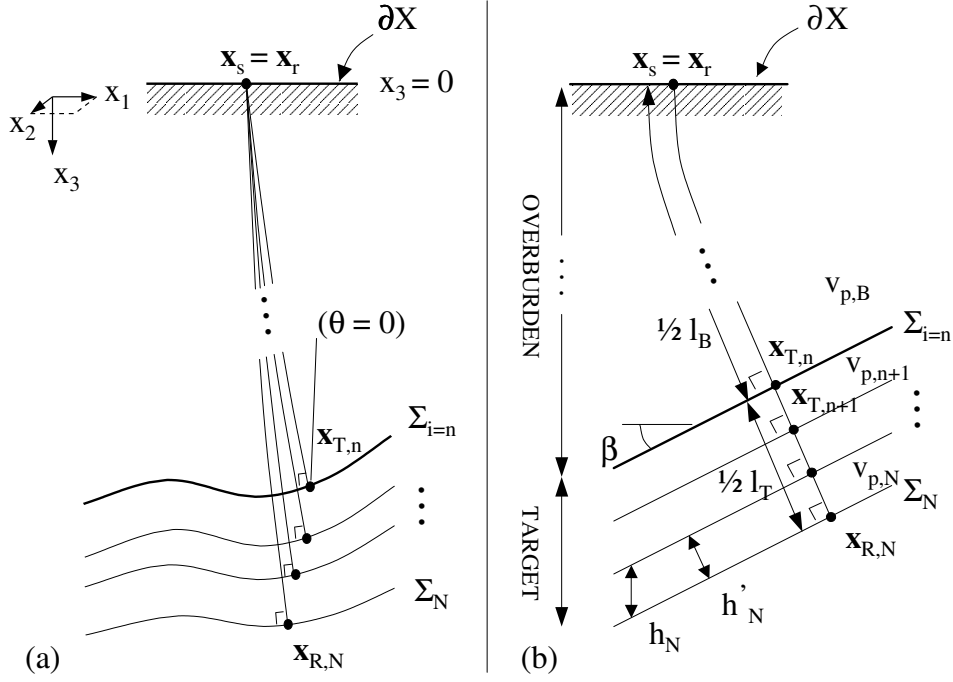


Figure 3.13: (a) NI-rays to a sequence of $N - n$ smooth target layers; angles of incidence are $\theta_i^\pm = 0$, source- and receiver-position $\vec{x}_s = \vec{x}_r$ at the surface ∂X . (b) Subsurface parameterisation for 1D convolutional RBSI.

The vertical component of the vectorial particle displacement amplitude function for the primary NI P-wave reflection response of the N -th plane reflector Σ_N in the target, due to an isotropic point source $S(\vec{x}; t) = F_0(t)A_0(\vec{x}_s)\delta(\vec{x} - \vec{x}_s)$, with A_0 the source strength and F_0 the wavelet, can be calculated using Eq. (3.24):

$$U_3^{(0)}(\vec{x}_s = \vec{x}_r, \vec{x}_{R,N}) = \frac{C_B(\vec{x}_s, \vec{x}_{T,n})R(\vec{x}_{R,N}, \theta_N^+ = 0)T_N(\vec{x}_s = \vec{x}_r)}{\mathcal{L}_B(\vec{x}_s = \vec{x}_r; \vec{x}_{T,n}) + \mathcal{L}_T(\vec{x}_{T,n}^+ = \vec{x}_{T,n}^-; \vec{x}_{R,N})} \quad (3.26)$$

where a separation between overburden and target has been introduced in the notation, with $\vec{x}_{T,n}$ the intersection point of the NI-ray with Σ_n , dividing the ray-path in parts through overburden and target, see Figure 3.13b. The

relative geometrical spreading has been separated in $\mathcal{L} = \mathcal{L}_B + \mathcal{L}_T$, with,

$$\mathcal{L}_T = \sum_{i=n+1}^N v_{p,i} l_i = 2 \sum_{i=n+1}^N v_{p,i} h'_i, \quad (3.27)$$

using Eqs. (3.23), (3.22), (3.18) and $l_i = 2h'_i$. C_B accounts for the overburden amplitude-effects other than geometrical spreading \mathcal{L}_B , such as overburden transmission losses and oblique ray-incidence at the surface. Note that for a homogeneous overburden, C_B and \mathcal{L}_B take the form,

$$C_B = A_0(\vec{x}_s) C_0(\vec{x}_s = \vec{x}_r), \quad (3.28)$$

$$\mathcal{L}_B = 2v_{p,B} h'_B. \quad (3.29)$$

The factors from Eq. (3.26) that govern reflection and transmission in the target are: R , the NI Zoeppritz reflection coefficient for normal-incidence at reflection point $\vec{x}_{R,N}$ on interface Σ_N in the target [see Eq. (3.17)], and T_N , the product of NI Zoeppritz transmission coefficients in the target while the ray-pair crosses $N - n$ interfaces in the target,

$$T_N(\vec{x}_s = \vec{x}_r) = \prod_{i=n}^{N-1} T_i^+(\vec{x}_{T,i}, \theta_i^+ = 0) T_i^-(\vec{x}_{T,i}, \theta_i^- = 0), \quad (3.30)$$

where Eq. (3.16) has been used; $N > n$ and $n \geq 1$ (for $n = 1$, the overburden does not contain interfaces).

Removing overburden amplitude effects

Before applying 1D convolutional RBSI, amplitude effects due to wave propagation in the overburden C_B and \mathcal{L}_B need to be removed from the NI-data. After pre-processing, the signal in the target zone resembles a reflectivity-trace convolved with the source wavelet that may be modelled using 1D convolution: besides the target reflection information, only a small contribution of target spreading and transmission losses remains.

To see this, consider the following. The zero-offset particle displacement dataset $u_3(\vec{x}_s = \vec{x}_r; t)$ is pre-processed for 1D convolutional RBSI. The ver-

tical component of the amplitude function after processing $U_{3,A}^{(0)}$ is,

$$U_{3,A}^{(0)}(\vec{x}_s = \vec{x}_r, \vec{x}_{R,N}) = [\mathcal{L}_B/C_B]U_3^{(0)}(\vec{x}_s = \vec{x}_r, \vec{x}_{R,N}), \quad (3.31)$$

$$= RT_N \left(\frac{\mathcal{L}_B}{\mathcal{L}_B + \mathcal{L}_T} \right), \quad (3.32)$$

where $U_3^{(0)}$ is given by Eq. (3.26). If subsequently amplitude losses within the target, due to T_N and \mathcal{L}_T , are neglected (i.e. $T_N \approx 1$ and $\mathcal{L}_T/\mathcal{L}_B \ll 1$ as done in 1D convolutional RBSI), from Eq. (3.32) it follows that,

$$U_{3,A}^{(0)}(\vec{x}_s = \vec{x}_r, \vec{x}_{R,N}) \approx R(\vec{x}_{R,N}, \theta_N^+ = 0), \quad (3.33)$$

a condition for the application of a 1D convolutional inversion kernel on the dataset, since that type of forward modeller can only handle reflection coefficients, not spreading or transmission (see section 2.5).

Impact of target transmissions and spreading

From Eq. (3.26), the target amplitude-losses along the NI ray-path, $L_{\mathcal{L}}$ and L_T , that are not included by the 1D convolutional forward modeller, at $\vec{x}_{R,N}$ on Σ_N , as compared to $\vec{x}_{T,n}$ on the incidence-side of Σ_n read:

$$L_{\mathcal{L}}(H') = 1 - \frac{\mathcal{L}_B}{\mathcal{L}_B + \mathcal{L}_T(H')} \quad (3.34)$$

$$L_T(N) = 1 - T_N(\vec{x}_s = \vec{x}_r) \quad (3.35)$$

with $H' = \|\vec{x}_{T,n} - \vec{x}_{R,N}\| = \sum_{i=n+1}^N h'_i$. This set of two equations gives insight in the relationship of the last three conditions listed in Table 3.2. The amount of layers and contrast sizes affect L_T , whereas the total thickness of the inversion window is incorporated in $L_{\mathcal{L}}$. As an example, suppose that a maximum tolerable $L = L_{\mathcal{L}} + L_T$ has been set by the user, then choosing an inversion interval with a few low contrasting interfaces will allow inversion over a thicker total interval H' , since L_T will be low in that case.

Note that due to the fact that L_T should be small in the application regime of 1D convolutional RBSI, the amount of generated multiple-energy too is expected to be small, justifying the choice to model only the primary response in the inversion kernel of 1D convolutional RBSI.

Finally, note that in some shot pre-processing schemes for migration, an approximate spherical spreading removal is applied on the pre-stack unmigrated data, based on an average regional velocity function; for normal RBSI this would be unfavourable, but for 1D convolutional RBSI this will lessen the effect of Eq. (3.34), allowing inversion of thicker intervals.

In the next chapter, results of synthetic data tests are shown, set up to investigate the potential of 1D convolutional RBSI and the more general RBSI (discussed in this chapter) compared to that of SI (Chapter 2).

Box 3.1: The spelling of Snel's law

No, this is not a spelling error! Willebrord Snel van Royen (1580-1626) is the Dutchman from Leiden after whom the law of refraction was named. But why do we use a spelling with 'll'? The problem lies in the fact that for his scientific publications, following the fashion of that time, Snel used a latinised form of his last name: Snellius. If we introduce the latinisation operator for Dutch spelling as \mathcal{L}_{NL} , we can write this process as $\text{Snellius} = \mathcal{L}_{NL}(\text{Snel})$, notice the double 'l' needed for proper Dutch pronunciation; in English this would not be done.



In the English-speaking world, the ending *-ius* was recognised as Latin and removed (this is the de-latinisation operator for English spelling \mathcal{L}_{EN}^{-1}), but not the 'l'! In equations:

$$\begin{aligned}\mathcal{L}_{NL}^{-1}\{\mathcal{L}_{NL}(\text{Snel})\} &= \text{Snel}, \\ \mathcal{L}_{EN}^{-1}\{\mathcal{L}_{NL}(\text{Snel})\} &= \text{Snell},\end{aligned}$$

the last of which is the form we see in publications up to today.

Synthetic data tests

In the previous chapter, the method of ray-based stochastic inversion was introduced. To investigate the potential of this new method for reservoir parameter estimation in comparison with conventional stochastic inversion (discussed in Chapter 2), several synthetic data tests were performed and the results are presented in this chapter.

The synthetic data tests are presented in the following order: first, a subsurface is discussed with widely separated Gaussian-shaped interfaces that bound layers with smoothly varying layer densities; this subsurface is suitable for testing RBSI in ‘layer-stripping’ mode against SI, in estimating density distributions for each layer from top to bottom. Also, a wedge-like density anomaly is examined, to investigate the effect of dip-dependent migration-induced wavelet stretch on SI.

Subsequently, a setting is explored that consists of a dipping plane thin layer; SI is used to estimate the P-wave velocity and thickness of the layer. This simple setting is appropriate to further investigate the detrimental effect of dip-dependent migration-induced wavelet stretch on the reservoir parameter estimation capabilities of SI. To that end, the layer dip is varied from 0° to 60° . Naturally, the corresponding normal-incidence data for RBSI do not contain this migration stretch.

The subsurface setting with a single dipping layer is then expanded to five

plane-parallel thin layers with layer-velocity contrasts, similar to the flank of a structure present in the real dataset that will be investigated in Chapter 5. In this setting, SI is tested against 1D convolutional RBSI (also called ‘reduced RBSI’) in estimating layer thicknesses and P-velocities.

The same comparative test is also performed on a target with five plane-parallel layers below a laterally varying layered overburden. In contrast to the previous setting, the five layers are not strictly plane-parallel (while strict plane-parallel layering is assumed in 1D convolutional RBSI), dips are laterally varying, and the overburden is not homogeneous.

Next, 1D convolutional RBSI is tested on a model in which the layers have a lithology, specified by the rock models that are used in the next chapter on the real data; an example of a rock parameter to be inverted for in this case is the sand-fraction of a sand-shale mixture. The difference with the previous cases is that a rock model is inserted describing the relation between rock/pore fluid properties and the bulk elastic parameters.

Finally, a simple offset test is performed, to investigate the effect of angle-range substacks on the SI inversion result, and to see if the redundancy in the RBSI parameter estimates on different angle-gathers can reduce overall estimation uncertainty.

Below, the chapter begins with a description of the first synthetic data tests, done to determine lateral layer-density variations.

4.1 Lateral layer-density variations

In order to make a comparison of capabilities of SI versus RBSI for determining laterally variable layer-properties, a series of synthetic data tests is performed using a Gaussian density model presented in Figure 4.1, and a wedge-like density model shown in the inset of Figure 4.8 [van der Burg et al., 2004; Verdel et al., 2004]; wave propagation velocities in both models are chosen to be constant throughout the model. The parameter to be inverted for by both SI and RBSI is the layer density.

■ 4.1.1 Gaussian density model

An (x_1, x_3) -slice through the Gaussian density model is shown in Figure 4.1. The subsurface is invariant in the x_2 -direction, and has constant wave prop-

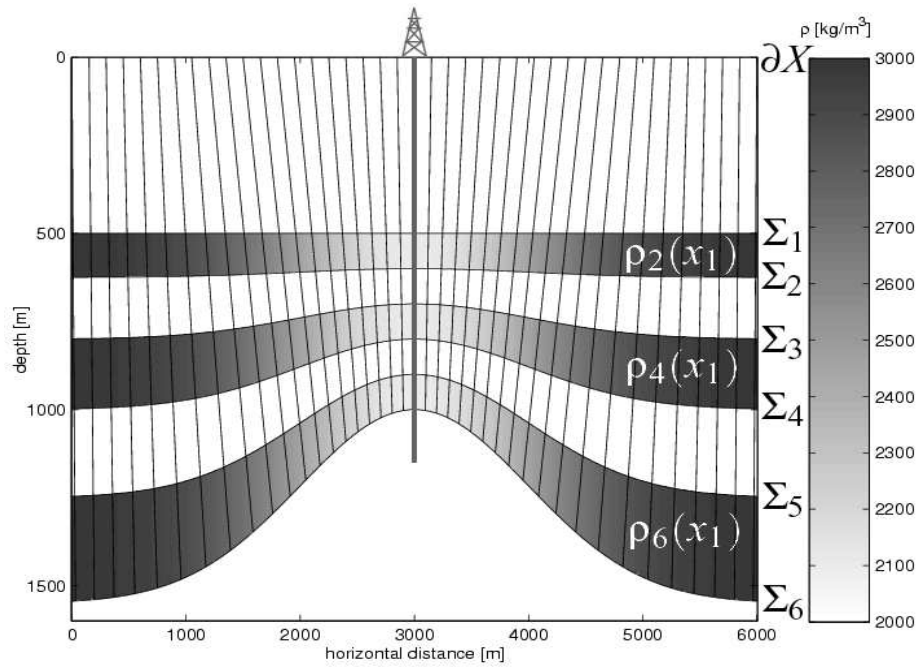


Figure 4.1: Normal-incidence rays to interface Σ_6 in a Gaussian density model (note that the angles seen in the plot are distorted due to the vertical exaggeration).

agation velocities (resulting in straight rays) of $v_p=2500$ m/s and $v_s=v_p/1.7$. In the following, the model geometry is defined first. Subsequently, the computation of the normal-incidence dataset for RBSI and the migrated dataset for SI is clarified. Finally, the density estimates obtained by SI and RBSI are compared.

Model geometry

Using z for x_3 for notational convenience, the subsurface density distribution is described as follows: density is constant at 2000 kg/m³ outside three contrasting layers that are bounded by Gaussian reflectors Σ_i . The depths z_i of these reflectors (interfaces) are described as a function of horizontal

distance x_1 , i.e. $\{\vec{x} \in \Sigma_i \mid z = z_i(x_1)\}$, with,

$$z_i(x_1) = z_{max,i} - \Delta z_i \exp \frac{-(x_1 - \mu)^2}{2\sigma^2} \quad \forall \quad i \in \{1, 2, \dots, 6\}, \quad (4.1)$$

in which $\sigma = 1000$ m, $\mu = 3000$ m, $\Delta z_i = z_{max,i} - z_{min,i}$, where $z_{max,i}$ and $z_{min,i}$ can be read from Figure 4.1. The interfaces are ‘ C_2 -smooth’: $z_i(x_1)$ is twice continuously differentiable with respect to horizontal distance x_1 .

The contrasting layers contain, also Gaussian, layer-density variations $\rho_k(x_1)$,

$$\rho_k(x_1) = \rho_{max} - \Delta\rho \exp \frac{-(x_1 - \mu)^2}{2\sigma^2} \quad \forall \quad k \in \{2, 4, 6\}, \quad (4.2)$$

with σ, μ the same as in Eq. (4.1), and $\Delta\rho = (\rho_{max} - \rho_{min}) = (3000 - 2100)$ kg/m³. See Figure 4.1.

The model just described obeys all standard ray-tracing validity conditions. Moreover, it is assumed for the numerical tests that interbed multiples have been removed from the pre-stack unmigrated data, that serve as input for the RBSI inversion. The underlying motivation for this choice is that any zero-offset interbed multiple event in the model described above could be modelled (and thus removed) with ray-tracing.

Furthermore, the minimum layer thicknesses are chosen such that there is no wavelet interference on the migrated or zero-offset data; in this way, RBSI can be performed in layer-stripping mode (section 3.1.3).

The added benefit of the absence of wavelet interference is, that dip-dependent migration-induced wavelet stretch will not yet influence SI density estimation in the Gaussian density model: the peak amplitude and the corresponding vertical traveltime, needed by SI for the density estimation, are not affected by the stretching. Hence, the SI estimates depend entirely on the ability of migration to correctly recover the reflection amplitudes and reflector position.

Normal-incidence dataset

Elastodynamic ray-tracing is used to numerically simulate the vertical component of the zero-offset particle velocity dataset $\dot{u}_3(\vec{x}_s = \vec{x}_r, \vec{x}_R; t)$ obtained by a zero-offset acquisition experiment. The acquisition (using omnidirectional point sources) is performed along the x_1 -axis at the free sur-

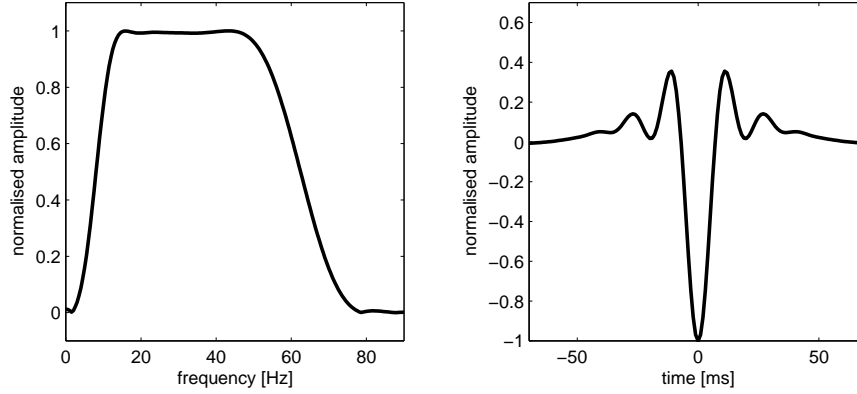


Figure 4.2: Hanning-tapered zero-phase bandpass wavelet with corner frequencies 4-12-50-75 Hz. Left: Amplitude spectrum. Right: Signal in time domain.

face ∂X , so that acquisition and subsurface (invariant in the x_2 -direction) together form a 2.5D configuration.

The dataset $\dot{u}_3(\vec{x}_s = \vec{x}_r, \vec{x}_R; t)$ is computed for 601 source/receiver-positions with 10 m spacing at the surface ∂X , using a Hanning-tapered zero-phase bandpass wavelet $\dot{\mathcal{F}}_0(t)$ with corner frequencies 4-12-50-75 Hz (Figure 4.2). With the choice of model- and acquisition parameters described in the geometry subsection above, $\dot{u}_3(\vec{x}_s = \vec{x}_r, \vec{x}_R; t)$ is caustic-free and only contains normal-incidence ($\theta_n^+ = 0$)-reflections. Thus the ray-theoretical expression with the analytical wavelet \dot{F}_0 [after Eq. (3.2), notice the additional $\partial/\partial t$],

$$\dot{u}_3(\vec{x}_s = \vec{x}_r, \vec{x}_R; t) = \text{Re}\{U_3^{(0)}(\vec{x}_s = \vec{x}_r, \vec{x}_R)\dot{F}_0(t - \tau(\vec{x}_s = \vec{x}_r, \vec{x}_R))\} \quad (4.3)$$

simplifies to,

$$\dot{u}_3(\vec{x}_s = \vec{x}_r, \vec{x}_R; t) = U_3^{(0)}(\vec{x}_s = \vec{x}_r, \vec{x}_R)\dot{\mathcal{F}}_0(t - \tau(\vec{x}_s = \vec{x}_r, \vec{x}_R)) \quad (4.4)$$

with the amplitudes $U_3^{(0)}(\vec{x}_s = \vec{x}_r, \vec{x}_R)$ of this dataset described by Eq. (3.24), with $A_0(\vec{x}_s) = v_p \forall \vec{x}_s$. Moreover, due to the homogeneous velocity model, in Eq. (3.24), the normal-incidence reflection coefficient given by Eq. (3.17) simplifies to,

$$R^+(\vec{x}_R, \theta_n^+ = 0) = \frac{\rho_{n+1}(\vec{x}_R) - \rho_n(\vec{x}_R)}{\rho_{n+1}(\vec{x}_R) + \rho_n(\vec{x}_R)}. \quad (4.5)$$

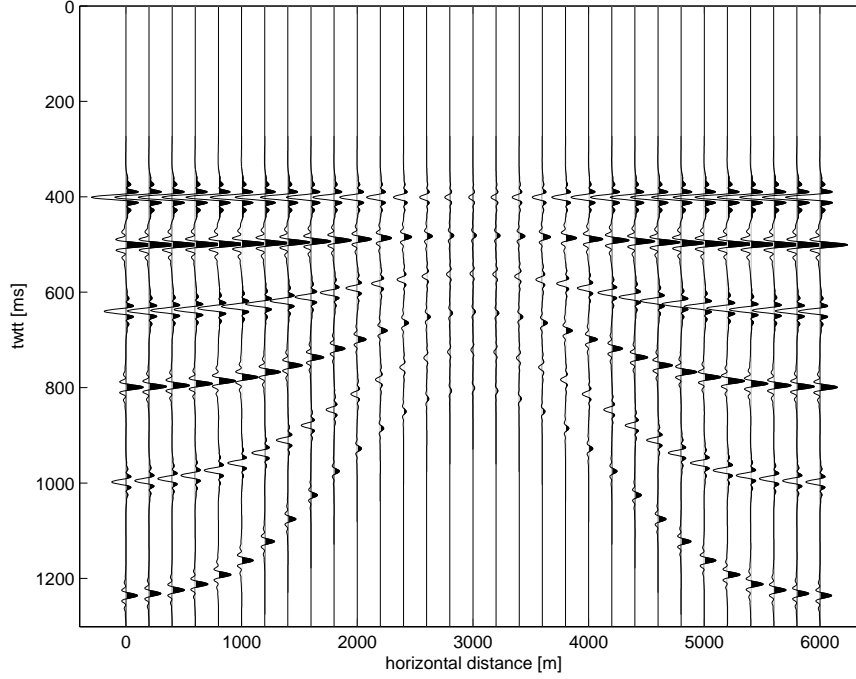


Figure 4.3: Zero-offset dataset $\dot{u}_3(\vec{x}_s = \vec{x}_r, \vec{x}_R; t)$ corresponding to Figure 4.1.

The transverse and in-plane relative geometrical spreading are given by equations (3.20) and (3.21). In Figure 4.3, every 20th trace of $\dot{u}_3(\vec{x}_s = \vec{x}_r, \vec{x}_R; t)$ is shown.

PreSDM migrated dataset

To migrate $\dot{u}_3(\vec{x}_s = \vec{x}_r, \vec{x}_R; t)$, a true-amplitude (TA) Kirchhoff pre-stack depth migration (PreSDM) algorithm based on Eq. (2.54) is used. In order to provide a high quality migration image for SI, the following parameters are provided to the PreSDM algorithm: the migration output grid $(\Delta x_1, \Delta x_3)$ is 10×2 m, with origin at $(x_1, x_3) = (0, 0)$. The migration half-aperture is 4000 m. The migration operators are calculated on a dense ray-trace diffraction point grid of 10×10 m, with rays spraying up from each diffraction point to points with 10 m x_1 -spacing at the surface (within the migration aperture).

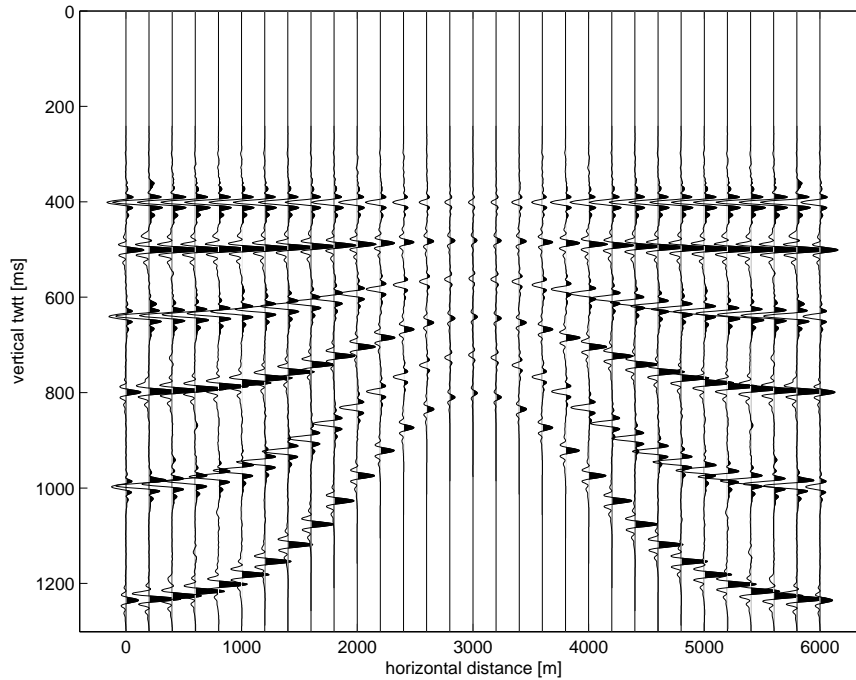


Figure 4.4: True-amplitude zero-offset depth migration of $\dot{u}_3(\vec{x}_s = \vec{x}_r, \vec{x}_R; t)$ with the laterally constant density model from the well displayed in Figure 4.1.

Velocity and density distributions are specified as analytical functions, using a layer-based parameterisation. Time-sampling after 1D vertical depth-to-time conversion is 1 ms (equalling the sampling of the normal-incidence dataset).

In Figure 4.4, the data are shown after ‘true-amplitude’ PreSDM (and 1D vertical depth-to-time conversion) of $\dot{u}_3(\vec{x}_s = \vec{x}_r, \vec{x}_R; t)$ with the exact P-wave velocity model, while using a laterally *constant* density model ($\rho_k = 2100 \text{ kg/m}^3$) such as derived from the density log taken in the hypothetical well at $x_1 = 3000 \text{ m}$. This is a reasonable assumption, as, prior to inversion, density information is only available at this well location (see Figure 4.1) and no further prior information on density is available. The quotes around ‘true-amplitude’ emphasise that the migration-image contains incorrect reflection strengths due to usage of the wrong density model; transmission losses in

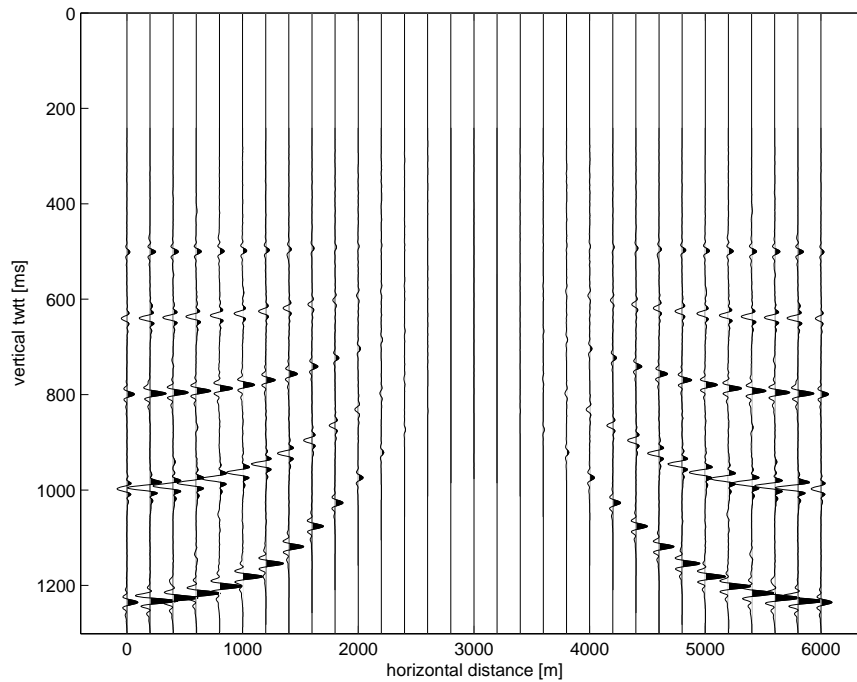


Figure 4.5: Difference (scaled) between Figure 4.4 and migration using exact density model (not shown) obtained from RBSI; differences measure up to 25%.

the true-amplitude migration operators are therefore calculated incorrectly. Consequently any subsequent inversion for target reservoir layer densities, and related parameters as porosities and pore fluid saturations, applied on that image, is bound to fail.

Figure 4.5 shows the difference between Figure 4.4 and the migrated result using the correct, laterally variable, density model described by Eq. (4.2) such as can be obtained from the pre-stack data using RBSI (see the next subsection). The difference becomes larger further away from the well location because of the increasing difference between assumed and actual layer densities, and deeper down in the model because of the accumulating errors due to incorrect transmissions. This is also demonstrated in Figure 4.6 which shows the reflection amplitude along Σ_6 after true-amplitude PreSDM using both a laterally constant density model (black line) and the exact density

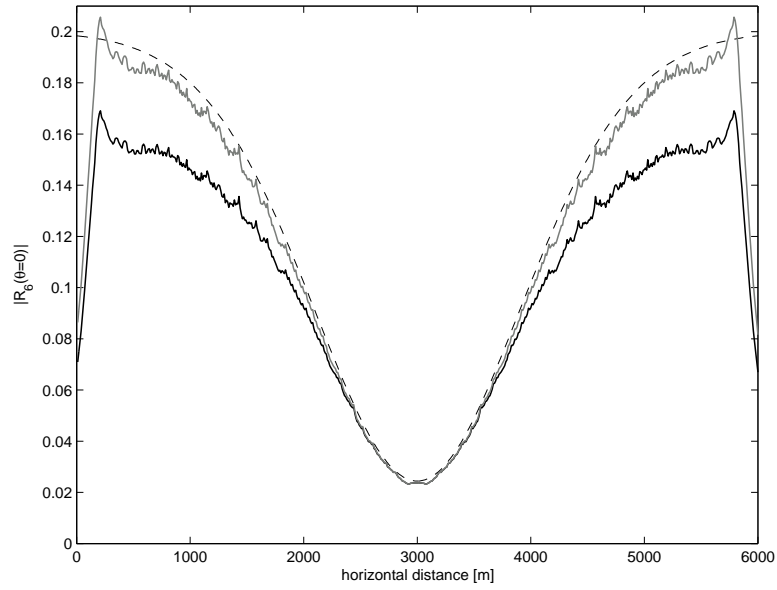


Figure 4.6: Reflection-amplitude along interface Σ_6 after migration using constant-density layers (black line) and exact density model (grey) as compared to the theoretical $R(\vec{x}_R, \theta_6^+ = 0)$ (dashed).

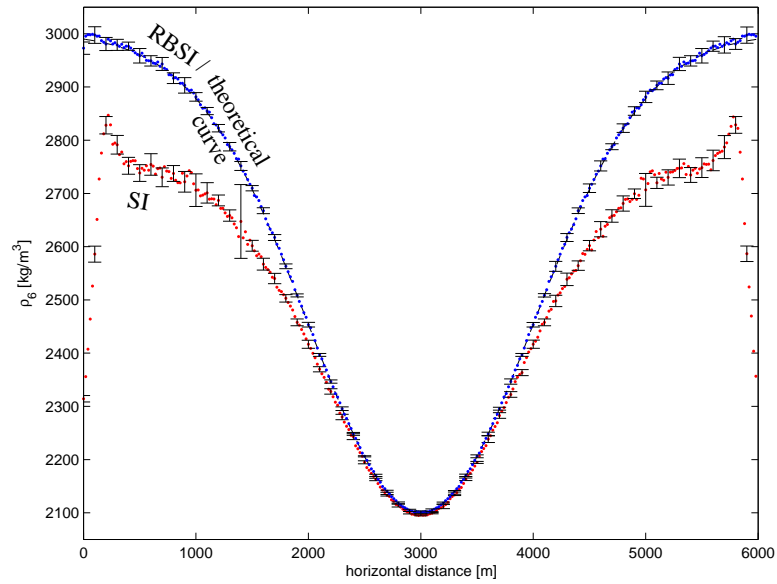


Figure 4.7: Density ρ_6 determined from SI and RBSI, the latter converging to desired value. Error bars denote posterior standard deviations.

model (grey line), in comparison with the theoretical reflection coefficient (dashed line), which is the ideal true-amplitude PreSDM result. Note that the amplitude artifacts in the x_1 -intervals $[0, 300]$ m and $[5700, 6000]$ m are due to Kirchhoff migration boundary effects.

Inversion: SI vs. RBSI

The goal set for inversion is the estimation of the laterally varying density of the sixth layer, $\rho_6(x_1)$. SI inverts the PreSDM migrated dataset obtained using the constant density model ($\rho_k = 2100 \text{ kg/m}^3$), while RBSI inverts the normal-incidence dataset.

The following information is supplied to both inversions as prior knowledge: subsurface P-wave velocity is constant at $v_p = 2500 \text{ m/s}$, and $v_s = v_p/1.7$. Note that for transmissions at overlying interfaces the angle of incidence is nonzero (except at $x_1 = 3000 \text{ m}$), so that P-S conversions do occur. Exact positions are known for all interfaces Σ_i . The prior density distribution for the contrasting layers two, four and six are given in the form of a normal pdf, with constant mean $\mu(\rho_k) = 2100 \text{ kg/m}^3$ and standard deviation $\sigma(\rho_k) = 800 \text{ kg/m}^3$. For the other layers, density is known to be 2000 kg/m^3 . Finally, the exact wavelet is supplied to RBSI and the exact zero-dip wavelet to SI (both wavelets are assumed to have been correctly derived from a seismic-to-well tie at the well location).

RBSI is performed in layer-stripping mode, starting with the estimation of $\rho_2(x_1)$ below interface Σ_1 . However, notice that in contrast with the procedure explained on p. 64, at the second interface Σ_2 it is chosen to invert again for $\rho_2(x_1)$, above Σ_2 (and not for ρ_3 below Σ_2 , since $\rho_3 = 2000 \text{ kg/m}^3$ is already known prior to inversion). This yields estimates for $\rho_2(x_1)$ at the reflection point positions on Σ_1 and Σ_2 .

Subsequently, the $\rho_2(x_1)$ -estimates found with RBSI at the irregularly distributed reflection points on each interface Σ_1 and Σ_2 are interpolated to a regular lateral interval of 10 m, coinciding with the migration output grid. These interpolated values for $\rho_2(x_1)$ at both interfaces are averaged to obtain the final estimate (for the RBSI standard deviations, the plain relation $\bar{\sigma}(\rho_2) = [\sigma_{\Sigma_1}^2(\rho_2) + \sigma_{\Sigma_2}^2(\rho_2)]^{1/2}/2$ is used, a slightly more accurate equation leading to a smaller $\bar{\sigma}$ is given on p. 148). The same procedure is repeated for the estimation of $\rho_4(x_1)$ and finally $\rho_6(x_1)$, with RBSI each time re-using

the obtained knowledge on the overlying layers.

SI inverts the migrated data for $\rho_6(x_1)$ directly.

In Figure 4.7, inversion results are shown for $\rho_6(x_1)$: SI (lower curve) versus RBSI; error bars denote standard deviations. The reflection strengths as determined from RBSI are almost identical to those described by theory (Eq. 4.5), whereas the SI-results, including their error bars, map outside the desired results (the artifacts in SI-estimates for the x_1 -intervals $[0, 300]$ m and $[5700, 6000]$ m are due to migration boundary effects).

■ 4.1.2 Wedge-like density model

For the previous model, dip-dependent migration wavelet stretch did not have a negative impact on the density estimation by SI, because no wavelet interference was present on the migrated data. Although the dips of the six interfaces are different for a given x_1 away from the apex, which means that each interface is represented by a differently stretched wavelet on a given trace from the migration image, this imposes no problem to SI in finding the

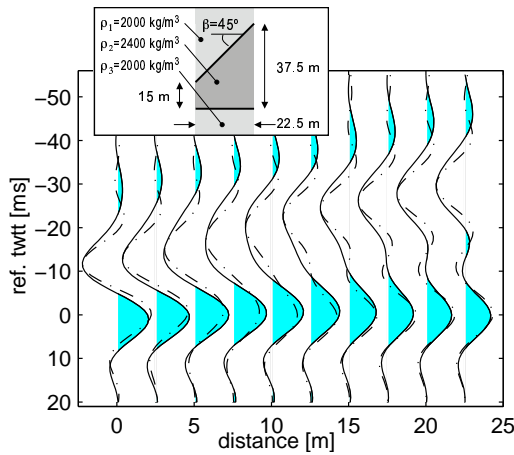


Figure 4.8: Detail of ideal migration result of wedge model (see inset). Var-wig: with migration stretch (input for SI). Dash-dot: without wavelet stretch.

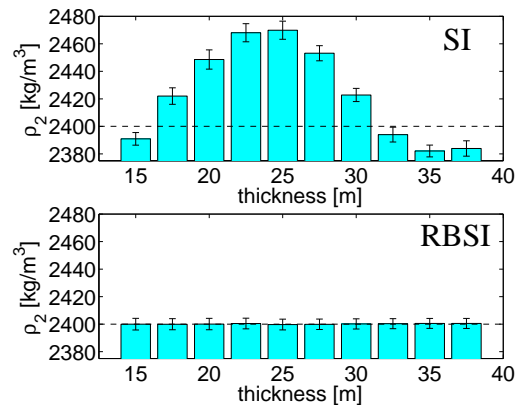


Figure 4.9: Density ρ_2 as determined from SI (top) and RBSI (bottom). Dashed line: desired result. Error bars denote posterior standard deviations.

correct peak amplitudes and corresponding two-way traveltimes. However, as soon as two interfaces come closer than a wavelength to each other, wavelet interference arises on the migrated image, and the constant wavelet assumption of SI will become a problem in the density estimation: the actual interference pattern of two interfaces, having different dip, on the migration image can become significantly different compared to the interference pattern of two equally shaped wavelets as forward modelled by SI.

Model geometry

In order to systematically investigate the detrimental effect of dip-dependent migration-induced wavelet stretch on SI, the three contrasting layers of the Gaussian layer model are replaced by a single wedge-like layer with a density of 2400 kg/m^3 (background-density amounts 2000 kg/m^3 , see the inset of Figure 4.8), such that the separation of the interfaces becomes smaller than a wavelength. The wavelet interference pattern changes as layer thickness decreases. As in the previous test, the normal-incidence dataset contains only the unconverted primary P-wave reflection response.

Ideal migrated datasets

Figure 4.8 shows a detail of two ‘ideal’ migration results (ideal in the sense that all migration artifacts besides the wavelet-stretch—the effect considered here—were suppressed). The one without the effect of wavelet stretch (wiggle display) was generated by 1D convolution of the exact spiky reflectivity trace (computed using Eq. (2.65), with $\theta = 0^\circ$) with the wavelet for 0° dip, the one that includes it (varwig display) uses the stretched wavelet for 45° dip for the upper interface. Only the first, fictitious, case fulfils the wavelet requirements for SI.

Inversion: effect of migration wavelet stretch on SI

The barplots in Figure 4.9 represent the inversion results for the density of the middle layer obtained with SI and RBSI respectively (the latter inverted the normal-incidence data that have no wavelet stretch). The prior knowledge supplied to the inversion methods was the same as in the previous test (see p. 104), of course apart from the fact that the three contrasting layers

have been replaced by a single wedge with prior $\mu(\rho) = 2400 \text{ kg/m}^3$ and $\sigma(\rho) = 800 \text{ kg/m}^3$. It can be seen that RBSI determines the density of the middle layer much better than SI: for SI, the posterior estimates $\mu(\rho)$ are often more than $2\sigma(\rho)$ away from the desired values.

4.2 Lateral P-wave velocity and thickness variations

The tests discussed so far involved the estimation of laterally varying layer-density. In this section, three numerical tests are discussed which have been conducted to compare the capability of SI versus 1D convolutional RBSI in determining lateral P-wave velocity (v_p) and thickness (h) variations.

The subsurface models in which the tests are done, have increasing complexity: the first model contains a single dipping layer only, the second has five plane-parallel dipping layers, and the last has a target of five layers in an anticlinal setting with laterally varying dips.

Before advancing to the comparative tests, first a further analysis on the detrimental effect of migration wavelet stretch on SI is done. The two numerical examples were published in [van der Burg et al. \[2005\]](#).

■ 4.2.1 Single dipping layer

In the migrated domain in vertical two-way traveltime, the inversion domain of SI, dip-dependent migration wavelet stretch $n_0(\beta)$ is present. The detrimental effect of it is analysed on the ability of SI to estimate v_p and h from the migration image. 1D convolutional RBSI operates in the unmigrated domain that is stretch-free, hence is expected to give superior results.

Model geometry

A series of synthetic data tests is performed on a model representing the flank, locally dipping with angle β , of a subsurface structure with a well at the apex (Figure 4.10). At the apex, the reflector dip β is zero, so that the seismic-to-well tie is done on a portion of the migrated section without migration stretch on the wavelet [i.e. $n_0(\beta = 0^\circ) = 1$, see Eq. (2.63)]. The 2.5D isotropic-elastic subsurface has uniform ρ , constant background $v_p =$

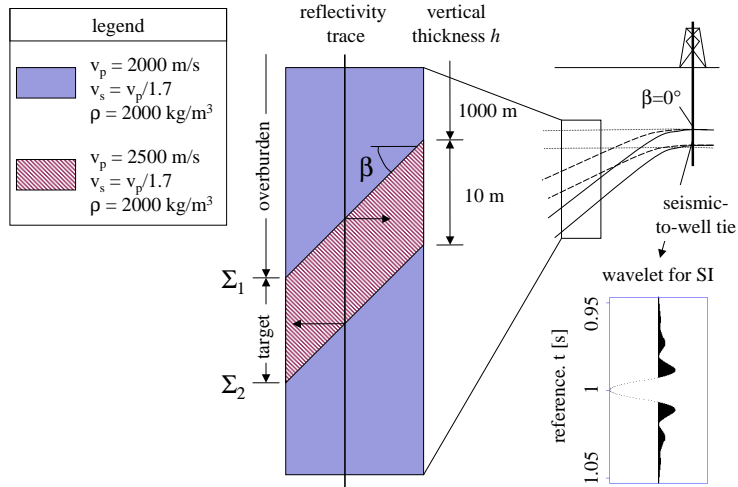


Figure 4.10: Subsurface model with a single v_p -contrast and dip angle β ; v_p and h of the target layers to be inverted for. The wavelet for SI was derived from a seismic-to-well tie at zero dip.

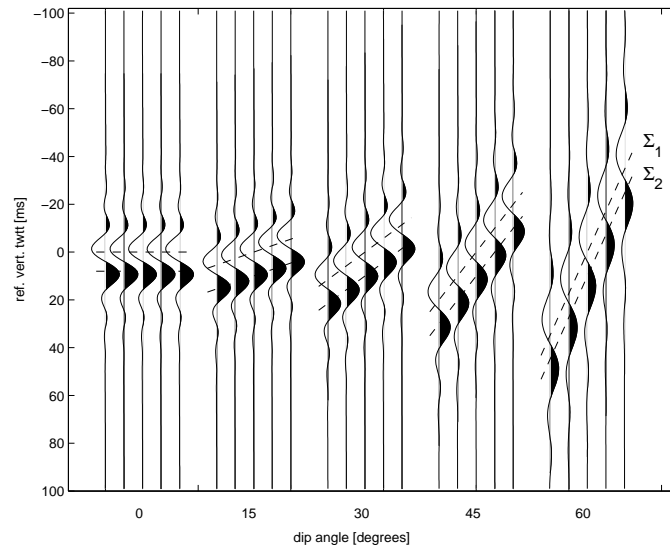


Figure 4.11: $n_0(\beta)$ on a detail of ideal migration results, for the subsurface model of Figure 4.10 with dip angle as indicated. Trace separation is 10 m. Dashed lines denote contrasts Σ_i .

2000 m/s and contains a single contrasting, thin layer with $v_p = 2500$ m/s and $h = 10$ m ($< \lambda_d$).

Ideal migrated and normal-incidence datasets

Figure 4.11 shows a set of true-amplitude pre-stack depth migrated, 1D vertical depth-to-time converted, ideal migration images, each corresponding to a different dip of the flank. These images are constructed by first computing the exact spiky reflectivity traces using Eq. (2.65), with $\theta = 0^\circ$; one trace is sketched in Figure 4.10. Subsequently, for each dip β , these traces are convolved with the wavelet from the normal-incidence dataset stretched by the corresponding factor $n_0(\beta)$. Hence, on the ideal migration images, all migration artifacts besides the clearly visible wavelet-stretch—the effect considered here—are suppressed.

The normal-incidence dataset is computed using the same Hanning-tapered zero-phase bandpass wavelet with corner frequencies 4-12-50-75 Hz as used in the previous tests. A (pre-processed) trace from this dataset, for 0° dip, is shown on the left-hand side of Figure 4.18.

SI inversion: effect of migration wavelet stretch

The experiments for SI involve the estimation of unknown layer properties v_p and h , using the exact wavelet derived at $\beta = 0^\circ$, on a single trace from a set of true-amplitude pre-stack depth migrated, 1D vertical depth-to-time converted, ideal migration images, each image corresponding to a different layer dip.

As prior knowledge, the exact mean values $\mu(v_p)$ and $\mu(h)$, and the exact position of Σ_1 are supplied to SI in the experiments. The prior standard deviations were $\sigma(v_p) = 1000$ m/s and $\sigma(h) = 5$ m. Also the relation $v_s = v_p/1.7$ is given, as well as the velocities and density of the overlying and underlying layer.

Figure 4.12 shows the v_p and h of the middle layer, estimated by SI for the various dip angles. For higher dip angles, inversion results deviate considerably more than two standard deviations (2σ) from the desired values.

To further investigate the SI results, consider Figure 4.13. In Figure 4.13a, one SI-modelled trace (dashed) is plotted on top of the corresponding input trace (varwig) from the migration image (Figure 4.11), for each dip angle β .

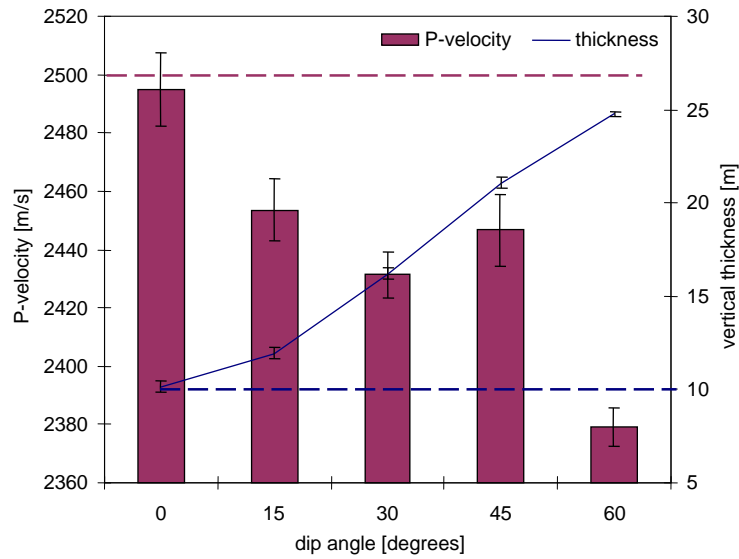


Figure 4.12: v_p and h as determined from SI, for the various dips indicated on the horizontal axis. Error bars denote posterior $\sigma(v_p)$ and $\sigma(h)$. Dashed horizontal lines denote desired values for v_p (grey) and h (black) respectively.

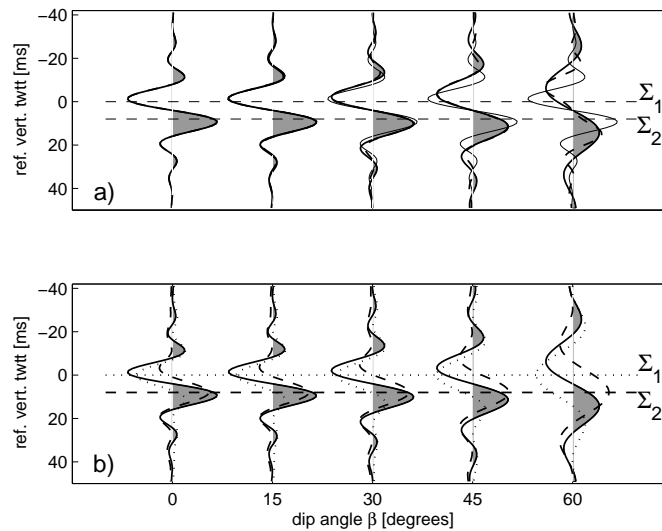


Figure 4.13: a) Quality of the match between input traces (varwig) from the migration image (Figure 4.11) and SI-modelled traces after inversion (dashed) using the zero-dip wavelet. Zero-dip input is repeated in thin lines for all dips. b) Migration response per Σ_i , showing the dip-dependent wavelet required for a correct SI.

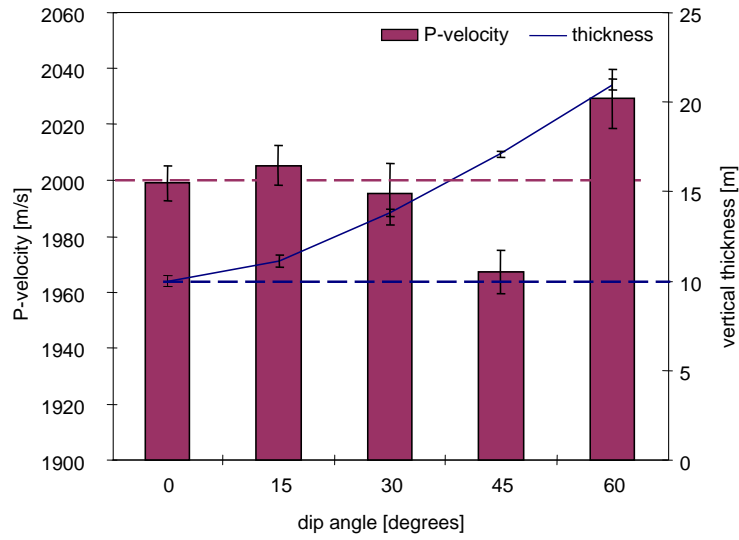


Figure 4.14: v_p and h as determined from SI in a model like Figure 4.10, yet with swapped P-velocities. Error bars denote posterior $\sigma(v_p)$ and $\sigma(h)$. Dashed lines denote desired values.

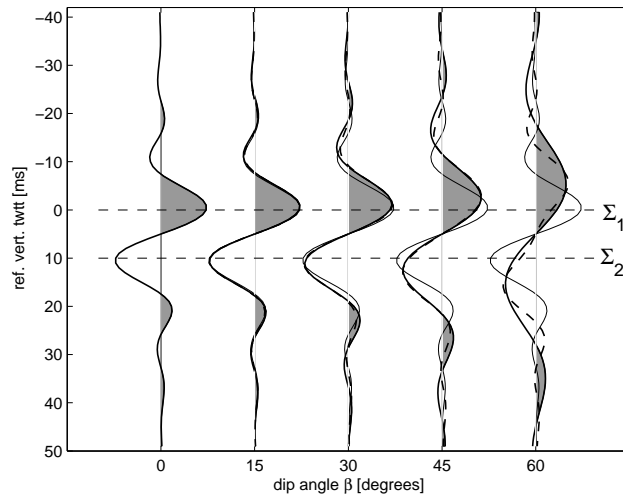


Figure 4.15: SI-modelled traces (dashed) using the zero-dip wavelet, on SI input traces (varwig) from the migration image. In thin lines: input at zero-dip.

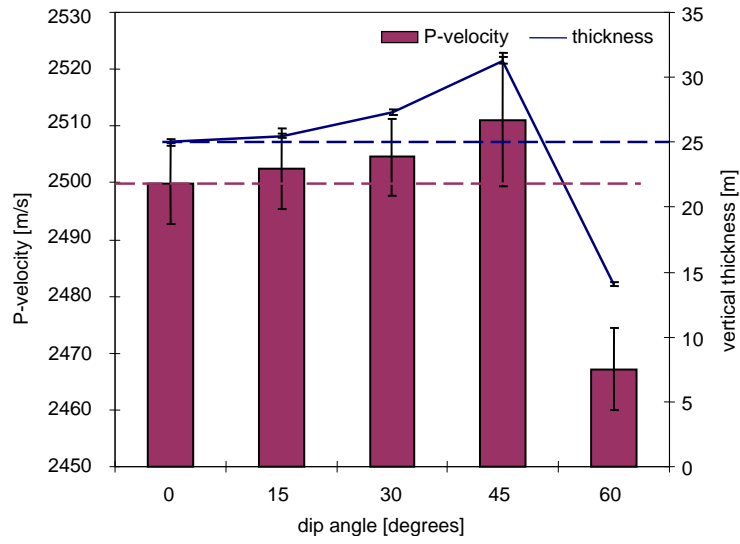


Figure 4.16: v_p and h as determined from SI in a model like Figure 4.10, yet with $h = 25$ m and underlying layer- $v_p = 3000$ m/s. Error bars denote posterior $\sigma(v_p)$ and $\sigma(h)$. Dashed lines denote desired values.

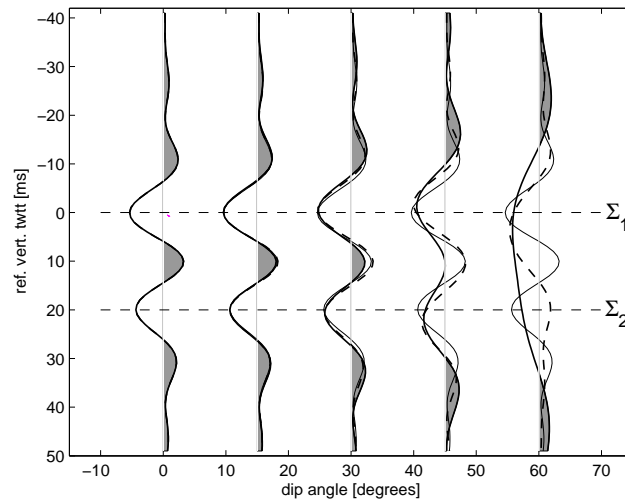


Figure 4.17: SI-modelled traces (dashed) using the zero-dip wavelet, on SI input traces (varwig) from the migration image. In thin lines: input at zero-dip.

These SI-modelled traces provide inversion diagnostics by convolving the most likely SI outcome with the supplied wavelet.

Notice in Figure 4.13a that the match with traces from migration is relatively good. In this case, though, the adequate match results in misestimates in v_p and h that stem from positioning- and amplitude-misalignments due to matching with the wavelet derived at zero-dip. The good fit is thus misleading: the inversion algorithm adjusts the model to correct for forward modelling errors.

Also in Figure 4.13a, the input traces without migration stretch are displayed as thin lines: these traces are equal to the zero-dip input trace. Only these traces fulfil the wavelet requirements of SI when using the wavelet derived at zero dip angle, $\beta = 0^\circ$. Figure 4.13b shows for each dip the corresponding stretched wavelet that would have given correct SI results. These wavelets are readily visible on the migration image if only a single interface would have been present: the dotted traces correspond to a migration image in which only the upper interface Σ_1 is present, the dashed traces to an image with only the lower interface Σ_2 , and finally the varwig traces show the composed signal corresponding to the actual situation.

Finally, notice that in Figure 4.12 thicknesses as found by SI are always overestimated and P-velocities underestimated. An undesirable systematic overestimation of reservoir volume by SI at increasing dip angles would be the result. To test if the thickness-overestimation also occurs for different layer properties, the original model of Figure 4.11 was changed firstly by interchanging the P-wave velocities so that the layer- v_p becomes 2000 m/s and elsewhere $v_p = 2500$ m/s, and secondly by thickening the middle layer to 25 m, while increasing P-wave velocity of the underlying layer from 2000 m/s to 3000 m/s.

The inversion results obtained in these two altered models are given in Figures 4.14 and 4.16. SI-modelled traces and traces from the migration image, for the two modified models at varying dips can be seen on Figures 4.15 and 4.17. The results show that the final misestimation-behaviour of SI is indeed dependent on the geometry of the inversion-target. No *systematic* overestimation of thicknesses by SI occurs when using the zero-dip wavelet, as Figure 4.16 gives an example of thickness *underestimation* (and P-wave velocity *overestimation*) — although the large difference between the modelled and actual trace in this particular example will not go unnoticed during

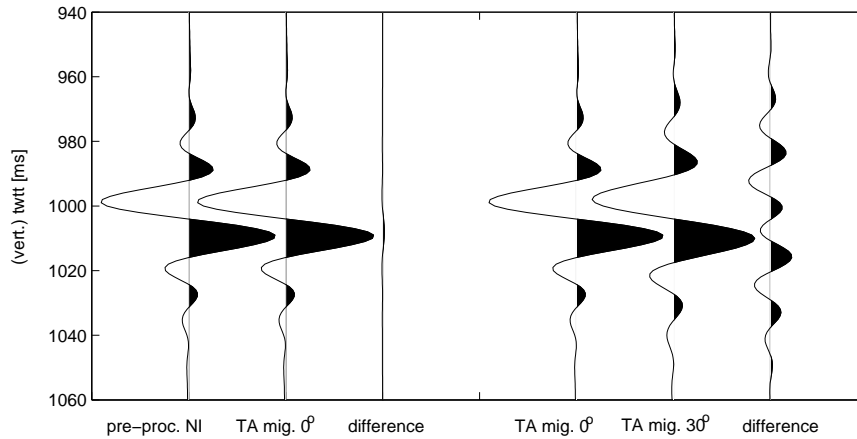


Figure 4.18: Left: Comparison between a trace from the pre-processed normal-incidence dataset and a trace from the data after TA PreSDM, at 0° dip. Right: Comparison between traces from the data after TA PreSDM at 0° dip and 30° dip.

subsequent quality control of the inversion.

1D convolutional RBSI inversion

In order to test 1D convolutional RBSI in a manner most analogous to SI, with varying dip in the model, the *real* layer-thickness measured along the direction of the normal to the interfaces is kept constant at $h' = 10$ m, as was the vertical layer-thickness for SI; also the one-way ray-path through the homogeneous overburden is kept constant at 1000 m, as was the depth to the reference reflector for SI. In the absence of migration wavelet stretch, this means that the normal-incidence traces for all dip angles β are equivalent: therefore, the remainder of this discussion is restricted to one normal-incidence trace only. Naturally, the v_p -values of Figure 4.10 are used in the modelling test.

The pre-processed normal-incidence trace suitable for inversion with 1D convolutional RBSI, i.e. from which overburden losses have been removed via Eq. (3.31), is shown as leftmost trace on Figure 4.18. Notice the small difference, shown on the third trace, with the true-amplitude pre-stack depth

migrated, 1D vertical depth-to-time converted trace at zero dip (second trace). Hence, it is no surprise that the 1D convolutional RBSI results for *all* dip angles practically coincide with the zero-dip (ideal) SI result: 1D convolutional RBSI finds posterior $\mu(v_p) = 2497$ m/s with $\sigma(v_p) = 17$ m/s, and $\mu(h) = 9.96$ m with $\sigma(h) = 0.41$ m.

The small difference is explained by the fact that the amplitude-losses in the target (L_T and $L_{\mathcal{L}}$), causing errors in the 1D convolutional RBSI results as they are neglected in the 1D convolutional RBSI scheme (see p. 93), are small, especially compared with the difference between the zero-dip and the 30° migrated traces caused by migration-induced wavelet stretch, illustrated by the rightmost three traces of Figure 4.18, that are causing SI misestimates. To be precise, L_T and $L_{\mathcal{L}}$ are both 0.012; compare also with the losses found in the experiment discussed in the following subsection.

■ 4.2.2 Five plane-parallel dipping layers

In the previous one-layer test, 1D convolutional RBSI had an easy task in estimating reservoir properties, due to the absence of interfaces within the target reservoir zone and the modest target-thickness; the effect of neglecting amplitude-losses in the target was small. In the following, the performance of 1D convolutional RBSI vs. SI for estimation of layer P-wave velocities and thicknesses will be tested in a more realistic setting: a sequence of five plane-parallel dipping layers.

Model geometry and datasets

The single-layered model of Figure 4.10 is extended to five, plane-parallel, thin layers ($h_i < \lambda_d$) with fixed dip of $\beta = 30^\circ$ (Figure 4.19). The first layer is chosen to be significantly thicker than the others; therefore, its top interface Σ_1 will appear relatively free of interference on the seismic data (and hence clearly distinguishable), so that it can serve as reference reflector for the inversion target.

Figure 4.20 shows the datasets on which inversion is applied: on the left, for 1D convolutional RBSI, NI-traces acquired in the subsurface model of Figure 4.19, from which overburden amplitude-losses [due to geometrical spreading \mathcal{L}_B in the homogeneous overburden and amplitude-effects other than geometrical spreading C_B , see Eqs. (3.28)-(3.29)] are removed. On

the right, for SI, the true-amplitude pre-stack depth migrated, 1D depth-to-vertical-time converted, ideal migration image; notice the wavelet stretch.

Inversion: SI vs. 1D convolutional RBSI

The aim set for inversion is the estimation of unknown vertical thicknesses h and v_p for each of the five layers in the target. Both types of inversion are supplied with the following prior information: the correct number of target layers, exact layer-densities, $v_s = v_p/1.7$, and finally ρ , v_p and v_s for overburden and underlying halfspace are exactly known. The correct wavelet is assumed to have been derived from the normal-incidence section for 1D convolutional RBSI, and from the migrated section, at a horizontal part of the target, for SI.

The prior knowledge on the layer-parameters to be inverted for, v_p and h , is contained in the form of normal pdfs, parameterised by mean μ and standard deviation σ : for all layer P-wave velocities, the prior mean $\mu(v_p)$ coincides with true v_p , whereas the uncertainty is described by a standard deviation of $\sigma(v_p) = 250$ m/s. For all layer-thicknesses h , prior mean $\mu(h)$ coincides with true h , with an uncertainty described by a standard deviation of $\sigma(h) = 5$ m for the first (thick) target layer and $\sigma(h) = 1$ m for the remainder of the target-layers. The two-way traveltimes to the reference reflector is known exactly up to a standard deviation of 2 ms.

First, an SI reference test is done at zero-dip ($\beta = 0^\circ$), to get a feeling for the best achievable estimation accuracy: the migration image of the structure at $\beta = 0^\circ$ and the zero-dip wavelet used in SI form the ideal combination. The inversion results are given in Table 4.1. It can be seen that the ideal SI estimates closely match the desired results, only for the thinnest (third) layer a deviation of about one σ occurs in v_p and h .

Next, a trace from the migrated section at $\beta = 30^\circ$ is inverted with SI; the inversion results are given in Table 4.2. Notice from the small standard deviations that the inversion seems to have resulted in quite accurate parameter estimates for all layers. Finally, a trace from the normal-incidence section is inverted with 1D convolutional RBSI; the inversion results are given in Table 4.3 (note that true layer-thickness measured along the direction of the normal to the layer-interfaces, $h' = h \cos \beta$, is inverted for in this case).

The inversion results are summarised in Figure 4.21, which gives misesti-

Table 4.1: Exact vs. estimated layer-parameters for SI for a model with zero dip; this is the ideal SI result. Velocity v_p is in [m/s], vertical thickness h is in [m].

| Layer no. | property | exact | posterior μ | posterior σ |
|-----------|----------|-------|-----------------|--------------------|
| 1 | v_p | 2500 | 2500 | 9 |
| | h | 50 | 50.1 | 0.3 |
| 2 | v_p | 2000 | 1996 | 22 |
| | h | 8 | 8.2 | 0.7 |
| 3 | v_p | 2500 | 2619 | 126 |
| | h | 5 | 4.4 | 0.6 |
| 4 | v_p | 2000 | 2004 | 19 |
| | h | 10 | 10.5 | 0.8 |
| 5 | v_p | 2500 | 2519 | 73 |
| | h | 7 | 6.9 | 0.8 |

Table 4.2: Exact vs. estimated layer-parameters for SI. Velocity v_p is in [m/s], vertical thickness h is in [m].

| Layer no. | property | exact | posterior μ | posterior σ |
|-----------|----------|-------|-----------------|--------------------|
| 1 | v_p | 2500 | 2556 | 8.9 |
| | h | 50 | 47.0 | 0.2 |
| 2 | v_p | 2000 | 2168 | 8.4 |
| | h | 8 | 11.4 | 0.6 |
| 3 | v_p | 2500 | 2086 | 6 |
| | h | 5 | 7.4 | 0.7 |
| 4 | v_p | 2000 | 2168 | 13 |
| | h | 10 | 10.6 | 0.6 |
| 5 | v_p | 2500 | 2333 | 19 |
| | h | 7 | 7.4 | 0.9 |

Table 4.3: Exact vs. estimated layer-parameters for 1D convolutional RBSI. Velocity v_p is in [m/s], true thickness h' is in [m].

| Layer no. | property | exact | posterior μ | posterior σ |
|-----------|----------|-------|-----------------|--------------------|
| 1 | v_p | 2500 | 2496 | 8 |
| | h' | 43.3 | 43.2 | 0.4 |
| 2 | v_p | 2000 | 2003 | 30 |
| | h' | 6.9 | 6.6 | 0.6 |
| 3 | v_p | 2500 | 2476 | 106 |
| | h' | 4.3 | 4.3 | 0.6 |
| 4 | v_p | 2000 | 2026 | 17 |
| | h' | 8.7 | 9.2 | 0.6 |
| 5 | v_p | 2500 | 2427 | 63 |
| | h' | 6.1 | 6.0 | 0.7 |

mates in layer-parameters obtained from both types of inversion. 1D convolutional RBSI results are much closer to the desired values than SI results. From Table 4.2 it follows that most of the SI-estimates are more than 2σ away from the desired values. Table 4.3 shows that this does not happen for 1D convolutional RBSI, although for the lower two layers the estimates deviate from the desired values by about σ . Also from the v_p -estimates by 1D convolutional RBSI in Figure 4.21 one can infer that the performance deteriorates for the deeper layers.

In Figure 4.22a, the cause of the observed deteriorating performance of 1D convolutional RBSI for the deeper layers is visualised. On the left, an input trace for 1D convolutional RBSI is shown (varwig), from the pre-processed NI dataset of Figure 4.20a; the match with the 1D convolutional RBSI-modelled trace (not shown) is almost perfect. The trace on the right of Figure 4.22a however, shows the difference with the hypothetical ideal pre-processed NI-trace for 1D convolutional RBSI (left, thin line) which has losses in the target due to spreading and transmission also corrected for (the difference was scaled by a factor 5 for visibility). The difference is increasing with two-way traveltimes and hence is causing the 1D convolutional RBSI

misestimates for the lower layers.

Using Eqs. (3.34) and (3.35), it is found that in the chosen model ($n=5$), the neglected target amplitude losses $L_{\mathcal{L}}$ and L_T are 0.087 and 0.060 approximately — values that still give satisfactory inversion results (Table 4.3).

Importantly, the amplitude errors due to neglect of target amplitude losses are considerably smaller than those occurring by neglect of migration stretch (compare with Figure 4.22b, trace on the right, which was not amplified). Hence, SI estimates can be expected to be worse than those obtained by 1D convolutional RBSI.

The cause of the SI misestimates is visualised in Figure 4.22b: on the left the SI-modelled trace (dashed) is plotted on top of the corresponding input trace (varwig) from the migration image on the right-hand side of Figure 4.20. Also visible on the left, in thin lines, is the hypothetical ideal trace for SI without migration stretch — fulfilling the wavelet requirements of SI when using the wavelet derived at zero-dip. This trace was picked from the migration image of a subsurface similar to that displayed in Figure 4.19, yet with horizontal layers ($\beta = 0^\circ$). The trace on the right-hand side of Figure 4.22b shows the difference, causing SI misestimates, between the real and hypothetical trace for SI.

Finally note that, due to the fact that in the application regime of 1D convolutional RBSI, L_T should be small (which implies the absence of large impedance contrasts in the target zone), the amount of generated multiple-energy is expected to be small too, justifying the choice to model only the primary response in the inversion kernel of 1D convolutional RBSI.

■ 4.2.3 Gaussian model with target of five layers

In order to test the capabilities of SI versus 1D convolutional RBSI in determining v_p and h for a thin-layered structure with laterally varying dips under an inhomogeneous overburden, a new model is synthesised from the interfaces of the Gaussian model and the target of five layers discussed in the previous section. First, the model geometry is discussed. Subsequently, the datasets to be inverted are presented: the ideal migrated and normal-incidence dataset. Finally, the inversion results are compared.

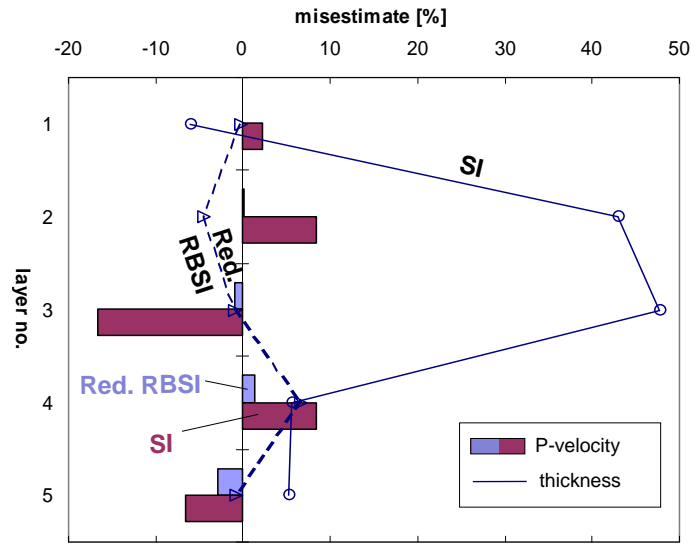


Figure 4.21: Misestimates in v_p and h resp. h' determined from SI and the better performing 1D convolutional RBSI (labelled as ‘Reduced RBSI’). Prior μ_{v_p}, μ_h coincide with desired values; prior σ_{v_p}, σ_h were 10%.

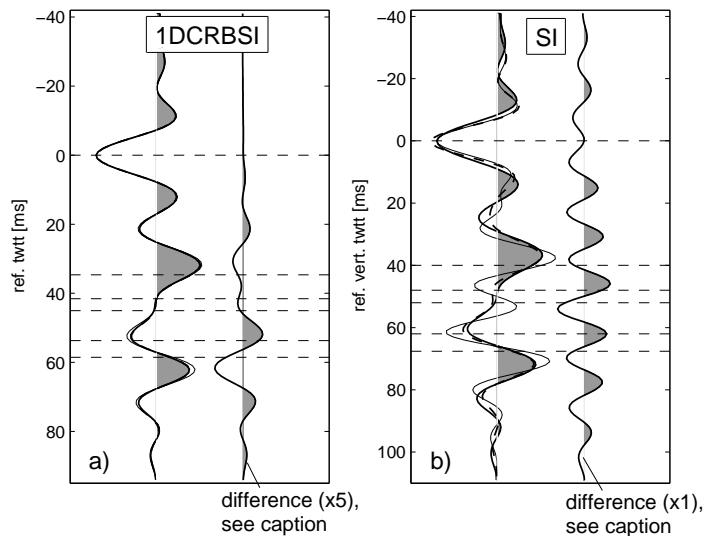


Figure 4.22: a) Pre-processed normal-incidence trace (left, varwig), hypothetical trace without target losses (left, thin line), and difference $\times 5$ (right). b) Left: trace from the TA PreSDM image (varwig), SI-modelled trace (dashed) and trace from the TA PreSDM image for dip $\beta = 0^\circ$ (thin line). Right: difference between the traces from the TA PreSDM image. Dashed lines denote interfaces.

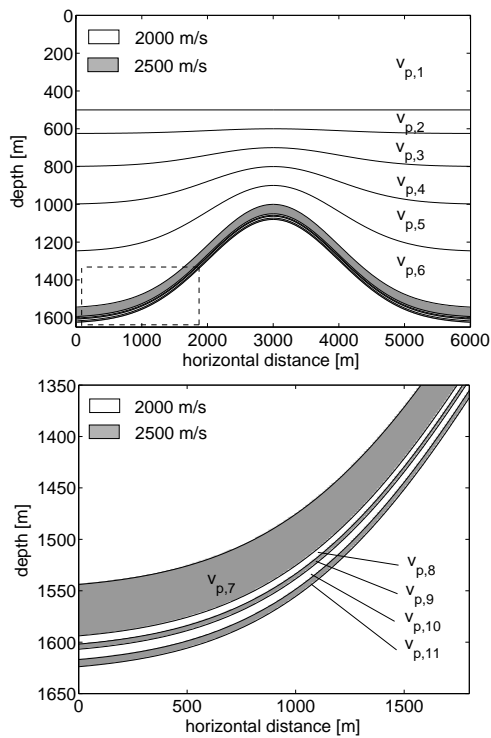


Figure 4.23: *P-velocity distribution. Below, an enlargement of the dashed area shows distribution in the target.*

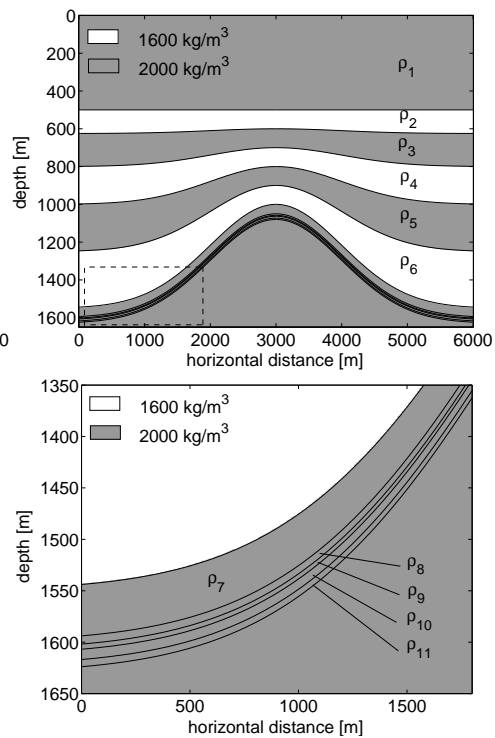


Figure 4.24: *Density distribution. Below, an enlargement of the dashed area shows distribution in the target.*

Model geometry

As in the tests before, the model properties are invariant in the x_2 -direction so that the variations are restricted to the (x_1, x_3) -plane, and data acquisition (using point sources and 3D spreading) is performed along the x_1 -direction to obtain a 2.5D configuration.

In constructing the new model, the six interfaces from the Gaussian density model are re-used for the overburden, and five thin layers having constant vertical thicknesses equal to those in the model discussed in the previous subsection are inserted below the sixth interface, to create a thin-layered

target interval with laterally varying dips suited for testing SI vs. 1D convolutional RBSI. All interfaces are depicted in Figure 4.23.

Applying the overburden/target parameterisation introduced in Figure 3.13 of the previous chapter, the reference reflector has number $n = 6$, the total number of interfaces in the model is $N = 11$, with six target interfaces $\{\Sigma_6, \dots, \Sigma_{11}\}$, and the number of target layers is $N - n = 5$.

From the description given above, it follows that the position of the overburden interfaces including the target reference reflector Σ_6 can again be calculated using Eq. (4.1), whereas the positions of the additional five target interfaces below the reference reflector are calculated by applying a translation in depth to Σ_6 ,

$$z_i(x_1) = z_{i-1}(x_1) + h_i \quad \forall \quad i \in \{7, 8, \dots, 11\}, \quad (4.6)$$

with h_i the (laterally constant) vertical target layer-thicknesses in [m] given by $h_i = \{50, 8, 5, 10, 7\}$ for $i \in \{7, 8, 9, 10, 11\}$, i.e. equal to vertical layer-thicknesses in the model discussed in the previous subsection.

Note that this target configuration is favourable to SI in the sense that dips β for all target interfaces are the same for a given x_1 (which means that the associated dip-dependent migration wavelet stretch $n_0(\beta)$ in the target will be constant per trace from the migrated image), whereas the locally plane-parallel layer assumption for 1D convolutional RBSI is not fully satisfied since dips are not exactly the same along reflector-normals.

The elastic layer-properties are distributed as follows: layer-density ρ_k alternates between 1600 kg/m^3 and 2000 kg/m^3 in the overburden, while in the target it is constant at 2000 kg/m^3 (Figure 4.24),

$$\rho_k = 1800 - 200 \cdot (-1)^k \quad \forall \quad k \in \{1, 2, \dots, 6\}, \quad (4.7)$$

$$\rho_k = 2000 \quad \forall \quad k \in \{7, 8, \dots, 11\}. \quad (4.8)$$

P-wave velocity is constant at 2000 m/s in the overburden, while in the target it alternates between 2500 m/s and 2000 m/s (Figure 4.23),

$$v_{p,k} = 2000 \quad \forall \quad k \in \{1, 2, \dots, 6\}, \quad (4.9)$$

$$v_{p,k} = 2250 - 250 \cdot (-1)^k \quad \forall \quad k \in \{7, 8, \dots, 11\}. \quad (4.10)$$

Everywhere, layer S-wave velocity is calculated as $v_p/1.7$.

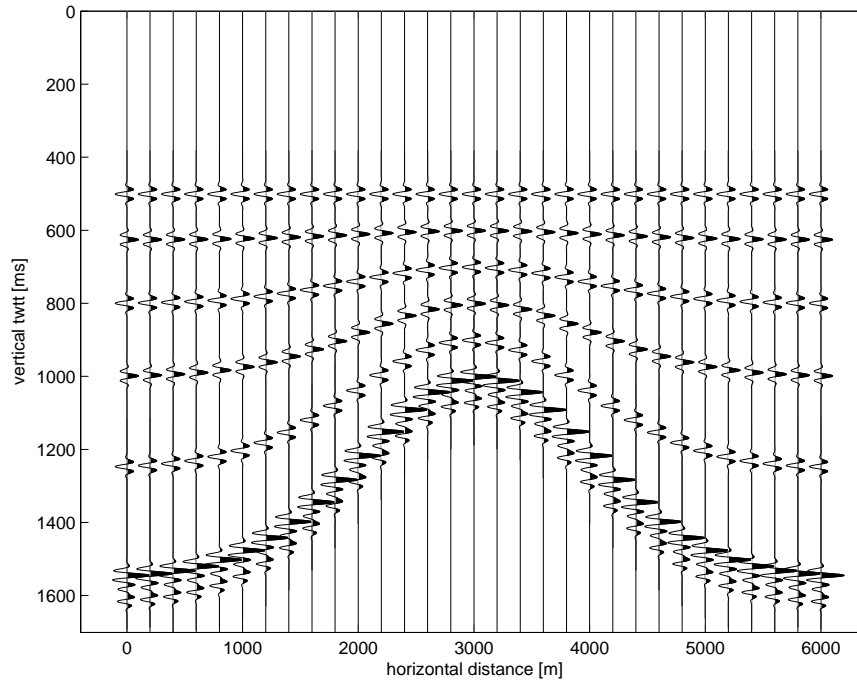


Figure 4.25: *Ideal depth migrated image after 1D vertical depth-to-time conversion, for the Gaussian model with fine-layered target.*

Ideal migrated dataset

SI inverts the pre-stack depth migrated, 1D vertical depth-to-time converted image of the normal-incidence data for layer-thickness and P-wave velocity in the target. In Figure 4.25, every 20th trace of this migrated dataset is displayed. Note that again the ideal migrated image was constructed (see the text below), so that the effect of dip-dependent migration wavelet stretch on SI can be isolated; the effects of e.g. illumination and limited lateral resolution were suppressed.

This ideal migration image is generated by first applying a 1D vertical depth-to-time conversion [Eq. (2.42)] to the model of elastic properties in depth, using the exact P-wave velocity model. In this way, the exact position of all interfaces in vertical two-way traveltime is known, as well as the size of the

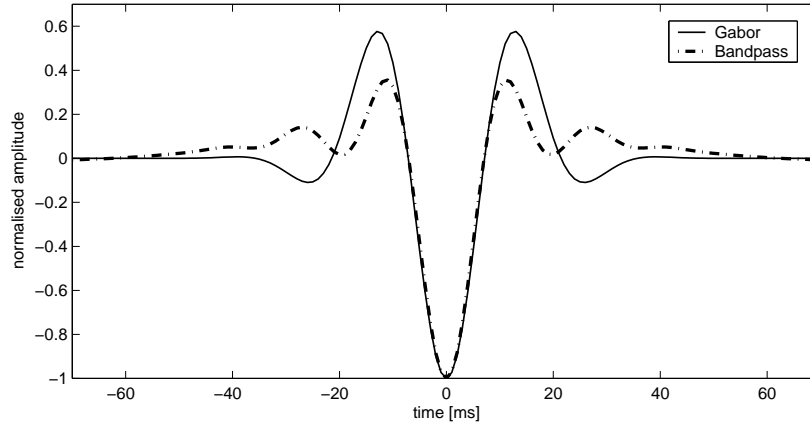


Figure 4.26: Comparison of the Gabor and Hanning-tapered bandpass zero-phase wavelets mentioned in the text.

impedance contrasts associated with the interfaces.

Subsequently every 10 m in the x_1 -direction, an acoustic impedance trace is synthesised from the density and P-wave velocity models in vertical two-way traveltimes, with which the normal-incidence reflection coefficients are calculated using Eq. (3.17). Subsequently, a spiky reflectivity trace can be computed via Eq. (2.65), and convolved with a varying, dip-dependent, wavelet which has the proper migration wavelet stretch $n_0(\beta)$ depending on the local dips β of the reflectors encountered. The stretch is calculated using Eq. (2.63), and applied to the original Gabor wavelet derived at zero-dip. (which is equal to the wavelet from the normal-incidence dataset).

The zero-phase Gabor wavelet is given by [Hubral and Tygel, 1989, Eq. (1)],

$$w(t) = \cos(2\pi f_d t) e^{-(2\pi f_d t/\gamma)^2}, \quad (4.11)$$

with t the two-way traveltimes, $f_d = 35$ Hz the dominant frequency and parameter $\gamma = 4$. Note that at zero-dip in the chosen model, the two-way traveltimes coincides with vertical two-way traveltimes, so that the equation above also applies to the zero-dip wavelet present on the depth-to-time converted migrated image. Also, note from Figure 4.26, that at least the central peak of this wavelet is very similar in shape to the Hanning-tapered zero-phase bandpass wavelet with corner frequencies of 4-12-50-75 Hz used in

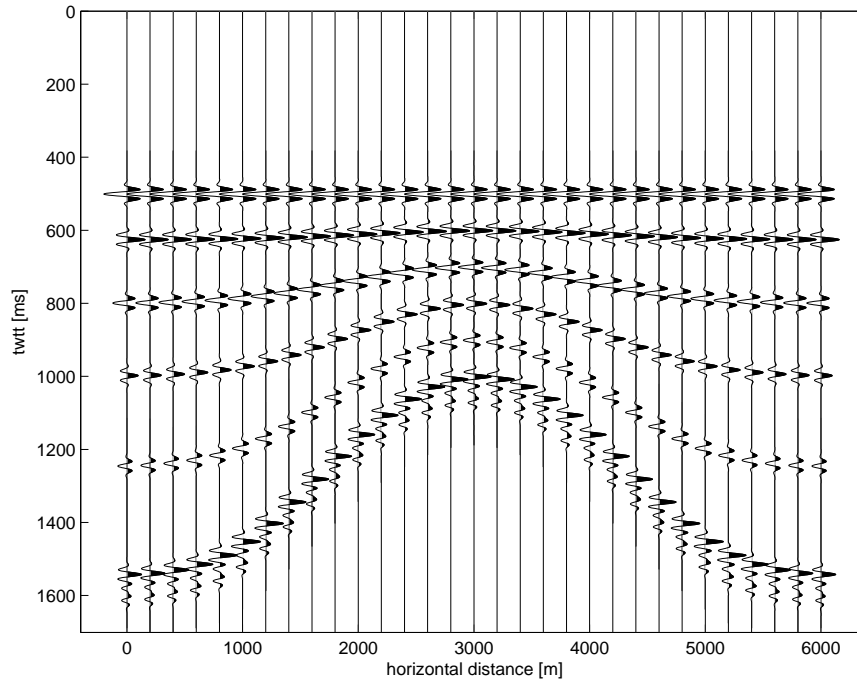


Figure 4.27: NI-dataset \dot{u}_3 for the Gaussian model with fine-layered target.

the previous tests. The change of wavelet is a consequence of using a different (more advanced) modelling software for the remaining tests.

Normal-incidence dataset

The normal-incidence dataset $\dot{u}_3(\vec{x}_s = \vec{x}_r; t)$ for 1D convolutional RBSI is generated using elastodynamic ray-tracing. It is displayed in Figure 4.27. The acquisition configuration was equal to that used for the Gaussian density model of section 4.1 (see the first two paragraphs of the subsection named ‘Normal-incidence dataset’), apart from the fact that the source wavelet was the Gabor wavelet mentioned above.

The dataset needs to be pre-processed before it can be used for 1D convolutional RBSI: the overburden amplitude losses (Figure 4.28), calculated by elastodynamic ray-tracing to the reference reflector, are removed using

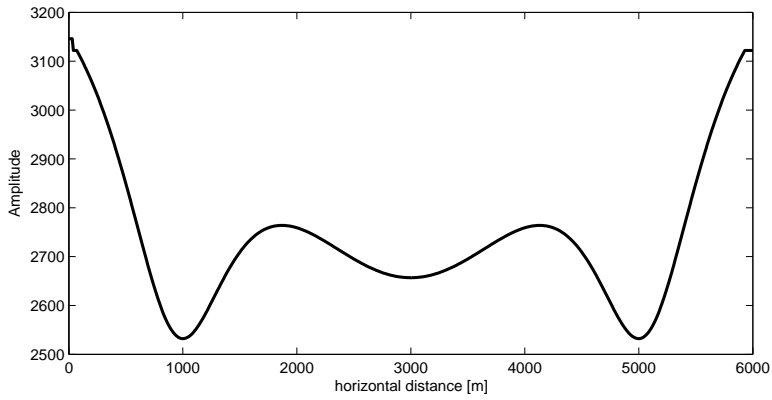


Figure 4.28: Factor $[\mathcal{L}_B/C_B]$ from Eq. (3.31) calculated for the current model.

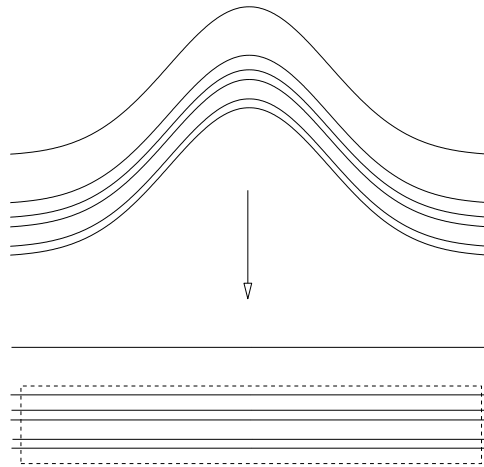


Figure 4.29: Sketch of the effect of flattening of the layers in the target along the reference horizon (bold) for the current model.

Eq. (3.31), to compensate for the effect on target-reflection amplitude of the laterally varying overburden.

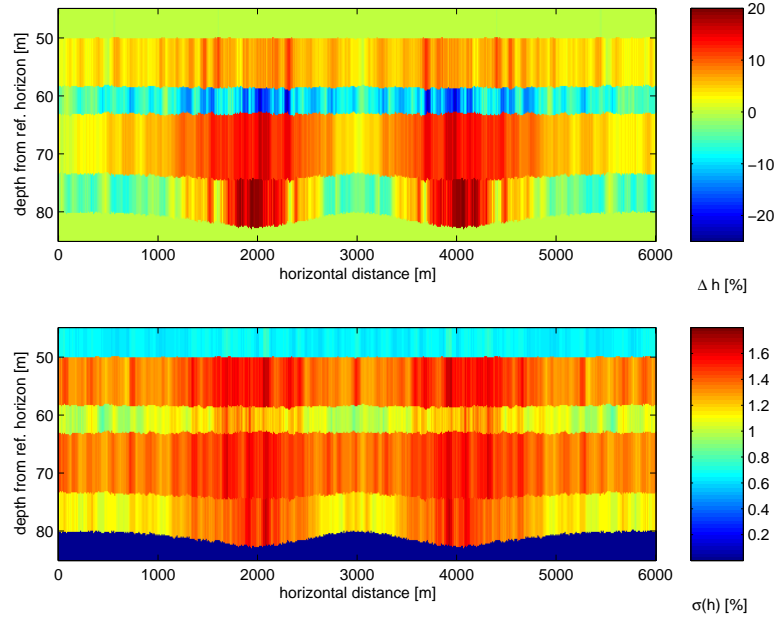


Figure 4.30: Reservoir model geometry as found by SI (flattened along reference reflector). Depicted in colour SI h misestimates in % (top) and posterior $\sigma(h)$.

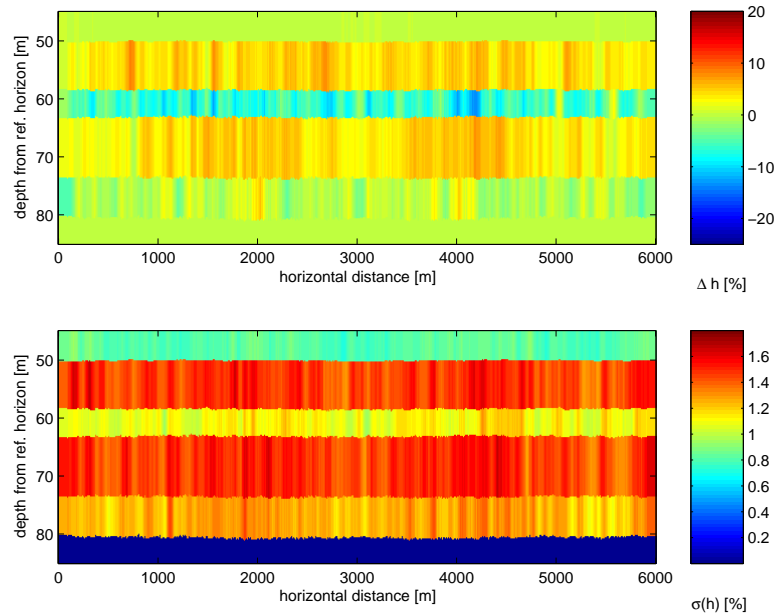


Figure 4.31: As above but for 1D convolutional RBSI. Notice the improved h estimates (while posterior $\sigma(h)$ approximately remains equal).

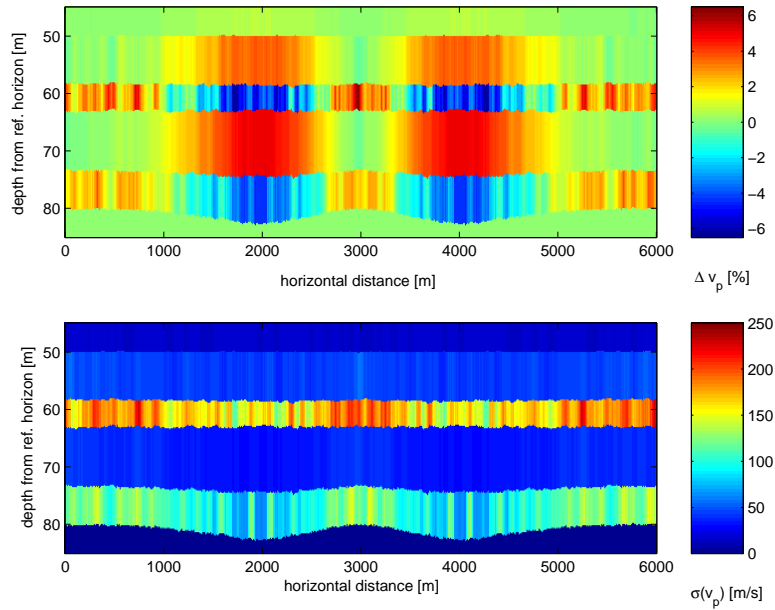


Figure 4.32: Reservoir model geometry as found by SI (flattened along reference reflector). Depicted in colour SI v_p misestimates in % (top) and posterior $\sigma(v_p)$.

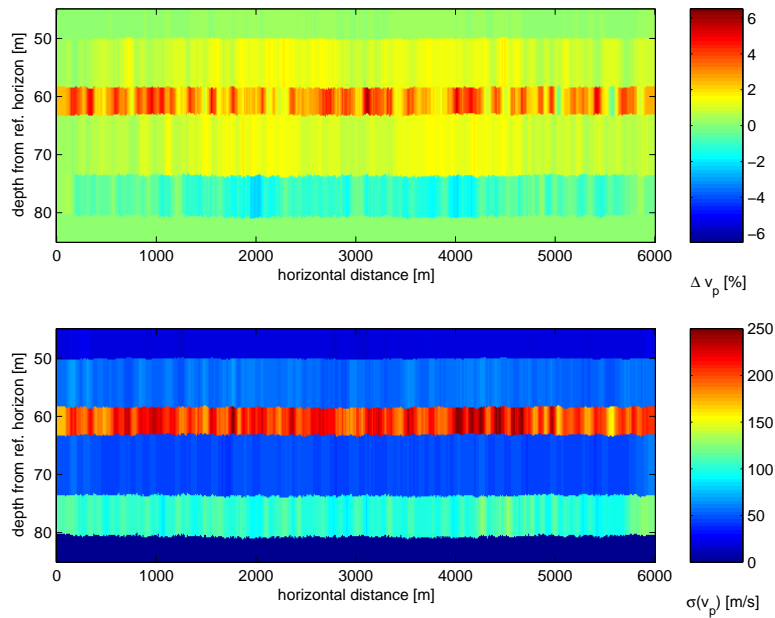


Figure 4.33: As above but for 1D convolutional RBSI. Notice the improved v_p estimates (while posterior $\sigma(v_p)$ approximately remains equal).

Inversion: SI vs. 1D convolutional RBSI

The goal set for inversion is the estimation of vertical thicknesses h and P-wave velocity v_p for each layer in the target. In the following, first, the knowledge on the inversion target available before inversion is given. Then, the SI and 1D convolutional RBSI results are discussed. Finally, the effect is investigated of target spreading losses on 1D convolutional RBSI.

Note that 1D convolutional RBSI inverts for true layer-thickness h' , which afterwards was converted to vertical layer-thickness h using the local dip at the reflection points on the top interfaces of the target-layers. The reflection points at the reference reflector (the top-target interface) are known from ray-tracing, as well as the dips since the reference reflector is picked from the migration image. The reflection points with the lower target interfaces are calculated using the h' -estimates and assuming straight ray-paths in the target (following the convention for 1D convolutional RBSI). To obtain the dips of the lower target interfaces, the prior knowledge is used that in the target the layer-dip stays unchanged in the vertical direction.

Furthermore, the h - and v_p -estimates for 1D convolutional RBSI, found at irregularly distributed reflection points on each target-interface, are interpolated to a regular lateral interval of 10 m, coinciding with the migration output grid, so that a direct comparison with the estimates obtained by SI can be made.

Prior knowledge The prior knowledge for both type of inversions involves the correct number of target layers, with exact layer-densities, $v_s = v_p/1.7$, and finally ρ , v_p and v_s for overburden and underlying halfspace exactly known. The correct wavelet is assumed to be derived from the normal-incidence section (1D convolutional RBSI), and from the horizontal part of the zero-offset migrated section (SI).

The prior knowledge on each layer-parameter to be estimated is contained in the form of normal pdfs, parameterised by mean μ and standard deviation σ : for all layer-P-velocities, the prior mean $\mu(v_p)$ coincides with true v_p , whereas the uncertainty is described by a standard deviation of $\sigma(v_p) = 250$ m/s. For all layer-thicknesses h (and h'), prior mean $\mu(h)$ coincides with true h (and h'), with an uncertainty described by a standard deviation of $\sigma(h) = 5$ m for the first (thick) target layer and $\sigma(h) = 1$ m for the

remainder of the target-layers. The normal distributions were bounded at a minimum value of 0; during the stochastic inversion, samples drawn outside this bound were rejected. The two-way traveltime to the reference reflector was known exactly up to a standard deviation of 2 ms.

Inversion results To facilitate the observation of thickness misestimates, the estimated reservoir model is displayed after flattening along the reference reflector, and with only a portion of the bottom of the first target layer shown; the inside of the dashed frame on Figure 4.29 gives an impression of what the reservoir geometry then ideally should look like.

Also, for improved display, a six-point moving average filter is applied on the h - and v_p -estimates for each layer in the lateral direction. With a trace spacing of 10 m on the migrated image (also 1D convolutional RBSI results are interpolated to this spacing before filtering), this means that lateral variations smaller than 60 m are smoothed away. To get a feeling for the size of this smoothing, notice that the lateral resolution at target level on a *real* (i.e. not ideal) migration image of the considered subsurface structure would be $\Delta r \approx \lambda_d z / L \approx 60$ m too [Eq. (2.57)], with dominant wavelength $\lambda_d = v_p / f_d = 2000 \text{ m/s} / 35 \text{ Hz} \approx 60$ m, depth of observation $z = 1250$ m and half-aperture $L = 2500/2$ m.

The posterior reservoir models obtained after SI and 1D convolutional RBSI are depicted in Figures 4.30 and 4.31. For each of these two figures, the colours in the top subfigure indicate the thickness misestimates in %, whereas in the lower subfigure they depict the absolute standard deviations. Comparing with the lower image on Figure 4.29, it is clearly visible that SI overestimates layer-thicknesses (apart from the thickness of the thinnest layer) in the parts of the reservoir that have strong dips. In contrast, 1D convolutional RBSI thickness estimates do not suffer from the dips (although they have slightly higher posterior standard deviations).

The posterior v_p -estimates for SI and 1D convolutional RBSI are depicted, in a similar way as the thicknesses, in Figures 4.32 and 4.33. For SI, it can be seen that a thickness overestimate leads to a P-wave velocity underestimate and vice-versa (while deviations are not as large as those observed in SI-estimated thickness). 1D convolutional RBSI does a better job in v_p -estimation, although misestimates increase for the lower layers due to the neglect of spreading and transmission losses in the target — a similar

behaviour was previously seen in the five plane-parallel dipping layers test (Figure 4.21).

Effect of target spreading losses on 1D convolutional RBSI In order to investigate whether an (approximate) removal of the target spreading based on the prior reservoir model improves the 1D convolutional RBSI v_p -estimates, the test is rerun on the pre-processed NI-data with target spreading losses removed. As described in the subsection named ‘Prior knowledge’, the prior model used in this test coincides with the exact model.

This removal of target geometrical spreading losses is done as follows: for each normal-incidence ray, the loss-factor $\mathcal{L}_B/(\mathcal{L}_T(H') + \mathcal{L}_B)$ [taken from Eq. (3.34)] is calculated at the intersection points of the normal-incidence ray with the prior target interfaces (assuming straight rays through the target perpendicular to the reference interface, conform with 1D convolutional RBSI, and using prior layer- v_p). Linear interpolation of the loss-factor is performed in-between the interfaces, to calculate the loss as a function of two-way traveltime. Finally, each trace from the NI-data is divided by the corresponding loss-function to obtain the desired output: traces with amplitudes in the target that are amplified more with increasing distance from the reference interface.

The v_p - and h -estimates obtained with 1D convolutional RBSI after removal of target spreading losses and the previous 1D convolutional RBSI results are displayed together in Figures 4.34 and 4.35 (for improved display, again a six-point moving average filter is applied per layer in the lateral direction). It can be seen that the misestimation error in v_p has been reduced for the fifth and second layer, while for the first layer the error has become slightly worse. The thickness estimates have slightly improved for the first layer. The standard deviations are not displayed, since for both h and v_p they show virtually no change.

In conclusion, removing the target spreading losses (based on a good prior model) before applying 1D convolutional RBSI improves v_p - and h - estimates, as expected. However, for this particular model the improvements are modest; for targets with a larger overall thickness, larger improvements may be expected. The described procedure may give the possibility to extend the application regime of 1D convolutional RBSI to such targets with larger total thickness.

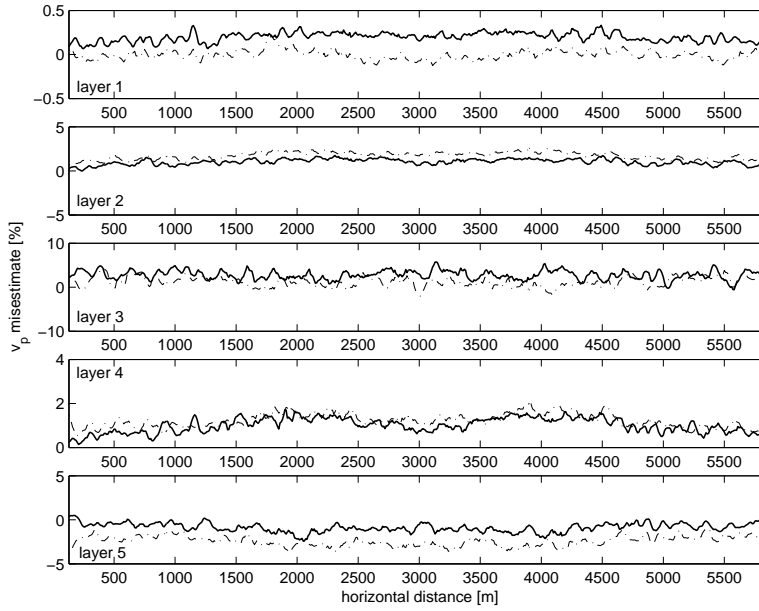


Figure 4.34: 1D convolutional RBSI v_p -misestimates, inverting pre-processed NI-data with (solid) and without spreading (dash-dot) in the target corrected for.

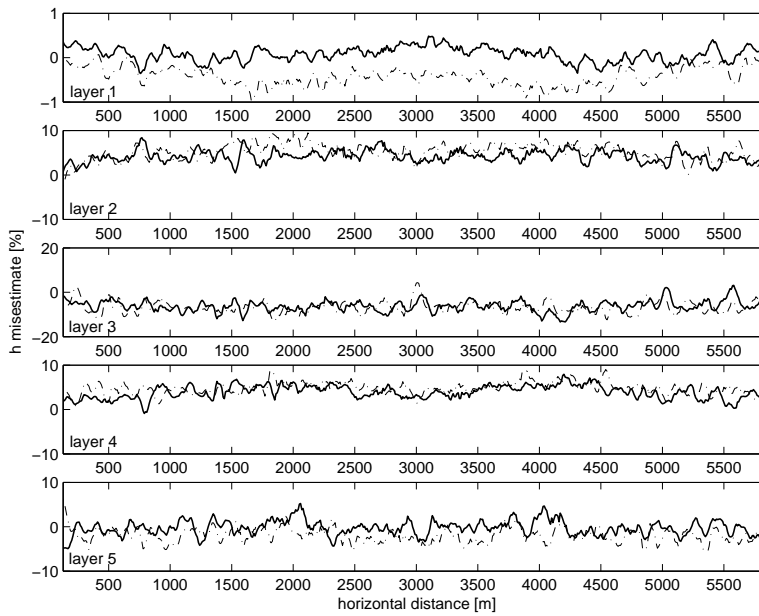


Figure 4.35: 1D convolutional RBSI h -misestimates, inverting pre-processed NI-data with (solid) and without (dash-dot) spreading in the target corrected for.

4.3 Rock model test

A look back to Figure 2.12 learns that in the forward modelling kernel of the inversion algorithm, from initial rock- and pore-fluid parameters, the elastic layer parameters are calculated using a rock/fluid property model (the ‘rock model’). So far, a very simple rock model has been used, in the sense that the reservoir model was built directly from the elastic properties P-wave velocity, S-wave velocity and density. Before advancing to the next chapter where a more complicated rock model is used in the inversion of field data, it needs to be validated whether the parameters describing such a rock model can be correctly retrieved by the 1D convolutional RBSI inversion procedure.

The test has the following setup: first, a simple reservoir model is built of which the layer-properties are described by two rock models also encountered in the next chapter. Subsequently, using the rock models, the elastic parameters of each layer in the reservoir are calculated, so that an elastic model can be set up in which elastodynamic normal-incidence ray-tracing can be performed. Finally, the normal-incidence dataset thus obtained, after necessary processing, is inverted by 1D convolutional RBSI for a subset of reservoir parameters that are assumed unknown.

■ 4.3.1 Model geometry

In this rock model test, the geometry of the model with five plane-parallel layers is re-used (Figure 4.19); however, the dip of the layers is taken zero (since RBSI is unaffected by dip-dependent migration wavelet stretch anyway), so that the model varies only in the x_3 -direction.

Layers one, three and five consist of a sandstone-shale mixture, layers two and four consist of shale (which has higher propagation velocities). The rock models used to describe these two lithologies are given in the next subsection, followed by a specification of the rock-parameters and resulting elastic properties for the five layers in this test.

The elastic properties of the homogeneous isotropic elastic overburden and the halfspace underlying the target are $v_{p,B} = 2700$ m/s, $v_{s,B} = v_{p,B}/1.7$ and $\rho_B = 2300$ kg/m³. The reference reflector Σ_1 is placed at 1350 m depth, so that normal-incidence P-wave two-way traveltime from the surface at $x_3 = 0$ m to this reflector is 1000 ms.

■ 4.3.2 Rock models

The rock models used for the five target layers are the same as those used in the layers in the Gulf of Mexico field discussed in the next chapter: the shale model and the sandstone-shale mixture model.

To describe the relation between the rock properties of the shaly sandstone reservoir rocks typically encountered in the Gulf of Mexico region, and the elastic properties ρ , v_p and v_s , a rock model is used that takes advantage of property trends derived from well logs.

The effective media model that will be given in this section, can correctly describe the encountered alternating sequences of thin sand and shale layers for (near) normal incidence waves; for larger angles of incidence, the anisotropy of the rock should be taken into account. The effect of pore fluid/gas properties on the elastic properties of the rock is accounted for via the Gassmann equations [Mavko, 2005], which assume isotropic rocks, homogeneous mineral moduli, and low (i.e. seismic) frequency of propagating waves.

The model consists of a sandstone and shale counterpart, the part described next is the shale counterpart. After that, the sand counterpart and the mixed model for the shaly sandstone are described.

Shale model

With the shale model, the elastic properties of the shale can be calculated given as prior information a regional linear depth-trend in v_p derived for the particular rock from well logs, valid for a certain depth-range $[z_1, z_2]$ (with $z_2 > z_1$), and assuming a correlation between v_p and v_s , and v_p and ρ . Note that in this section, z is used as shorthand of the x_3 -direction to improve readability of the equations. The shale model is given by,

$$v_p(z) = v_p(z_0) + \frac{\partial v_p}{\partial z} (z - z_0), \quad \forall z \in [z_1, z_2] \quad (4.12)$$

$$v_s(z) = v_s(z_0) + \frac{\partial v_s}{\partial v_p} v_p(z), \quad \forall z \in [z_1, z_2] \quad (4.13)$$

$$\rho(z) = \hat{\rho} \left(\frac{v_p(z)}{\hat{v}_p} \right)^b, \quad \forall z \in [z_1, z_2] \quad (4.14)$$

with z_0 some convenient reference depth, $[z_1, z_2]$ the depth-interval for which the equations hold, and $\partial v_s / \partial v_p$ is determined from empirical linear fits to well log data. Note that often, extrapolation of the derived depth-trend in v_p

occurs to $z_0 = 0$ in order to simplify Eq. (4.12); in that case, $z_0 \notin [z_1, z_2]$, so that $v_p(z_0)$ itself can be non-physical, e.g. negative.

Eq. (4.13) has the form of Castagna's empirical relation between v_p and v_s [Mavko, 1998, Table 7.8.1]. Eq. (4.14) is the Gardner-Gardner-Gregory empirical relation between v_p and ρ [Mavko, 1998, Table 7.9.1] in dimensionless form ($\hat{\rho}$ and \hat{v}_p the average density and P-wave velocity in the model). Since Eq. (4.14) is in power law form, b can be determined from a $\ln(\rho(z)/\hat{\rho})$ vs. $\ln(v_p(z)/\hat{v}_p)$ cross-plot of the relevant log data.

Note that since the three elastic properties are assumed correlated, this model in fact is simpler than the 'basic' rock model in which ρ , v_p and v_s are inverted for independently.

Porous sandstone model

The porous sandstone model makes use of a regional linear depth-trend in v_p derived for the particular rock from well logs, valid for a certain depth-range $[z_1, z_2]$, and assumes linear correlation between v_p and v_s , and v_p and porosity ϕ , in order to calculate the elastic properties of the sandstone filled with a reference fluid, or fluid 1,

$$v_p(z) = v_p(z_0) + \frac{\partial v_p}{\partial z}(z - z_0), \quad \forall z \in [z_1, z_2] \quad (4.15)$$

$$v_s(z) = v_s(z_0) + \frac{\partial v_s}{\partial v_p} v_p(z), \quad \forall z \in [z_1, z_2] \quad (4.16)$$

$$\phi(z) = \phi(z_0) + \frac{\partial \phi}{\partial v_p} v_p(z), \quad \forall z \in [z_1, z_2] \quad (4.17)$$

in which z_0 is a convenient reference depth and $[z_1, z_2]$ is the depth-interval for which the equations hold, and $\partial v_s/\partial v_p$ and $\partial \phi/\partial v_p$ are determined from empirical fits to log data. Subsequently, the density is calculated as the simple volumetric average of the rock constituent densities,

$$\rho(z) = (1 - \phi(z))\rho_{\min} + \phi(z)\rho_{\text{fl},1}, \quad (4.18)$$

with ρ_{\min} the density of the mineral grains, and $\rho_{\text{fl},1}$ the density of the reference pore fluid.

To take into account the effect of pore fluid properties, for this porous sandstone model the fluid (or gas) substitution recipe described in Mavko [2005] is applied below. From the measured elastic properties ρ , v_p and v_s for the

sandstone with reference fluid 1, the bulk modulus K_1 and shear modulus μ_1 are calculated as follows:

$$K_1 = \rho \left(v_p^2 - \frac{4}{3} v_s^2 \right), \quad \mu_1 = \rho v_s^2. \quad (4.19)$$

The bulk modulus K_2 for the sandstone filled with the actual fluid 2 is calculated using the Gassmann substitution,

$$\frac{K_2}{K_{\min} - K_2} - \frac{K_{\text{fl},2}}{\phi(K_{\min} - K_{\text{fl},2})} = \frac{K_1}{K_{\min} - K_1} - \frac{K_{\text{fl},1}}{\phi(K_{\min} - K_{\text{fl},1})}, \quad (4.20)$$

with $K_{\text{fl},1}$ and $K_{\text{fl},2}$ the bulk moduli of fluids 1 and 2, K_{\min} the mineral modulus, and ϕ the porosity. The shear modulus μ_2 remains equal to μ_1 , i.e. the shear modulus is unaffected by fluids [Mavko, 2005]. The density ρ_2 of the sandstone filled with fluid 2 is calculated using,

$$\rho_2 = (1 - \phi)\rho_{\min} + \phi\rho_{\text{fl},2} = \rho_1 + \phi(\rho_{\text{fl},2} - \rho_{\text{fl},1}), \quad (4.21)$$

with ρ_1 and ρ_2 the density of rock with fluids 1 and 2, and $\rho_{\text{fl},1}$ and $\rho_{\text{fl},2}$ the density of fluids 1 and 2. Finally, the propagation velocities after fluid substitution can be calculated,

$$v_p = \sqrt{\frac{K_2 + \frac{4}{3}\mu_2}{\rho_2}}, \quad v_s = \sqrt{\frac{\mu_2}{\rho_2}}. \quad (4.22)$$

Laminated sandstone-shale model

The laminated sequence of the bulk of thin sand and shale layers are described using the previously discussed shale model for the shales and the sandstone model for the sands as follows,

$$\rho = SF\rho_{\text{Sst}} + (1 - SF)\rho_{\text{Sh}}, \quad (4.23)$$

$$\frac{1}{\rho v_p^2} = \frac{SF}{\rho_{\text{Sst}} v_{p,\text{Sst}}^2} + \frac{1 - SF}{\rho_{\text{Sh}} v_{p,\text{Sh}}^2}, \quad (4.24)$$

$$\frac{1}{\rho v_s^2} = \frac{SF}{\rho_{\text{Sst}} v_{s,\text{Sst}}^2} + \frac{1 - SF}{\rho_{\text{Sh}} v_{s,\text{Sh}}^2}, \quad (4.25)$$

with ‘Sst’ referring to sandstone properties, ‘Sh’ to shale properties, and SF the sand fraction in the mix (aka. net-over-gross). As in Eq. (4.18), bulk density is again calculated using a simple volumetric average. The velocities are calculated using the Reuss average, which assumes lamination perpendicular to the wave-path [Mavko, 2005]. Since the shales have no porosity, the bulk porosity can be calculated using the sand porosity only,

$$\phi = \phi_{\text{Sst}}SF. \quad (4.26)$$

■ 4.3.3 Exact rock parameters

The rock parameters for the shale and sandstone-shale mixture models specified below, the ‘true’ parameters that will be inverted for by 1D convolutional RBSI, are loosely based on the parameter values used in the Gulf of Mexico field example described in the next chapter. Everywhere, $z_0 = 0$ m and $[z_1, z_2] = [1000, 1500]$ m.

Shale layers

For the shale, in Eq. (4.12) $v_p(z_0) = 2650$ m/s and the term $\partial v_p/\partial z$ was set to zero. In Eq. (4.13), $v_s(z_0) = -600$ m/s, and $\partial v_s/\partial v_p = 0.617$. In Eq. (4.14), $\hat{v}_p = 2700$ m/s, $b = 0.215$ and $\hat{\rho} = 2313$ kg/m³. Thus the equations (4.12)-(4.14) become:

$$v_p(z) = 2650, \quad (4.27)$$

$$v_s(z) = -600 + 0.617 v_p(z), \quad (4.28)$$

$$\rho(z) = 2313 \left(\frac{v_p(z)}{2700} \right)^{0.215}. \quad (4.29)$$

Sandstone-shale mixture layers

The shale found in the sand-shale mixture is described using the parameters specified above. For the sandstone counterpart, in Eq. (4.15), $v_p(z_0) = 2400$ m/s and $\partial v_p/\partial z = 0$ s⁻¹. In Eq. (4.16), $\partial v_s/\partial v_p = 0.8335$ and $v_s(z_0) = -1200$ m/s. In Eq. (4.17), $\partial \phi/\partial v_p = -0.00012$ s/m and $\phi(z_0) = 0.635$. In Eq. (4.18), $\rho_{\text{min}} = 2650$ kg/m³ and $\rho_{\text{fl},1} = 1000$ kg/m³: the pore-space in the sandstone is chosen to be fluid-filled with water ($v_p = 1500$ m/s,

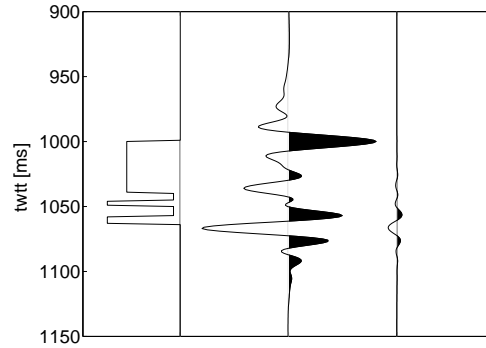


Figure 4.36: Left: *Acoustic impedance log.* Middle: *A single trace from pre-processed \dot{u}_3 .* Right: *difference with ideal input by generated 1D convolution.*

$\rho = 1000 \text{ kg/m}^3$). This is also the reference fluid, so that Gassmann substitution need not be done: the bulk elastic parameters for the fluid-filled sandstone follow directly from Eqs. (4.15)-(4.18):

$$v_p(z) = 2400, \quad (4.30)$$

$$v_s(z) = -1200 + 0.8335v_p(z), \quad (4.31)$$

$$\phi(z) = 0.635 - 0.00012v_p(z), \quad (4.32)$$

$$\rho(z) = 2650(1 - \phi(z)) + 1000\phi(z), \quad (4.33)$$

Finally, the elastic properties of the sand-shale mixture follow from Eqs. (4.23), (4.24) and (4.25).

The true values for the rock-parameters to be inverted for are listed in the third column of Table 4.4 (these values coincide with the prior mean values for the inversion; the $v_{p,Sst}$ listed is that of a sandstone fluid-filled with water). From these true values, and the other known parameters describing the rock, such as porosity, the true elastic parameters for each layer can be calculated using the rock model; these values are depicted in the third column of Table 4.5.

■ 4.3.4 Normal-incidence dataset

A normal-incidence data acquisition experiment is performed, with omnidirectional point sources and receivers placed at positions $\vec{x}_s = \vec{x}_r$ along a straight line at the surface; thus in combination with the model geometry, a 2.5D configuration is formed. The primary unconverted P-wave normal-incidence particle velocity dataset $\dot{u}_3(\vec{x}_s = \vec{x}_r; t)$ is calculated with elastodynamic ray-tracing, using in the target interval the exact elastic layer parameters listed in the third column of Table 4.5.

The normal-incidence data needs to be pre-processed before 1D convolutional RBSI can be performed; for the chosen model geometry, the processing involves merely the removal of the spherical spreading through the overburden (Eqs. 3.28 and 3.31, with $A_0 = v_{p,B}$ and $C_0 = 1$).

A single trace from \dot{u}_3 is shown in the centre of Figure 4.36; the peak amplitude is about 0.072. Also shown in this figure, on the left-hand side, is the acoustic impedance log, with minimum at $5.08 \cdot 10^6$ and maximum at $6.21 \cdot 10^6$ kg/(m²s). Furthermore, it is interesting to see the difference between the pre-processed normal-incidence trace and the ideal trace for 1D convolutional RBSI, generated by convolving the exact spiky reflectivity trace with the exact wavelet: this difference is shown on the right-hand side. Notice that differences due to neglecting the transmission losses and spherical spreading in the target accumulate for the lower layers; peak amplitude is about 0.007, or 10%.

■ 4.3.5 Estimated rock parameters by 1D convolutional RBSI

The parameters to invert for are for the shales: thickness h and P-wave velocity v_p . For the laminated sands, thickness h , sand-fraction SF , $v_{p,Sst}$ and $v_{p,Sh}$ are inverted for. Also, the two-way traveltime to the reference reflector is inverted for. The prior and posterior values of these rock-parameters are found in Table 4.4. Using the rock model formulations, the estimated bulk elastic layer-parameters were calculated from the rock-parameters, see Table 4.5 (fourth and fifth column).

Comparing the estimated values with the exact values, it can be seen that all exact parameters are within one standard deviation from the posterior means. Hence, this test on the ‘five plane-parallel layers’ model with shale and sand-shale rock models instead of the basic rock model, has shown that also the

Table 4.4: Prior distribution and 1D convolutional RBSI inversion results for the rock model test. P-Velocity v_p is in [m/s], h in [m]. Sand-fraction $0 \leq SF \leq 1$ is dimensionless. Layers two and four are shales, the others a sand-shale mixture.

| Layer no. | property | prior μ | prior σ | posterior μ | posterior σ |
|-----------|-------------|-------------|----------------|-----------------|--------------------|
| 1 | $v_{p,Sst}$ | 2400 | 120 | 2418 | 101 |
| | $v_{p,Sh}$ | 2650 | 133 | 2592 | 141 |
| | h | 50 | 5 | 49.9 | 1.2 |
| | SF | 0.6 | 0.2 | 0.55 | 0.27 |
| 2 | $v_{p,Sh}$ | 2650 | 133 | 2659 | 37 |
| | h | 8 | 1 | 7.6 | 1.2 |
| 3 | $v_{p,Sst}$ | 2400 | 120 | 2428 | 109 |
| | $v_{p,Sh}$ | 2650 | 133 | 2634 | 226 |
| | h | 5 | 1 | 6.0 | 1.5 |
| | SF | 0.9 | 0.2 | 0.81 | 0.17 |
| 4 | $v_{p,Sh}$ | 2650 | 133 | 2657 | 50 |
| | h | 10 | 1 | 9.6 | 0.9 |
| 5 | $v_{p,Sst}$ | 2400 | 120 | 2440 | 53 |
| | $v_{p,Sh}$ | 2650 | 133 | 2580 | 156 |
| | h | 7 | 1 | 7.3 | 0.8 |
| | SF | 0.9 | 0.2 | 0.85 | 0.20 |

parameters describing more complicated rock models can be retrieved successfully from the normal-incidence data using 1D convolutional RBSI.

4.4 Offset tests

To conclude this chapter, a test in a simple model containing a single interface is presented, in which the P-wave velocity of the underlying layer and two-way traveltime to the (reference) reflector is estimated. RBSI estimates these two parameters by inverting different pre-stack unmigrated angle-gathers. The RBSI results for the different specular reflection angles

Table 4.5: Calculated exact vs. estimated bulk elastic layer-parameters. Velocities v_p , v_s are in [m/s], density is in [kg/m³].

| Layer no. | property | exact | posterior μ | posterior σ |
|-----------|----------|-------|-----------------|--------------------|
| 1 | v_p | 2482 | 2481 | 49 |
| | v_s | 868 | 882 | 31 |
| | ρ | 2168 | 2175 | 39 |
| 2 | v_p | 2650 | 2659 | 37 |
| | v_s | 1035 | 1040 | 23 |
| | ρ | 2304 | 2305 | 7 |
| 3 | v_p | 2419 | 2456 | 96 |
| | v_s | 815 | 850 | 71 |
| | ρ | 2100 | 2124 | 29 |
| 4 | v_p | 2650 | 2657 | 50 |
| | v_s | 1035 | 1039 | 28 |
| | ρ | 2304 | 2305 | 9 |
| 5 | v_p | 2419 | 2448 | 37 |
| | v_s | 815 | 847 | 30 |
| | ρ | 2100 | 2114 | 33 |

θ are assembled into a single estimate for mean and standard deviation; subsequently these values are compared with the estimates obtained by SI on a single stacked migrated image. In this way, the claim that inverting on different angle-gathers should in principle lead to the same estimated parameters, made in section 3.1.1, is verified. Note that the effects of noise and wavelet-stretch due to normal moveout (NMO) and migration are not regarded in this test, so that the single effect of (stacking) the angle-dependent reflection coefficient $R(\theta)$ remains.

■ 4.4.1 Model geometry

An (x_1, x_3) -slice through the model is depicted on the left-hand side of Figure 4.37. One horizontal interface at $x_3 = 1000$ m separates two ho-

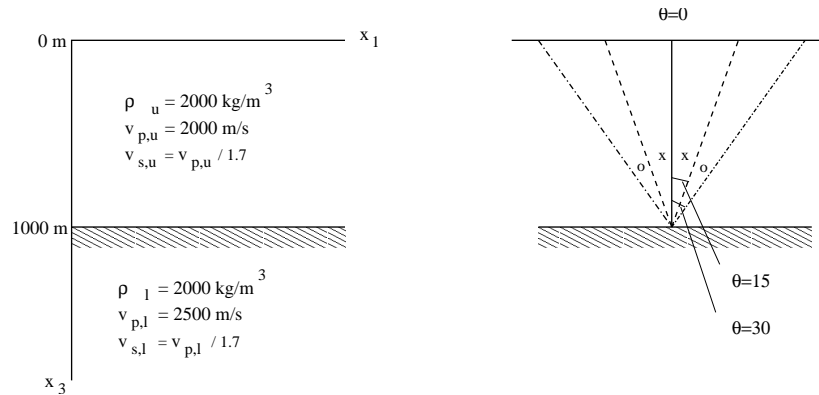


Figure 4.37: Left: Model geometry for the offset test. Right: Raypaths corresponding to reflection angles of 0, 15 and 30 degrees.

mogeneous isotropic elastic halfspaces, the upper with constant P-wave velocity $v_{p,u} = 2000 \text{ m/s}$, the lower with $v_{p,l} = 2500 \text{ m/s}$. S-wave velocity is calculated as $v_s = v_p/1.7$, while density for both layers is equal: $\rho_u = \rho_l = 2000 \text{ kg/m}^3$.

■ 4.4.2 Prestack unmigrated datasets

Responses are calculated using elasto-dynamic ray-tracing, for three different shot/receiver pairs with the same common midpoint; the acquisition is performed at the free surface $x_3 = 0$ with isotropic point sources, and receivers that record the vertical component of particle velocity \dot{u}_3 . Only a single midpoint position is considered since the model is laterally invariant. The shot/receivers are placed such, that the corresponding ray-pairs have 0° , 15° and 30° angle of incidence and reflection at the interface. The constant propagation velocities combined with the horizontal reflector cause the ray-paths to be straight and reflection points to be the same for common midpoint source/receiver pairs; see the right-hand side of Figure 4.37 for a sketch of the situation.

It is assumed that all amplitude effects besides the reflection have been suppressed, so that a single trace from particle velocity dataset $\dot{u}_3(\vec{x}_s, \vec{x}_r; t)$ has the peak of the source wavelet (Hanning-tapered 4-12-50-75 Hz zero-phase

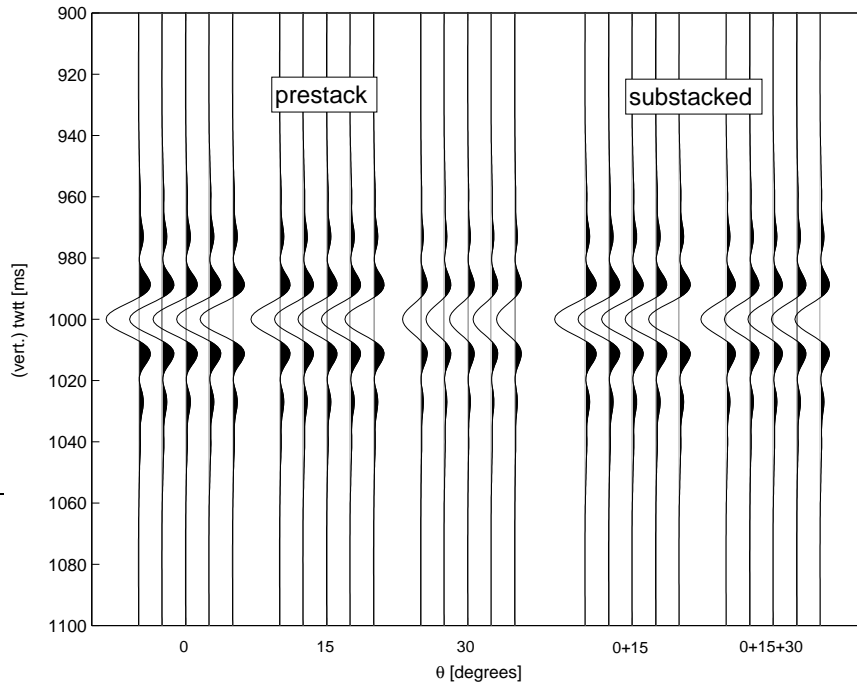


Figure 4.38: *Traces from the angle-gathers in two-way traveltime with moveout and moveout-stretch completely removed (left), and from the substacked ideal migrated images in vertical two-way traveltime (right). Angles and angle-ranges are indicated on the horizontal axis, respectively.*

bandpass) positioned at the two-way traveltime to the interface, and peak amplitude calculated by the full Zoeppritz equation. Also the moveout in traveltime compared to the normal-incidence response is assumed to be perfectly removed by a stretch-free NMO-correction for the 15° and 30° traces, to facilitate the comparison of the signals for the different offsets. Note that in practice, doing a stretch-free NMO-correction is not a trivial exercise [Dunkin and Levin, 1973; Perroud and Tygel, 2004]. On the left-hand side of Figure 4.38, five identical traces from each of the three angle gathers are depicted.

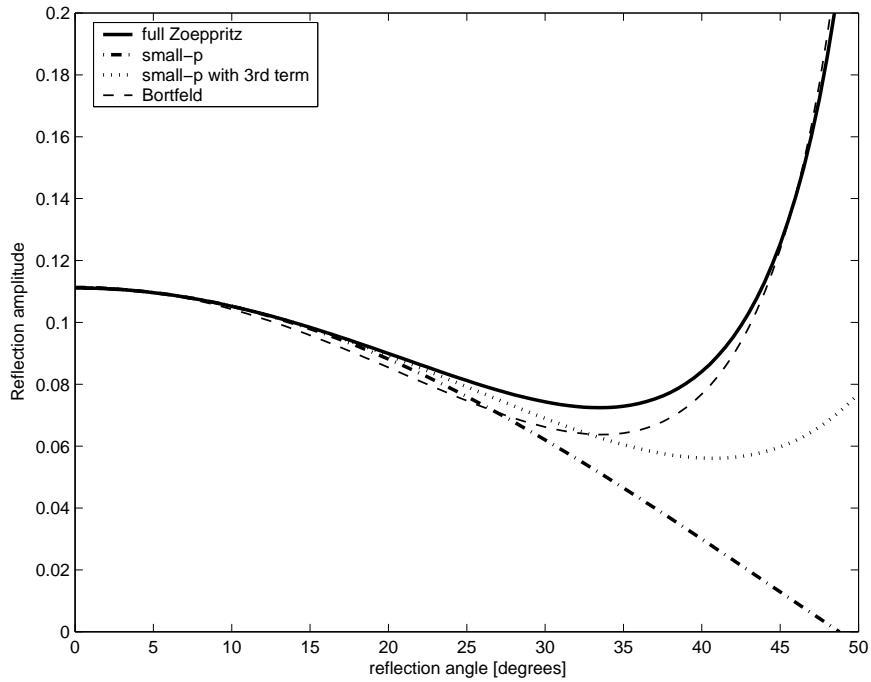


Figure 4.39: Reflection amplitudes for unconverted *P*-waves in the current model.

Reflection amplitude versus angle

The reflection amplitudes in Fig. 4.38 vary with reflection angle; how exactly they vary is better visualised by Figure 4.39. In this picture, the unconverted primary *P*-wave reflection amplitudes calculated using the full Zoeppritz equations are displayed by the solid line. Note that all plotted angles are in the subcritical range, i.e. the angles are smaller than the critical angle $\theta_c = \arcsin(v_{p,u}/v_{p,l}) \approx 53^\circ$ for which the transmitted ray is parallel to the interface. This calculation follows easily from Snell's law $\sin \theta / \sin \theta_t = v_{p,u}/v_{p,l}$, with θ the angle of incidence and θ_t the angle of refraction, and setting $\theta_t = 90^\circ$.

In practical applications, often the reflection amplitudes are not calculated using the full Zoeppritz equations, but rather using conceptually and computationally simpler approximations such as 'small-p' [Aki and Richards,

1980, p. 153] given in Eq. (4.34), valid for small θ ($< 30^\circ$) and small impedance contrasts, or the Bortfeld equations [Bortfeld, 1961]; the amplitudes calculated using these approximations are also depicted in Figure 4.39. Since the inversion software used for this test calculates reflection amplitudes using the small-p approximation, where ‘p’ stands for horizontal slowness, it needs to be explained in more detail. A well known form of the small-p approximation is [Gerritsma, 2003, chapter AVO/AVA],

$$R(\theta) \approx A + B \sin^2 \theta, \quad (4.34)$$

with,

$$A = R(\theta = 0) \approx \frac{1}{2} \left(\frac{\Delta v_p}{\bar{v}_p} + \frac{\Delta \rho}{\bar{\rho}} \right), \quad (4.35)$$

$$B = \frac{1}{2} \frac{\Delta v_p}{\bar{v}_p} - 2 \frac{\bar{v}_s^2}{\bar{v}_p^2} \left(\frac{\Delta \rho}{\bar{\rho}} + 2 \frac{\Delta v_s}{\bar{v}_s} \right), \quad (4.36)$$

in which B is called the AVO gradient, θ is the reflection angle, p is the horizontal slowness, the sine-term can be written as $\sin^2 \theta = (pv_{p,u})^2$, subscripts u, l are referring to upper and lower layer, and difference and averaging operations are defined as $\Delta \rho = \rho_l - \rho_u$, $\bar{\rho} = (\rho_l + \rho_u)/2$ (with equivalent formulations for v_p and v_s).

Note that the small-p approximation can optionally be made more accurate for large reflection angles by adding a third term [Shuey, 1985] (see Figure 4.39),

$$R(\theta) \approx A + B \sin^2 \theta + C[\tan^2 \theta - \sin^2 \theta], \quad (4.37)$$

with,

$$C = \frac{1}{2} \frac{\Delta v_s}{\bar{v}_s}. \quad (4.38)$$

In generating the pre-stack unmigrated traces, usage is made of the small-p approximation to calculate the full Zoeppritz reflection coefficients, in order to eliminate errors in the small-p-inversion estimates that are due to this approximation implemented in the software (the accuracy of the small-p approximation is not the effect under consideration).

■ 4.4.3 Ideal stacked migrated datasets

Because in this test we are merely interested in the effect on SI inversion capabilities of averaging the reflection coefficients by stacking, again usage is made of ideal migrated datasets. The horizontal interface is chosen to eliminate the dip-dependent migration wavelet stretch, migration stretch due to offset will occur (from Eq. (2.58) it follows that reflector dip β and specular reflection angle θ play a similar role in migration stretch) but is not modelled for the same reason.

With these simplifications, traces from the zero-offset migrated data in vertical two-way traveltime are equal to the final normal-incidence dataset described in the previous subsection. The same applies for the migrated 15° and 30° angle gathers and corresponding pre-stack unmigrated datasets.

However, in practice stacks of the migrated angle-gathers are made to increase the signal-to-noise ratio (S/N) on the migrated data, in which different angles are summed and averaged (in fact not angle- but offset-gathers are stacked in practice, but for this test both types are equivalent). For example, in the real dataset discussed in the next chapter, ‘near’, ‘mid’ and ‘far’ stacked migrated datasets are generated as final output of pre-stack depth migration, in which the ‘near’ stacked migrated dataset stacks up reflection angles at the inversion target of roughly 0° to 18° .

A stack is made for the 0° and 15° migrated angle gathers, and for the 0° , 15° and 30° migrated angle gathers. Five traces from the stacked migrated datasets are displayed on the right-hand side of Figure 4.38; only a small portion of traces from each migrated dataset is shown since the model is laterally invariant.

■ 4.4.4 Inversion results: SI vs. RBSI

For both inversions, the prior knowledge is: $v_{p,u} = 2000$ m/s, $\rho_u = \rho_l = 2000$ kg/m³ and $v_s = v_p/1.7$. Also the exact wavelet is known for the normal-incidence and zero-offset migrated data. The prior knowledge on the parameters to be estimated is: $v_p = 2500 \pm 1000$ m/s, $t_R = 1000 \pm 4$ ms. For SI, the inversion uses the wavelet derived from the zero-offset migrated data (which was not substacked). The inversion results are presented in Table 4.6. First of all, the two-way traveltimes to the reference reflector are estimated very well by both methods, the largest standard deviation is smaller than

Table 4.6: Inversion results for v_p of the underlying layer and t_R to the interface. The upper three rows refer to RBSI results, the lower two to SI (on substacks).

| θ | $R(\theta)$ | $\mu(v_p)$ [m/s] | $\sigma(v_p)$ [m/s] | $\mu(t_R)$ [ms] | $\sigma(t_R)$ [ms] |
|----------|-------------|------------------|---------------------|-----------------|--------------------|
| 0° | 0.1111 | 2495 | 102 | 1000.27 | 1.47 |
| 15° | 0.0979 | 2515 | 58 | 1000.06 | 0.64 |
| 30° | 0.0620 | 2519 | 88 | 1000.61 | 3.07 |
| 0-15° | | 2466 | 75 | 1000.09 | 1.28 |
| 0-30° | | 2376 | 56 | 1000.07 | 0.62 |

0.3%; it is therefore most interesting to concentrate on the v_p -estimates.

Regarding the v_p -estimates for SI and RBSI, it can be concluded that the stacking of gathers up to 15° has only marginal effect; this is closely related to the shape of the reflection amplitude-versus-angle curve shown in Figure 4.39: in the 0-15° interval, reflection amplitude does not change radically so that the zero-offset assumption in SI does not introduce large errors. However for the stack up to 30°, a significant deviation larger than $2\sigma(v_p)$ in the v_p estimate does occur.

Again concentrating on the v_p -estimates, from Table 4.6 it can also be seen that the standard deviations for the individual RBSI inversions seem to be slightly larger than that of SI. However, if results for the individual RBSI inversions are aggregated together to calculate the overall mean $\bar{\mu}(v_p)$ and standard deviation $\bar{\sigma}(v_p)$ [pers. comm. J.Leguijt],

$$\frac{1}{\bar{\sigma}^2} = \frac{1}{\sigma_0^2} + \frac{1}{\sigma_{15}^2} + \frac{1}{\sigma_{30}^2} \Rightarrow \bar{\sigma} = 44, \quad (4.39)$$

$$\bar{\mu} = \bar{\sigma}^2 \left[\frac{\mu_0}{\sigma_0^2} + \frac{\mu_{15}}{\sigma_{15}^2} + \frac{\mu_{30}}{\sigma_{30}^2} \right] = 2507, \quad (4.40)$$

in which the subscripts refer to θ of the inverted angle-gathers, it can be seen that the aggregated mean is closer to the real value than the SI mean, and the aggregated standard deviation is smaller. Hence, the final estimates obtained with RBSI are more accurate than those obtained with SI.

Finally, notice that in practice the lower S/N on the individual angle-gathers compared to the migrated (sub)stacks is likely to negatively influence $\bar{\sigma}$, al-

though it is unlikely to introduce a bias in the $\bar{\mu}$ as is present in the $\mu(v_p)$ estimated by SI.

4.5 Discussion

The benefits of ray-based inversion as compared to existing 1D inversion have been demonstrated, for zero-offset acquisition, in the tests of the first two sections of this chapter. Two issues have been addressed using zero-offset data: lateral layer-density determination, and inversions in strongly dipping subsurface structures.

The results from the laterally varying density model show that RBSI, contrary to SI, can correctly determine lateral layer-density variations, a requirement for true-amplitude PreSDM: if lateral density variations are present, these should be specified for the Kirchhoff-type migration algorithm in order to compute true-amplitude migration operators, and eventually to generate a migration result on which SI could correctly operate.

In strongly dipping subsurface structures, migration stretch severely affects SI and should be accounted for in some way, before inverting for v_p , h , ρ and related reservoir parameters as porosity and pore-fluid content in a strongly dipping target reservoir sequence. 1D convolutional RBSI, a specific implementation of RBSI, however, operates in the pre-stack domain where this stretch is non-existent.

The performed synthetic data tests on the single dipping layer and five plane-parallel dipping layers model and also the Gaussian model with a target of five layers have shown that 1D convolutional RBSI, in its proper application regime, resolves v_p and h much better than SI. The same has also been shown for RBSI in determining ρ in the wedge-like density model.

Subsequently, in the simple offset test, assuming a stretch-free NMO and stretch-free migration of non-zero offset data, it has been shown that assembling the RBSI results on different common-angle gathers leads to more accurate parameter estimates, than the estimates obtained with SI on the corresponding ideal migrated substack. It should be noted though, that the performance of SI is closely related to the shape of the reflection amplitude-versus-angle curve for the reflector of interest: in the example shown, SI performance on the 0-15° substack was not much worse than RBSI, because reflection amplitude remained fairly constant for that angle-range. For 0-

30°, significant SI misestimations did arise. In this respect, it is interesting to mention that the ‘near’ migrated substack of the real dataset discussed in the next chapter contains reflections from the target with angles up to roughly 20°.

Finally, the results obtained in the rock model test have shown that also the parameters specified via a rock/fluid property model can be retrieved with RBSI. This is an important observation with regard to the next chapter, in which SI will be tested against RBSI on a real-life dataset. In this real-data case, the target reservoir is parameterised using rock models that describe the relation between the desired reservoir rock/fluid parameters per layer and the bulk elastic layer-parameters.

Field data test

For testing 1D convolutional RBSI and comparing it with conventional stochastic trace inversion (SI), a real-life dataset from the Gulf of Mexico, acquired above a hydrocarbon reservoir with a strong structural dip, was kindly made available by Shell Offshore Inc. of New Orleans, United States of America. By using 1D convolutional RBSI to invert these data, a first impression is obtained of the potential of this newly developed method for estimating reservoir properties in a realistic case.

For a fair comparison, both methods perform a seismic-to-well tie at the same calibration well on a horizontal part of the target, and both make use of the same prior information. At the dipping part of the target, the reservoir parameter estimates are compared with the measurements taken in a later evaluation well drilled after the initial inversion was done, i.e. a so-called ‘blind well’ test is carried out.

This chapter is structured as follows. First, the data acquisition and processing sequence are briefly summarised. Also, the available migrated and pre-stack unmigrated data that result from the processing are presented. Next, the strategy is presented for making the comparison between standard and novel inversion. Then, a selection is made from the 3D data-cube: the in-

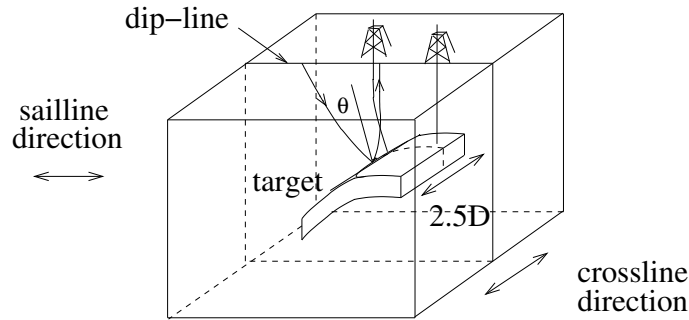


Figure 5.1: Dip-line in 3D seismic data-cube: around this selected sailline, the subsurface is assumed laterally invariant in the crossline direction. A specular ray-pair is shown to the top interface of the target, with reflection angle θ .

version is restricted to a single sailline. The migrated data is inverted by standard stochastic trace inversion, and the pre-stack unmigrated data by 1D convolutional RBSI. Finally, the reservoir parameter estimates obtained with both methods are compared with values observed at the second well on the slope. From the comparison, conclusions are drawn. Portions of this chapter have been taken from [van der Burg et al. \[2007\]](#).

5.1 Seismic data description

The deep water Gulf of Mexico field in which the inversion tests are done, is a hydrocarbon-bearing reservoir consisting of layers of sheet sands and shales. The reservoir contains a horizontal part and a dipping part with dips to a maximum of 31° , see the sketch of the target in Figure 5.1. A 3D high-resolution seismic survey was conducted over the area.

In the following, first the acquisition parameters relevant to the inversion are described. Then, the processing sequence as applied by Shell to the seismic data is given. This sequence consists of two main parts: a pre-processing part to prepare the pre-stack unmigrated data for migration, and the true-amplitude pre-stack depth migration (TA PreSDM) itself.

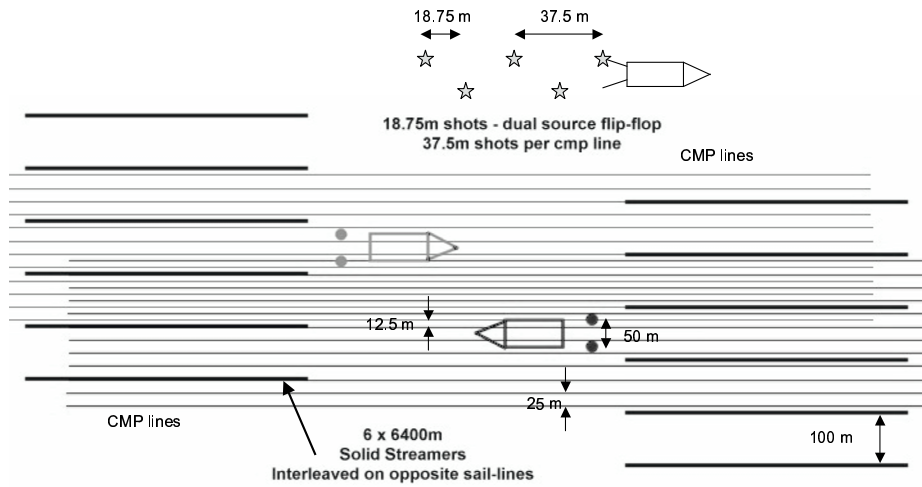


Figure 5.2: Dual source flip-flop interleaved marine data acquisition. Numbers are from Table 5.1 . ‘Streamers’ are cables incorporating hydrophones. CMP stands for common-midpoint (between source and hydrophone). [Source: Shell E&P Co.]

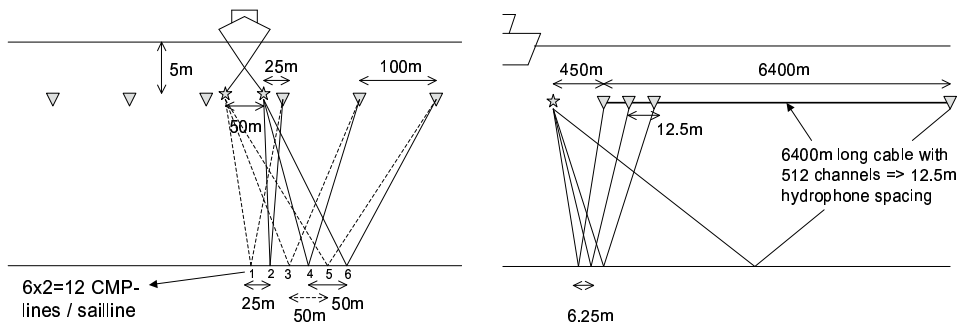


Figure 5.3: CMP-distance is 25 m crossline non-interleaved (left), so 12.5 m interleaved: this is the crossline binsize. Inline CMP-distance equals half the hydrophone spacing, 6.25 m (right): this is the inline binsize.

Table 5.1: *Main acquisition parameters.*

| Parameter | Value |
|------------------------------|--|
| Shooting direction | 315° from due N, interleaf lines at 135° |
| No. of source arrays | 2 |
| Source depth | 5 m |
| Gun spacing | 50 m |
| Cable configurations | 6 cables × 512 channels |
| Cable depth | 5 m |
| Cable spacing | 100 m |
| Cable length | 6400 m |
| Shot interval | 18.75 m |
| Shot interval per CMP-line | 37.5 m |
| Offset range [†] | 450 - 6750 m |
| Offset increment | 75 m |
| Fold | 84 |
| Binsize (inline × crossline) | 6.25 m × 12.5 m |
| Recording length | 6.6 s |
| Time sampling interval | 0.002 s |

■ 5.1.1 Acquisition parameters

The seismic data discussed in this chapter were recorded in an acquisition campaign that was a follow-up of a previous 3D seismic survey. It was deployed to support well placement, to reduce uncertainty and to allow pre-stack interpretation. To succeed in these goals, a very large usable signal bandwidth of up to 80 Hz was needed. The desired high-frequency preservation and structural detail called for an unusually fine spatial sampling at the surface of 6.25 m inline × 12.5 m crossline (which was later interpolated to 6.25 m), and a temporal sampling of 2 ms.

[†]Note that the source document stated a range of 450 - 6300 m, however 6750 m is

Because the geometry of the target was already known from the previous survey, the acquisition configuration could be optimised by sailing the marine acquisition vessel approximately in dip-lines over the target, see Figure 5.1. In Table 5.1, a summary is given of the acquisition parameters. The vessel towed 6 streamers, each 6400 m long and with 512 channels, at 5 m below sea-level; acquisition was done in a so-called ‘dual-source flip-flop interleaved’ mode (Figure 5.2). This yielded the desired fine spatial sampling in the crossline and inline directions, see Figure 5.3. A total of 2 TeraByte of data were collected.

■ 5.1.2 Processing before migration

This section describes the processing applied by Shell to prepare the data for TA PreSDM. The resulting pre-stack dataset is inverted by 1D convolutional RBSI (after some additional pre-processing described in section 5.6). Figure 5.4 shows the complete TA PreSDM workflow; here the part from ‘Areal binning’ up to the so-called ‘Inverse 3D NMO/DMO’ is discussed. Note that during the processing care has been taken to preserve the amplitude behaviour as well as possible.

The 3D raw data were delivered by the marine acquisition contractor in sail-line/shot sort, which means that for each line that the vessel has sailed over the acquisition area, the hydrophone data recorded after each firing of the airgun-array are stored sequentially on magnetic tape; the sailline direction is called ‘inline’ in the following, whereas the direction perpendicular to it is called ‘crossline’. Upon arrival of the data in the processing centre, areal binning was applied, using a rectangular Bin grid of 6.25 m × 12.5 m (inline × crossline) laid out over the survey area. During the binning, the midpoint of every source-receiver pair is used to decide to which Bin the corresponding trace should be assigned.

Subsequently, to improve the interpretability of the data, the airgun-wavelet present on the data was shaped to zero phase by applying a depulse filter (a procedure also known as signature deconvolution), and a shot-receiver consistent scaling was applied for removal of variations in the source strength and the receiver sensitivity.

consistent with the fold and offset increment within a CMP-gather. Consequently, it is assumed that the last 8 channels per cable are inactive/discarded.

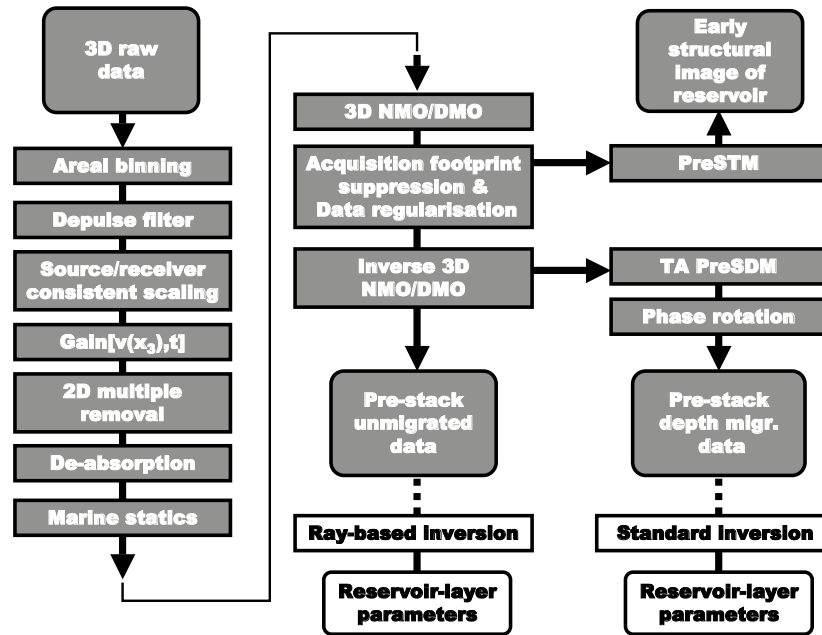


Figure 5.4: Processing workflow for TA PreSDM. The flow after inverse NMO/DMO is given in greater detail in Figure 5.6. Also indicated are the entry-points for ray-based and standard inversion.

Surface-related multiple removal was achieved using two different techniques: the first subtracts predicted multiples, the second applies filtering in the so-called $\tau - p$ domain. Multiple elimination could only be employed in 2D mode, not in the more optimal 3D mode, to ensure a timely delivery of the processed data. As a result, some residual multiple energy remained present on the data.

To enhance the visibility of deep reflectors, a rudimentary correction for spherical spreading loss was applied to the data, using a gain-function depending on two-way traveltime and a laterally constant regional velocity function. De-absorption was done to take into account energy dissipation during wave-propagation in the subsurface, followed by marine static corrections to compensate for up to 4 ms time shifts in comparison with neighbouring sailines.

Table 5.2: *Pre-stack data parameters changed by processing before migration.*

| Parameter | Value |
|------------------------|--------------|
| Offset range | 450 - 6325 m |
| Offset increment | 125 m |
| Fold | 48 |
| Time sampling interval | 0.004 s |

After that, a 3D normal moveout (NMO) / dip moveout (DMO) - inverse NMO/DMO sequence was applied to the data. The reasons for this were two-fold: firstly, it was desired to obtain an early structural image of the target via pre-stack time migration (PreSTM), before applying the CPU-intensive and hence time consuming TA PreSDM. To improve the positioning of structures on this image, 3D DMO must be applied to remove the dip-dependent part of moveout with offset on CMP-gathers [Black et al., 1993; Deregowski, 1986]; after DMO, the reflection point smear in the CMP-gathers has been compensated for, enabling a correct NMO/stack of dipping planar reflectors [Sheriff, 2002]. For the DMO, a common-offset Kirchhoff summation method was used, which correctly handles the wavelet phase.

The second reason for the NMO/DMO - inverse NMO/DMO step is that it allows acquisition footprint suppression and data regularisation. During the inverse DMO, an offset depopulation was done from 80 to 48 offsets, with output offsets ranging from 450 m to 6325 m with 125 m offset increment. After inverse NMO/DMO of the data ready for PreSTM, the data were suitable for PreSDM, see Figure 5.4. In Figure 5.5 a portion of these data is shown: the 575 m common-offset gather for sailline 2313, which is the dip-line selected for inversion with 1D convolutional RBSI (section 5.3.1). The reflectors seen around 4000 ms on the right-hand side mark the target for inversion. On these high quality data, pre-stack interpretation is attainable and pre-stack inversion should be feasible.

In Table 5.2, a subset of pre-stack data parameters is given after data regularisation and offset depopulation. Notice the smaller offset range due to the discarding of offset outliers.

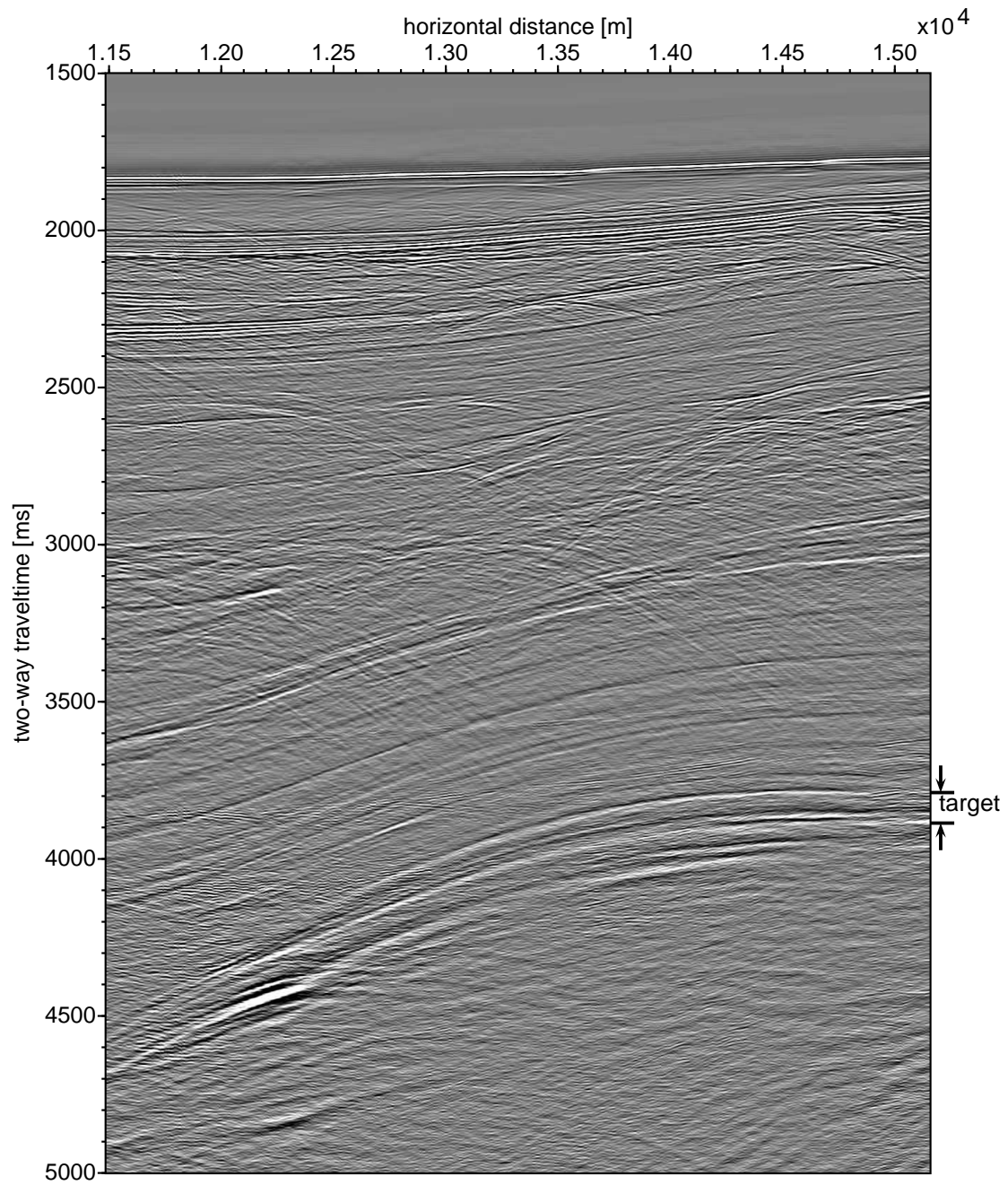


Figure 5.5: Portion of a common-offset gather for sailline 2313; the offset is 575 m.

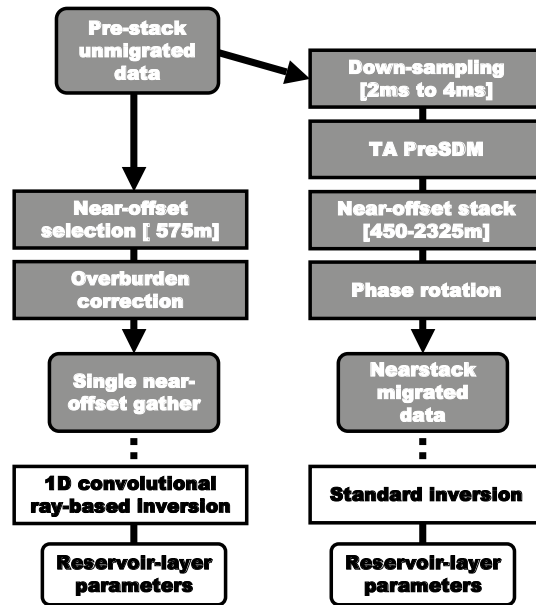


Figure 5.6: Detail of flowsheet depicted in Figure 5.4 after inverse 3D NMO/DMO, with the RBSI-branch made specific for 1D convolutional RBSI.

■ 5.1.3 True-amplitude pre-stack depth migration

A common-offset true-amplitude pre-stack P-wave Kirchhoff depth migration (see section 2.4.1) was applied on each offset gather from the pre-processed pre-stack data, using the velocity model obtained from velocity analysis during a preceding pre-stack time migration and traveltimes inversion. The P-wave velocity model used for the migration was a grid with an inline/crossline/depth spacing of 100 m. The migration operator grid was sampled twice as dense, with a spacing of 50 m.

The migration output was available in vertical two-way traveltimes (suitable for SI); conversion to the depth domain can be done easily via Eq. (2.42) using the migration P-wave velocity model. A down-sampling of the pre-stack unmigrated data from 2 ms to 4 ms two-way traveltimes had to be performed, to obtain a manageable datasize for the processing centre where the PreSDM was done; 4 ms is also the output sampling in vertical two-way time after mi-

gration. The spatial output sampling in the inline and crossline direction was 12.5 m, twice the size of the inline Binsize. Consequently, for a given distance along the inline direction, the data before migration contain twice as many traces as the migrated data.

After pre-stack migration, a stack was made for the 16 nearest-offsets from 450 m to 2325 m in order to increase the signal-to-noise ratio to facilitate structural interpretation; the tuning thickness on this ‘nearstack’ migrated result in the target area is 11 m. Stacks were also made for mid-offsets from 2450 m to 4325 m, and for far-offsets from 4450 m to 6325 m, to enable amplitude-versus-offset (AVO) analysis.

Prior to inversion, a phase-rotation of 90° was applied to the image, an operation sometimes applied to facilitate the interpretation of inversion results in the target. The flow from pre-processed pre-stack unmigrated data to the nearstack migrated result is summarised in Figure 5.6 (right branch). In Figure 5.7, a portion of the nearstack migrated section at sailline 2313 is displayed. The reflectors seen inside the target interval (indicated on the right-hand side of the figure) mark the target for inversion.

5.2 Inversion strategy

To determine the best setup for the SI vs. 1D convolutional RBSI comparative test, it is necessary to review some of the exploration and production history of the reservoir under consideration.

On the migration image obtained from an earlier seismic dataset, a potential hydrocarbon reservoir was discovered. First, to prove hydrocarbon presence in the potential reservoir, based on the migration image, an exploration well was drilled. In this case it was placed through the horizontal part of the reservoir, visible around 3900 ms vertical two-way traveltime, between 14500 and 15000 m horizontal distance on Figure 5.7.

After the discovery, the new seismic dataset described in section 5.1 was acquired and migrated in order to reduce uncertainty in structure and reservoir properties for the development of the field and to support further well placement. SI was applied to invert the PreSDM migrated data, extrapolating the detailed knowledge at the exploration well over the flank of the structure.

However, based on results from synthetic tests done in Chapter 4, it is our suspicion that the artifacts due to migration deteriorate the inversion results

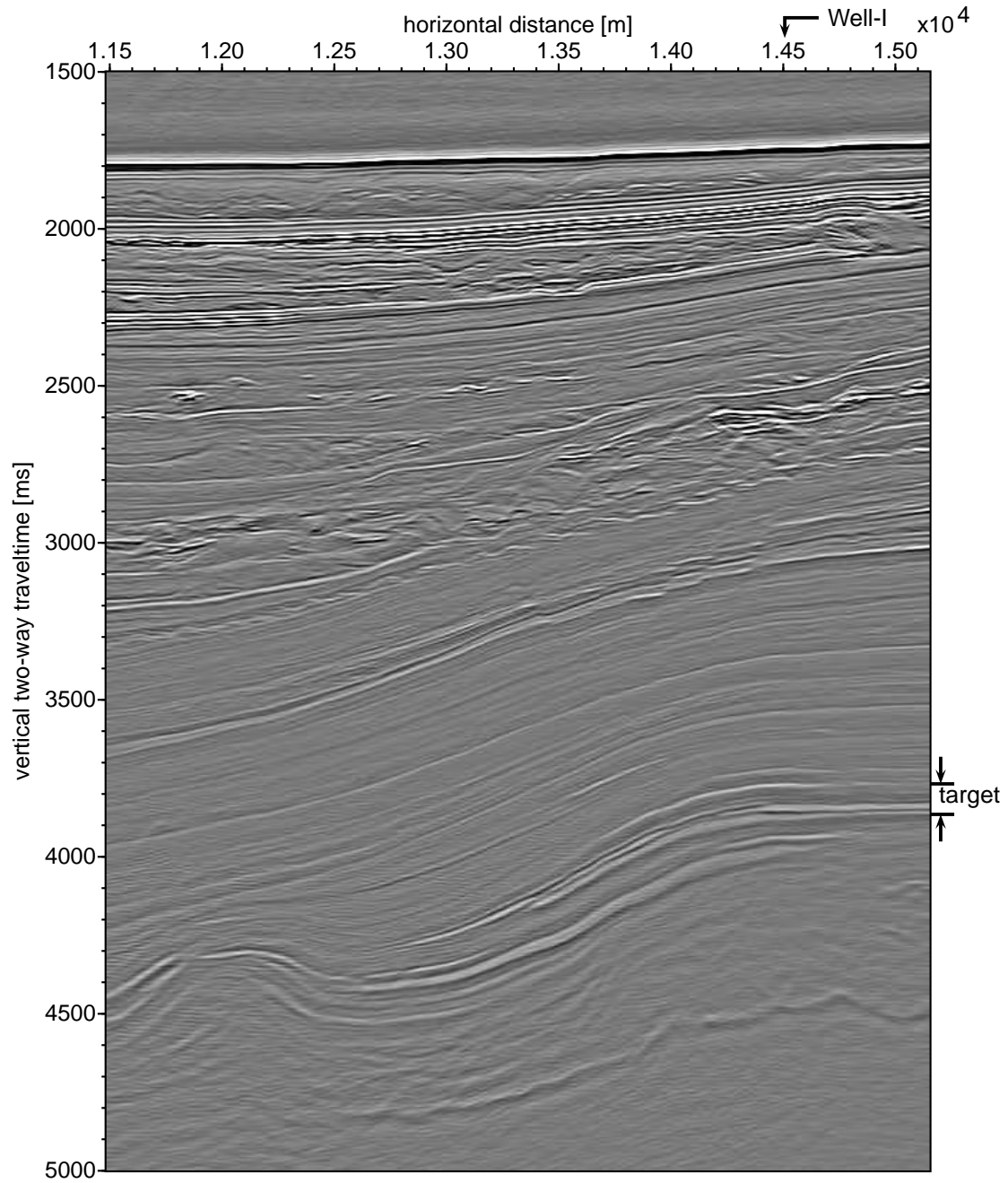


Figure 5.7: Portion of the nearstack migrated image for sailline 2313.

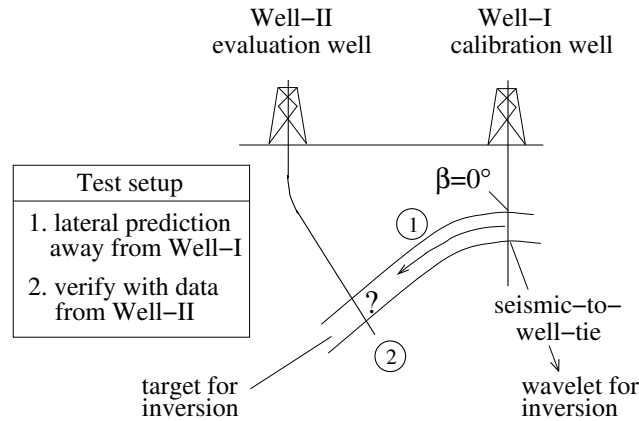


Figure 5.8: The capabilities in lateral prediction of target reservoir parameters away from Well-I (the exploration well) to the dipping part of the target at Well-II are tested for SI versus 1D convolutional RBSI.

precisely in this dipping part of the reservoir; this should become apparent by checking the inversion results with the logs of the second (appraisal) well, which was drilled right through the slope after the first inversion was done. In the comparative test (Figure 5.8), 1D convolutional RBSI is applied using the same prior information as the standard inversion (SI), to see whether more accurate results can be obtained in the flank of the structure during the first inversion process right after drilling of the first exploration well.

5.3 Seismic data selection for inversion

The selection (from the total data volume) of the migrated and pre-stack unmigrated data to be inverted is performed on the basis of three criteria: conformity to a 2.5D setting, proximity of wells, and data quality.

Obviously, the data should contain the reflections from both the horizontal and dipping part of the inversion interval (the reservoir zone): a reference reflector is needed that clearly indicates the position of the inversion interval on the data. In this case, the most prominent reflector in the inversion interval of which the interpreted position was available, is the top interface of the

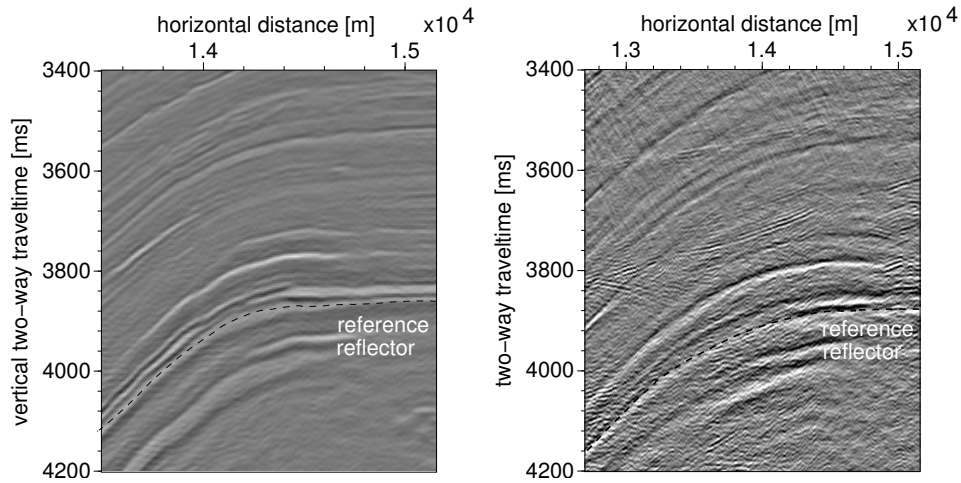


Figure 5.9: Reference reflector as visible on the migrated data (left) and on the 575 m common-offset gather before migration.

sheet sand at the bottom of the interval. It is clearly visible on both migrated and pre-stack unmigrated data (Figure 5.9; note that the phase-rotation applied to the migrated data [p. 160] complicates direct comparison with the unmigrated data). It has been used as reference reflector in inversions carried out before this research started, too.

■ 5.3.1 2.5D setting

Although no fundamental limitations exist that prevent the application of 1D convolutional RBSI in a 3D setting, the comparative tests against SI are performed in a 2.5D setting, so that data overhead is substantially reduced by confining the analysis to the migrated and pre-stack unmigrated data along a single sailline.

Hence, from the 3D data cube, a ‘dip-line’ is selected such that the subsurface (velocity model) and acquisition configuration locally are approximating a 2.5D setting (see again Figure 5.1). The migrated section along the selected sailline 2313 has already been shown in Figure 5.7. Figure 5.10 displays a crossline from the migrated data and the corresponding part of the migration velocity model, from which it can be inferred that the zone around

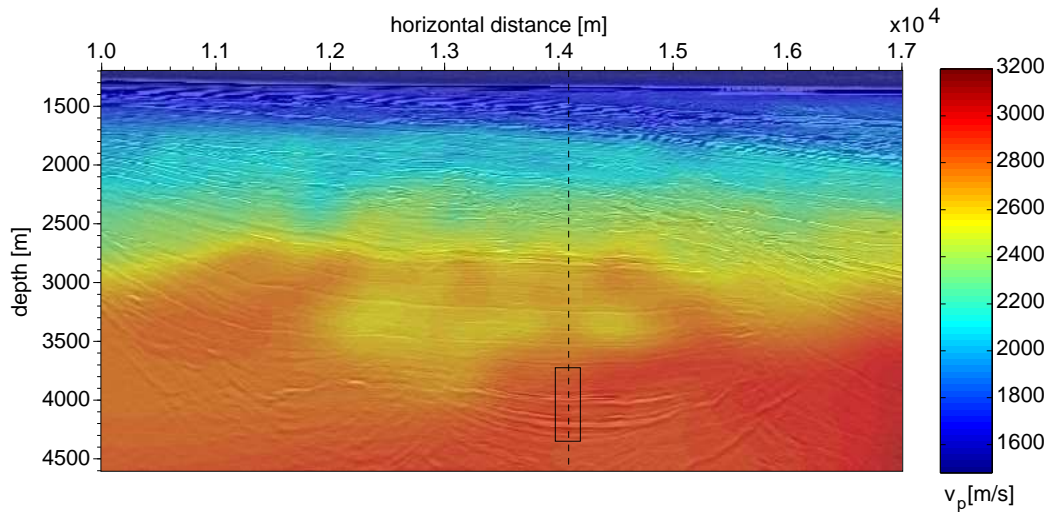


Figure 5.10: Cross-section at inline position 14500 m of the nearstack migrated image on top of the corresponding migration velocity model. The target area near the selected sailline (dashed) is indicated with a box.

the selected sailline comes close to being laterally constant.

■ 5.3.2 Proximity of wells

Apart from being located in a 2.5D setting, the selected sailline is conveniently close to the vertical well, ‘Well-I’, where the seismic-to-well tie is done: the offset in the crossline direction at the level of the reference reflector is 112.5 m. Also the well at the dipping part of the structure, ‘Well-II’, where the validation of inversion results is done, is not far from the sailline (250 m offset at target depth). Another potential validation well, ‘Well-III’ at the base of the slope, is at 220 m offset at target depth.

The well-paths of the mentioned wells in the target are displayed in the inline and crossline directions in Figure 5.11. The crossline is taken at the point where Well-II intersects the reference reflector. The picture shows again that the target remains approximately laterally constant in the crossline direction between sailline and Well-II.

Note that the close proximity to another well passing through the steepest

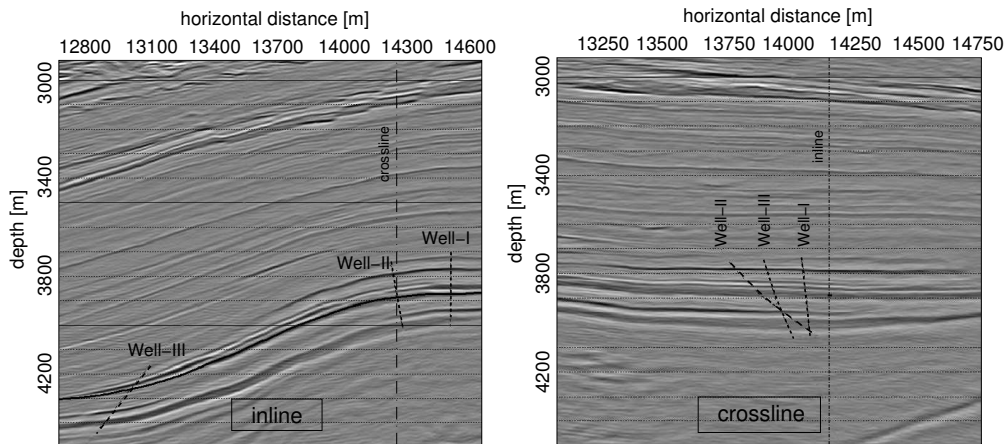


Figure 5.11: Well paths (dashed) projected on the migrated image, in the inline direction (left) and in the crossline direction at the inline position indicated with a dash-dotted line, where Well-II intersects the reference reflector (black line).

part of the reservoir had a strong weight too in the sailline-selection procedure; unfortunately however, later that particular well appeared unusable.

■ 5.3.3 Data quality

From the selected sailline, the migrated section has excellent quality, as can be seen in Figure 5.7. For this sailline, the pre-stack unmigrated gathers were available after the pre-processing mentioned in section 5.1.2. From these pre-stack data, ideally, 1D convolutional RBSI would be performed on a zero-offset gather. However, measuring true zero-offset data in practice is troublesome, therefore in reality the ‘first acceptable’ (in terms of data quality) common-offset gather close to zero-offset is inverted. This common-offset gather should contain reflections from the target with reflection angles θ' close to 0° ; how the θ' can be evaluated is explained in section 5.6.1. Using this common-offset gather instead of the zero-offset gather is tolerable as long as $R(\theta = \theta') \approx R(\theta = 0^\circ)$.

To select the first acceptable common-offset gather, a data quality analysis was done by visual inspection of the gathers for offsets closest to 0 m. In Figure 5.12, the portions containing reflections from the reservoir area of the first two available common-offset gathers (for offsets 450 m and 575 m)

are displayed. Also, the gather for offset 950 m is displayed, just to show the data quality for larger offsets. It can be seen that the gather for 450 m suffers significantly more from high-frequency noise around the target zone at 4000 ms than the gather for 575 m. Although already far away from zero-offset, the next available gather, for 700 m offset, was also inspected, but it was not of better quality than the gather for 575 m. Therefore, the common-offset gather for 575 m was chosen to be inverted with 1D convolutional RBSI. In the following, a closer look is taken at three noise events visible on the offset gathers: (remains of) multiples, triplications and diffractions.

Multiples

Some of the noise-events on the offset gathers are identified as remains of sea-bottom multiples not properly removed by the 2D multiple removal that was applied. To see this, in Figure 5.13 for the 450 m common-offset gather the sea-bottom is displayed in the upper image, and the target for inversion in the middle image. In the middle image, the remains can still be recognised of the multiple from the sea-bottom (a), the peg-leg multiple of (a) and the first strong reflector below the sea-bottom (b), and the multiple of (b).

Triplications and diffractions

A few other observations can be made from Figure 5.12: around 12000 m horizontal distance and 4500 ms two-way traveltime, a high-amplitude event occurs that is caused by seismic waves passing through a caustic point in the subsurface. This behaviour has been confirmed during the ray-tracing to the reference reflector for 1D convolutional RBSI, see section 5.6; it limits the range along the reservoir for which parameters can be estimated with this special case of RBSI. Furthermore, for recording times smaller than 3800 ms (which are outside the inversion window), faint tails from diffractions in the overburden are present in the data; the diffractions are better seen in Figure 5.5. Finally, the increasing traveltime to the reflectors due to the increasing offset can be seen in the respective gathers.

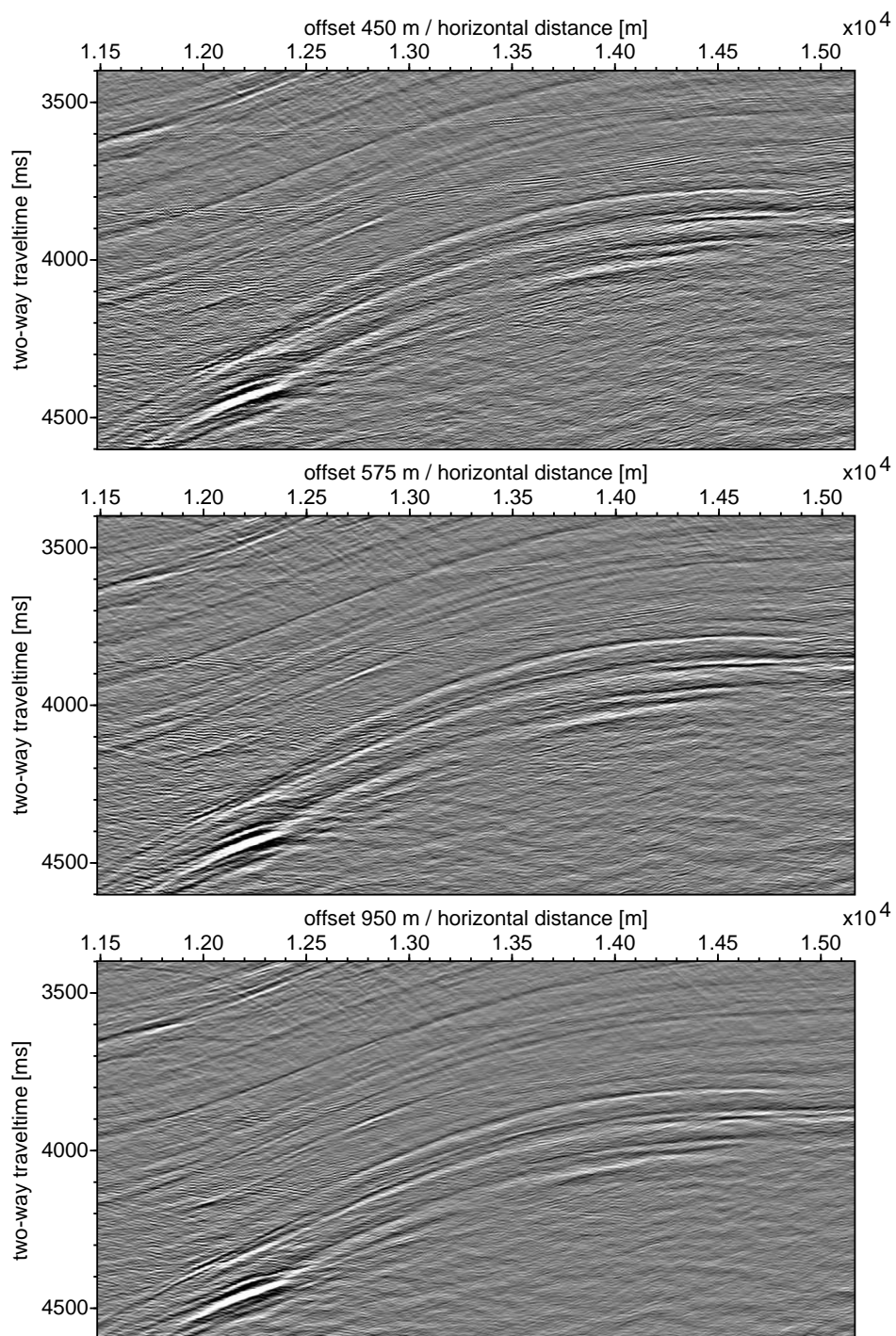


Figure 5.12: Three common-offset gathers along sailline 2313. See text for details.

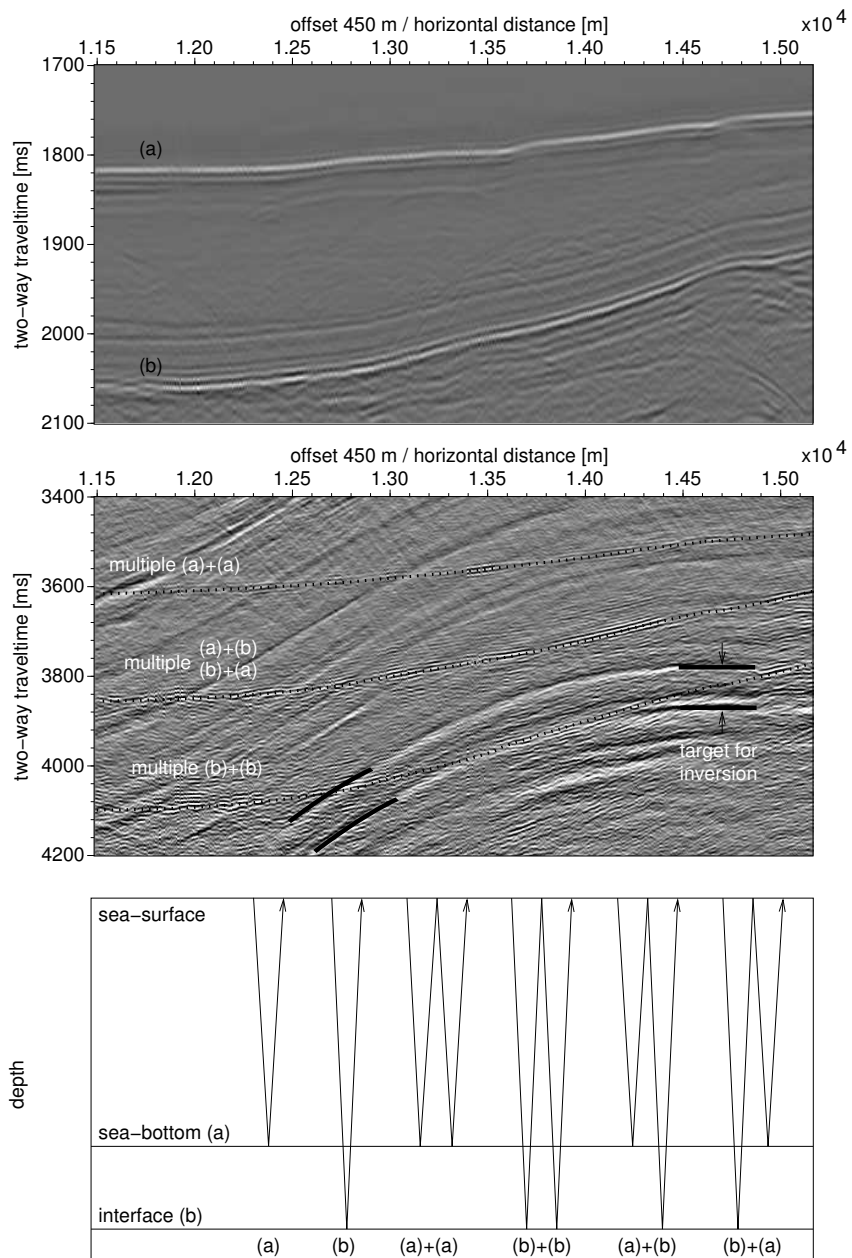


Figure 5.13: Two details from the 450 m common-offset gather, showing two strong primary reflections at the sea-bottom and below it (top) and associated multiple reflections in the target (middle). A sketch of the corresponding ray-paths is given in the bottom image.

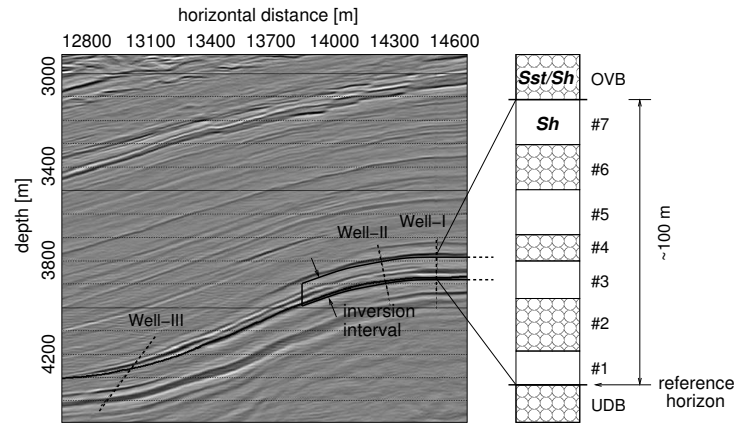


Figure 5.14: Inversion interval on the nearstack migrated image. The interval contains seven layers with two lithologies shale (Sh) and sand-shale mixture (Sst/Sh) arranged as shown in the enlargement.

5.4 Model geometry

The reservoir model consists of a sequence of seven layers situated directly above the reference horizon, see the right-hand side of Figure 5.14. This sequence is a subset from a larger sequence originally used for SI; the subset complies to the application regime of 1D convolutional RBSI. The total thickness of the subset is about 100 m, with layer-lithologies alternating between shale and sand-shale mixture.

In Figure 5.14, the bounds of the inversion interval are indicated in black lines on the nearstack migrated image; away from Well-I towards the left, the layer-dip is increasing to a maximum of 31 degrees. The inversion interval was chosen to extend laterally from the steepest part at 13800 m horizontal distance until 15100 m, situated on the horizontal part. See also Figures 5.18 and 5.24.

To describe the relation between the rock properties of the shaly sandstone reservoir rocks used in the model and typically encountered in the Gulf of Mexico region, and the elastic properties ρ , v_p and v_s , the shale and laminated sandstone-shale rock models are used that takes advantage of property trends derived from well logs. These models are described in section 4.3.2.

The reservoir rock-parameters that will be inverted for with both SI and 1D convolutional RBSI are the P-wave velocities $v_{p, \text{Sst}}$ and $v_{p, \text{Sh}}$, vertical thickness h , and sand-fraction SF . Only Gaussian distributions of these parameters are considered; the Gaussian distribution is uniquely described by the mean value μ and standard deviation σ , see section 2.1.

5.5 Applying SI

In the first part of the comparative test, SI is used to invert the nearstack migrated image for the unknown reservoir layer-parameters ($v_{p, \text{Sst}}$, $v_{p, \text{Sh}}$, h and SF). First, a wavelet for inversion is derived from the migrated data in the target zone, using a seismic-to-well match. Subsequently, a prior model for the reservoir-layer parameters is built. Finally, the migrated data are inverted for the unknown reservoir parameters.

■ 5.5.1 Wavelet derivation

A seismic-to-well match is done to derive the wavelet for SI from the migrated data, using the detailed log-information present at Well-I, the first-drilled well vertically penetrating the horizontal part of the target. The upper panel of Figure 5.15 shows the migrated data around this vertical well and the derived wavelet.

In the inversion process for the wavelet, a synthetic trace is built within the target interval using the impedance log of the well and a first estimate for the wavelet. Updating the wavelet until the mismatch between the synthetic trace and the corresponding portion of the migrated trace at the well position is minimised, yields the desired wavelet. Figure 5.16 shows the goodness-of-fit of the final synthetic trace and the traces from the migrated data around the well, in the inline and crossline direction. Note that the sailline along which the inversion will be done (displayed in Figure 5.15) is at approximately +100m crossline distance from Well-I.

The shape of the derived wavelet is plausible when comparing with the wavelet seen at the water-bottom (Figure 5.17), assuming that the water-bottom acts as a strong isolated reflector which thus shows the undistorted wavelet, and assuming that the wavelet shape does not change much while the wave is propagating through the subsurface.

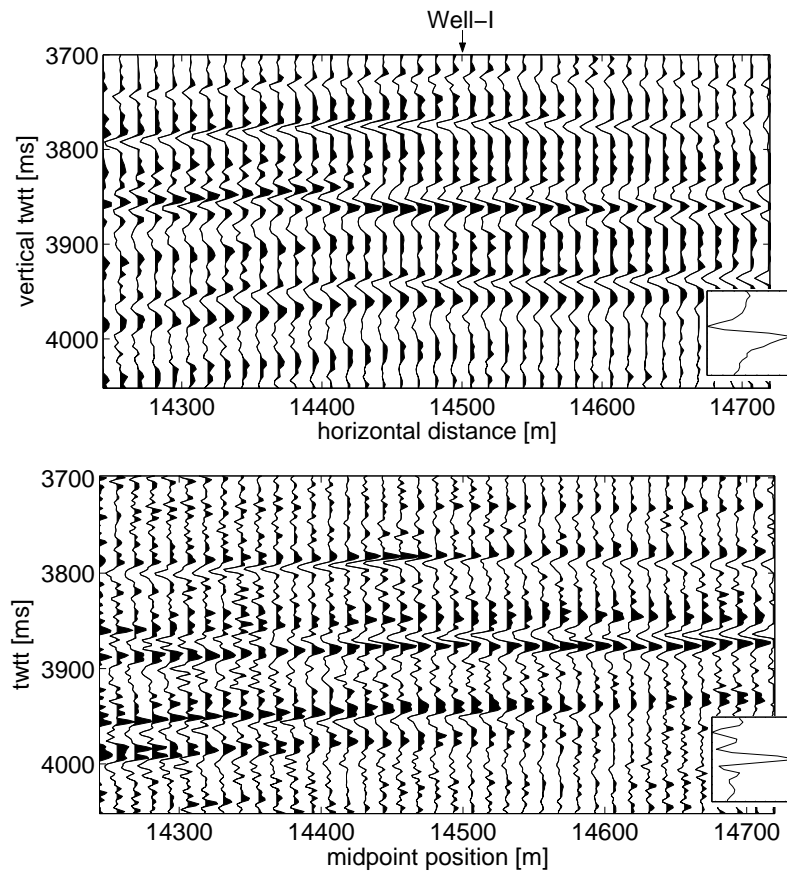


Figure 5.15: Good data quality on target level around Well-I, on the migrated substack (above) and on the 575 m common-offset gather, containing more high-frequency information. Insets show derived wavelets. Notice the 90° phase rotation applied to the migrated data, as indicated in Figure 5.4.

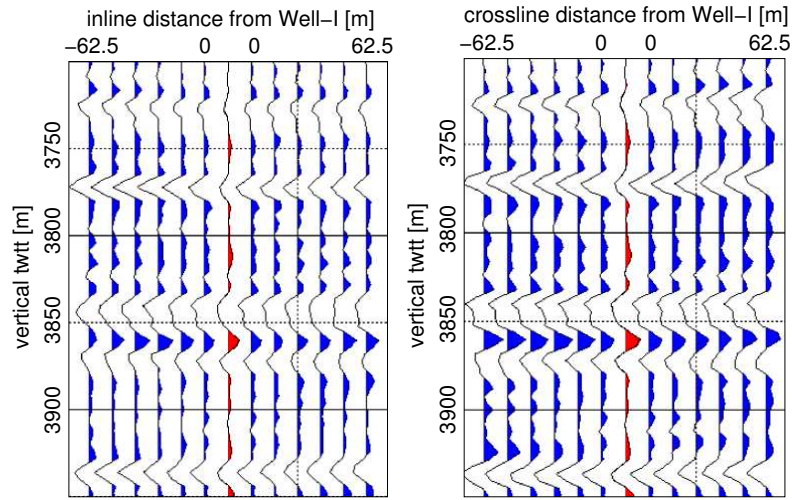


Figure 5.16: Goodness-of-fit between traces from the migration image near Well-I and a synthetic trace (middle) generated using the normal-incidence reflection information at the well and the derived wavelet; in the inline (left) and crossline direction.

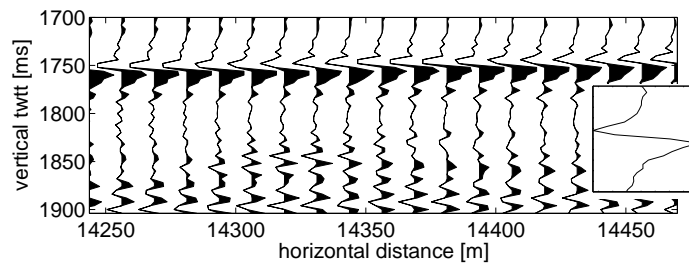


Figure 5.17: Wavelet seen on the migration image at the sea-bottom resembles derived wavelet (inset).

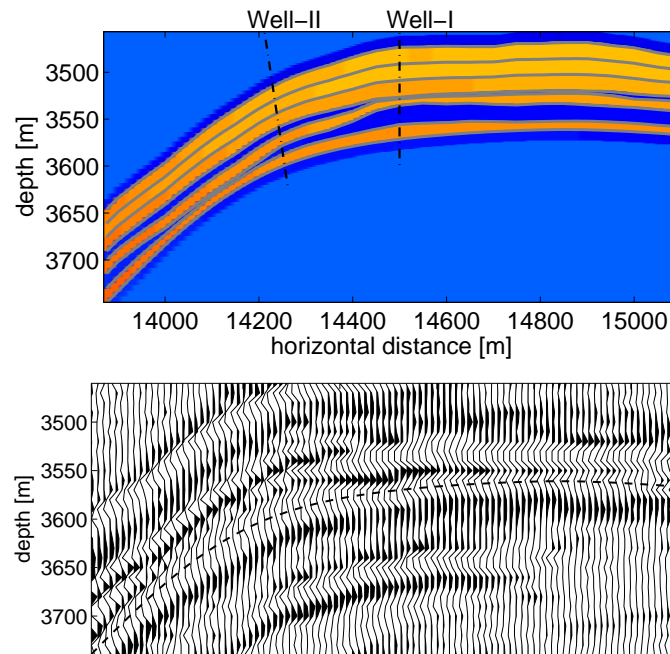


Figure 5.18: Prior interface positions and v_p -distribution (in colour, for legend see Figure 5.19 [middle-left]) of the inversion target (top), with the corresponding portion of the nearstack migrated image. Dashed line denotes reference reflector; $2\times$ vertical exaggeration.

■ 5.5.2 Prior model

The prior mean values (μ) and standard deviations (σ) for the layer-parameters vertical thickness (h), P-wave velocity (v_p) and sand-fraction (SF) are displayed in Figure 5.19 after flattening along the reference reflector (the mean values of v_p are shown before flattening as well in Figure 5.18). Although the mean vertical thicknesses can in principle be inferred from the interface positions, in the top panels of Figure 5.19 the vertical thickness is shown as a layer property, in order to make it easier to spot changes and to enable display of the thickness standard deviations. A prior model for v_p is used which has little variation in the lateral direction, whereas more lateral

variations occur in h . The prior sand-fraction is taken laterally constant.

■ 5.5.3 Inversion results

Posterior v_p , h and SF obtained from SI, inverting the migrated ‘near’ sub-stack containing offsets from 450-2325 m, are depicted in Figure 5.20. The seemingly rapid lateral changes in layer-thickness are due to the chosen way of plotting with much vertical exaggeration. The posterior standard deviations are smaller than the prior standard deviations in most places, indicating a inversion convergence.

Notice that before plotting, a five-point moving average was applied on the results obtained for the separate traces, so that with a trace spacing of 12.5 m on the migration image, lateral variations smaller than 62.5 m are smoothed away; a distance not chosen too large, since the lateral resolution on the migration image, at target level is $\Delta r \approx \lambda_d z / L \approx 210$ m (Eq. 2.57), with dominant wavelength $\lambda_d = v_p / f_d = 2500$ m/s / 35 Hz ≈ 70 m, depth of observation $z = 3500$ m and half-aperture $L = 2325/2$ m.

5.6 Applying 1D convolutional RBSI

In the second part of the comparative test, 1D convolutional RBSI is used to invert the pre-stack near-offset section for the unknown reservoir layer-parameters (v_p , v_{st} , v_p , v_{sh} , h and SF). First, the data from the 575 m common-offset gather containing the reflection information from the inversion target is selected by means of ray-tracing. Then, a wavelet for inversion is derived from the offset gather in the target zone, using a seismic-to-well match. Subsequently, the prior model for SI is transformed in such a way that 1D convolutional RBSI can make use of it. After that, an overburden amplitude correction is applied to the traces from the offset gather. Finally, the offset gather is inverted for the unknown reservoir parameters, and the results are transformed back to the SI-grid to make comparison feasible.

■ 5.6.1 Pre-stack seismic data selection

After the processing step of binning, each source-receiver pair in the pre-stack unmigrated data is assigned to a specific Bin. In order to select from

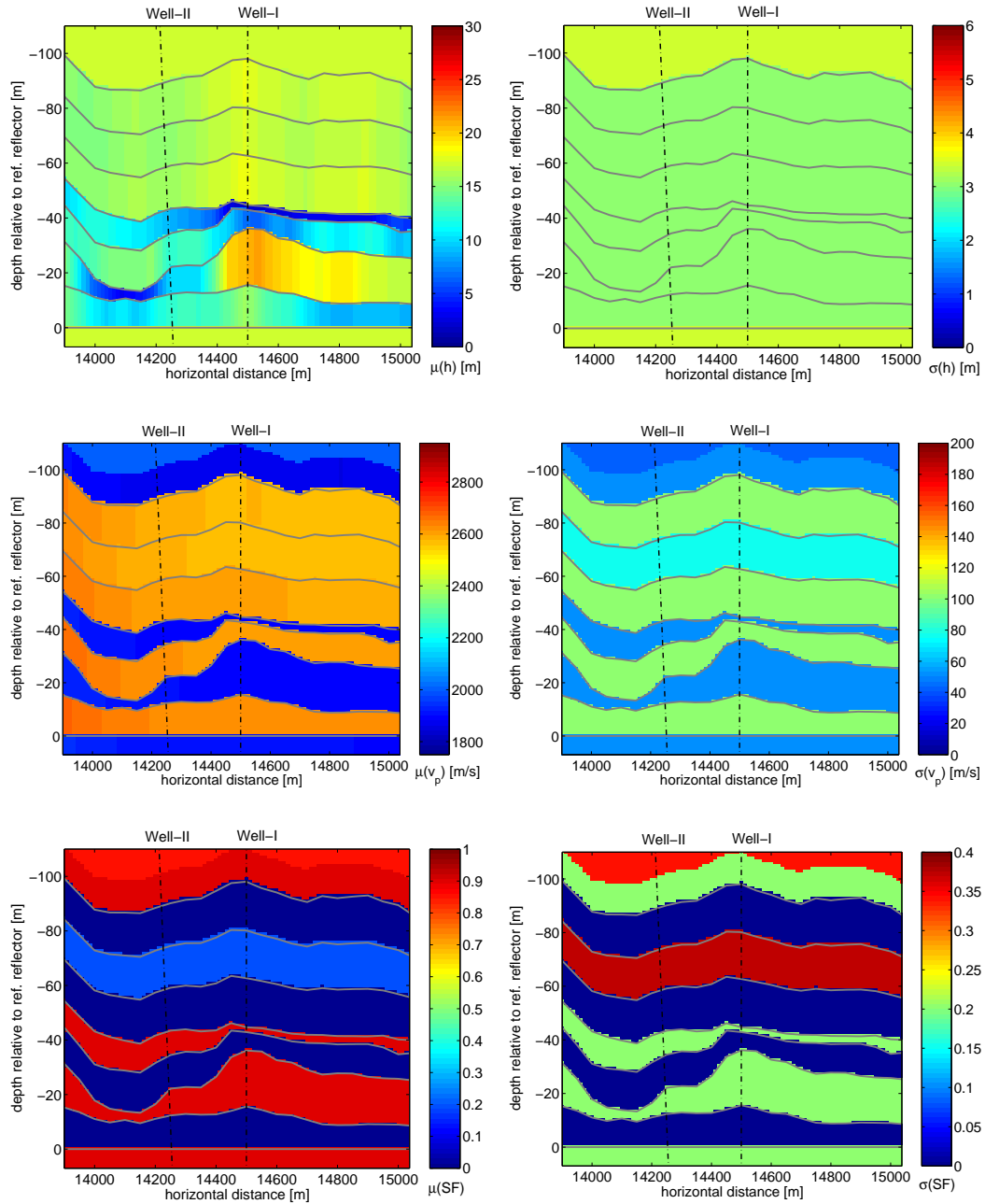


Figure 5.19: Overview of prior model for h (top), v_p (middle) and SF (bottom). The means (left) and standard deviations are displayed. For a clearer display, flattening is done along the reference reflector and the vertical scale is exaggerated.

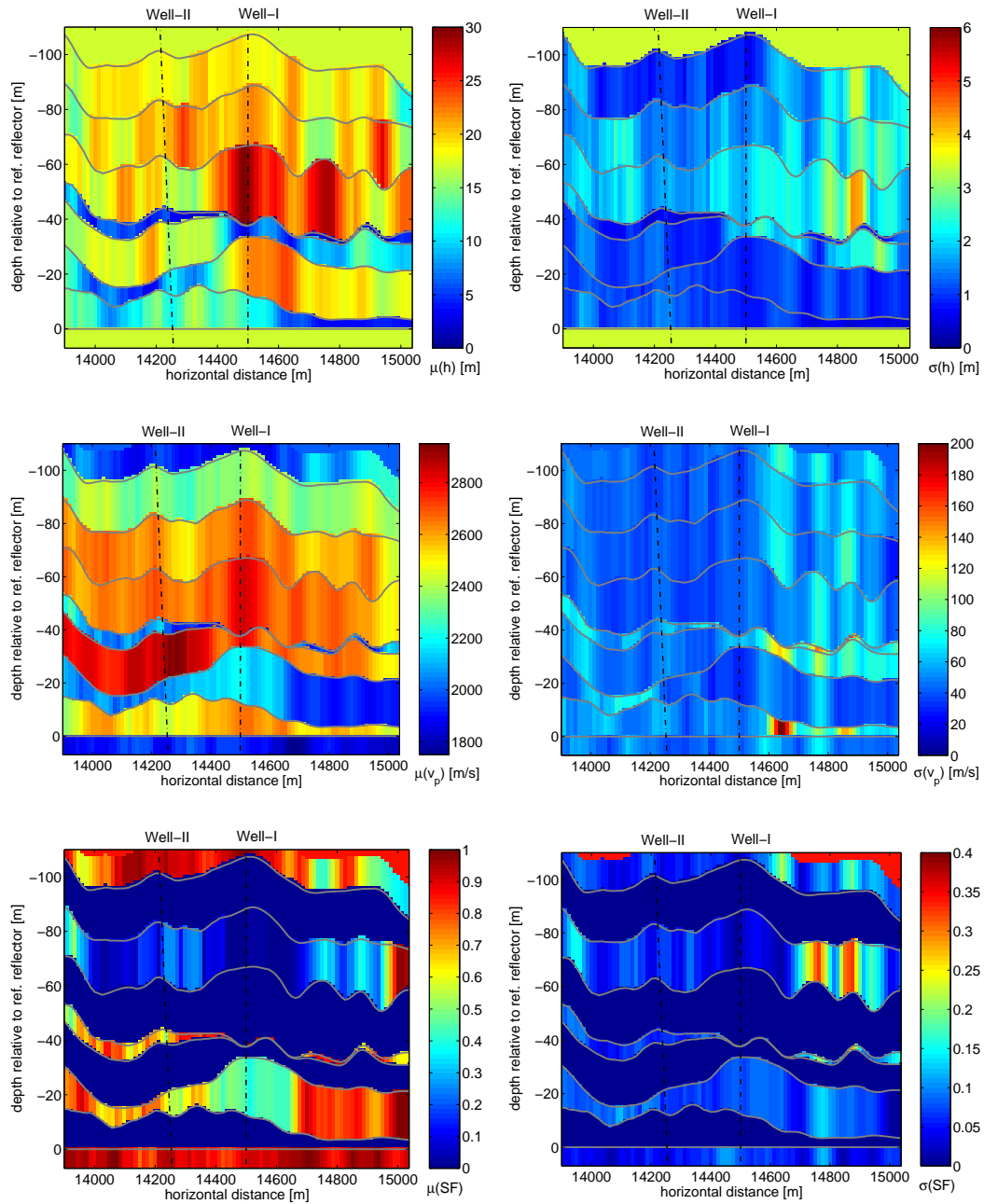


Figure 5.20: Overview of SI posterior estimates for h (top), v_p (middle) and SF (bottom). On the left-hand side, means are shown, on the right-hand side, the corresponding standard deviations.

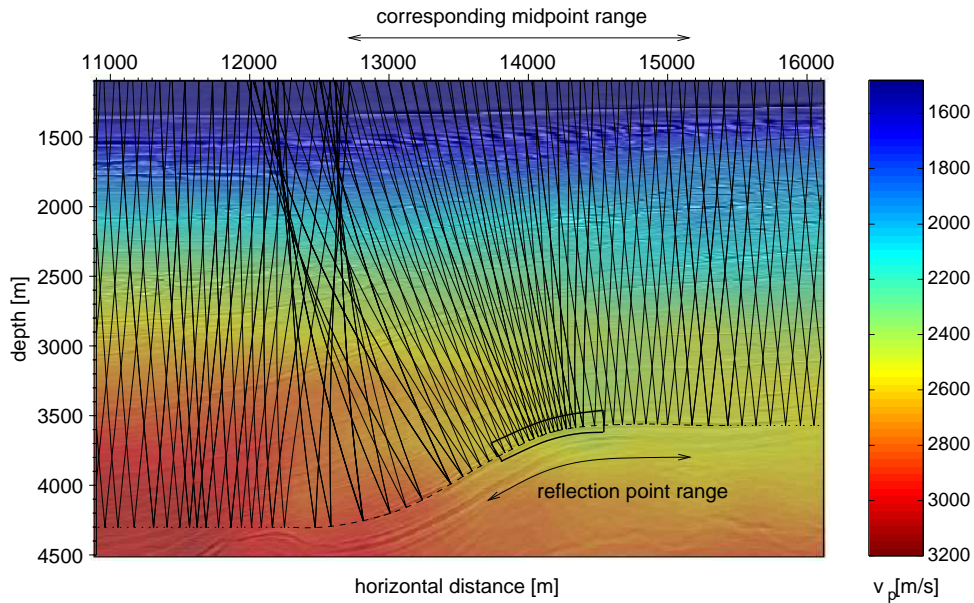


Figure 5.21: Elastodynamic ray-tracing in the migration P-wave velocity model to the reference reflector (dashed; dotted parts outside the area of interest have only a computational use). The migration image shown is in the background, the water-bottom is around 1300 m.

the pre-stack unmigrated data, in this case the 575 m common-offset gather, those Bins that contain reflection information on the specified inversion target, ray-tracing is done in the migration P-wave velocity model for PreSDM to the reference reflector. In this way, reflection point locations on the reference horizon are connected to surface Bins. During the process, also the two-way traveltimes to the reference reflector are calculated; these are required for tying the inversion window to the traces.

The ray-tracing is performed in a 2.5D setting, with the source-receiver pairs on sailline 2313 and no variation in the crossline migration P-wave velocity model and reference reflector surface. The source-receiver distance is 575 m. For convenience, the Bins on this single line will be referred to as common-midpoint positions (CMPs); CMP-separation was 6.25 m to mimic the acquisition configuration of the real data. Ray-tracing was performed for

CMP-positions from 10000 m to 18000 m in the sailline direction.

Figure 5.21 shows every 10-th ray traced through the migration velocity model to the reference reflector. The angles of incidence seen on this figure amount up to $\theta = 6^\circ$, considered close enough to $\theta = 0^\circ$ assumed by 1D convolutional RBSI in the target. The reference reflector is a mildly smoothed version from the original non- C_2 -smooth hand-picked interface between shale layer #1 and the underburden, which still fits the true reflector quite well as can be seen from the nearstack migration image in the background. Also, the migration velocity model was smoothed in a trade-off between kinematic accuracy and dynamic stability, see section 5.6.4.

Notice from the same figure that the P-wave velocity distribution is not conform to the subsurface structure. One possible explanation is that gravitational pull on the dipping layers causes a stress build-up in the down-dip direction, resulting in higher P-wave velocities in the lower-left of the image (assuming no lateral change in layer-lithology).

Figure 5.22 also shows that a range of source-receiver pairs exists which has more than one reflection point on the reference reflector: this limits the reservoir-range that can be inverted well by the new method to the part on the right-hand side of the steepest dip, because in the inversion window, a trace is assumed to contain only a single response from the same reflector. The assumed single-valuedness of pre-stack reflection events is not a fundamental limitation of RBSI. However, this assumption is made here for practical convenience. The chosen reflection point range is indicated with an arrow along the reference reflector. The corresponding midpoint-range is 12700-15100 m, which includes the vertical well at 14500 m. On the trace recorded at midpoint 12700 m, two arrivals from the reference reflector are separated at time-differences smaller than the length of the inversion window (100 ms). Finally, the box indicates a part of the reservoir of which enlargements are shown in Figure 5.24.

Figure 5.22 shows the seismic data for SI (top) and 1D convolutional RBSI in the chosen inversion range, flattened along the reference reflector. The offset data are plotted as a function of the reflection point position on the reference reflector to facilitate comparison with the migrated data for SI. Notice the trace density on the convex part of the slope for the offset data, the seemingly absent wavelet stretch on these close-to-zero-offset data, but also the lower signal-to-noise ratio because of the single fold.

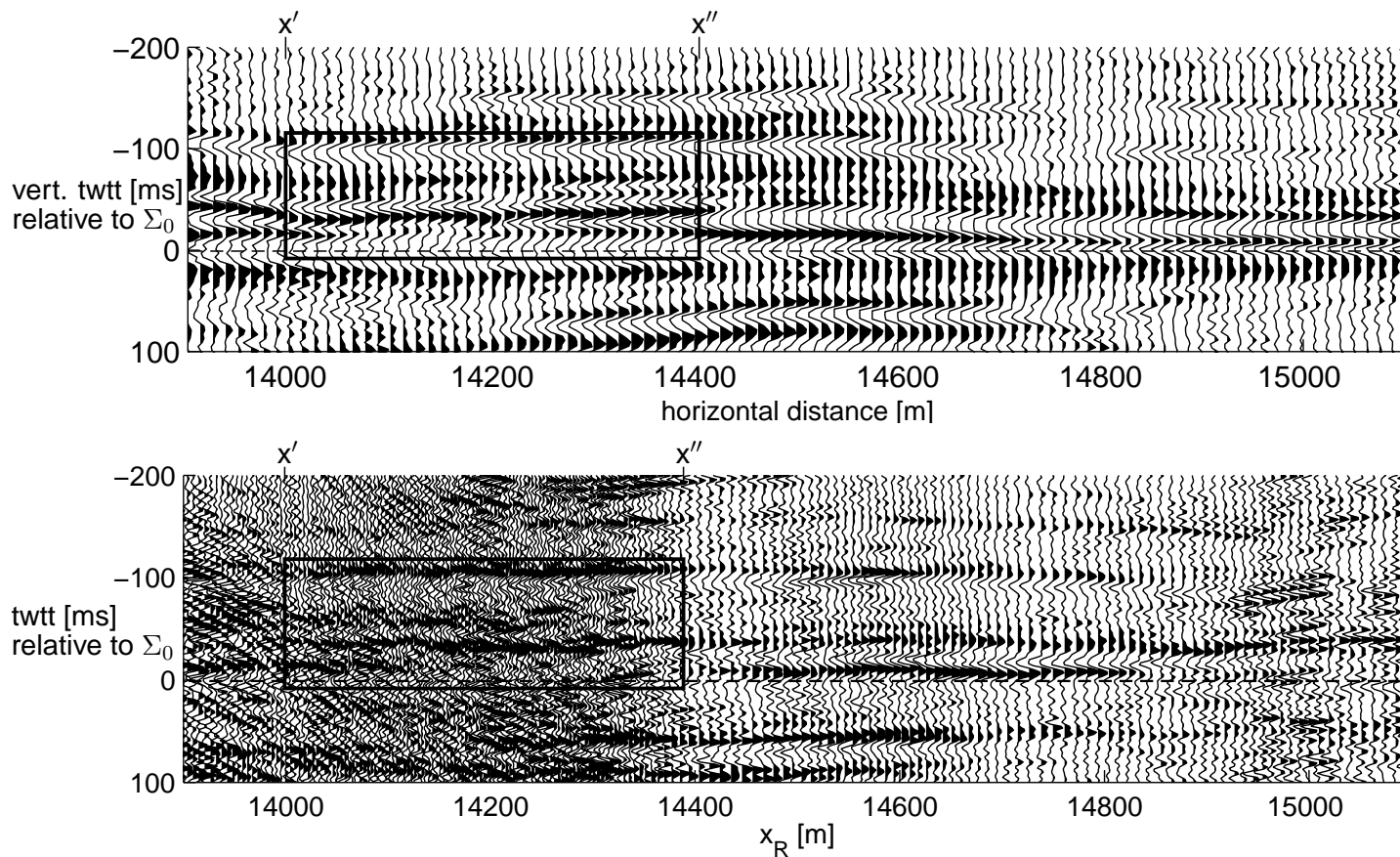


Figure 5.22: The inversion interval, between approximately -100 ms and 0 ms, displayed on seismic data flattened along the reference reflector Σ_0 at 0 ms, for SI (top, nearstack migrated) and 1D convolutional RBSI (bottom, 575 m common-offset gather, every 2nd trace plotted). Note that in the latter case, the traces are plotted as a function of x_R , irregularly distributed on Σ_0 ; see Figure 5.24. Boxes and coordinates x' and x'' correspond to those in Figure 5.24.

■ 5.6.2 Wavelet derivation

The seismic-to-well tie is repeated for the pre-stack unmigrated data, since it is expected that the derived wavelet will be much different because of the wavelet shaping applied to the migrated data. The lower panel of Figure 5.15 shows the area around the vertical well on the 575 m common-offset gather, and the wavelet derived for 1D convolutional RBSI. The trace from the offset gather that corresponds to the location of Well-I is found using the ray-tracing exercise discussed in the previous section; its midpoint position corresponds to the ray-pair which has the reflection point on the reference reflector at the position of Well-I. Before wavelet extraction, the rudimentary correction for spherical spreading loss applied to the data earlier on in the processing workflow for TA PreSDM (Figure 5.4) is removed from the data, by dividing the traces by (instead of multiplying them with) the same laterally constant traveltimes-dependent gain function.

The derived wavelet is shown again in the upper right of Figure 5.23. Note that also in the wavelet derivation for 1D convolutional RBSI, 1D convolution is applied in the forward modelling step. Consequently, the spherical spreading and transmission losses in the reservoir zone have been neglected, as well as the small extra traveltimes in the target due to having small offset data while assuming zero offset, and the slightly different reflection coefficients for small non-zero angles of incidence at the reflector. In a more general case of RBSI, a 3D elastodynamic ray-tracer would be used in the wavelet derivation, properly taking into account the above-mentioned effects.

The left-hand side of Figure 5.23 shows the goodness-of-fit of the final synthetic trace and the traces from the 575 m common-offset gather around the well. Contrary to the SI-case, where also crossline data were used in the wavelet derivation, the wavelet for 1D convolutional RBSI was derived exclusively using seismic data in the inline direction: pre-stack unmigrated data were only available on the selected sailline.

The shape of the derived wavelet is plausible when comparing with the wavelet seen at the water-bottom (Figure 5.23, bottom), again assuming that the water-bottom acts as a strong isolated reflector which thus shows the undistorted wavelet, and that the wavelet shape does not change much while the P-wave is propagating through the subsurface.

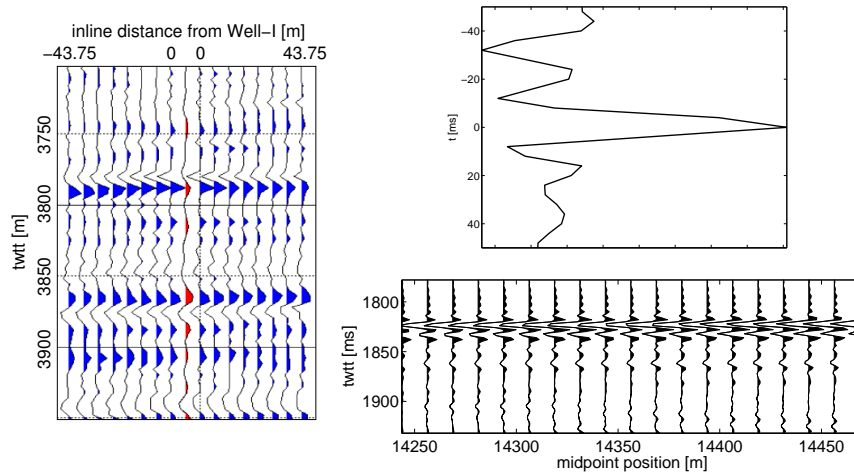


Figure 5.23: Counterclockwise from upper-right: derived wavelet for 1D convolutional RBSI; goodness-of-fit between traces from the offset gather around Well-I and synthetic trace (middle) generated using the reflectivity information at the well and the derived wavelet; wavelet seen at the sea-bottom resembles derived wavelet.

■ 5.6.3 Transforming the SI prior model

For a fair comparison with the SI-method, in 1D convolutional RBSI the same prior information should be used as was available to SI. However, for RBSI the layer properties and thicknesses need to be specified along the ray-path, which generally does not correspond with the vertical direction along which SI is operating: Figure 5.24 shows the situation for a portion of the current reservoir model, marked with a box on Figure 5.21.

To get things right for the RBSI prior model, a dip-dependent conversion of the SI prior model must be done; this conversion assumes that the target satisfies the application regime of 1D convolutional RBSI, mentioned in Table 3.2. As a consequence of the plane-parallel layering assumption, normal-incidence raypaths to the reference reflector are assumed to be going straight all the way through the inversion target. The SI layer-properties are evaluated along these NI-rays, starting from the reflection points on the reference reflector.

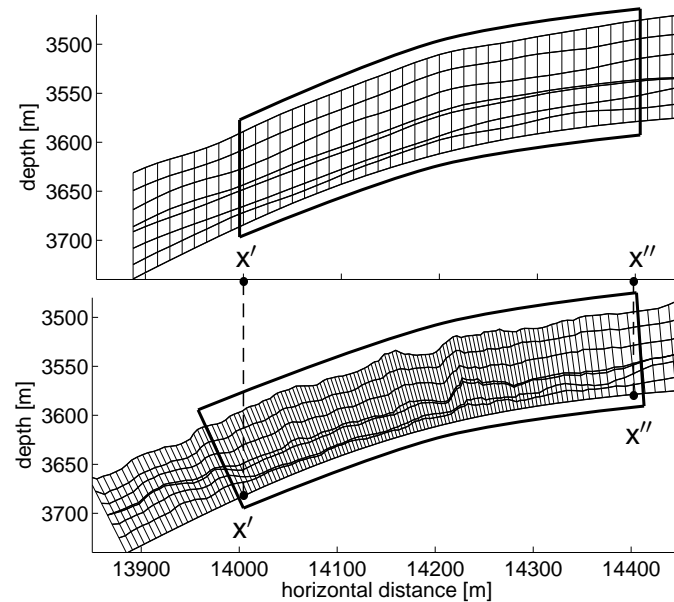


Figure 5.24: Difference in evaluation directions for SI (top) and 1D convolutional RBSI; plotted with the posterior layer positions from each method. Traces from the boxed areas bounded by x' and x'' are displayed in Figure 5.22.

Required data

For the conversion of the prior SI model, the following data are needed: the position and local dip β of the reference reflector, and the reflection point positions on the reference reflector; the corresponding two-way traveltimes are used to tie the inversion window to the unmigrated data.

For the current dataset, the reference reflector is chosen to be the lower bound of the inversion interval, clearly visible on the migrated and pre-stack unmigrated data (Figure 5.9). The reflector was accurately picked from the migrated data, and a mild smoothing was applied to obtain C_2 -smoothness. With the position of the reflector known, dips and normal vectors can be calculated easily.

The reflection point positions on the reference reflector and the corresponding two-way traveltimes have already been calculated by ray-tracing for pre-

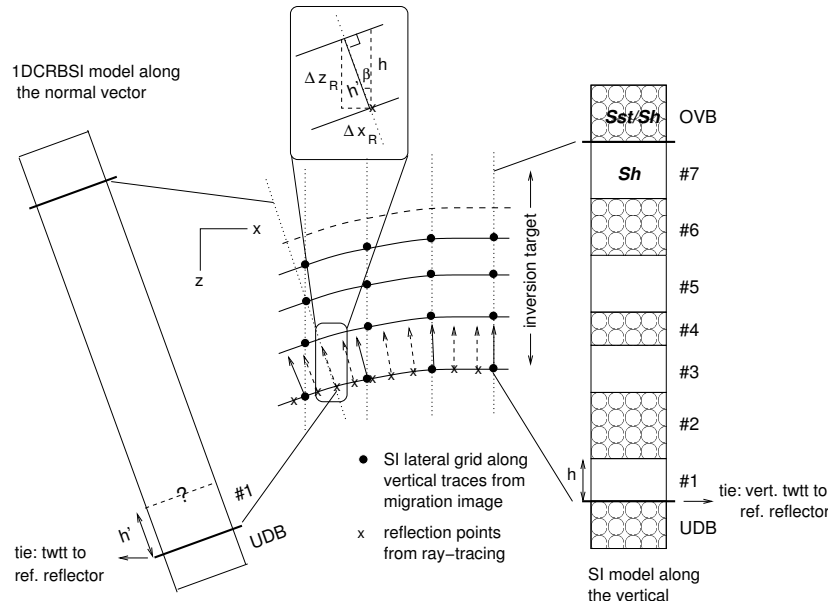


Figure 5.25: Building the model for 1D convolutional RBSI from the SI model. Dip is indicated with β , vertical layer-thickness (for SI) with h , true thickness is h' .

stack data selection in the previous section.

Building the model for 1D convolutional RBSI

Building the prior model for 1D convolutional RBSI starts at the reflection points on the reference reflector (Figure 5.25). The properties for the lowest layer (#1) in the inversion target, available in the sailline direction on a regular SI-grid of 12.5 m (indicated with dots in the figure), are linearly interpolated to the (irregularly distributed) reflection point positions on the reference reflector, indicated with crosses. This yields the rock properties for the lowest layer in the RBSI model, including the interpolated vertical layer thickness h , whereas true thickness h' is needed as indicated in the figure. Assuming plane-parallel layering, from the reflection points on the lowest layer, straight normal-incidence raypaths are calculated to the overlying layer-interfaces in the target. The length of such a raypath (h') is calculated

from the interpolated vertical thickness h and reflector dip β using the simple goniometric relation (inset of Figure 5.25),

$$h' = h \cos \beta, \quad (5.1)$$

that was introduced in Eq. 3.25. With h' , the set of parameters for the lowest layer in the model for 1D convolutional RBSI is complete: we may advance to the next layer, starting from the intersection points of NI-rays and the top interface of the current layer (for convenience, in the following these intersection points are also referred to as ‘reflection points’ on top of the layer).

The distances Δx_R and Δz_R needed to go from the reflection point at the reference interface to the reflection point at the overlying interface (inset of Figure 5.25), are given by,

$$\Delta x_R = h' \sin \beta, \quad (5.2)$$

$$\Delta z_R = h' \cos \beta. \quad (5.3)$$

At each intersection point of the NI-rays with overlying layers found in this way, the layer-properties of the next layer from the SI model are evaluated and interpolated using the procedure just described for the starting interface (the reference reflector). In calculating h' from h for the next layer, the dip at the intersection points is taken to be equal to the dip of the reference reflector at the same lateral position. Again the rays are constructed to the next interface, and the total procedure is repeated until the top interface of the inversion interval is reached, which completes the model for 1D convolutional RBSI.

Now that the traces from the unmigrated data containing reflection information from the target have been selected, and a 1D convolutional model for each trace has been built, only an overburden amplitude correction for each trace still needs to be applied before the 1D convolutional RBSI can start.

■ 5.6.4 Overburden amplitude correction

Apart from associating the reflection points on the reference horizon with the surface source/receiver midpoint positions, the elastodynamic ray-tracing through the migration velocity model to the reference horizon also yields the

laterally varying overburden losses needed for pre-processing the pre-stack unmigrated data in 1D convolutional RBSI.

To determine these overburden losses, first the primary P-wave reflection response of the reference reflector is computed using elastodynamic ray-tracing. As mentioned in section 5.6.1, the subsurface model for ray-tracing is generated by taking the model for PreSDM at the sailline and copying this model in the crossline direction to obtain a 2.5D setting; ray-tracing is performed along the sailline from isotropic point sources to receivers both placed at zero depth (the reference-level after source/receiver static corrections), with an offset of 575 m between source and receiver, and 6.25 m midpoint increment.

Subsurface model details relevant to amplitude

To clarify the amplitude calculation, a bit more detail on the subsurface model is needed: the subsurface model consists of three volumes with the water-bottom and reference reflector as separators. The main part consists of the migration velocity model defined on a 100×100 m grid. Above the water-bottom, a (nearly-) homogeneous water-column (with a slight depth gradient in P-wave velocity v_p) is situated. Below the reference reflector, a homogeneous halfspace with constant v_p is placed.

For computational convenience, throughout the model, density is constant at 2200 kg/m^3 , and S-wave velocity is specified as $v_s = \frac{1}{2}v_p$. Concerning the densities, taking a density of (slightly more than) 1000 kg/m^3 would have been more obvious for the seawater. However, since we are only interested in the lateral amplitude changes *relative* to the amplitude at the well where the seismic-to-well-tie is done, another convenient constant value will do. For the rest of the subsurface, insufficient density information is available to justify an inhomogeneous gridded density model.

Concerning the S-wave velocities, specifying an S-wave velocity for water means that the software interprets it as an elastic medium rather than an acoustic one. In this particular case, this only matters for transmission at the sea-bottom: there, a small amplitude error will arise due to P-S conversion on the water side, which in reality does not occur. However, a closer look at the computed Zoeppritz unconverted P-wave coefficients for transmission through the sea-bottom learns that the effect will be negligible: for the angles

of incidence at the sea-bottom ($\theta = 8^\circ - 15^\circ$), only a 0.2% variation in the transmission coefficient occurs. So in approximation the error made is laterally constant and does not influence the relative amplitude behaviour.

For unconverted primary P-waves, the S-wave velocity has no other effects on the calculated overburden amplitudes (i.e. disregarding the reflection coefficient): in the transport equations for P-waves, v_s does not appear, see Eq. (1.5). Hence the fact that, for example, taking a value of $v_p/v_s = 1.7$ instead of $v_p/v_s = 2$ would have been more physically plausible for the sandstones in the target [Mavko, 1998], is not a problem.

At the sea-surface, in reality the interface conversion coefficient C_0 at the receiver is constant and independent of the angle of incidence, hence of no importance to the preservation of the relative amplitude behaviour. Therefore, the free surface is omitted in the model for ray-tracing. To simulate the original hydrophone measurements, the calculated displacement amplitudes are not decomposed along the horizontal and vertical direction: the total displacement vector corresponds to pressures (measured by hydrophones) via the equation $-\nabla P = \rho(\partial^2 \vec{u}/\partial t^2)$ [Červený, 2001, Eqs. (2.1.4) and (2.1.15)], with P the pressure, ρ the density and \vec{u} the displacement vector.

The medium under the reference reflector is chosen as a homogeneous half-space with known elastic properties. With the medium properties above the reflector also specified by the model, the Zoeppritz unconverted P-wave reflection coefficient $R(\theta)$ at the reference reflector (with $\theta \approx 6^\circ$) is exactly known and can be divided out, leaving the desired overburden amplitude effects C_B/\mathcal{L}_B in the calculated amplitudes, see section 3.6.

Smoothing the velocity model

To obtain usable amplitudes, the original gridded migration velocity model (between the two interfaces at the waterbottom and target) needed to be somewhat smoothed[†], in a trade-off between kinematic accuracy and dynamic stability of the ray-tracing. Figure 5.26 illustrates this statement by showing ray-paths to the reference reflector and associated reflection amplitudes found by ray-tracing through the original migration P-wave ve-

[†]The approach of smoothing the velocity model and/or the computed ray-amplitudes to compensate for the sensitivity of ray-amplitudes to minor details in the model is proposed in Červený [2001, Chapter 5].

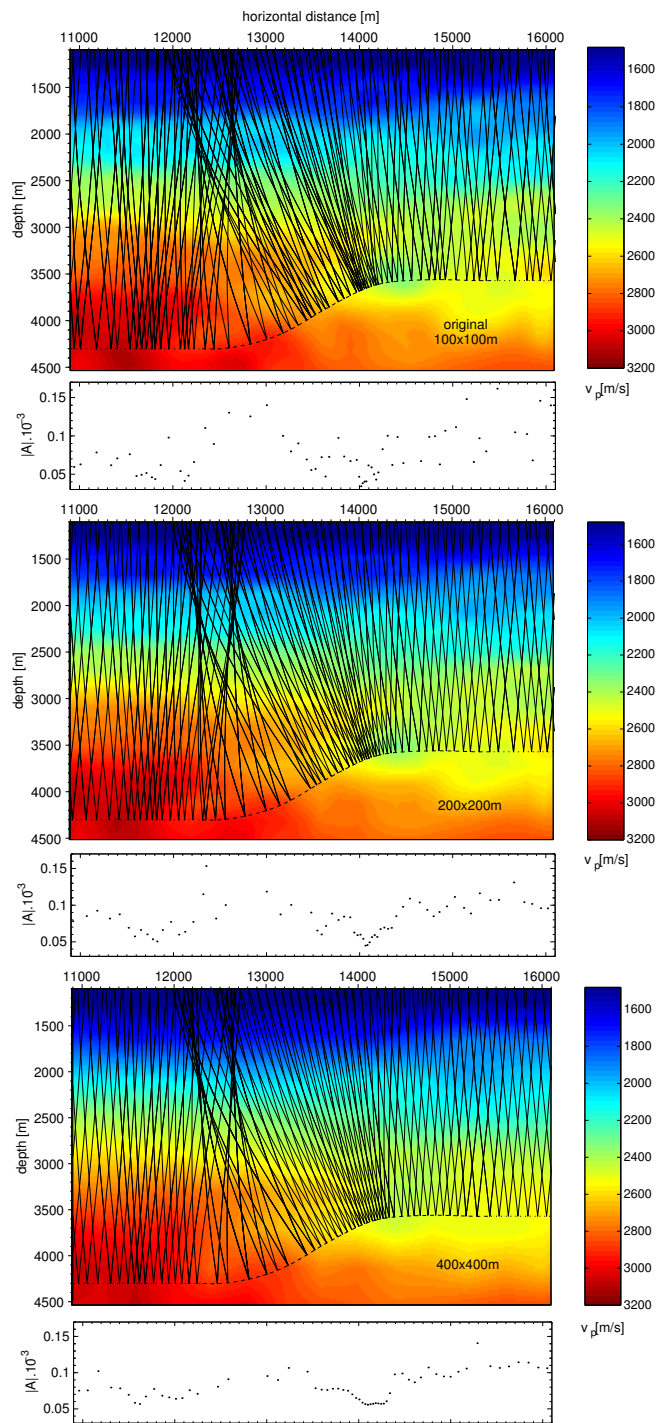


Figure 5.26: Reflection amplitudes for smoothed v_p -models. See text for details.

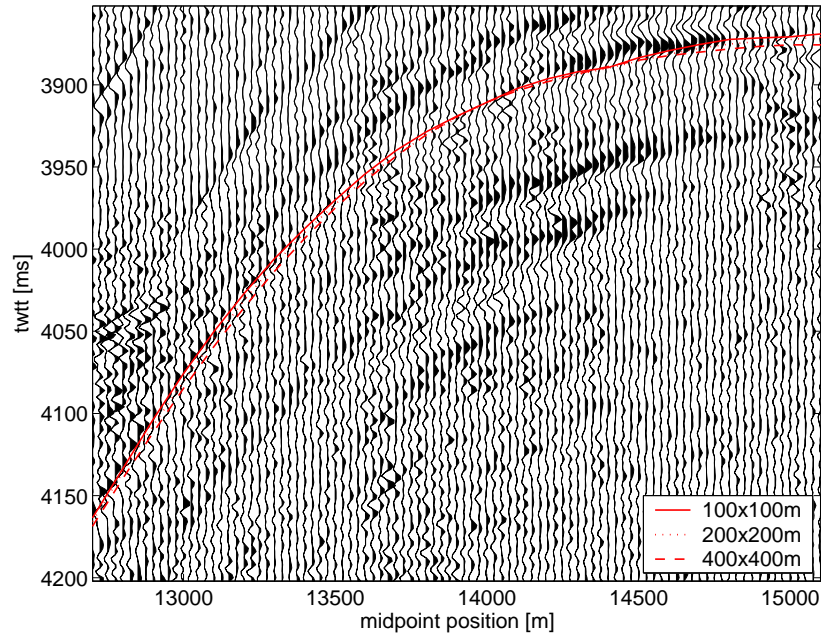


Figure 5.27: Effect of smoothing the migration velocity model on the traveltimes to the reference reflector calculated by ray-tracing. Background shows data from the 575 m offset gather; traveltimes calculated in the original model (100×100 m) are presumed to have the best fit to the data.

locity model (top) and two smoothed versions. The smoothing of the velocity model is done by resampling using linear interpolation the original 100×100 m grid to a larger grid indicated in the picture, and afterwards sampling it back again to the original 100×100 m.

From Figure 5.26 it can be seen that the amplitude behaviour is fairly chaotic for the original model (although it can already be noticed that reflection amplitudes are higher for the shallower part of the structure due to spherical spreading losses being lower), whereas in that case the traveltimes observed from the data are most accurately reproduced (Figure 5.27). Smoothing the velocity model stabilises the amplitude behaviour, but decreases the goodness of fit with the traveltimes from the data.

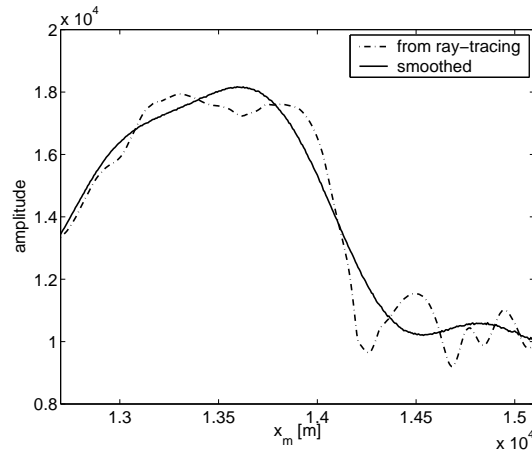


Figure 5.28: Overburden amplitude correction. After smoothing, the corrections are applied to the traces from the offset gather.

Final amplitude correction

The final amplitude correction \mathcal{L}_B/C_B is indicated with the solid line in Figure 5.28. The figure confirms the intuition that reflections from deeper interfaces need to be amplified more because the waves have experienced more spherical spreading loss on their way from source via reflector to receiver. Lateral amplitude variations faster than the lateral resolution on the migration image (which is about 210 m in the selected reservoir-range, using Eq. 2.57), that are still present after ray-tracing through the 400×400 m smoothed model (dash-dotted line), are smoothed away using an 8-th degree polynomial fit.

Note that the amplitude correction depicted in Figure 5.28 was normalised with respect to the value of this correction at Well-I before applying it to the data, to avoid having to redo the wavelet derivation for inversion (which was done on the offset gather after undoing the rudimentary correction for spherical spreading loss).

Finally notice that, differently from the theory discussed in section 3.6, the reference horizon is chosen to be the bottom reflector of the inversion target, so that the term \mathcal{L}_B also contains a small term due to ray-traversal through

the coarse migration velocity model in the target. Hence, if the overburden correction \mathcal{L}_B/C_B is applied to the traces, the reflection amplitudes for the target interfaces above the reference interface are slightly too high for the 1D convolutional kernel (while they are slightly too low below the reference interface for the example of section 3.6). This effect may be neglected as long as the target satisfies the application regime for 1D convolutional RBSI.

■ 5.6.5 Inversion results

The layering obtained from 1D convolutional RBSI, inverting the near offset gather, was already shown in Figure 5.24. Notice again the different evaluation direction along the normals to the reference reflector, which should improve capability of resolving reservoir-layers on the slope: as shown in synthetic data tests of Chapter 4, SI is hampered by dip-dependent migration-induced wavelet stretch.

After resampling to the grid used by SI (upper part of Figure 5.24), using the ‘inverse’ of the procedure described in section 5.6.3, and after applying a five-point moving average filter, the h , v_p and SF -estimates are shown in Figure 5.29. As was done in smoothing the overburden amplitudes, in choosing the width of the moving-average filter, care was taken not to smooth more than the lateral resolution on the migration image.

At the end of this chapter, a full comparison of inversion results of SI and 1D convolutional RBSI is given in Figures 5.31-5.33. The estimated thickness of the total package does not vary so much laterally (i.e. with increasing reflector dips) than was the case for SI. Notice the decreased total package thickness as compared to SI, a result expected for the dipping part of the reservoir. The anomalous depressions with a peak in between, in the right-most part of the reservoir above 14800 m, correspond to a portion of the seismic data with low reflection amplitude and a portion with strong remains of water-bottom multiples (Figure 5.13); inversion results in that part should not be trusted too much, as indicated by the very high standard deviations $\sigma(h)$ and $\sigma(v_p)$ for the depressions. Also the estimates for SI have a somewhat larger uncertainty in the same area.

In doing all these observations, it should be realised though, that the only place where a quantitative judgement of the inversion results can be made, is at the well location: this is the subject of the next section.

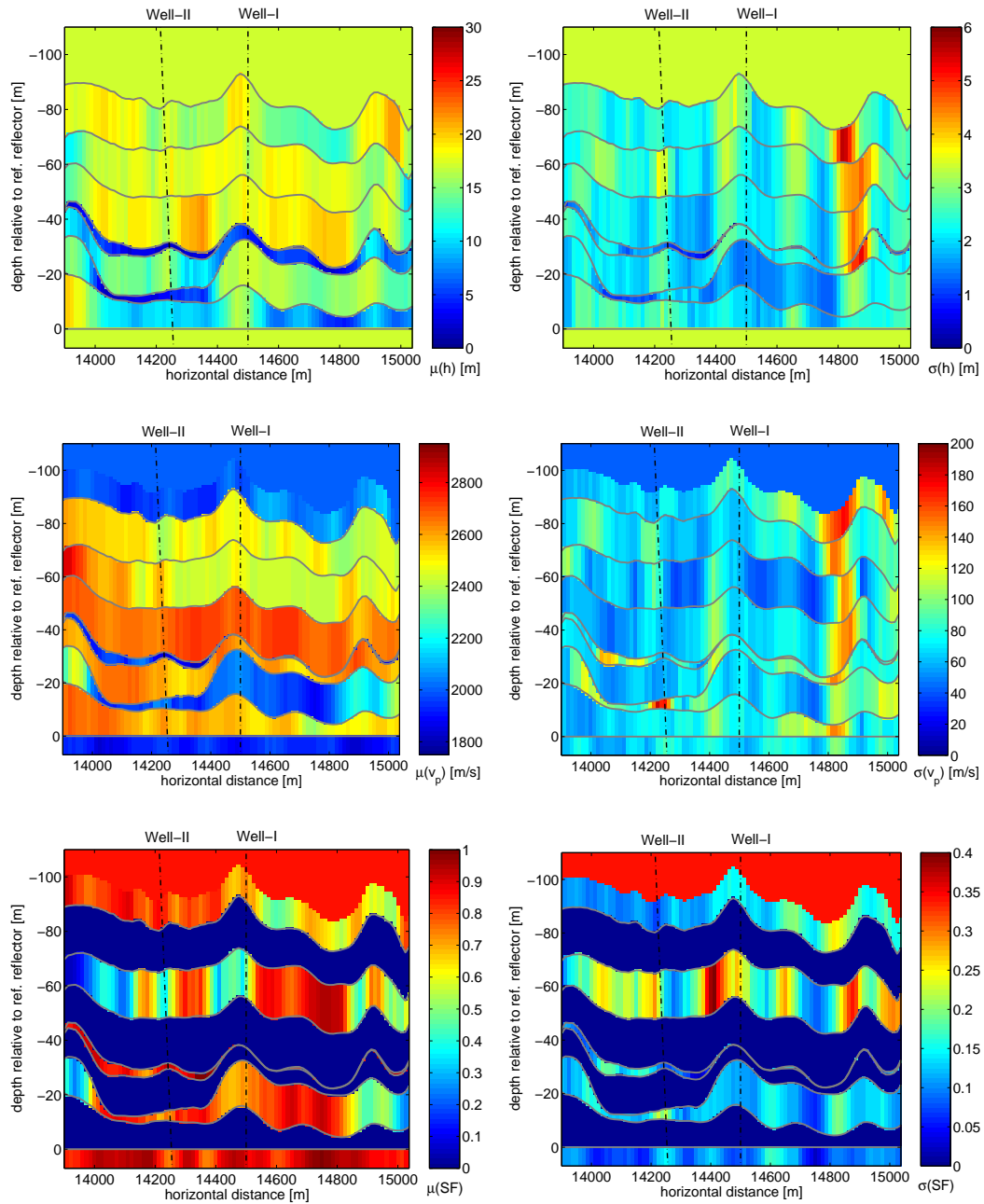


Figure 5.29: Overview of 1D convolutional RBSI posterior estimates for h (top), v_p (middle) and SF (bottom). On the left-hand side, means are shown, on the right-hand side, the corresponding standard deviations.

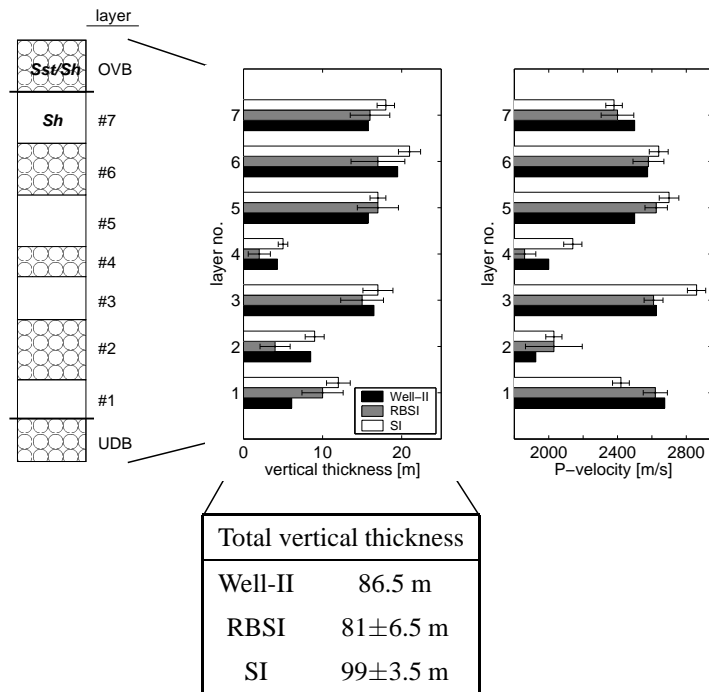


Figure 5.30: Vertical thickness h and P -wave velocity v_p at Well-II versus estimations for SI and 1D convolutional RBSI. Error bars denote standard deviations. Layer-numbering upward from reference reflector.

5.7 Comparison at Well-II

In the third part of the comparative test, the inversion results obtained with the old and new method are compared with the values found at Well-II in Fig. 5.30. A wide range of well-logs is available for interpretation of the sand and shale layers at Well-II, including gamma-ray, sonic (P- and S-wave), density and neutron. Gamma-ray and sonic logs are well suited to discern between sand and shale, since the rock properties for which these two logs are sensitive, clay-content and wave propagation velocity, are much different for the respective lithologies [Peeters, 1995; Ellis, 1987].

All logs for this deviated well are available in true vertical depth, converted from logging-depth along the well-trajectory. From the column of target layers (Figure 5.14, right-hand side), the sandstone-shale mixture layers UDB, #2, #4 and OVB are well discernable using the gamma-ray and sonic, due to

their high sand-fraction. In the area around Well-II, it is more troublesome to discern sand-shale mixture layer #6 due to its low sand-fraction, and consequently its low contrast with the surrounding shale-layers; additional trends from the neutron log were needed. After interpretation of the layers, per layer the average P-wave velocity was determined from the ‘blocked’ sonic (P) log.

Figure 5.30 shows that, generally, SI overestimates the layer-thicknesses, while 1D convolutional RBSI estimates are slightly better, with the values from Well-II within one standard deviation from the estimated means; however for the two thin layers #2 and #4 SI thickness-estimates are better (but still overestimated). The v_p -estimates are closer to the actual values using the new method.

Standard deviations are higher for the new method, due to the higher amount of noise on the offset gather as compared to the nearstack migrated section. The philosophy for ‘full’ RBSI is to reduce these standard deviations by adding more measurements (offset gathers) into the inversion; now only slightly less than 2% of all pre-stack data was used (one from 48 offsets). Moreover, an estimate with a larger standard deviation does not necessarily have to be worse: take for example the P-wave velocity estimates for layer #2. For this layer, the means are estimated about the same, however SI gives a misleadingly small standard deviation: the true value falls well outside the error bar.

The total package thickness of 86.5 m at Well-II is overestimated by SI, as predicted by theory, to 99 ± 3.5 m - the new method somewhat underestimates the package-thickness, but remains within one standard deviation from the true value: 81 ± 6.5 m.

Finally, note that Well-II is at a crossline distance of 200 m from the section; changes in reservoir properties may have occurred along this direction assumed invariant in the 2.5D configuration, although an inspection of the seismics does not suggest this (see the right-hand side of Figure 5.11).

5.8 Discussion

Inversion results from the Gulf of Mexico field dataset, shown in this chapter, indicate that the new method, 1D convolutional RBSI, has improved accuracy on the dipping part of the reservoir, where SI suffers from wavelet

stretch due to migration.

1D convolutional RBSI ideally inverts the normal-incidence dataset; in the field data the 575 m offset gather appeared to be the subset from the pre-stack unmigrated data closest to normal incidence with a useable signal-to-noise ratio. It is important to check and undo any pre-processing operations on the pre-stack unmigrated data that disturb the relative reflection amplitude behaviour.

To determine which part of the offset gather contains the reflection information from the inversion target and calibration well, elastodynamic ray-tracing was done down to the reference reflector picked from the migration image. Ray-tracing requires this reflector to be C_2 -smooth. In principle, this information could also have been obtained from the Kirchhoff-type migration preceding the inversion, by interpolations in the ray-trace diffraction grid. During wavelet derivation from the offset gather, again a 1D convolutional forward modeller was used, thereby neglecting the spherical spreading and transmission losses in the target, as well as the small extra traveltime (about 0.5% extra) in the target due to having small offset data while assuming zero-offset, and the small (i.e. non-zero) reflection angles of about 6° leading to slightly different reflection coefficients.

The SI prior model along the vertical direction of the traces from the migration image are transformed in a model for 1D convolutional RBSI along normal incidence rays to the reference reflector. Hereby those rays are assumed to go straight all the way through the inversion target, a consequence of the plane-parallel layering assumption for 1D convolutional RBSI.

A laterally varying overburden amplitude correction is applied to the offset gather before the actual inversion is done. The amplitudes required for this operation come from the same elastodynamic ray-tracing applied earlier for the positioning. In determining the overburden losses, the velocity model for ray-tracing needs to be somewhat smoothed, in a trade-off between kinematic accuracy and dynamic stability.

The time needed to invert a single trace (from the migrated and the pre-stack data, respectively) is the same for SI and 1D convolutional RBSI.

A further investigation of the performance of RBSI on these data is recommended: only 2% of the available pre-stack data has been used with 1D convolutional RBSI, whereas with 'full' RBSI each of the remaining common-offset gathers could be used as an independent means of verification of the

result obtained with 1D convolutional RBSI. Also, contrary to the 1D convolutional variant, the general method is capable of handling rays that have passed through caustic points. To obtain correct ray amplitudes also *near* the caustic points, one could make use of extensions of the ray method such as Gaussian beams in RBSI.

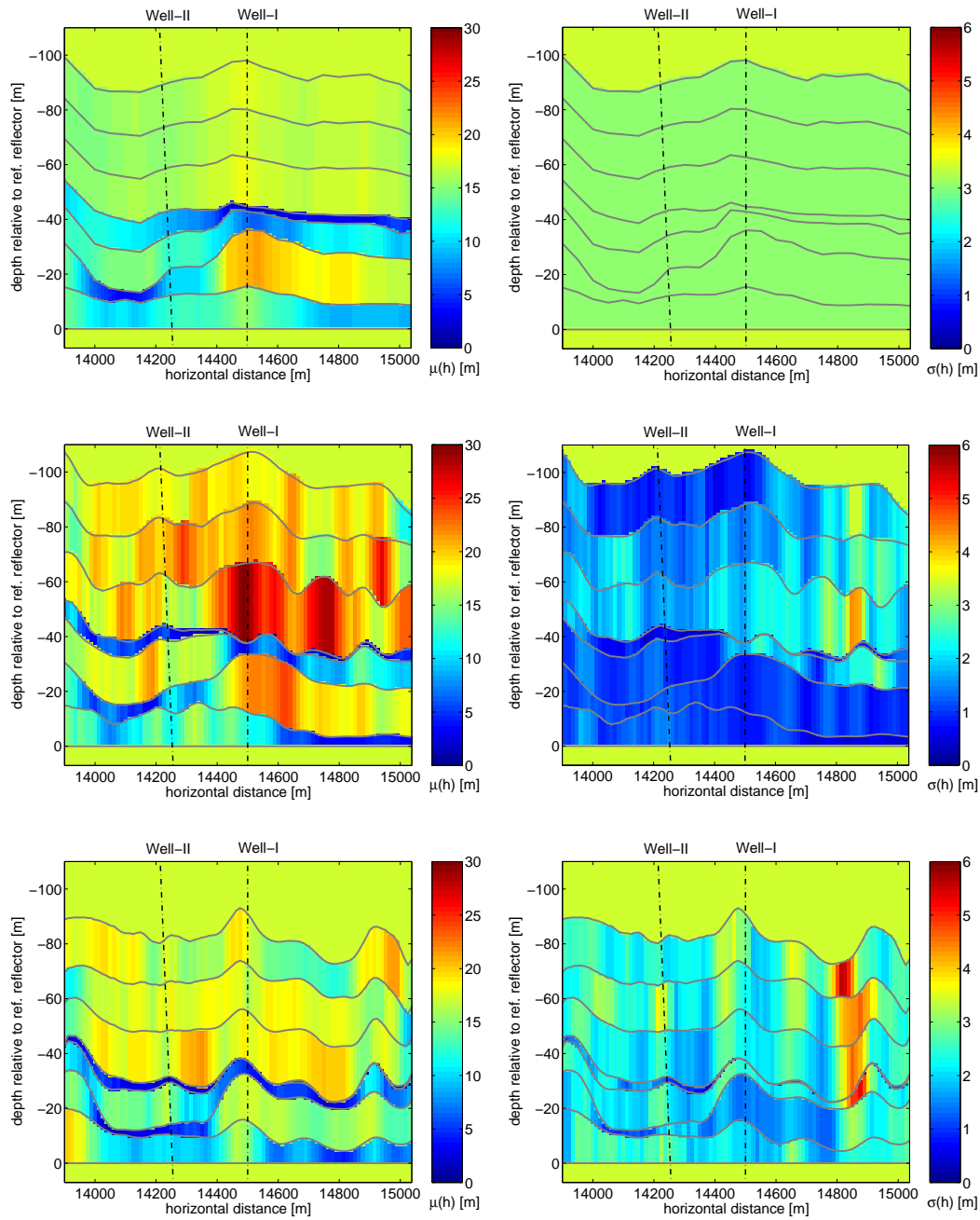


Figure 5.31: Overview of inversion results for thickness h . The means (left) and standard deviations are displayed for, from top to bottom, the prior model, SI estimates and 1D convolutional RBSI estimates.

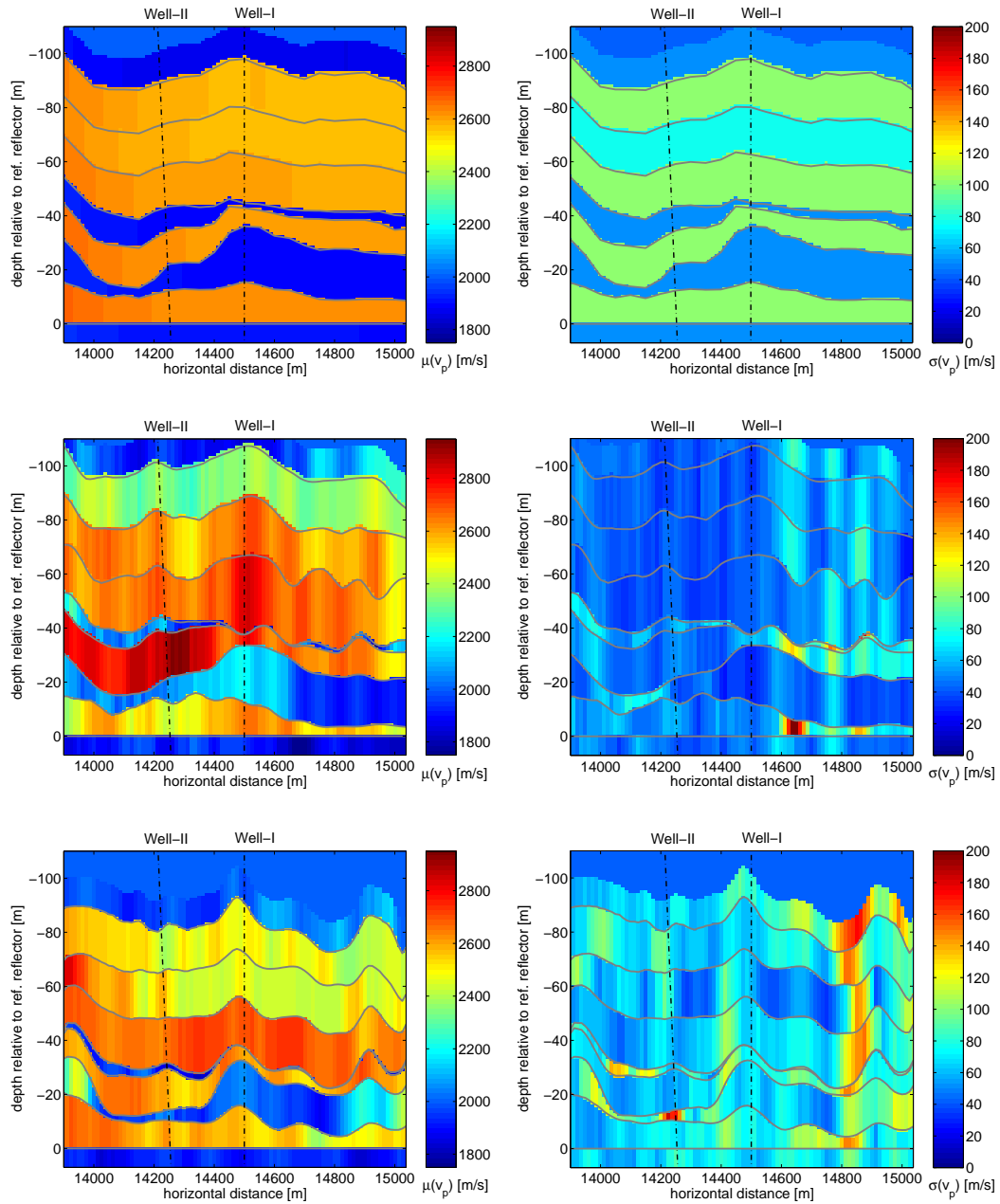


Figure 5.32: Overview of inversion results for P -wave velocity v_p . The means (left) and standard deviations are displayed for, from top to bottom, the prior model, SI estimates and 1D convolutional RBSI estimates.

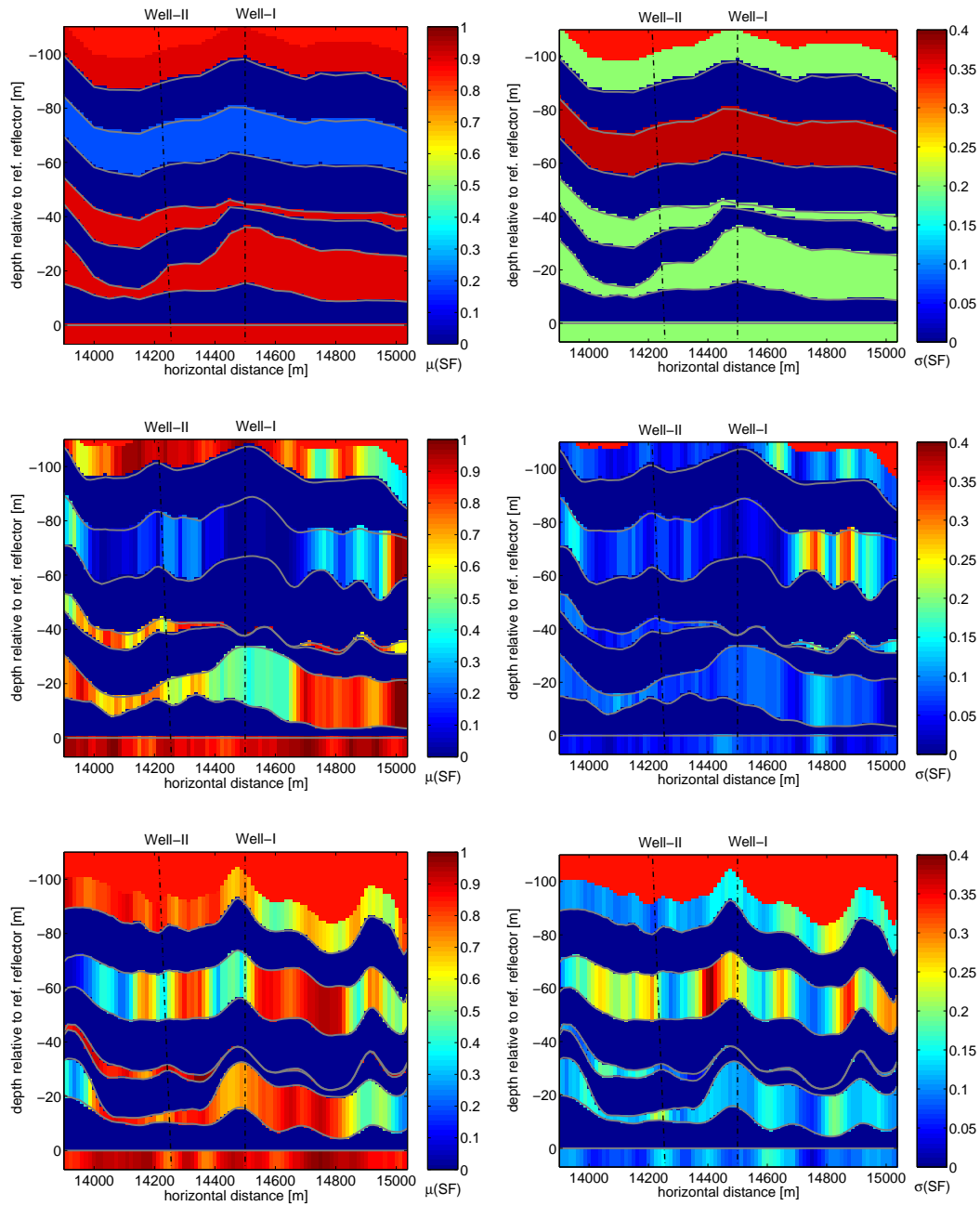


Figure 5.33: Overview of inversion results for sand-fraction SF . The means (left) and standard deviations are displayed for, from top to bottom, the prior model, SI estimates and 1D convolutional RBSI estimates.

Conclusions and recommendations

In this work, a new method for reservoir parameter estimation was introduced that inverts pre-stack seismic reflection data before migration using stochastic inversion along ray-paths. The novelty in the technique is the combination of ray-tracing and stochastic inversion, in order to use the original wave-path and reflection angle information contained in the pre-stack data for estimating reservoir parameters including uncertainties. The method is called ray-based stochastic inversion and can be regarded as a generalisation of current amplitude-variation-with-offset or -angle (AVO/AVA) techniques. By using a 3D elastodynamic ray-tracer to forward model reflection responses from the target, more ‘physics’ is put into the inversion kernel, as compared to the 1D convolutional model used in conventional stochastic inversion methods. Moreover, the usage of the ray-tracer as forward modelling engine makes it possible to interweave seismic trace inversion with Kirchhoff-type migration, in which ray-tracing is used as well.

The new method can be applied instead of standard stochastic inversion techniques for reservoir parameter estimation in a structurally complex subsurface with substantial lateral velocity variations and significant reflector dips. Also, a simplification of the new method was presented that makes use of local 1D convolutional forward modelling in the target depth interval, and inverts normal-incidence data. Although 1D convolution is less suitable than 3D ray-tracing in forward modelling of the reflection response in the target interval, it has the distinct practical advantage of being readily available in common inversion software.

6.1 Conclusions

From the results of the synthetic data tests and the field data test, three main conclusions can be drawn.

- The distortion of the wavelet in the seismic migration image as a function of reflector dip and reflection angle is an important effect that is not taken into account by conventional trace inversion techniques. The new method operates in the pre-stack unmigrated domain, therefore it is not affected by this migration-induced wavelet stretch.
- The pre-stack data before migration inverted by the new method contain the original angle-dependent reflection information needed for a good inversion for reservoir parameters. To the contrary, conventional trace inversion techniques operate on migrated (sub)stacks, where angle-dependent reflection information is sacrificed for better signal-to-noise ratio with respect to reflector positioning.
- When applied on normal-incidence data, the new method inverts along ray-paths that are perpendicular to the reflectors, the direction which offers optimal resolution for discerning the layering in the reservoir.

6.2 Recommendations for further research

A list of recommendations for further research is given on the next page.

- Rays calculated on the diffraction grid for preserved-amplitude Kirchhoff-type migration could be re-used in ray-based stochastic inversion for ray-tracing through the known overburden, to save computing time, and to integrate inversion with migration.
- In the field data test (Chapter 5), only a small portion of the available pre-stack data was used when 1D convolutional ray-based stochastic inversion was applied. With the general form of ray-based stochastic inversion, all common-offset gathers could be used as an independent means of verification of the obtained results. Also, contrary to the 1D convolutional variant, the general method is capable of dealing with multi-valuedness.
- To overcome the fact that ray amplitudes near caustic regions in the subsurface are unreliable, in ray-based stochastic inversion extensions of the ray-method such as Gaussian beams could be used as forward modeller instead of standard ray-method.
- The positions of diffracting edges could be determined using edge-diffraction migration techniques, so that areas in the unmigrated data suffering from diffraction events can be marked and avoided using the present implementation of ray-based stochastic inversion (of which the ray-tracer cannot forward model edge diffractions).
- For improved understanding of the influence that noise and stacking have on the reservoir parameter estimates obtained with the conventional and new methods, the offset test from Chapter 4 could be repeated with added noise of appropriate level pre- and post-stack.
- To better understand the effect of neglecting interbed multiples in the reflection response from the target, the new method could be tested with synthetic data that include these multiple arrivals, e.g. generated by finite-difference modelling.
- For improved forward modelling of the seismic reflection response from a thin-layered target, generally dominated by significant amounts of energy from multiple reflections, the wave propagation within the target could be modelled using a method for automated dynamic ray-tracing of these multiple reflections in addition to the required ray-tracing of the single P-wave reflections.

Bibliography

- Aki, K. and Richards, P. (1980). *Quantitative Seismology*, volume 1 of *Books in Geology*. W. H. Freeman and Company, San Francisco, 1st edition.
- Bakker, P. M. (1998). Phase shift at caustics along rays in anisotropic media. *Geophysical Journal International*, 134 (2), pp. 515–518.
- Berryhill, J. R. (1977). Diffraction response for nonzero separation of source and receiver. *Geophysics*, 42 (06), pp. 1158–1176. Discussion in GEO-43-06-1269-1269 with reply by author.
- Black, J. L., Schleicher, K. L. and Zhang, L. (1993). True-amplitude imaging and dip moveout. *Geophysics*, 58 (01), pp. 47–66.
- Bleistein, N., Cohen, J. and Stockwell Jr., J. (2001). *Mathematics of Multidimensional Seismic Imaging, Migration, and Inversion*. Springer, New York.
- Bortfeld, R. (1961). Approximation to the reflection and transmission coefficients of plane longitudinal and traverse waves. *Geophysical Prospecting*, 9, pp. 485–502.
- Bracewell, R. N. (1986). *The Fourier Transform and Its Applications*. McGraw-Hill.

- Brown, R. (1994). Image quality depends on your point of view. *The Leading Edge*, 13 (06), pp. 669–673.
- Brühl, M., Vermeer, G. J. O. and Kiehn, M. (1996). Short note - Fresnel zones for broadband data. *Geophysics*, 61 (02), pp. 600–604. Discussion and reply in GEO-62-1-381.
- van der Burg, D., Drijkoningen, G. and Margrave, G. (2006). Delft internet-based introduction course on reflection processing with Matlab. *First Break*, 24 (8), pp. 57–60.
- van der Burg, D., Verdel, A. and Wapenaar, K. (2004). Ray-based stochastic inversion. *74th Ann. Internat. Mtg.*, pp. 1607–1610. Soc. of Expl. Geophys.
- van der Burg, D., Verdel, A. and Wapenaar, K. (2005). Ray-based stochastic inversion for reservoir parameters using 1D convolutional forward modeling. *75th Ann. Internat. Mtg.*, pp. 1441–1444. Soc. of Expl. Geophys.
- van der Burg, D., Verdel, A. and Wapenaar, K. (2007). Ray-based stochastic inversion: improving reservoir characterisation in a Gulf of Mexico field. *77th Ann. Internat. Mtg.*. Soc. of Expl. Geophys.
- Castagna, J. P. (1993). Petrophysical imaging using AVO. *The Leading Edge*, 12 (03), pp. 172–178.
- Červený, V. (2001). *Seismic Ray Theory*. Cambridge University Press.
- Červený, V., Molotkov, I. A. and Pšenčík, I. (1977). *Ray Method in Seismology*. Univerzita Karlova, Praha.
- Červený, V. and Ravindra, R. (1971). *Theory of seismic head waves*. University of Toronto Press.
- Chen, J. and Schuster, G. T. (1999). Resolution limits of migrated images. *Geophysics*, 64 (4), pp. 1046–1053.
- Chen, Q. (1992). *Critical concentration models for the mechanical and acoustic properties of porous materials*. Ph.D. thesis, Stanford University.

- Deregowski, S. M. (1986). What is DMO? *First Break*, 4 (7), pp. 7–24.
- Draganov, D., Wapenaar, K., Mulder, W., Singer, J. and Verdel, A. (2007). Retrieval of reflections from seismic background-noise measurements. *Geophysical Research Letters*, 34, pp. L04305.
- Duijndam, A. J. W. (1987). *Detailed Bayesian inversion of seismic data*. Ph.D. thesis, Delft University of Technology.
- Duijndam, A. J. W. (1988a). Bayesian estimation in seismic inversion, part 1: Principles. *Geophysical Prospecting*, 36, pp. 878–898.
- Duijndam, A. J. W. (1988b). Bayesian estimation in seismic inversion, part 2: Uncertainty analysis. *Geophysical Prospecting*, 36, pp. 899–918.
- Duijndam, A. J. W. and Drijkoningen, G. G. (1997). *Parametric Inversion with Seismic Applications*. Delft University of Technology, 4th edition. Course notes MP4640.
- Dunkin, J. W. and Levin, F. K. (1973). Effect of normal moveout on a seismic pulse. *Geophysics*, 38 (04), pp. 635–642.
- Ellis, D. V. (1987). *Well Logging for Earth Scientists*. Elsevier.
- Fried, D. L. (1966). Optical resolution through a randomly inhomogeneous medium for very long and very short exposures. *J. Opt. Soc. Am.*, 56, pp. 1372–1379.
- Gerritsma, P. H. A. (2003). *Advanced topics in seismic data processing*. Centre for Technical Geoscience (CTG), Delft. Course notes TG115.
- Gray, S. H., Etgen, J., Dellinger, J. and Whitmore, D. (2001). Seismic migration problems and solutions. *Geophysics*, 66 (5), pp. 1622–1640.
- Guilloux, Y., Roberts, R., Bedingfield, J., Carr, M. and Mesdag, P. (2004). A case study of inversion of long offset p-wave seismic data into elastic parameters. *66rd Mtg.*, pp. D–8. Eur. Assn. Geosci. Eng.
- de Haas, J. C. (1992). *Elastic Stratigraphic Inversion, an Integrated Approach*. Ph.D. thesis, Delft University of Technology.

- Hertweck, T., Jäger, C., Goertz, A. and Schleicher, J. (2003). Aperture effects in 2.5D Kirchhoff migration: A geometrical explanation. *Geophysics*, 68 (5), pp. 1673–1684.
- Hubral, P. and Tygel, M. (1989). Analysis of the Rayleigh pulse (short note). *Geophysics*, 54 (05), pp. 654–658. Discussion and reply in GEO-56-1-148-149.
- Kallweit, R. S. and Wood, L. C. (1982). The limits of resolution of zero-phase wavelets. *Geophysics*, 47 (07), pp. 1035–1046.
- Kanasewich, E. R. and Phadke, S. M. (1988). Imaging discontinuities on seismic sections. *Geophysics*, 53 (03), pp. 334–345. Discussion in GEO-54-2-273-273.
- Khaidukov, V., Landa, E. and Moser, T. (2004). Diffraction imaging by focusing-defocusing: An outlook on seismic superresolution. *Geophysics*, 69 (6), pp. 1478–1490.
- Landa, E., Shtivelman, V. and Belchinsky, B. (1987). A method for detection of diffracted waves on common-offset sections. *Geophys. Prosp.*, 35 (04), pp. 359–373.
- Leguijt, J. (2001). A Promising Approach to Subsurface Information Integration. *63rd Mtg.*, pp. L–35. Eur. Assn. Geosci. Eng.
- Levin, S. A. (1998). Resolution in seismic imaging: Is it all a matter of perspective? *Geophysics*, 63 (02s), pp. 743–749.
- Mavko, G. (1998). *The rock physics handbook: tools for seismic analysis in porous media*. Cambridge university press, Cambridge, UK.
- Mavko, G. (2005). *Introduction to Rock Physics*. Stanford University. Course notes GP262.
- Mayne, W. H. (1962). Common reflection point horizontal data stacking techniques. *Geophysics*, 27 (06), pp. 927–938.
- Moore, G. E. (1965). Cramming more components onto integrated circuits. *Electronics Magazine*, 38 (8).

- Newman, P. (1975). Amplitude and phase properties of a digital migration process. Republished in: *First Break*, 8 (11), pp. 397–403, 1990.
- O’Doherty, R. F. and Anstey, N. A. (1971). Reflections on amplitudes. *Geophysical Prospecting*, volume 19, pp. 430–458. Eur. Assn. Geosci. Eng.
- Oldenburg, D. W., Scheuer, T. and Levy, S. (1983). Recovery of the acoustic impedance from reflection seismograms. *Geophysics*, 48 (10), pp. 1318–1337.
- Peeters, M. (1995). *Petrophysics: Basic Wireline Log & Core Analysis for Hydrocarbons, Coal, Minerals & Ground-Water*. Delft University of Technology. Course notes MP2400.
- Perez, G. and Marfurt, K. (2007). Improving lateral and vertical resolution of seismic images by correcting for wavelet stretch in common-angle migration. *Geophysics*, 72 (6), pp. C95–C104.
- Perroud, H. and Tygel, M. (2004). Nonstretch NMO. *Geophysics*, 69 (2), pp. 599–607.
- Popov, M. M. (1982). A new method of computation of wave fields using Gaussian beams. *Wave Motion*, 4, pp. 85–97.
- van Riel, P. and Berkhout, A. J. (1985). Resolution in seismic trace inversion by parameter estimation. *Geophysics*, 50 (09), pp. 1440–1455.
- Sambridge, M. and Mosegaard, K. (2002). Monte Carlo methods in geophysical inverse problems. *Reviews of Geophysics*, 40 (3), pp. 1–29.
- Schleicher, J., Tygel, M. and Hubral, P. (1993). 3-D true-amplitude finite-offset migration. *Geophysics*, 58 (08), pp. 1112–1126. Discussion in GEO-60-3-921.
- Sheriff, R. E. (1980). Nomogram for Fresnel-zone calculation (short note). *Geophysics*, 45 (05), pp. 968–972.
- Sheriff, R. E. (2002). *Encyclopedic dictionary of applied geophysics*. Number 13 in Geophysical references series. Society of Exploration Geophysicists, Tulsa, USA.

- Sheriff, R. E. and Geldart, L. P. (1995). *Exploration Seismology*. Cambridge University Press, 2nd edition.
- Shuey, R. T. (1985). A simplification of the Zoeppritz-equations. *Geophysics*, 50 (04), pp. 609–614. Errata in GEO-50-9-1522.
- Simmons, J. L. and Backus, M. M. (1994). AVO modeling and the locally converted shear wave. *Geophysics*, 59 (08), pp. 1237–1248.
- Tarantola, A. (2005). *Inverse problem theory and methods for model parameter estimation*. Society for Industrial and Applied Mathematics, Philadelphia, USA.
- Toxopeus, G., Petersen, S., Thorbecke, J. and Wapenaar, K. (2004). Simulating high-resolution inversion: Decomposing the resolution function. *74th Ann. Internat. Mtg.*, pp. 1798–1801. Soc. of Expl. Geophys.
- Toxopeus, G., Petersen, S. and Wapenaar, K. (2003). Improved geological modeling and interpretation by simulated migrated seismics. *73rd Ann. Internat. Mtg.*, pp. 2445–2448. Soc. of Expl. Geophys.
- Trorey, A. W. (1970). A simple theory for seismic diffractions. *Geophysics*, 35 (05), pp. 762–784.
- Tygel, M., Schleicher, J. and Hubral, P. (1994). Pulse distortion in depth migration. *Geophysics*, 59 (10), pp. 1561–1569. Discussion in GEO-60-6-1942-1949.
- Vanelle, C., Spinner, M., Hertweck, T., Jäger, C. and Gajewski, D. (2006). Traveltime-based true-amplitude migration. *Geophysics*, 71 (6), pp. S251–S259.
- Veeken, P. C. H. and Da Silva, M. (2004). Seismic inversion methods and some of their constraints. *First Break*, 22 (6), pp. 47–70.
- Verdel, A. (1983). *Adaptation of a program package for two-dimensional dynamic ray tracing to interactive use, with applications to seismological modeling problems*. Master's thesis, University of Utrecht.

- Verdel, A., van der Burg, D. and Wapenaar, K. (2004). Ray-based stochastic inversion. *66rd Mtg.*, pp. C–31. Eur. Assn. Geosci. Eng.
- Vermeer, G. J. O. (1990). *Seismic Wavefield Sampling*. Society of Exploration Geophysicists.
- Walden, A. T. (1985). Non-Gaussian reflectivity entropy and deconvolution. *Geophysics*, 50 (12), pp. 2862–2888.
- Wapenaar, C. P. A. and Berkhout, A. J. (1989). *Elastic Wave Field Extrapolation*. Elsevier.
- Wapenaar, K. (1998). Short Note - Reciprocity properties of one-way propagators. *Geophysics*, 63 (05), pp. 1795–1798.
- Wapenaar, K., van Wijngaarden, A. J., van Geloven, W. and van der Leij, T. (1999). Apparent AvA effects of fine layering. *Geophysics*, 64 (6), pp. 1939–1948.
- White, R. and Simm, R. (2003). Good practice in well ties. *First Break*, 21 (10), pp. 75–83.
- Widess, M. B. (1973). How thin is a thin bed? *Geophysics*, 38 (06), pp. 1176–1254.
- Yilmaz, O. (2001). *Seismic data analysis: processing, inversion and interpretation of seismic data*. Society of Exploration Geophysicists, Tulsa, USA, 2nd edition.
- Young, G. B. and Braile, L. W. (1976). A computer program for the application of Zoeppritz's amplitude equations and Knott's energy equations. *Bulletin of the Seismological Society of America*, 66 (6), pp. 1881–1885.

Curriculum Vitae

Dennis Wilhelmus van der Burg was born at Zoetermeer (near The Hague), the Netherlands, on the 11th of November, 1976. He attended secondary school at the Oranje Nassau College in Zoetermeer, where he obtained the VWO diploma in 1995. In that same year he started his study Mining and Petroleum Engineering at the Delft University of Technology.

He received his 'propedeuse' in 1996 and continued for his M.Sc. degree. In 2002 he was awarded the title of 'Mijnbouwkundig Ingenieur' cum laude. His M.Sc. thesis dealt with the source decomposition and receiver composition of electrokinetic signals and was under the supervision of prof. dr. ir. C.P.A. Wapenaar and A.R. Shaw, M.Sc.

Later in 2002, he started with his Ph.D. research, a joint project between the Exploratory Research department of Shell International Exploration and Production B.V. in Rijswijk, and the section Applied Geophysics and Petrophysics in the department of Geotechnology, faculty of Civil Engineering and Geosciences at the Delft University of Technology. The project was under the supervision of drs. A.R. Verdel at Shell, and of prof. dr. ir. C.P.A. Wapenaar at the Delft University of Technology. The work on the project was presented at several conferences around the world. In 2005, the presentation at the annual meeting of the Society of Exploration Geophysicists in Houston, USA, ranked in the top 25 papers presented.

Acknowledgements

The research presented in this thesis was carried out at two locations: the Exploratory Research department of Shell International Exploration and Production B.V. in Rijswijk, and the department of Applied Geophysics and Petrophysics, section of Geotechnology, Faculty of Civil Engineering and Geosciences at Delft University of Technology. I would like to thank all colleagues at both departments for the pleasant time and inspiring scientific discussions. Especially, I would like to thank Arie Verdel and Kees Wapeenaar for all their input and advice. Arie Verdel, my daily supervisor, was of invaluable help in choosing the right directions during the research, and was always prepared to give additional explanations or to thoroughly review anything I wanted to publish or present. Also I would like to thank Michiel Groeneveld for his continuous support to this long-term project in the fast-moving world of Shell.

In Rijswijk, I am much indebted to Jaap Leguijt, Boudewijn Salomons, Mark Verschuren, Sevgi Tiğrek, Barbara Cox, Diederik van Daalen, Peter Bakker, Wicky Derks and Kees van der Kolk for helping me out with using the various Shell-software packages; without you I would not have been able to get a quick start. Also, I would like to thank Paul Gary, who was — despite all the troubles in hometown New Orleans due to hurricane Katrina — taking care of all the arrangements required between Rijswijk and Houston for obtaining the field data from the Gulf of Mexico. Wouter de Koning made a beautiful

design for the graphics dealing with wave propagation and the poster for the 2004 SEG-conference in Denver; I am sure I had the best looking poster at that conference! I re-used the background of the poster for the cover of this thesis.

In Delft, I would like to thank Guy Drijkoningen for pointing me to the effects of migration wavelet stretch, and for the joyful time I had in setting up and giving the practical course ‘Introduction to Reflection Seismology’; we even got a paper out of it: [van der Burg et al. \[2006\]](#). Also, I would like to express my gratitude to Rick Donselaar for giving me the opportunity to see the differences between seismic scale and reservoir scale in the field during the Huesca-fieldwork, and to Maaïke van Tooren: I very much enjoyed creating the website for the Museum of Mineralogy and Geology, and occasionally giving guided tours in the museum.

Now some thanks to other colleagues and students. In Rijswijk: Annemieke, Patrick [great museum visits we have done!], Hennie, Wolf [who kept my German language skills up-to-date by lending me a very good German book and German Macintosh magazines], Susanne, Andreas, Boris, Alex, ‘hiking friends’ Bart and Mari, Leontine, Christen, Oras, Anton and Sergey all the way from Yekaterinburg, Chintan, Colin and Mun. In Delft: Gerrit [the Japan-trip was fabulous!], Friso, Deyan, Jan, Guus [that old HP workstation is running NeXT now], Antonio, Aletta and Petar from the ‘Balkan’ room, Oana, Lili, Marit, Wiebke, Christiaan, Ali, Karel, Daria, Nihed and of course all my other roommates from room 3.120.

I end with expressing my gratitude to my parents Wim and Cornelia and my brother Serge for their faith, support and patience.